Heteroepitaxial boron-doped diamond: from synthesis to application

Thesis

for the attainment of the
PhD degree in Natural Sciences
(Dr. rer. nat.)

submitted by

André F. Sartori

Lehrstuhl für Experimentalphysik IV
Institut für Physik
Universität Augsburg

April 2016

Universität Augsburg
Mathematisch-Naturwissenschaftlich-
Technische Fakultät

First examiner: Prof. em. Dr Bernd Stritzker
Second examiner: Prof. Dr Hubert Krenner

Date of the oral examination: 31.05.2016

Dedicated to my parents.
Dedicado aos meus pais.

Contents

Preface

Diamond is much more than a precious gemstone desired for its brilliance, beauty and hardness. It is a material with extraordinary properties that has found a place at the leading edge of technology, earning the reputation of material of the future, despite being known for thousands of years. The development of techniques to synthesise diamond in the laboratory, such as HPHT (high-pressure, high-temperature synthesis) and CVD (chemical vapour deposition), opened the way for its application in many fields of technology as anti-wear coatings, high-quality optical elements, radiation detectors and dosimeters. More recently, fascinating new potential applications appeared in quantum computing, high-power high-frequency electronics, lasing systems, in biochemical and electrochemical sensing, as nanoscale magnetometers, in water treatment and purification systems, and others. The production of synthetic (man-made) diamond has developed to an industrial level, with major players already established, such as *Element Six* (from the *De Beers Group*) and *Sumitomo* supplying various grades of diamond (single- and polycrystalline, doped and undoped, large and small, from industrial grade to optical and electronic grade, etc.), as shown in **Figure 1**. Synthetic diamond is also continuously gaining importance in the jewellery business (*Scio Diamond*, *Diamond Foundry*, *Brilliant Earth*, *Diamond Nexus* and others), where the colour and transparency of the grown gemstones can be precisely tuned for the desired product. Lower costs and the implicit advantage of a "conflict-free" source are important benefits in the competition with brilliants manufactured from natural crystals. But still, diamond technology is in its infancy, and much progress still has to be made before it can claim part of the dominance that silicon enjoys and become a ubiquitous element in daily life.

Arguably, the main bottleneck for the massive application of diamond in cutting-edge technology is the difficulty to grow high-quality crystals with economically relevant sample size, or to grow large crystals with high enough quality or specific properties for the desired applications. Diamond single crystals of the highest quality can be obtained by CVD growth on a HPHT substrate in a clean environment up to areas of ~1 cm^2, whereas wafer-size (2″, 4″ or more) polycrystalline samples are already established. The polycrystalline nature prevents diamond devices from achieving the ultimate performance levels expected from single crystal diamond (SCD) in certain applications. Therefore, other technological approaches are being developed by different research groups to bridge that gap, the two most relevant being homoepitaxy combined with tiling, and heteroepitaxy. The former involves laterally aligning several individual small high-quality crystals and overgrowing them homoepitaxially by CVD to produce a larger crystal, while the latter involves growing wafer-size single crystals, using a platform other than diamond as the substrate. Each method has its advantages and disadvantages.

This work focuses on diamond grown heteroepitaxially on iridium single crystal films, which is the field of expertise of our research group. This technique enables, in a very streamlined fashion, the growth of diamond films and bulk crystals of several cm^2 and up to 1-2 mm thick, which can be then processed (cut, shaped, polished, etc.) according to the final application. Diamonds synthesised in this way possess distinct, or rather, unique characteristics in terms of residual structural defects, which are inherent to the heteroepitaxial growth process. Characterising these defects and studying their influence on the performance of devices manufactured from heteroepitaxial diamond is of paramount importance for first applications in the near future, as well as for further material optimisation strategies.

Many of the diamond-based technologies of interest require semiconducting or conducting diamond in their structure, and due to the particular nature of heteroepitaxial diamond, there is an interest to investigate how the dopant, *i.e.* boron, behaves in this distinct environment, and how it changes heteroepitaxial diamond growth and the properties of this material. This topic is not only technologically relevant, but also scientifically, because it addresses fundamental aspects of diamond synthesis, impurity incorporation and defect formation, which are relevant to the whole diamond community. From a technological point of view, it is of interest to assess the performance of devices and sensors realised with such special material, and to place them in the spectrum of diamond-based devices alongside the existing solutions. The ultimate goal behind this work is, therefore, to develop heteroepitaxial diamond to a level which facilitates the realisation of competitive high-end electronic devices and sensors.

This thesis is presented in a logical (rather than chronological) sequence, *i.e.* from synthesis to application, revolving around heteroepitaxial diamond, but with special emphasis on boron-doped diamond. It is organised in the following way:

- Chapter 1 (the basics): presentation of fundamental aspects and properties of diamond, followed by a description of growth techniques with particular focus on heteroepitaxy on Ir, and a brief description of other relevant concepts/techniques used in this work;
- Chapter 2 (synthesis): presentation of studies of the growth environment of diamond during MWPCVD (microwave plasma-enhanced chemical vapour deposition), involving interaction of gas precursors, growth rate and boron-doping;
- Chapter 3 (properties): studies of structural properties and defects in the grown crystals, focussing mainly on identification and characterisation of dislocations in the diamond;
- Chapter 4 (application): presentation of a comprehensive electrochemical characterisation of B-doped heteroepitaxial diamond applied as electrochemical sensors;
- Chapter 5 (application): presentation of first results of Schottky diode rectifiers for high-power, high-frequency switching, manufactured from heteroepitaxial diamond.

Chapter 1 sets the common background to all the others, and the thesis is finished by a global summary in chapter 6. At the very end, in chapter 7, a collection of supplementary information referred to in specific parts of the thesis is given for consultation.

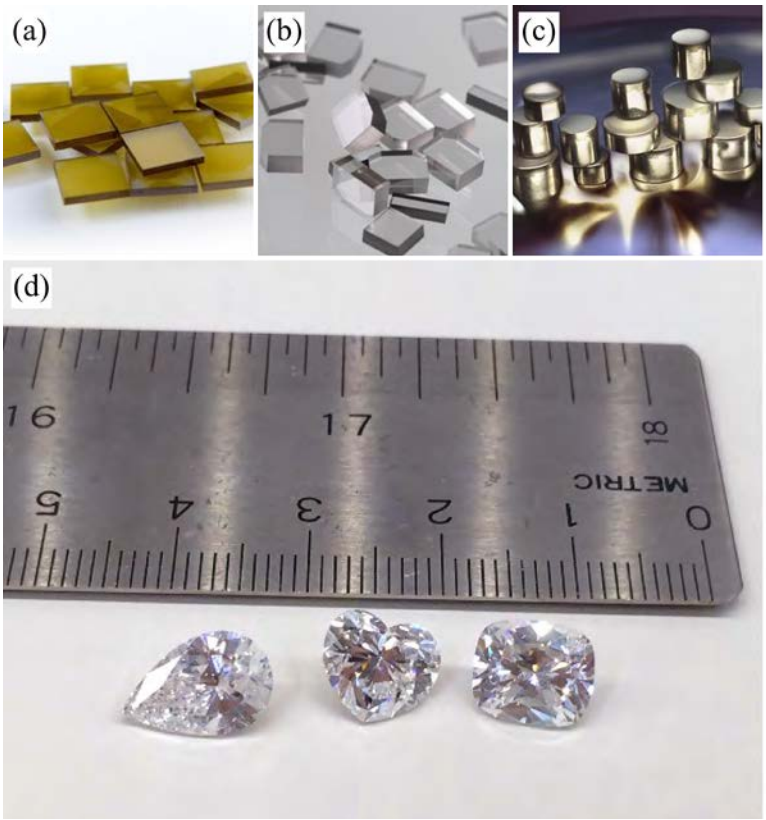

Figure 1: (a) HPHT crystals, (b) homoepitaxial diamond single crystals grown by CVD, (c) polycrystalline diamond-coated steel, (a-c) from *Element Six*[1], (d) three colourless HPHT-grown diamond gems produced by *New Diamond Technology*[2].

---

[1] Website: http://www.e6.com/wps/wcm/connect/E6_Content_EN/Home/Materials+and+products/

[2] The Quarterly Journal of the Gemological Institute of America, vol. 51, no. 3 (2015).

1 Fundamentals

1.1 Diamond properties

Diamond is one of the few allotropic forms of carbon (the sixth element in the periodic table, symbol **C**), among lonsdaleite, amorphous carbon, graphite, fullerenes, carbon nanotubes and graphene. In the cubic allotrope, 8 carbon atoms per unit cell are arranged in the so-called diamond lattice, a structure that can be understood as two interpenetrated face-centred cubic (fcc) Bravais lattices shifted along the body diagonal by $\left(1/4,1/4,1/4\right)a$, with $a = 0.3567\,\mathrm{nm}$ at 20 °C [1]. In this structure, the carbon atoms are sp^3-hybridised, *i.e.*, the 2s and the three 2p orbitals combine to form a tetrahedral assembly, allowing each carbon atom to bond with 4 other neighbours (see **Figure 1-1**). At ambient conditions, diamond is a metastable phase, while graphite has a lower total energy (the Gibbs free energy of graphite is 2.87 kJ/mol less than that of diamond). The nearest-neighbour distance between the covalently bonded carbon atoms in diamond is 0.154 nm at room temperature, a small value compared with other semiconductors (*e.g.* 0.234 nm for Si) [2].

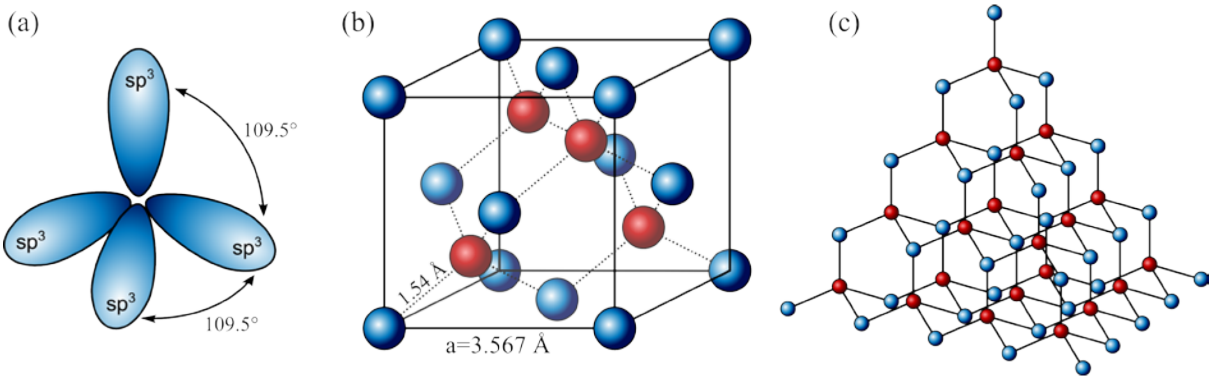

Figure 1-1: (a) sp^3-hybridised orbitals of a carbon atom. (b) Diamond unit cell. The underlying structure is fcc with a diatomic base. One of the two atoms is sitting on the lattice point (blue) and the other one (red) is shifted by $a/4$ along each axis. This forms a tetrahedral structure (c) where each atom is surrounded by four equal-distanced neighbours.

The tetrahedral bonding environment with short and strong bonds results in the highest atomic packing of all solid materials ($1.77\times10^{23}\,\mathrm{cm}^{-3}$). Furthermore it gives rise to unique mechanical properties, like the highest Young's modulus, $E \cong 1100\,\mathrm{GPa}$, and the highest thermal conductivity, $\kappa \cong 2500\ \mathrm{W\,m^{-1}\,K^{-1}}$ (reported for high-quality type IIa single crystals) [1]. Pure diamond is electrically an insulator.

In contrast to diamond, in graphene the carbon atoms are sp^2-hybridised, each forming strong in-plane σ-bonds with its three nearest neighbours in a honeycomb (hexagonal) structure. The remaining fourth electron in the non-hybridised p$_z$ orbital forms additional in-plane π-bonds. The double bonds, which are delocalised, reduce the interatomic distance from 0.154 nm (pure σ-bond in diamond) to 0.142 nm and cause a highly anisotropic in-plane conductivity. Stacking many of such sheets gives rise to graphite, where the layers are weakly bound by van der Waals forces. The interlayer distance is 0.335 nm. As a consequence, the layers can be easily displaced and separated, giving bulk graphite the softer mechanical properties that it is known for. Imperfect diamonds, namely those of a polycrystalline nature, possess defects and grain boundaries containing graphitic (sp^2) and/or amorphous (sp^2/sp^3) carbon.

The electronic band structure and the phonon dispersion curves of diamond are shown, respectively, in **Figure 1-2** (a) and (b). The most important feature in (a) is the energy gap between CB_{min} (conduction band minimum) and VB_{max} (valence band maximum), which has a value of $E_G = 5.49\,\mathrm{eV}$ and is indirect, meaning that for an electron to be excited from the valence band to the conduction band it needs to gain 5.49 eV and also transfer momentum with the lattice by means of a phonon.

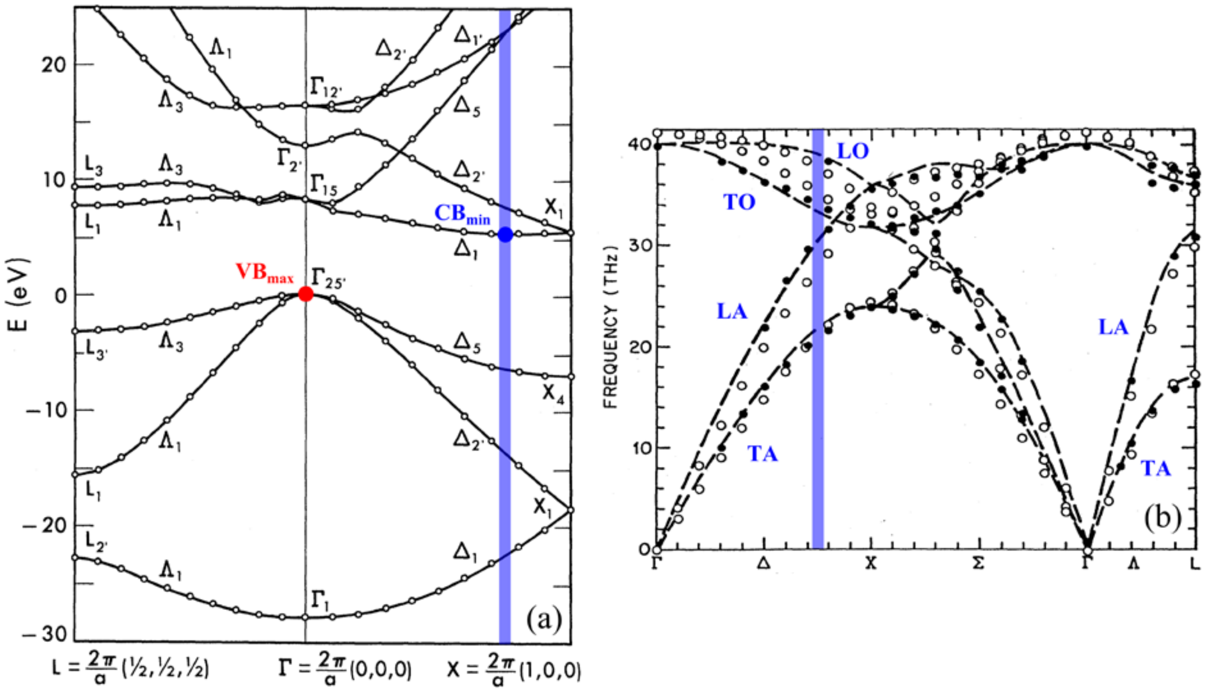

Figure 1-2: (a) The electronic band structure of diamond [3]. (b) The phonon dispersion curves of diamond [4]. The position of the conduction band minimum (CB_{min}) at $\vec{k} = 0.76\pi/a[100]$ is marked by the blue lines, the valence band maximum (VB_{max}) is marked in red, and the vibrational modes for TA (transverse acoustic), LA (longitudinal acoustic), TO (transverse optical) and LO (longitudinal optical) phonons are also indicated in (b).

An excited electron-hole pair in diamond forms a pseudo-hydrogenic system due to coulombic attraction between them, forming an exciton with a binding energy $E_x = 80\,\mathrm{meV}$ and an effective radius $r_{ex} = 1.58\,\mathrm{nm}$. At low temperature, once excited to the conduction band, the electron will de-excite rapidly (in picoseconds) to the minimum in the conduction band, located at a wave vector $k = 0.76 \pm 0.002$ of the zone-boundary value along the $\langle 001 \rangle$ axes. Similarly, the hole will de-excite to its minimum energy in the valence band at $k = 0$. Recombination of the electron-hole pair in diamond requires the wave vector to be conserved by emitting a phonon with $k_{001} = 0.76 \pm 0.002$. Selection rules result in three of the phonons at that wave vector being identifiable: TA (transverse acoustic), TO (transverse optical) and LO (longitudinal optical). See **Figure 1-2** (b). The energy of the photon emitted by recombination of the exciton is then reduced from the free exciton bandgap energy E_{Gx} by the energy $\hbar\omega$ of each phonon (see **Table 1-1**) [2, 5]:

$$h\nu = E_{\mathrm{Gx}} - \hbar\omega \tag{1.1.1}$$

This recombination mechanism results in diamond having a characteristic luminescence spectrum with near-bandgap peaks due to excitonic recombination involving different phonons. The most intense of them is $\mathrm{FE}^{\mathrm{TO}}$ (free exciton recombination assisted by a transverse optical phonon) at ~235 nm. Impurities such as boron or phosphorus will introduce emission peaks from impurity-bound excitons (BE), while other types of defects involving nitrogen, silicon, dislocations, etc. will manifest in several peaks and bands in the visible spectrum, due to impurity/defect-related energy levels in the bandgap.

Table 1-1: Phonon energies, exciton energy gaps and binding energies measured at 100 K [5].

Parameter	**Energy (eV)**	**Description**
$\hbar\omega_{\mathrm{TA}}$	0.087 ± 0.002	Transverse acoustic phonon at the conduction band minimum
$\hbar\omega_{\mathrm{TO}}$	0.141 ± 0.001	Transverse optical phonon at the conduction band minimum
$\hbar\omega_{\mathrm{LO}}$	0.163 ± 0.001	Longitudinal optical at the conduction band minimum
$\hbar\omega_{\mathrm{R}}$	0.167 ± 0.002	Zone centre (Raman) phonon
E_{Gx}	5.409 ± 0.002	Indirect exciton energy gap related to the upper valence bands
E'_{Gx}	5.416 ± 0.002	Indirect exciton energy gap related to the lower valence band
E_{x}	0.080 ± 0.005	Binding energy of the indirect exciton
E_{G}	5.490 ± 0.005	Indirect energy gap related to the upper valence bands
$E_{4\mathrm{x}}$	0.053 ± 0.002	Binding energy of the upper valence band indirect exciton to the neutral boron acceptor
$E'_{4\mathrm{x}}$	0.048 ± 0.002	Binding energy of the lower valence band indirect exciton to the neutral boron acceptor

With diamond being a homopolar solid, in its pure form it does not have electrostatic dipole moments. The derivative of the dipole moment with respect to any deformation is also zero, and so diamond does not satisfy the necessary condition for first-order absorption of infrared radiation with the creation of a phonon. However, two-phonon processes are possible, and give rise to absorption structures at around 2000 cm^{-1}. The triply degenerate optical phonon modes at the Γ point result in one characteristic peak centred at 1332.4 cm^{-1} in Raman scattering. Stress can shift and split the Raman peak into 2 or 3 components. Inhomogeneous stress (micro stress) is a common source of peak broadening. Furthermore, finite crystal size effects can contribute to an increased full width at half maximum (FWHM) of the Raman line [6].

1.2 Diamond synthesis

The synthesis of diamond was the goal of alchemists since historical times, and only in the 20th century were diamond crystals synthesised in high-pressure high-temperature (HPHT) cells. Later, diamond films were prepared using CVD (chemical vapour deposition). See **Figure 1-3** to identify the two growth regimes in the phase diagram of carbon. The earliest reports of CVD growth of diamond were from Russia, the United States, and Japan. Stimulated by both the unique characteristics of the material and its potential applications (and supported by the achievement of higher deposition rates), by the late 1980s, researchers from around the world were preparing diamond films using home-made plasma-enhanced or hot filament CVD systems [7], while commercial CVD systems for diamond growth started to become available.

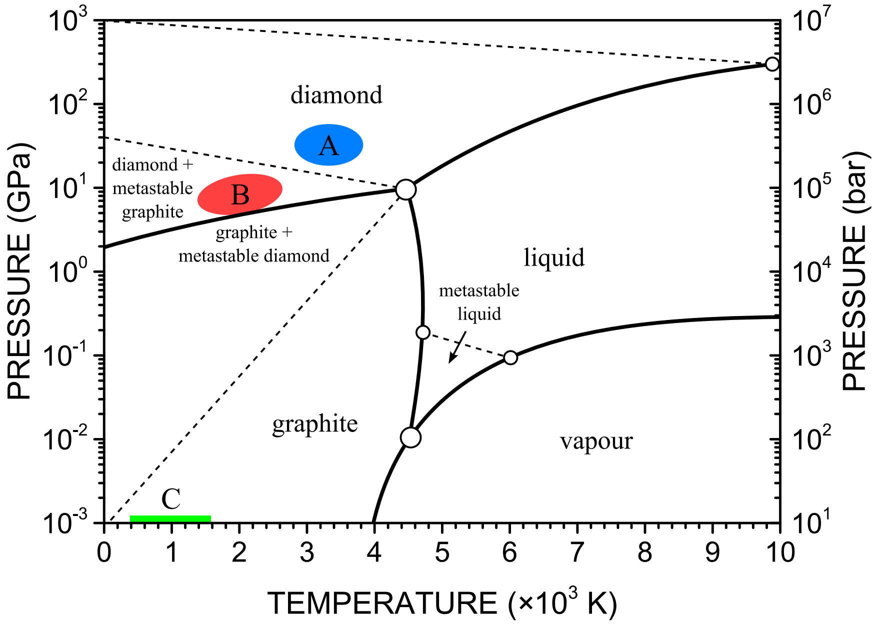

Figure 1-3: Phase diagram of carbon, according to [1, 8-10]. “A” marks the region of high-pressure high-temperature (HPHT) synthesis, “B” marks the region of catalysed HPHT synthesis and “C” marks the region of metastable chemical vapour deposition (CVD). The boundary between diamond and graphite is given by $P(\mathrm{GPa}) = 1.26 + 0.0025 \times T(\mathrm{K})$ [1].

Today, CVD diamond films are prepared with high purity, and these materials resist electrical breakdown in high electric fields (20 MV cm^{-1} [11]), and exhibit electron and hole mobility values which are the highest among wide bandgap semiconductors ($\mu_p = 1800$ cm^2 V^{-1} s^{-1} and $\mu_n = 2200$ cm^2 V^{-1} s^{-1}) [12]. Other authors reported even higher values [13].

1.2.1 High-pressure high-temperature (HPHT) synthesis

High pressure diamond is synthesised from other forms of carbon (especially graphite) at conditions where diamond is thermodynamically more stable than graphite. However, the diamond stable condition (see **Figure 1-3**) is not sufficient for the synthesis, because the activation energy of direct conversion (solid-solid transformation) from graphite to diamond is very large, and very high temperatures and pressures are required. This is achieved with powerful multi-anvil-type presses. The high-pressure, high-temperature (HPHT) synthesis can generate diamond in single crystal form, polycrystalline aggregates and powder, depending on the conditions. Single crystal synthesis can be direct or catalysed by the addition of other elements, especially metals, which act as solvents for carbon. Other elements can also be used, and they catalyse HPHT diamond formation through different mechanisms [1].

It is understood that HPHT diamond grows from solutions supersaturated with carbon. In the presence of a temperature gradient in the catalyst solution, carbon dissolved in a higher temperature region is transported to a cooler region, and there the solution becomes supersaturated. When a seed crystal is placed at the cooler region, the carbon precipitates on the seed, and a large crystal grows. This mechanism, termed the “temperature gradient method” can produce large crystals above 1 cm in lateral size.

1.2.2 Microwave plasma-enhanced chemical vapour deposition (MWPCVD)

Chemical vapour deposition of diamond is a complex chemical process that relies on the activation of gas precursors, usually $H_2 + CH_4$, by an ionising (*e.g.* microwave) or thermal (*e.g.* hot filament) source, to produce radicals which react on the surface of the substrate to promote diamond growth.

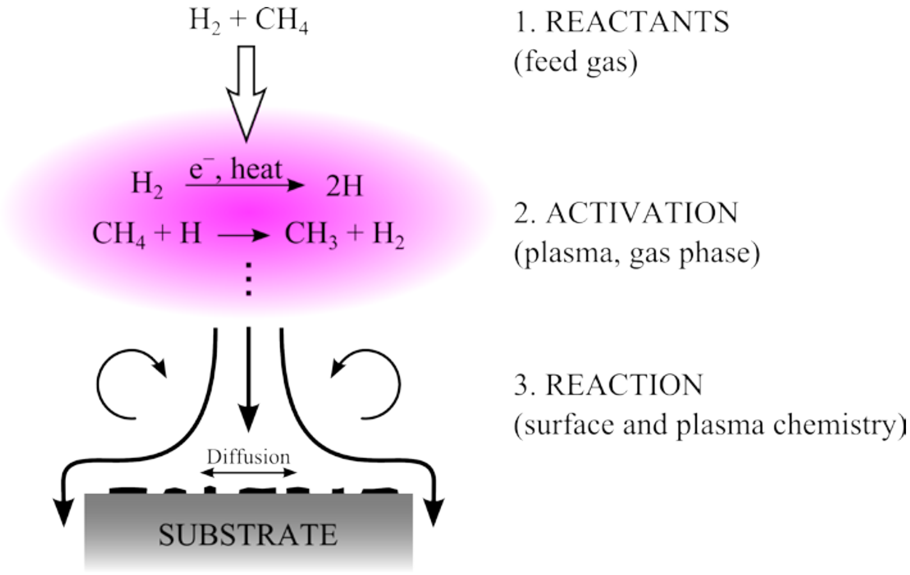

Figure 1-4: Schematic of processes occurring during diamond CVD [5].

Atomic hydrogen is the key element driving CVD of diamond. In low-pressure (~20-40 mbar) plasma-enhanced systems, such as microwave, RF or DC arcjet reactors, the external energy input couples directly to the free electrons in the plasma, producing energetic electrons which may have several eV of energy, and may directly produce H according to equation (1.2.1). This reaction proceeds through successive vibrational excitation of H_2 by electron impact, leading finally to dissociation [5]. When the pressure increases above ~130 mbar, dissociation of H_2 by collisions with heavier particles becomes significant and the plasma temperature can reach 3000-5000 K.

$$\mathrm{H_2 + e^- \rightarrow 2H + e^-} \tag{1.2.1}$$

The steady-state level of atomic hydrogen in the reactor is determined by a balance of the H atom production rate and the consumption (recombination) rate. Under typical low-pressure conditions, the rate of homogeneous recombination, which is pressure-dependent, is slow, and H atoms can diffuse to the substrate before recombining in the gas. The rate of direct recombination reaction can be represented by:

$$\mathrm{2H + M \rightarrow H_2 + M}\,, \tag{1.2.2}$$

where M is a foreign body.

In the presence of a small amount of hydrocarbon, the reaction (1.2.2) competes with two other paths:

$$\mathrm{H + CH}_{y-1}\mathrm{ + M \rightarrow CH}_{y}\mathrm{ + M} \tag{1.2.3}$$

$$\mathrm{H + CH}_{y} \rightleftharpoons \mathrm{CH}_{y-1}\mathrm{ + H_2}\,, \tag{1.2.4}$$

where the indice *y* ranges from 4 to 1 and is used to represent “H-shifting” reactions driven by atomic hydrogen.

H is strongly consumed at the diamond surface, which acts as a sink, and is a predominant radical in the CVD environment. At the same time, the concentration of carbon-containing radicals, especially CH_3^*, increases with increasing hydrocarbon content, and is independent from the source, whether it is CH_4 or C_2H_2 [5]. The following mechanism is believed to take place at the diamond surface, in what is considered to be the “standard model” for MWPCVD of diamond [14]:

1. The diamond lattice is stabilised and prevented from rearranging to graphitic carbon by termination with hydrogen atoms (or similar chemical species);
2. The H atoms created by the gaseous activation process also abstract hydrogen from the surface C−H bonds, thereby creating surface radical sites;
3. These radical sites will occasionally react with gas phase carbon-containing radicals, resulting in an adsorbed carbon species. Much more frequently, however, the radical sites are simply refilled by recombining with gaseous H atoms. This constant turnover

of the surface-terminating species (hydrogen) further drives the surface chemistry to dehydrogenate the adsorbed carbon species and to incorporate carbon into the lattice;

4. Finally, the atomic hydrogen, and, to a lesser extent, other gaseous species, react with any sp or sp^2 carbon sites on the surface, converting them into sp^3-bonded carbon.

There are several proposed mechanisms which attempt to explain how a methyl radical is added to the relevant (100):H(2×1) reconstructed diamond surface. In this configuration, it is required that the 5-membered rings are opened so that an additional carbon atom can be inserted and form the 6-membered rings of sp^3 diamond. Such a mechanism is illustrated in **Figure 1-5**. From simulation, this model was able to reproduce the kinetics of diamond growth over a wide range of parameters and it showed good agreement with measured growth rates. The most significant result was that it validated the assumption of CH_3 being the dominating growth species accounting for diamond growth in the different systems [5].

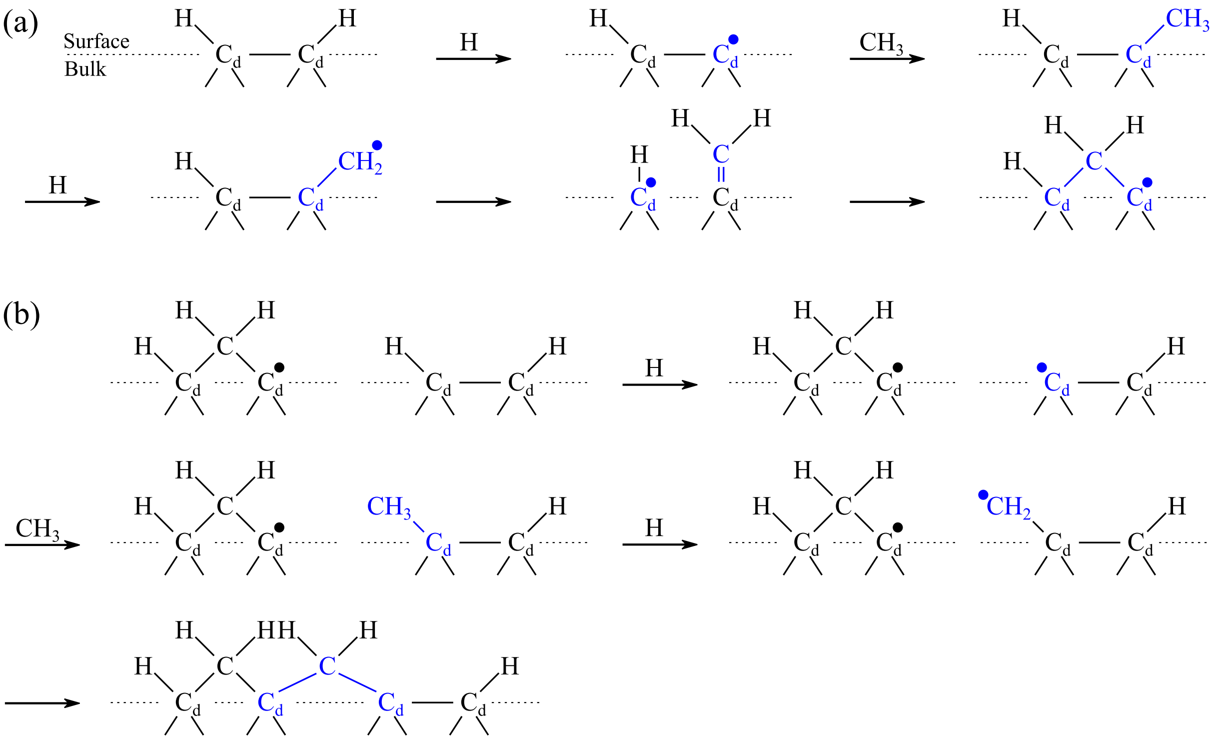

Figure 1-5: (a) Mechanism for dimer opening and carbon insertion [15]. (b) Closing of the new surface layer by a through-bridging mechanism [16].

The mechanism shown above does not account for the experimental observation that CVD-grown (001) surfaces are smooth. If carbon is able to incorporate everywhere on the surface (as the model implies), a rough surface would result unless some form of surface migration was occurring. Harris and Goodwin [16] suggested that the incorporation may occur preferentially at steps, due to lower steric hindrance at these locations. Later, Bauer *et al.* showed that the growth rate of diamond increases substantially when the diamond surface has a miscut (off-axis angle) of a few degrees away from the [001] direction [17]. This procedure adds atomic steps to the diamond surface, facilitating incorporation and increasing growth rate, in agreement with the hypothesis discussed earlier by Harris and Goodwin. Off-axis growth is nowadays a common strategy to improve not only the deposition rate, but also the quality of the CVD crystals, by suppressing the formation of hillocks and non-epitaxial crystallites.

1.3 Heteroepitaxial diamond growth

Heteroepitaxy consists of growing a crystalline material in crystallographic registry with its substrate, which is another crystalline material. Following the success for other materials like GaN, heteroepitaxy has been adopted as a strategy to grow diamond over very large areas (e.g., 2-4″ wafer-size) to overcome the limitations of homoepitaxial growth [18]. Critical factors for the successful growth of diamond on another material are the following:

- Stability in the diamond growth environment;
- Chemistry, *i.e.* the binding between carbon and substrate material, carbide formation and dissolution of carbon in the substrate material;
- Geometry, *i.e.* crystal structure and low lattice mismatch;
- Availability in high-quality and as large area samples.

Several different platforms for diamond heteroepitaxy were investigated in the past, many of which led to oriented growth, *e.g.* on sapphire, silicon, compound semiconductors (c-BN, 3C-SiC), metal carbides (TiC), carbide-forming (Co, Ni) and non-carbide forming metals (Pt, Re, Ir). Some of these materials resulted in poor oriented growth of diamond, while others excelled, namely Ir [19].

Crucial for the growth of diamond on a foreign material is the nucleation step, and the high nucleation barrier resulting from the large surface energy of diamond is a very challenging aspect of it. A modification of the seeding technique (deposition of tiny diamond particles) employed for polycrystalline growth on various substrates yielded oriented growth on different metal substrates (Pt, Ni, Co), but with rather poor crystalline quality. Currently, bias-enhanced nucleation (BEN) is the most efficient process to generate epitaxial diamond islands. Since Ir is now the established platform for diamond heteroepitaxy, exclusive focus will be given to it. For a more detailed review of the development of diamond heteroepitaxy, please refer to [18, 20].

1.3.1 Diamond nucleation

In classical nucleation theory the critical cluster size, above which further growth of a particle is more probable than its decay, is called the nucleus size. For homogeneous nucleation of a spherical particle with radius r, the critical size is given by the change in the free energy between the gas phase and the solid phase, which is composed of a bulk contribution ($\propto r^3$) and a surface contribution

$(\propto r^2)$. For a positive supersaturation, the bulk contribution is negative, *i.e.* condensation of particles is energetically favourable. In contrast, formation of a free surface gives a positive energy contribution. The sum of both yields a maximum in the free energy at a small radius, which corresponds to the formation energy of the nucleus. In heterogeneous nucleation, *i.e.* when condensation takes place on a solid surface, the surface energy of the substrate and the interface deposit-substrate energy have to be taken into account as additional contributions [18].

A simple transfer of this concept to diamond is hampered by the complexity of diamond CVD, since it involves a metastable phase that has to be stabilised, and requires conditions which suppress nucleation and growth of the thermodynamically stable graphite phase. In diamond, breaking bonds and forming a free surface costs a high amount of energy (about 6 J m^{-2}). Reconstruction and surface termination can significantly modify this value. However, the generally low nucleation densities $(<10^6\,\mathrm{cm}^{-2})$ on untreated non-diamond substrates confirm the existence of a high energy barrier for nucleus formation [18]. Only on c-BN, with its similar crystal structure, bonding and surface energy, the barrier is apparently low enough for spontaneous, high-density nucleation [21, 22].

1.3.1.1 Bias-enhanced nucleation (BEN) on Ir

In 1991 Yugo *et al.* introduced a method which was later termed “bias-enhanced nucleation” (BEN), in a microwave plasma (MWPCVD) setup [23]. The method consists in applying a negative DC voltage of typically 100-300 V to the substrate and having a gas composition with high methane concentrations. The microwave discharge is combined with a DC discharge that produces a localised region of higher electrical field strength in the plasma, directly above the substrate, similar to the cathode fall region in a classical glow discharge [24]. As a consequence, positive ions (*e.g.* CH_3^+) are accelerated to energies that induce the critical processes for *in situ* nuclei formation at, or just below the surface [25]. Extended studies, performed for the BEN process on silicon, revealed that critical factors for the achievement of oriented nucleation are [18]:

- The duration of the biasing procedure: epitaxial diamond crystallites are only observed within a well-defined process time window;
- Choosing textured growth conditions adapted to the specific growth surface, *e.g.* (001) or (111), otherwise renucleation and twinning will lead to a polycrystalline film covering the initially oriented nuclei;

Both conditions are directly connected to the fact that during BEN on Si the diamond nuclei can immediately start to grow in size.

The first report on diamond heteroepitaxy using Ir/MgO(001) as a substrate was presented by Sawabe *et al.* in 1996 [26]. Iridium is a metal that neither forms carbides, nor does it take up any significant amount of carbon even under intense ion bombardment during BEN [27]. The nucleation density is extremely high, in the order $10^{11}\,\mathrm{cm}^{-2}$, usually only oriented grains are found, the binding to diamond is very strong, and the lattice mismatch between the two materials is only 7.1%. Such properties allowed smooth layers with excellent epitaxial alignment to be achieved at very low film thickness [28]. Since that seminal report, iridium emerged as the most promising substrate for heteroepitaxial diamond wafer technology. Its actual implementation requires a careful control and profound understanding of the nucleation process, of the textured growth process, and a concept for upscaling.

The nucleation process on Ir, which differs completely from the processes taking place on any other material [18, 20], unfolds in the following way: immediately after BEN, no epitaxial diamond crystals are observable. Instead, scanning electron microscopy (SEM) images using the appropriate in-lens detector reveal a pattern formation consisting of well-defined bright areas, called “domains” [29-31]. Nucleation on Ir apparently proceeds under etching conditions for which the bulk phase of diamond is unstable, thus being incompatible with classical nucleation theory. With subsequent application of standard diamond growth conditions, diamond crystals evolve from the domain areas [29], with local areal densities of $\sim 2\times10^{11}\,\mathrm{cm}^{-2}$ [32]. High-resolution TEM (HRTEM) and X-ray photoelectron spectroscopy (XPS) analyses have shown that the deposit formed by BEN consists of a closed carbon layer with a thickness ranging from 1-2 nm [32]. One other group has reported a thickness of 8 nm [33], a value that is far from all observations in our lab. The definitive proof of the presence of crystalline diamond structures in the pure nucleation layer was derived from X-ray photoelectron diffraction (XPD) measurements [34, 35]. The data suggests a highly defective diamond structure in the BEN layer, which can be attributed to the harsh ion bombardment during BEN. The bombardment completely suppresses vertical diamond growth [36], while lateral growth remains possible, thus yielding a conclusive mechanism for “domain” formation [18]. This mechanism is able to explain the observation that the diamond crystals which evolve from the nucleation layer after BEN are, essentially, all epitaxially oriented, with a low angular spread.

1.3.2 Mechanism of texture improvement

The excellent initial alignment of epitaxial crystals on iridium (~1° angular spread) enables a very efficient reduction of mosaic spread in the subsequent growth of thick layers [37]. On a densely nucleated surface, coalescence of the diamond grains and the formation of a closed layer occur at a thickness below 100 nm in the subsequent growth step. At this stage, individual grains can still be clearly seen. When the growth of thicker films continues this feature gets lost progressively, as shown in **Figure 1-6**. After a few tens of µm the film transforms into a continuous single crystal with low mosaic spread, but still with a high density of structural defects, namely dislocations [38].

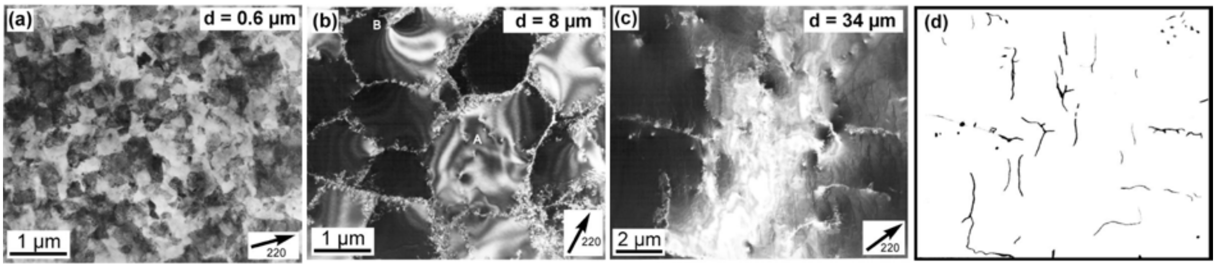

Figure 1-6: (a-c) Plan-view TEM images of epitaxial diamond layers on Ir/$SrTiO_3$(001) with different thicknesses. (d) Schematic drawing of the defect lines in the TEM image shown in (c) [37].

The dramatic improvement in crystalline quality is explained in terms of the substitution of low angle grain boundaries between two neighbouring grains by energetically more favourable disclinations. In other words, when the misorientation between them is small enough, the grain boundary stops at a certain point in the film and growth develops as a continuous crystal, leaving a disclination behind (see **Figure 1-7**). When a partial wedge disclination is formed instead of a grain boundary, the misorientation between grains is partially accommodated by elastic deformation [37].

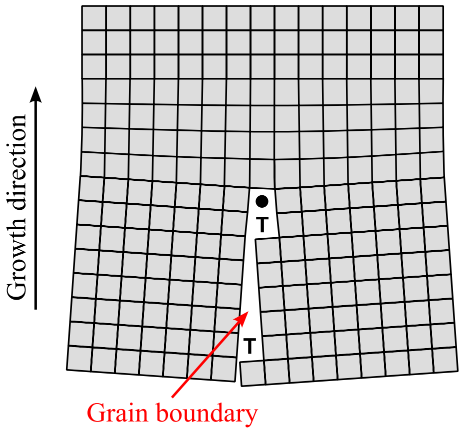

Figure 1-7: Schematic representation of stopping a low-angle grain boundary by introduction of a disclination (black dot) [39].

1.3.3 Scaling up: silicon-based multilayer structures

Because Ir is a rare and expensive material, and producing bulk Ir single crystals would be cost[1] prohibitive, growth on iridium always means on iridium layers grown epitaxially on another substrate. Heteroepitaxial Ir films have been grown on MgO(001), $SrTiO_3$(001), sapphire and YSZ/Si(001) for nucleation and growth studies of diamond on Ir [28, 40-43]. From an epitaxy point of view, and taking into account potential upscaling, all these substrates are suitable. For example, available wafer sizes are at least 2″ for $SrTiO_3$ and MgO, 8″ for Al_2O_3 (sapphire), and 12″ for Si. However, from a production point of view, Si offers the important advantage of a better fit of the thermal expansion coefficient with diamond. **Figure 1-8** compares the thermal stress induced in a thin

---

[1] Prices in December 2015 in unit of USD/oz t.: (Ir) 525; (Au) 1075; (Pt) 871. Source: *BASF Catalysts*.

diamond layer on thick substrates of various materials, after cooling down from the deposition temperature, with Si resulting in much lower thermal stress than the three oxides. As a consequence, the grown diamond film becomes much less prone to delamination.

Heteroepitaxial growth of Ir on Si requires the insertion of a buffer layer in order to avoid them reacting to form iridium silicides, which possess different crystal structures and low symmetry. $SrTiO_3$ and yttria-stabilised zirconia (YSZ) turned out to be suitable candidates. The mosaic spread in these oxide buffer layers is typically above 1° (FWHM). Nevertheless, single crystal iridium films with one order of magnitude lower angular spread can be grown on top [44]. The nucleation and growth of high-quality epitaxial diamond films has been shown on both $Ir/SrTiO_3/Si(001)$ [45] and Ir/YSZ/Si(001) [42]. In the meantime, Ir/YSZ/Si samples with (001) and (111) orientations are available in 4″ wafer size, and epitaxial diamond films have been deposited on both of these types of substrates [43, 46].

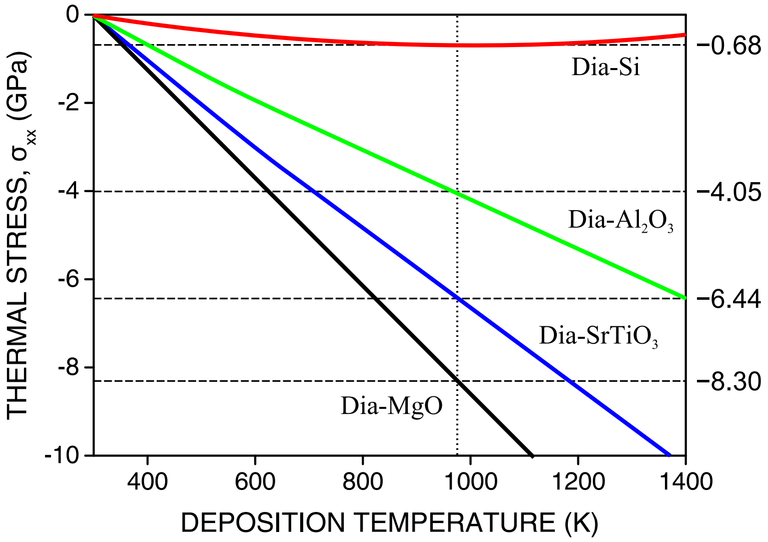

Figure 1-8: Thermal stress σ_{xx} in diamond layers on different substrates, versus deposition temperature [42]. The vertical line and the numbers at the right-hand side indicate the values for a rather low deposition temperature of 700 °C. Nevertheless, the compressive stress for the oxide single crystals varies from −4 GPa for sapphire to more than −8 GPa for MgO.

Figure 1-9 gives an overview of the Diamond/Ir/YSZ/Si(001) stack with FWHM values for the polar and azimuthal angular spread of, respectively, 0.16° and 0.34° for the diamond, measured over 10 cm^2 [42]. Since then, both tilt and twist have been improved to values below 0.1° (see **Figure 1-10**). They currently represent the state of the art for diamond-on-iridium layers. Successful scaling-up of the Ir/YSZ/Si(001) substrates to 4″ wafer dimensions has been shown [42], and the transfer of the BEN process to 4″ substrates is currently in progress.

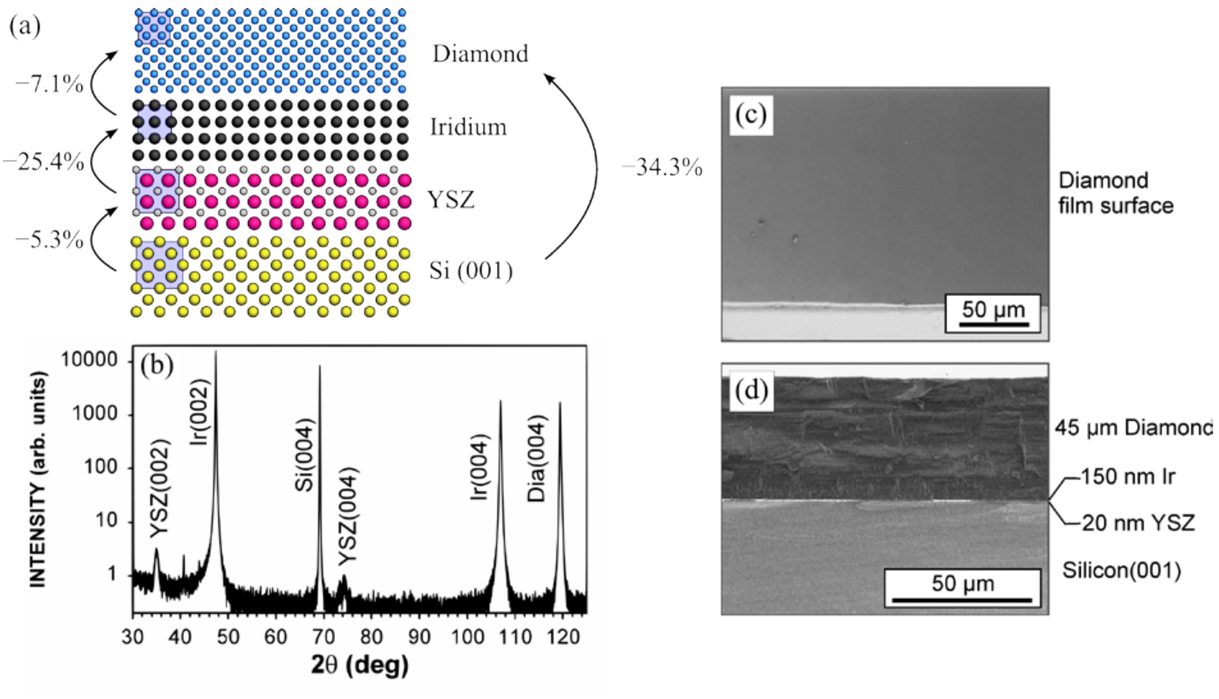

Figure 1-9: (a) Schematic view of the Diamond/Ir/YSZ/Si(001) epitaxial multilayer structure [42]. In the YSZ crystal the large spheres correspond to the oxygen ions. The numbers indicate the lattice mismatch between consecutive layers. (b) XRD θ-2θ scan showing the epitaxial alignment of the different layers/materials. (c, d) Surface and cross section SEM images of a representative sample.

The figure below shows the texture (tilt and twist) improvement of diamond films grown on Ir/YSZ/Si(001), as a function of film thickness. It highlights the potential of this structure for the fabrication of high-quality, large-area diamond, but also its limitations.

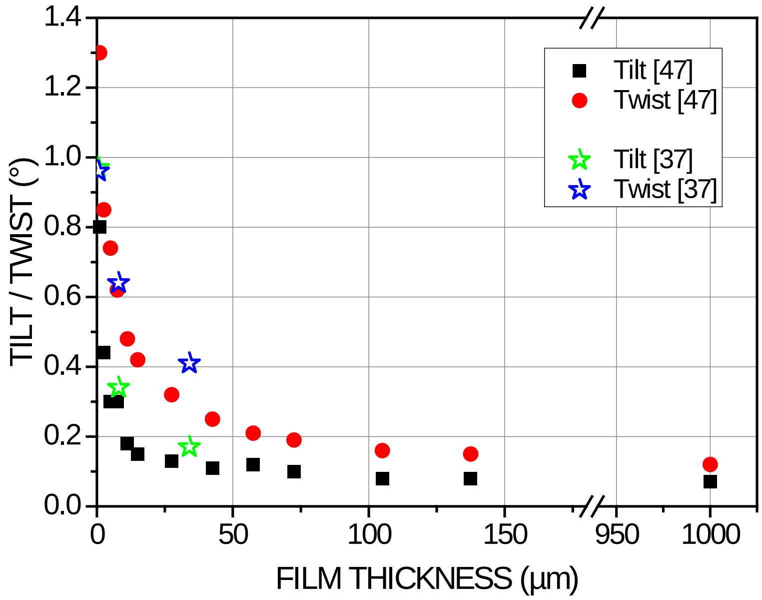

Figure 1-10: Texture improvement of heteroepitaxial (001)-oriented diamond on Ir as a function of film thickness, reproduced from [47]. Full symbols correspond to diamond films on Ir/YSZ/Si(001), 4° off-axis substrate. Open symbols correspond to diamond films on Ir/$SrTiO_3$(001) for comparison.

1.4 Defects and impurities in diamond

Defects in a real crystal can be divided into chemical impurities, nonstoichiometry and lattice defects. Lattice defects are: a) point defects (interstitials, vacancies, substitutions and antisites); b) line defects (dislocations); c) area defects (crystal surfaces, grain boundaries, twin boundaries, stacking faults, domain boundaries, homo- and heterojunctions, growth striations, growth sector boundaries, etc.), and volume defects (inclusions, precipitates and clusters of point defects) [48]. Due to the nature of diamond epitaxy on iridium, the most relevant types of defects are generally threading dislocations (individual or clusters), and impurities such as N, Si and B.

1.4.1 Dislocations

Dislocations are line defects arising from the distortion of the crystal lattice caused by the introduction of an extra lattice plane (edge-type dislocation) or by torsion of the lattice (screw-type dislocation), as illustrated in **Figure 1-11**. They are characterised by a *Burgers vector* $\vec{b}$.

The Burgers vector can be derived from the *Burgers circuit*, which is any atom-to-atom, closed path taken in the crystal where a dislocation is enclosed. If the same atom-to-atom sequence is made in a dislocation-free crystal, the circuit will not close, and the vector required to complete/close this circuit is then the Burgers vector [48, 49].

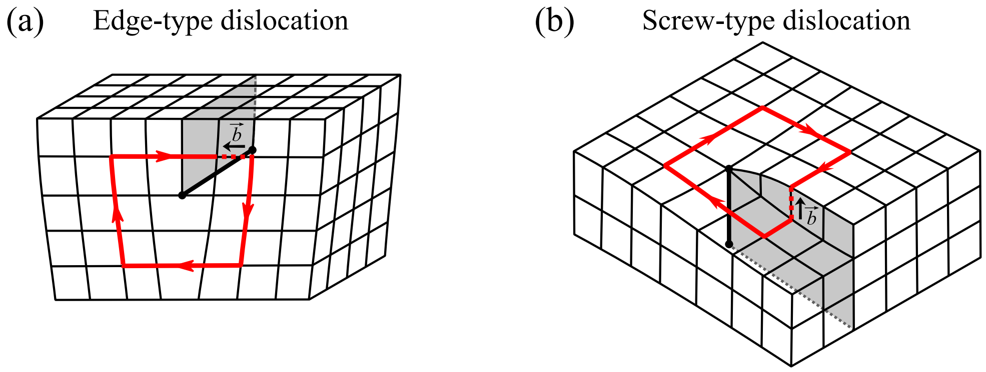
(a) Edge-type dislocation (b) Screw-type dislocation

Figure 1-11: Schematic view of (a) an edge-type dislocation and (b) a screw-type dislocation in a cubic lattice. The bold black lines represent the dislocation lines, the red curves correspond to the Burgers circuit, and the black arrows indicate the direction of the Burgers vectors.

Dislocations are found in all types of diamond, natural and synthetic. In homoepitaxial layers they are either continuations of the defects existing in the seed, or they nucleate from defects on the surface of the substrate (*e.g.*, due to mechanical polishing). Dislocations are especially inherent to heteroepitaxial diamond due to the nature of the growth process: the merging of the initial small diamond grains formed after nucleation, with starting mosaic spread of ~1°, leads to high dislocation densities on the order of $>10^{10}\ \text{cm}^{-2}$. As the crystal grows, the polygonised network of grain boundaries shown in **Figure 1-6** decomposes into individual or agglomerated dislocations.

Remarkably, not only the mosaic spread, but also the dislocation density can be reduced significantly within a few ten μm under appropriate growth conditions, as recently shown by our group [50]. Interaction processes between dislocations with different Burgers vectors lead to a decrease [51] of the dislocation density with film thickness, which follows roughly a $1/d$ law (see **Figure 1-12**). In the mm range the dislocation density can be decreased down to $\sim 10^7\ \text{cm}^{-2}$.

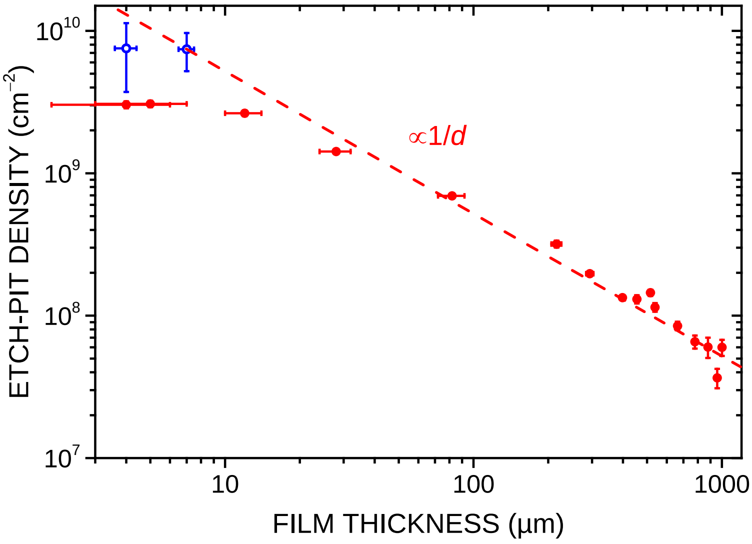

Figure 1-12: Dislocation density derived from the analysis of etch-pits (red squares) and from TEM measurements (blue open circles) *versus* the crystal thickness. The dashed red line shows a $1/d$ fit in the range 20-1000 μm. Reproduced from [50].

In heteroepitaxial diamond on iridium the dislocations are characterised by a Burgers vector which is typically of the $a/2\langle 110\rangle$ family. The long-range strain field can be calculated analytically for the different configurations. The core energy depends on the reconstruction, which is studied theoretically, *e.g.* by DFT (Density Functional Theory) calculations [52, 53].

Generally speaking, dislocations have a detrimental effect in the properties of diamond, especially electrical and optical, and it is the goal for high-end applications that the dislocation density be minimised. More on this subject will be presented in upcoming chapters.

1.4.2 Nitrogen

Nitrogen (**N**) is the most common impurity in natural diamond. Its presence led to the classification scheme for diamonds: type I diamonds are nitrogen-containing; type II diamonds are not (or with very small concentrations). In natural diamond the nitrogen is normally aggregated (type Ia), but in synthetic diamonds it is mainly in the form of single substitutional atoms (type Ib). Although in this form it is a donor, its ionisation energy of ~1.7 eV [6] is too high to be useful as an n-type dopant for electronic applications.

The optical properties and particular attributes of nitrogen-containing diamond, which are of interest in gemmology, are not relevant here, but it is worth mentioning that certain defects involving nitrogen, particularly the nitrogen-vacancy (NV) complexes, have recently been under the spotlight in quantum information processing, single-spin magnetometry, and plasmonics [54]. They exploit the fact that the spin state of a negatively charged NV centre (NV^-) can be initialised and read out optically, and that the charge state (NV^0 or NV^-) of this complex can be controlled electronically by designing FET structures on the diamond.

Most important in the context of this thesis is, however, the special role that nitrogen plays in MWPCVD of (001)-oriented diamond as a growth catalyst [55]. When nitrogen is added to the gas phase in quantities of a few ppm during diamond CVD, the growth rate is reported to increase by up to an order of magnitude [56-58]. It is proposed [55] that once nitrogen incorporates into the diamond lattice, donor electrons from sub-surface N lengthen and weaken the (100):H(2×1) surface dimer bonds, allowing growth species to directly incorporate in sp^3 configuration, thus facilitating the nucleation of new atomic terraces (see **Figure 1-13**). This model would suggest, however, that incorporation of other donor impurities, such as phosphorus (an n-type dopant with even lower activation energy), would lead to a similar effect. The lack of experimental observation to corroborate this hypothesis leaves the possibility for other explanations for the nitrogen-induced growth rate enhancement of diamond still open.

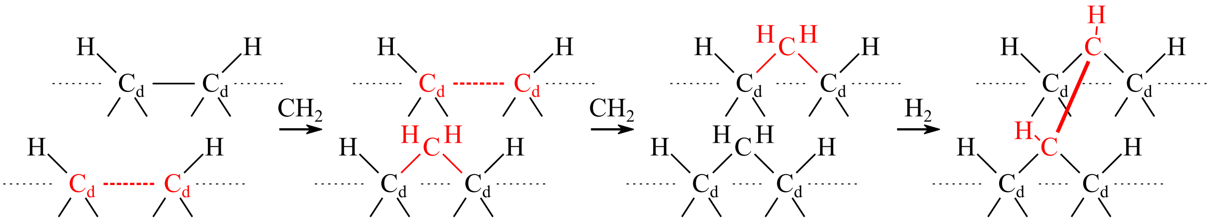

Figure 1-13: Growth model with N-doping of (100):H(2×1) diamond. (1) The extra electron from a sub-surface N migrates to the surface and opens a dimer bond. (2) A CH_2 adsorbs to the open dimer and the neighbouring dimer is opened. (3) Another CH_2 adsorbs to the open dimer and the next dimer (not shown) is opened. (4) H_2 is abstracted and a new isolated dimer is formed on the upper terrace [55].

Dunst *et al.* [59] have shown that, contrary to the above mechanism, the nucleation of new lattice planes may not be a decisive step for the nitrogen-induced growth acceleration. Instead, nitrogen is deemed to compete for adsorption with other growth species, and once adsorbed, it catalyses further incorporation of carbon-containing species. The growth rate of on-axis and off-axis, (001)-oriented samples in nitrogen-rich conditions were identical in that study, which was performed in a low-pressure regime (30 mbar). This result differed from studies in a high-pressure regime (~200 mbar) [17], where the growth rate of diamond was shown to increase when its surface has a miscut angle of a few degrees away from the [001] direction, presumably due to preferential incorporation of growth species at atomic steps.

The influence of nitrogen on the microstructure of the diamond surface was discussed by de Theije *et al.* [58]. In the presence of nitrogen, besides the nucleation of new atomic terraces being enhanced, also step bunching occurs due to nitrogen impurities on the surface hampering the lateral propagation of atomic steps. This phenomenon is strongly anisotropic, with a tendency for large step/terrace structures being formed aligned parallel to the [110] direction [58, 60]. Such structures were nicely reproduced from simulation, although the predicted slowdown of the growth rate contradicted the experimentally observed increase.

1.4.3 Boron

Boron (**B**) is undoubtedly the most technologically relevant impurity in diamond. It is the only known shallow dopant, with activation energy of 0.368 eV, and is found in natural diamond (type IIb). The incorporation of boron attributes a blue tonality to the crystals [1]. Being a very rare type, the Hope Diamond is an example of what is probably the most famous blue diamond currently known. Boron can also be introduced into synthetic high-pressure high-temperature (HPHT) crystals and CVD diamond layers, in the latter case using gas precursors such as B_2H_6 (diborane) or $B(CH_3)_3$ (trimethylborane), which decompose in the hot plasma into active BH_x species and incorporate into the lattice in concentrations as high as $\sim 10^{21}\,\text{cm}^{-3}$, more particularly when growth occurs on $\{111\}$ crystallographic facets. At such high concentrations ($> 3\times10^{20}\,\text{B cm}^{-3}$), apart from turning black in colour, the material undergoes a metal-to-insulator transition (MIT) [61, 62], becoming highly electrically conductive at room temperature (see **Figure 1-14** (a)). This is due to the activation energy of the boron acceptors decreasing towards zero with increasing doping concentration (see **Figure 1-14** (b) and **Figure 1-17**). At liquid helium temperature, heavily (metallic) B-doped diamond was found to be a superconductor [63, 64].

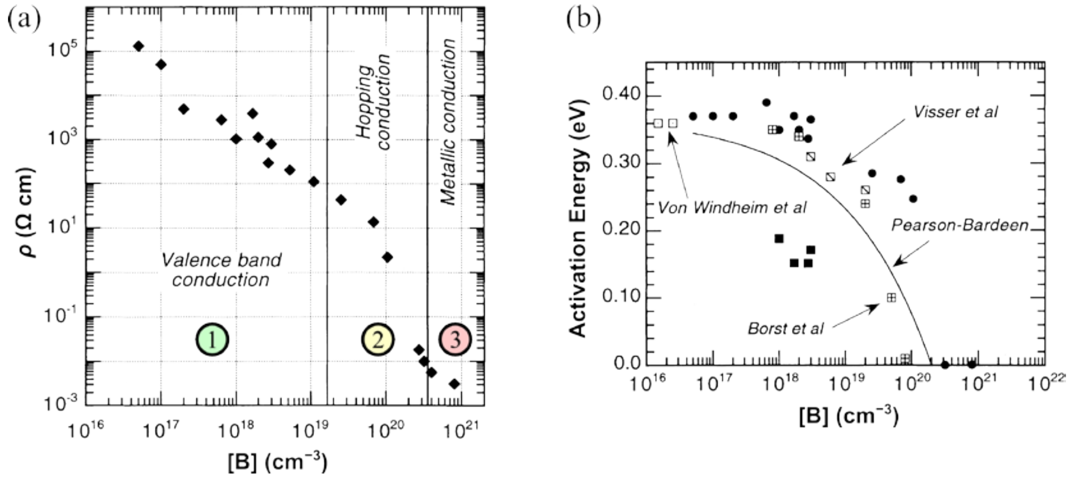

Figure 1-14: (a) Room temperature resistivity as a function of doping concentration. Regions 1, 2 and 3 correspond to, respectively, low-medium, high and heavy doping levels. (b) Activation energy as a function of doping concentration. Reproduced from [65].

The increase in B-doping concentration is associated with a decrease of the hole mobility (see **Figure 1-15**), which can be detrimental to the performance of diamond-based electronic devices, such as high-frequency transistors [66]. This difficulty has led to the concept of δ-doping [67], which consists in growing a ~2 nm thick heavily B-doped layer in between two intrinsic layers of several tens of nm [68, 69]. In this particular case, a carrier delocalisation from the δ-doped region into the intrinsic regions occurs, and in this way a large number of carriers are made available in the high mobility region of the device. However, producing sharp B-doping profiles in diamond remains a challenge [70].

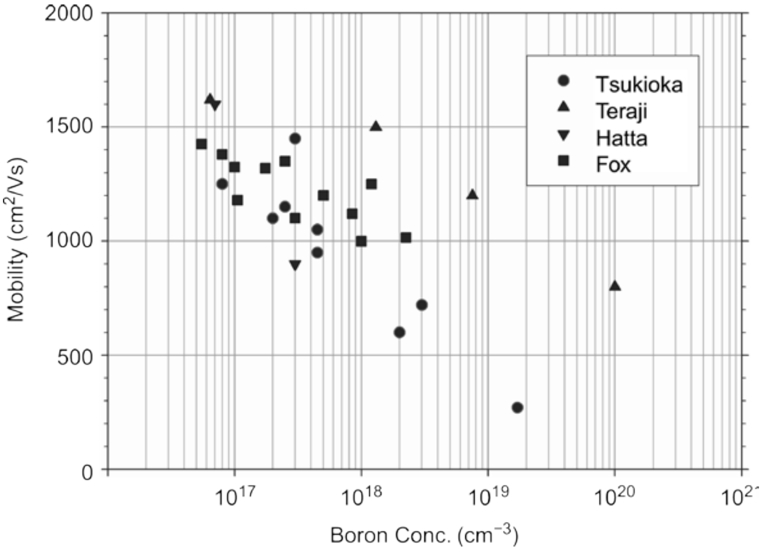

Figure 1-15: Hall mobility at room temperature *versus* dopant concentration in boron-doped, single-crystal CVD diamond, from several authors. Reproduced from [71].

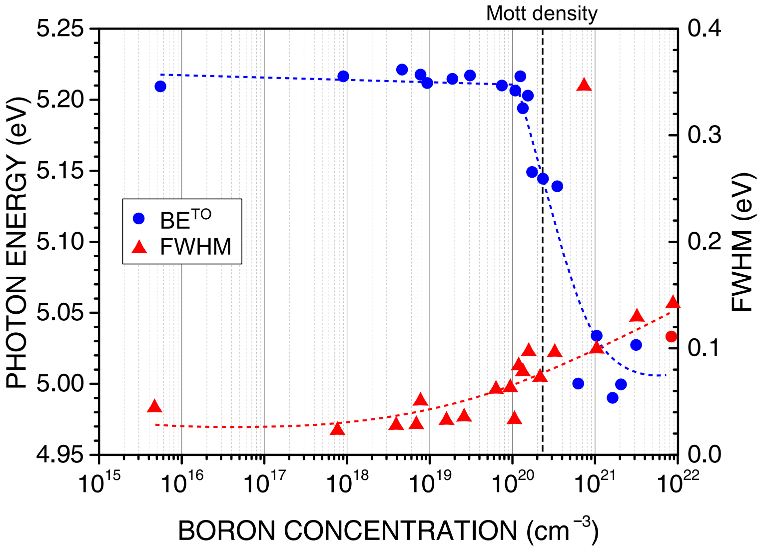

Figure 1-16: Photon energies of the boron-bound exciton (BE^{TO}) transition and related line widths (full width at half maximum) as a function of B concentration in diamond. The Mott density line marks the transition to metallic conductivity following a theoretical estimate and Hall measurements. Reproduced from [72].

Contrary to undoped diamond, boron-doped diamond has a very distinct absorption spectrum due to the introduced characteristic vibrational states, which allow the estimation of the B concentration from IR and Raman spectroscopy [73-76]. The presence of B also leads to the emission of characteristic near bandgap peaks due to bound exciton (BE) recombination in electro- and cathodoluminescence [77, 78]. The photon energy due to recombination of BE varies with doping concentration according to **Figure 1-16**. See section 1.6.1 for more details.

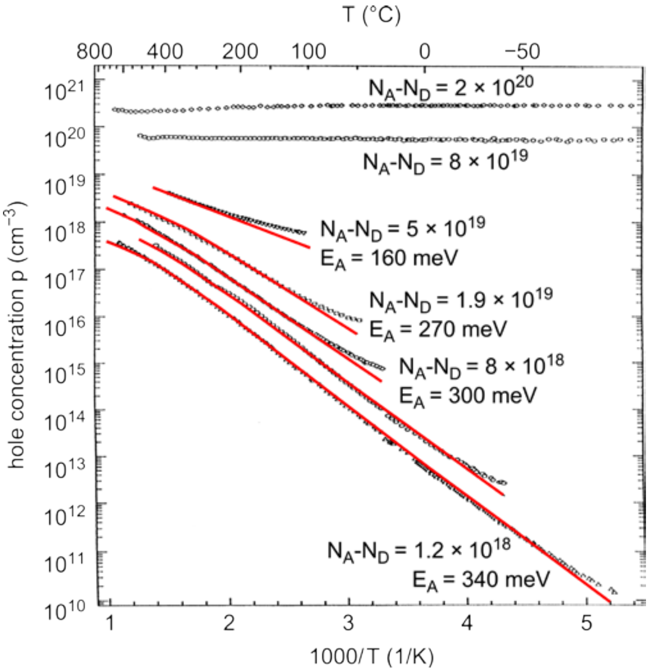

Figure 1-17: Carrier concentration *vs.* reciprocal temperature of B-doped homoepitaxial diamond layers with different doping levels. Reproduced from [79].

In terms of its influence on the surface morphology of diamond, B introduced in moderate concentrations apparently does not change the growth mechanism from the undoped case [55]. It promotes the growth of smooth (001) surfaces without step bunching and without any significant change in growth rate. In high concentrations, B leads to hillock formation and roughening of the surface.

As a result of the larger covalent radius of boron ($r_B = 0.088$ nm) when compared to that of carbon ($r_C = 0.077$ nm), the introduction of substitutional boron atoms into diamond leads to an expansion of the lattice parameter. This has been found to follow the linear interpolation attributed to Vegard as long as the boron content is lower than $\sim 3 \times 10^{20}\,\text{cm}^{-3}$ in MWPCVD epitaxial layers [62, 80, 81]. In homoepitaxial layers the cell shows a tetragonal distortion, as long as the growth proceeds in a pseudomorphic way. Under these conditions the boron concentration can be deduced from the simple measurement of the out-of-plane lattice constant by XRD. As soon as relaxation occurs and dislocations are inserted, which also create a mosaic spread, a full analysis of the strain tensor (including the in-plane component) is required.

1.4.4 Oxygen

Oxygen (**O**) can be a beneficial element in the gas phase during MWPCVD. Very few, if any, oxygen atoms actually become incorporated into diamond during the growth process, but very often the presence of oxygen improves the quality of the diamond by turning it from a less transparent to a more transparent crystal, due to the preferential etching of sp^2 carbon and attenuation of impurity incorporation [82-84] (more on the etching properties of oxygen will follow). The relationship between oxygen, carbon and hydrogen during diamond growth is represented in the well-known Bachmann's diagram in **Figure 1-18**.

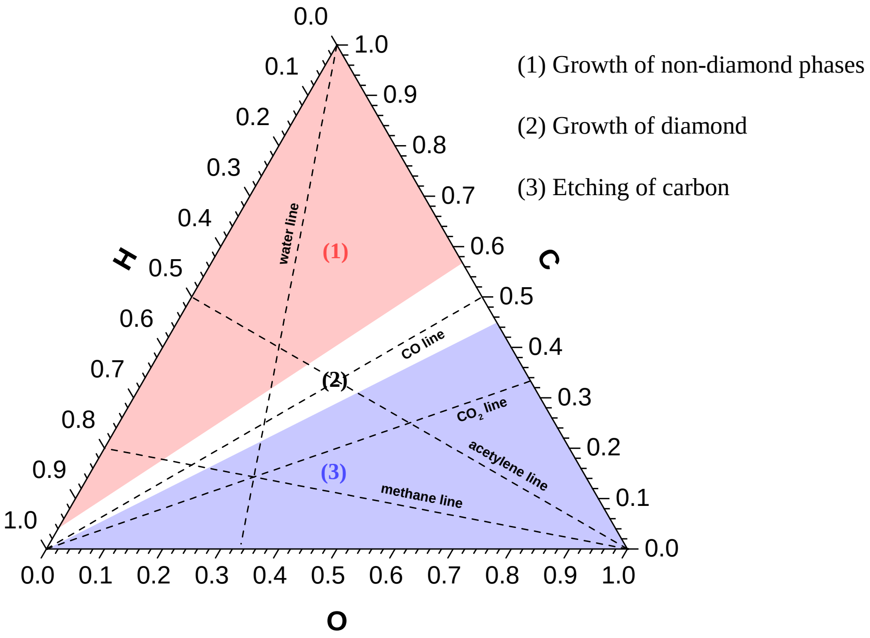

Figure 1-18: Bachmann's diagram for stable diamond growth (white area) [85]. Oxygen-rich gas compositions (lower region) lead to pure carbon etching (no growth), while small concentrations of oxygen lead to improved crystalline quality.

1.4.5 Silicon

Silicon (**Si**) is a particularly relevant impurity in heteroepitaxial and polycrystalline diamond due to the immediate source of this element from the silicon wafers used as substrate. Exposed to the hot and chemically active plasma during CVD, Si is released into the gas phase and incorporates substitutionally into the diamond lattice, distorting the lattice due to its size and generally forming complexes with vacancies (SiV centres). It is a significant trap for carriers and should be avoided in high-end diamond-based electronic devices [6]. Similarly to the nitrogen-vacancy centres, SiV centres are receiving more attention for the potential application as narrow-band, bright single photon emitters [86].

1.5 Fundamentals of diamond etching

The study of diamond etching started with the aim of understanding the genesis of natural diamond, and later developed to become a tool for revealing the occurrence and distribution of point, linear and planar defects in natural and HPHT diamond crystals. Soon after the use of the chemical vapour deposition became widespread, efforts were made in processing the grown material by gas phase etching to smoothen the surface of polycrystalline films and remove graphitic or amorphous carbon present in the grain boundaries [1].

Without activation, no chemical etchant attacks diamond at room temperature. At higher temperatures diamond is no longer chemically inert and is eroded by oxygen and oxygen compounds, molten and solid metals [87, 88] and by hydrogen. At temperatures above 2000 K the metastable diamond phase spontaneously turns into graphite at atmospheric pressure. Graphitisation can also occur at lower temperatures when catalysed with solid or molten metals [1].

1.5.1 Hydrogen etching

Diamond is etched by the attack of atomic hydrogen, either neutral or ionised, with most studies focussing on hydrogen radicals produced by the activation of H_2 by hot filament and plasma [89-92]. Reports on plasma-activated hydrogen etching have shown the formation of flat $\{001\}$ surfaces covered by monoatomic steps parallel to $[110]$, due to (2×1) reconstruction of the plasma-polished $\{001\}$ faces [89, 93]. It is also suggested, based on quantum mechanical and kinetic Monte Carlo studies of the occurrence of hydrogen etching during diamond CVD that, like growth, also the etching of $\{001\}$ diamond must proceed layer-wise involving steps [1, 94].

1.5.2 Oxygen etching

Diamond is very susceptible to oxidation: compared with hydrogen, oxygen etching sets in at lower temperatures and proceeds at much higher rates, and activation to atomic or ionic oxygen is not needed.

Work on diamond etching using activated (*i.e.* atomic) oxygen points to chemical etching being predominant over sputtering, proceeding by a continued chemisorption of oxygen at the diamond surface followed by desorption as CO and CO_2. The surface chemistry is activated by the chemical and kinetic energy of the impinging oxygen radicals or ions generated by RF [95, 96], microwave [97] and ion beams [98], or by foreign ions such as Xe^+ [99]. This has the advantage that the temperature of the surfaces being etched can be kept very low, down to 100 °C, 0 °C or even −140 °C. A detailed understanding of the surface processes during activated oxygen etching is lacking, although the mechanisms possibly share similarities with the thermal oxidation of diamond [1].

From thermochemical studies of oxidative diamond etching it was found that the oxidation rate of single crystal diamond is fastest for $\{111\}$ surface, followed by $\{110\}$ and $\{100\}$, and that the rate-limiting step in the process involves breakage of one C−C bond. It was also observed that oxygen chemisorbed on a diamond surface desorbs as CO and, to a lesser extent, as CO_2. Depending on the etching conditions (pressure and temperature), different combinations of functional groups such as ketone (C=O), ether (C−O−C), lactone [C(O)−O−C] and carboxylic anhydride [C(O)−O−C(O)] can be present on the crystalline surfaces [1, 100], with a rough trend of the more complex structures not surviving at higher temperatures. On $\{001\}$ single crystals there is a predominance of bridging ketone and ether groups on both (1×1) and (2×1) reconstructed surfaces. The termination of the diamond surface after oxidation is not so important for the etching of defects (chapter 3.3), but may be relevant when oxygen-terminated diamond is used for the fabrication of devices, such as in chapters 4 and 5, due to surface/interfacial states being generated by functional groups adsorbed on the diamond surface.

1.5.3 Etching of dislocations

In the case of pristine diamond faces, such as $\{111\}$ and $\{100\}$, etching proceeds mostly layer by layer and the surface remains flat due to “kinetic smoothing” [101]. However, in the presence of stress and weaker bonds due to crystal defects, such as dislocations, stacking faults and grain boundaries, a local preferential 2D nucleation of monolayer etch-pits occurs, followed by lateral expansion of growth steps. In the case of a line defect such as a dislocation, it serves as a continuous source for nucleation, which leads to the development of etch-pits large enough to be visible by microscopy techniques. Examination of these features formed after etching provides information on the defect structure in the crystals [1, 48]. Due to the high etching anisotropy, oxidation is often the preferred method to expose defects in the diamond crystals and films [1, 102, 103].

The usefulness of the etching technique lies in the formation of visible, sharp, contrasting etch-pits at dislocation sites. The necessary condition for the formation of visible etch-pits is the proper ratio of the three dissolution rates (see **Figure 1-19**): v_n is the etch rate along the dislocation line, directed normal to the surface; v_t is the tangential etch rate describing the lateral spreading of elementary steps of the surface; v_f corresponds to the etch rate along the lateral side of the pit; v_s is the etch rate of the surface in areas free from dislocations, also directed normal to the surface. The absolute values of these rates are governed by the nature and composition of the etchant, as well as by the etching conditions, *e.g.* temperature, pressure, stirring of the etchant, etc., and also by the presence of impurities segregated along the dislocation lines [48].

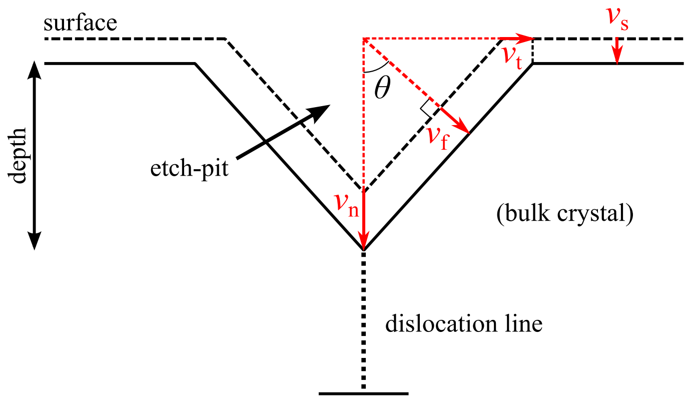

Figure 1-19: Schematic description of the different etch rates involved in the formation of an etch-pit at a dislocation site [48, 103].

Denoting the rate along the surface of the pit in **Figure 1-19** by v_{f}, the condition for etch-pit formation is when $v_{\mathrm{f}} \gg v_{\mathrm{s}}$. When $v_{\mathrm{f}} \ll v_{\mathrm{s}}$, the dissolving surface remains practically smooth. In other words, the plane of a crystal with maximum dissolution rate has minimum tendency to form etch-pits, and vice-versa.

The condition for stable etch-pit formation is therefore the following [48]:

$$v_{\mathrm{f}} > v_{\mathrm{s}} \cos\theta \tag{1.5.1}$$

1.6 Electron-matter interactions

The wave-particle dualism postulated by Louis de Broglie (Nobel Laureate in 1929) establishes that moving matter has a corresponding wavelength λ, which is given by:

$$\lambda = \frac{h}{p} = \frac{h}{mv} \tag{1.6.1}$$

where p is the momentum of the body, m is its mass, v its velocity and h is Planck's constant (6.626×10^{-34} m^2 kg s^{-1}). This relationship allows a direct correlation between the kinetic energy of an electron, $E = 1/2\left(mv^2\right)$, and wavelength, which is given by:

$$\lambda = h\big/\sqrt{2m_0E} \tag{1.6.2}$$

where m_0 is the rest mass of the electron (9.109×10^{-31} kg). Considering an electron accelerated in an electric field, its kinetic energy results in $E = qV$, where q is the electron charge and V is the acceleration voltage, and equation (1.6.2) then becomes:

$$\lambda = h\big/\sqrt{2m_0qV} \tag{1.6.3}$$

For high acceleration voltages, *e.g.* hundreds of kV or more, typically used during transmission electron microscopy (TEM) experiments, the electrons travel close to the speed of light, and therefore equation (1.6.3) must include a relativistic term, which then becomes [104]:

$$\lambda = \frac{h}{\sqrt{2m_0 qV}} \times \frac{1}{\sqrt{1+\frac{qV}{2m_0 c^2}}} = \frac{h}{\sqrt{2m_0 qV\left(1+\frac{qV}{2m_0 c^2}\right)}} \tag{1.6.4}$$

where c is the speed of light in vacuum $(2.998\times10^{8}\ \mathrm{m\ s^{-1}})$.

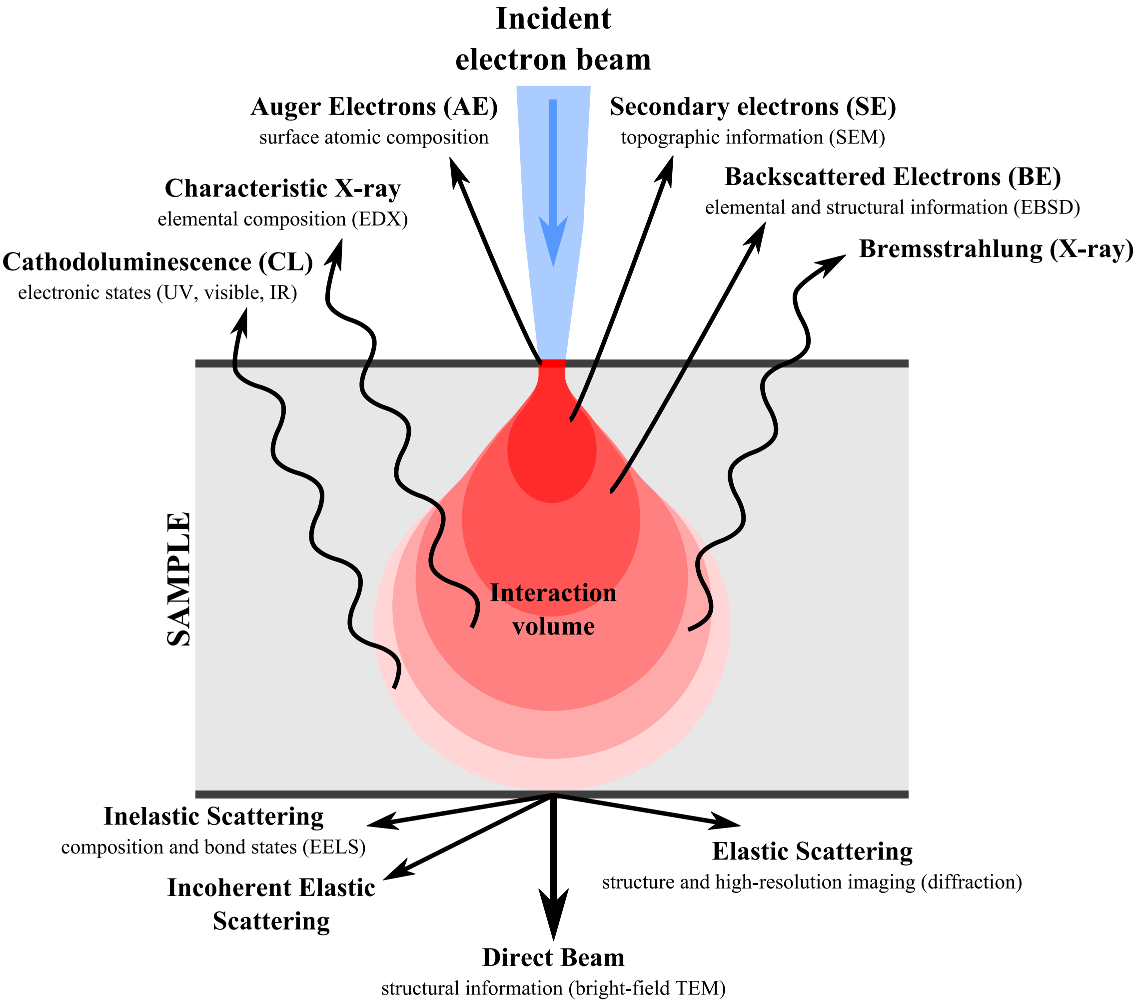

Figure 1-20: Illustration of the different effects produced by electron-beam interaction with matter. Adapted from [105].

The interaction of electrons with known energy (and hence wavelength) with the atomic environment of a target specimen enables a wide range of electron microscopy and spectroscopy techniques. Absorption, elastic and inelastic collisions with the atoms of the specimen will alter their energy, momentum and/or phase, resulting in transmission, scattering and/or diffraction of the electrons, as well as the emission of photons. Upon detection and analysis, they can yield information about the atomic/elemental, structural and electronic properties of the sample. **Figure 1-20** summarises the different types of interactions an electron can undergo when impinged on a material.

The electron-matter interactions illustrated above are the basis of several standard techniques used throughout this thesis, namely cathodoluminescence (CL), scanning electron microscopy (SEM), transmission electron microscopy (TEM) and its derivatives, *i.e.* bright-field TEM, dark field TEM, diffraction, electron energy loss spectroscopy (EELS), etc. Apart from CL, all other techniques were performed with commercial equipment.

1.6.1 Cathodoluminescence (CL)

Cathodoluminescence consists in the generation of electron-hole (e-h) pairs in a semiconductor by an impinging electron beam with high enough energy, followed by the recombination of the e-h pairs with emission of characteristic photons which carry information about the material.

The process by which e-h pairs are generated in cathodoluminescence is more complex than in photoluminescence, because the excitation process in the former case is an indirect process involving multiple steps, whereas in the latter process an e-h pair is directly generated by an absorbed photon. The properties of light, such as energy/wavelength or polarisation directly affect the e-h pair generation phenomenon. Furthermore, the excitation intensity is temporally and spatially homogeneous in the generation region [106], unlike in CL.

On the other hand, in cathodoluminescence several processes take place: X-ray emission by excitation of an inner shell, Auger electron emission, secondary electron emission by a cascade process, etc. As the Auger electrons generated at the first stage lead to other Auger effects, the number of Auger electrons increases substantially. In its turn, secondary electrons, which are induced from the collision of incident electrons with electrons in the valence band, also increase in number. Each incident electron in the cascade process generates $\sim 10^3$ secondary electrons, while the ratio of the Auger effect to the collision process is not precisely known. For an electron beam of a few keV, electron emission by the Auger effect is higher than X-ray emission [106].

The cascade process in the material occupies an approximately spherical volume, as shown in **Figure 1-21**. The diameter L_R (µm) can be determined from [106]:

$$L_\mathrm{R} = \frac{0.02764 A \cdot E^{5/3}}{\rho Z^{8/9}}, \tag{1.6.5}$$

where A is the atomic mass, Z is the atomic number, ρ (g cm^{-3}) is the density of the material and E (keV) is the acceleration voltage.

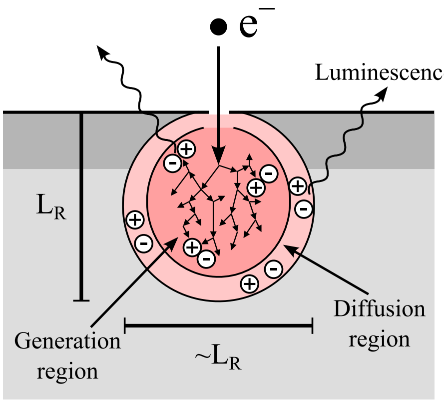

Figure 1-21: Representation of the electron cascade process in a semiconductor led by incident (primary) electrons with high energy (keV range). The secondary electrons have kinetic energies of ~5-10 eV and diffuse in a spherical volume while excited. Image adapted from [106].

The depth L_R is typically a few hundred nanometres in semiconductors for an electron beam of a few keV. The e-h pairs generated by the secondary electrons recombine in the generation and diffusion regions, thus emitting light by luminescence. A wide range of electronic transitions in diamond can be then probed with cathodoluminescence, allowing the investigation of optical properties and defects in the material.

The spatial resolution in CL is nearly as large as L_R and plays a role, for example, in CL imaging in scanning electron microscopes. It should also be considered when measuring thin films.

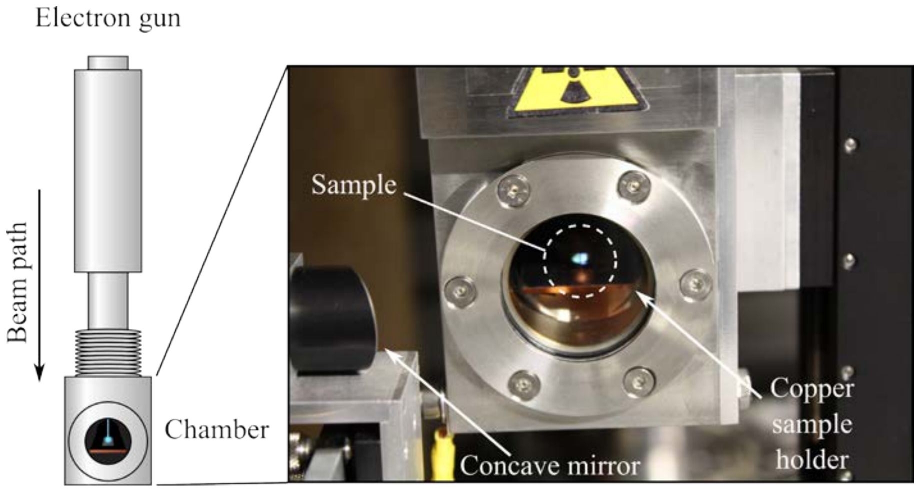

Figure 1-22: Sketch of the cathodoluminescence setup used in this thesis. The sample is placed inside a vacuum chamber on a copper holder cooled by liquid nitrogen. An electron gun is connected to the vacuum chamber in a vertical configuration. The acceleration voltage, filament current and *x-y* positioning of the beam are adjusted externally. The light emitted from the sample is collected through an optical window and directed to the entrance slit of a T64000 spectrometer by an arrangement of concave and flat mirrors on an optical table.

Particularly relevant has been the use of CL to quantify the dopant concentration of boron or phosphorus in diamond from the intensity/shift of emission peaks of impurity-bound excitons [78, 107-110]. In CL spectra of diamond films in the energy region close to the bandgap, the presence of boron gives rise to a phonon-assisted electronic transition attributed to boron bound excitons, BE^{TO}, next to the free exciton transition peak, FE^{TO}. The intensity ratio of both features can be compared with calibration curves in literature [77, 78]. This method to deduce the boron concentration is sensitive down to minimum concentrations of 0.1 ppb (~10^{13} cm^{-3}) and over many orders of magnitude [78]. At concentrations of ~100 ppm, equivalent to ~10^{19} cm^{-3}, the BE^{TO} peak broadens, increasingly overlaps with the FE^{TO} peak (which decreases) and shifts to lower energies (see **Figure 1-16**). The reason for this is believed to be due to bandgap shrinkage. This shift can then be used to derive the B content [110].

Cathodoluminescence measurements in this work were performed using a home-made setup illustrated in **Figure 1-22**. It is comprised of 1) a vacuum chamber, 2) a removable copper sample holder, 3) a RHEED[2] electron gun with external electronic controls for acceleration voltage, filament current, focus/size and *x*-*y* position, 4) rotary and turbo pumps connected in series with the chamber, 5) an external feed for liquid nitrogen to cool the copper sample holder, 6) an optical table with a set of concave and flat mirrors and finally 7) a T64000 spectrometer.

References

1. M. H. Nazaré and A. J. Neves; *Properties, Growth And Applications Of Diamond*, 1st ed., Datareview Series, ed. M.H. Nazaré and A.J. Neves, 2000, Institution of Electrical Engineers (IEE).
2. Gordon Davies; *Basic Properties of Diamond: Phonon Spectra, Thermal Properties, Band Structure*, in *CVD Diamond for Electronic Devices and Sensors*, 2009, John Wiley & Sons, Ltd.
3. W. Saslow, T. K. Bergstresser, and Marvin L. Cohen; Band Structure and Optical Properties of Diamond. *Physical Review Letters*, 1966. **16**(9): p. 354-356. DOI: 10.1103/PhysRevLett.16.354.
4. E. O. Kane; Phonon spectra of diamond and zinc-blende semiconductors. *Physical Review B*, 1985. **31**(12): p. 7865-7876. DOI: 10.1103/PhysRevB.31.7865.
5. M.A. Prelas, G. Popovici, and L.K. Bigelow; *Handbook of industrial diamonds and diamond films*, 1st ed., 1998, Marcel Dekker.
6. Alison Mainwood; *Point Defects, Impurities and Doping*, in *CVD Diamond for Electronic Devices and Sensors*, 2009, John Wiley & Sons, Ltd.
7. Robert J. Nemanich, John A. Carlisle, Atsushi Hirata, and Ken Haenen; CVD diamond—Research, applications, and challenges. *MRS Bulletin*, 2014. **39**(06): p. 490-494. DOI: 10.1557/mrs.2014.97.
8. Francis P. Bundy; The P, T phase and reaction diagram for elemental carbon, 1979. *Journal of Geophysical Research: Solid Earth*, 1980. **85**(B12): p. 6930-6936. DOI: 10.1029/JB085iB12p06930.
9. F. P. Bundy, W. A. Bassett, M. S. Weathers, R. J. Hemley, H. U. Mao, and A. F. Goncharov; The pressure-temperature phase and transformation diagram for carbon; updated through 1994. *Carbon*, 1996. **34**(2): p. 141-153. DOI: 10.1016/0008-6223(96)00170-4.
10. J. Steinbeck, G. Braunstein, M. S. Dresselhaus, T. Venkatesan, and D. C. Jacobson; A model for pulsed laser melting of graphite. *Journal of Applied Physics*, 1985. **58**(11): p. 4374-4382. DOI: 10.1063/1.335527.
11. M. I. Landstrass, M. A. Plano, M. A. Moreno, S. McWilliams, L. S. Pan, D. R. Kania, and S. Han; Device properties of homoepitaxially grown diamond. *Diamond and Related Materials*, 1993. **2**(5–7): p. 1033-1037. DOI: 10.1016/0925-9635(93)90269-8.

---

[2] Reflection high-energy electron diffraction.

12. J. Millan, P. Godignon, and A. Perez-Tomas; Wide Band Gap Semiconductor Devices for Power Electronics. *Automatika*, 2012. **53**(2): p. 107-116. DOI: 10.7305/automatika.53-2.177.
13. Jan Isberg, Johan Hammersberg, Erik Johansson, Tobias Wikström, Daniel J. Twitchen, Andrew J. Whitehead, Steven E. Coe, and Geoffrey A. Scarsbrook; High Carrier Mobility in Single-Crystal Plasma-Deposited Diamond. *Science*, 2002. **297**(5587): p. 1670-1672. DOI: 10.1126/science.1074374.
14. J. E. Butler, Y. A. Mankelevich, A. Cheesman, Ma Jie, and M. N. R. Ashfold; Understanding the chemical vapor deposition of diamond: recent progress. *Journal of Physics: Condensed Matter*, 2009. **21**(36): p. 364201. DOI: 10.1088/0953-8984/21/36/364201.
15. Barbara J. Garrison, Eric J. Dawnkaski, Deepak Srivastava, and Donald W. Brenner; Molecular Dynamics Simulations of Dimer Opening on a Diamond {001}(2x1) Surface. *Science*, 1992. **255**(5046): p. 835-838.
16. Stephen J. Harris and D. G. Goodwin; Growth on the reconstructed diamond (100) surface. *The Journal of Physical Chemistry*, 1993. **97**(1): p. 23-28. DOI: 10.1021/j100103a007.
17. Th Bauer, M. Schreck, and B. Stritzker; Homoepitaxial diamond layers on off-axis Ib HPHT substrates: Growth of thick films and characterisation by high-resolution X-ray diffraction. *Diamond and Related Materials*, 2006. **15**(4–8): p. 472-478. DOI: 10.1016/j.diamond.2005.09.028.
18. M. Schreck; *Heteroepitaxial Growth*, in *CVD Diamond for Electronic Devices and Sensors*, 2009, John Wiley & Sons, Ltd.
19. Yutaka Ando and Atsuhito Sawabe; *Heteroepitaxy of Diamond*, in *Physics and Applications of CVD Diamond*, 2008, Wiley-VCH Verlag GmbH & Co. KGaA.
20. Matthias Schreck, Jes Asmussen, Shinichi Shikata, Jean-Charles Arnault, and Naoji Fujimori; Large-area high-quality single crystal diamond. *MRS Bulletin*, 2014. **39**(06): p. 504-510. DOI: 10.1557/mrs.2014.96.
21. S. Koizumi, T. Murakami, T. Inuzuka, and K. Suzuki; Epitaxial growth of diamond thin films on cubic boron nitride {111} surfaces by dc plasma chemical vapor deposition. *Applied Physics Letters*, 1990. **57**(6): p. 563-565. DOI: 10.1063/1.103647.
22. Koizumi Satoshi and Inuzuka Tadao; Initial Growth Process of Epitaxial Diamond Thin Films on cBN Single Crystals. *Japanese Journal of Applied Physics*, 1993. **32**(9R): p. 3920. DOI: 10.1143/JJAP.32.3920.
23. S. Yugo, T. Kanai, T. Kimura, and T. Muto; Generation of diamond nuclei by electric field in plasma chemical vapor deposition. *Applied Physics Letters*, 1991. **58**(10): p. 1036-1038. DOI: 10.1063/1.104415.
24. M. Schreck, T. Baur, and B. Stritzker; Optical characterization of the cathode plasma sheath during the biasing step for diamond nucleation on silicon. *Diamond and Related Materials*, 1995. **4**(5–6): p. 553-558. DOI: 10.1016/0925-9635(94)05214-X.
25. J. C. Arnault and H. A. Girard; *Diamond Nucleation and Seeding Techniques: Two Complementary Strategies for the Growth of Ultra-thin Diamond Films*, in *Nanodiamond*, 2014, The Royal Society of Chemistry.
26. Ohtsuka Kazuki, Suzuki Kazuhiro, Sawabe Atsuhito, and Inuzuka Tadao; Epitaxial Growth of Diamond on Iridium. *Japanese Journal of Applied Physics*, 1996. **35**(8B): p. L1072. DOI: 10.1143/JJAP.35.L1072.
27. Th Bauer, M. Schreck, F. Hörmann, A. Bergmaier, G. Dollinger, and B. Stritzker; Analysis of the total carbon deposition during the bias enhanced nucleation of diamond on Ir/$SrTiO_3$ (001) using ^{13}C-methane. *Diamond and Related Materials*, 2002. **11**(3–6): p. 493-498. DOI: 10.1016/S0925-9635(01)00626-4.
28. M. Schreck, H. Roll, and B. Stritzker; Diamond/Ir/$SrTiO_3$: A material combination for improved heteroepitaxial diamond films. *Applied Physics Letters*, 1999. **74**(5): p. 650-652. DOI: 10.1063/1.123029.
29. M. Schreck, Th Bauer, S. Gsell, F. Hörmann, H. Bielefeldt, and B. Stritzker; Domain formation in diamond nucleation on iridium. *Diamond and Related Materials*, 2003. **12**(3–7): p. 262-267. DOI: 10.1016/s0925-9635(02)00361-8.
30. B. Golding, C. Bednarski-Meinke, and Z. Dai; Diamond heteroepitaxy: pattern formation and mechanisms. *Diamond and Related Materials*, 2004. **13**(4–8): p. 545-551. DOI: 10.1016/j.diamond.2004.01.040.
31. A. Chavanne, J. Barjon, B. Vilquin, J. Arabski, and J. C. Arnault; Surface investigations on different nucleation pathways for diamond heteroepitaxial growth on iridium. *Diamond and Related Materials*, 2012. **22**: p. 52-58. DOI: 10.1016/j.diamond.2011.12.005.

32. R. Brescia, M. Schreck, S. Gsell, M. Fischer, and B. Stritzker; Transmission electron microscopy study of the very early stages of diamond growth on iridium. *Diamond and Related Materials*, 2008. **17**(7–10): p. 1045-1050. DOI: 10.1016/j.diamond.2008.01.115.
33. N. Vaissiere, S. Saada, M. Bouttemy, A. Etcheberry, P. Bergonzo, and J. C. Arnault; Heteroepitaxial diamond on iridium: New insights on domain formation. *Diamond and Related Materials*, 2013. **36**: p. 16-25. DOI: 10.1016/j.diamond.2013.03.010.
34. S. Kono, M. Shiraishi, N.I. Plusnin, T. Goto, Y. Ikejima, T. Abukawa, M. Schimomura, Z. Dai, C. Bernarski-Meinke, and B. Golding; X-ray photoelectron diffraction study of the initial stages of CVD diamond heteroepitaxy on Ir(001)/$SrTiO_3$. *New Diamond Frontier Carbon Technology*, 2005. **15**(6).
35. S. Gsell, S. Berner, T. Brugger, M. Schreck, R. Brescia, M. Fischer, T. Greber, J. Osterwalder, and B. Stritzker; Comparative electron diffraction study of the diamond nucleation layer on Ir(001). *Diamond and Related Materials,* 2008. **17**(7–10): p. 1029-1034. DOI: 10.1016/j.diamond.2008.02.040.
36. F. Hörmann, M. Schreck, and B. Stritzker; First stages of diamond nucleation on iridium buffer layers. *Diamond and Related Materials*, 2001. **10**(9–10): p. 1617-1621. DOI: 10.1016/S0925-9635(01)00431-9.
37. M. Schreck, A. Schury, F. Hörmann, H. Roll, and B. Stritzker; Mosaicity reduction during growth of heteroepitaxial diamond films on iridium buffer layers: Experimental results and numerical simulations. *Journal of Applied Physics*, 2002. **91**(2): p. 676-685. DOI: 10.1063/1.1424059.
38. M. Schreck, F. Hörmann, H. Roll, J. K. N. Lindner, and B. Stritzker; Diamond nucleation on iridium buffer layers and subsequent textured growth: A route for the realization of single-crystal diamond films. *Applied Physics Letters*, 2001. **78**(2): p. 192-194. DOI: 10.1063/1.1337648.
39. X. Jiang and C. L. Jia; The coalescence of [001] diamond grains heteroepitaxially grown on (001) silicon. *Applied Physics Letters*, 1996. **69**(25): p. 3902-3904. DOI: 10.1063/1.117564.
40. Takeyasu Saito, Shigenori Tsuruga, Nobutaka Ohya, Katsuki Kusakabe, Shigeharu Morooka, Hideaki Maeda, Atsuhito Sawabe, and Kazuhiro Suzuki; Epitaxial nucleation of diamond on an iridium substrate by bias treatment, for microwave plasma-assisted chemical vapor deposition. *Diamond and Related Materials*, 1998. **7**(9): p. 1381-1384. DOI: 10.1016/S0925-9635(98)00216-7.
41. C. Bednarski, Z. Dai, A. P. Li, and B. Golding; Studies of heteroepitaxial growth of diamond. *Diamond and Related Materials*, 2003. **12**(3–7): p. 241-245. DOI: 10.1016/S0925-9635(02)00287-X.
42. S. Gsell, T. Bauer, J. Goldfuss, M. Schreck, and B. Stritzker; A route to diamond wafers by epitaxial deposition on silicon via iridium/yttria-stabilized zirconia buffer layers. *Applied Physics Letters*, 2004. **84**(22): p. 4541-4543. DOI: 10.1063/1.1758780.
43. M. Fischer, S. Gsell, M. Schreck, R. Brescia, and B. Stritzker; Preparation of 4-inch Ir/YSZ/Si(001) substrates for the large-area deposition of single-crystal diamond. *Diamond and Related Materials*, 2008. **17**(7–10): p. 1035-1038. DOI: 10.1016/j.diamond.2008.02.028.
44. S. Gsell, M. Fischer, R. Brescia, M. Schreck, P. Huber, F. Bayer, B. Stritzker, and D. G. Schlom; Reduction of mosaic spread using iridium interlayers: A route to improved oxide heteroepitaxy on silicon. *Applied Physics Letters*, 2007. **91**(6): p. 061501-3. DOI: 10.1063/1.2768003.
45. T. Bauer, S. Gsell, M. Schreck, J. Goldfuß, J. Lettieri, D. G. Schlom, and B. Stritzker; Growth of epitaxial diamond on silicon via iridium/$SrTiO_3$ buffer layers. *Diamond and Related Materials*, 2005. **14**(3–7): p. 314-317. DOI: 10.1016/j.diamond.2004.10.028.
46. M. Fischer, R. Brescia, S. Gsell, M. Schreck, T. Brugger, T. Greber, J. Osterwalder, and B. Stritzker; Growth of twin-free heteroepitaxial diamond on Ir/YSZ/Si(111). *Journal of Applied Physics*, 2008. **104**(12): p. 123531-5. DOI: 10.1063/1.3019046.
47. Martin Fischer; *Heteroepitaxie von Diamant auf Iridium/YSZ/Silizium: Untersuchungen zu Keimbildung, Wachstum und Schichteigenschaften*, in *Lehrstuhl für Experimentalphysik IV*, 2013, Universität Augsburg.
48. Keshra Sangwal; *Etching of crystals*, 1st ed., Defects in solids, ed. S. Amelinckx and J. Nihoul, 1987, Elsevier Science Publishers B. V.
49. D. Hull and D. J. Bacon; *Introduction to Dislocations*, 3rd ed., 2011, Pergamon.
50. C. Stehl, M. Fischer, S. Gsell, E. Berdermann, M. S. Rahman, M. Traeger, O. Klein, and M. Schreck; Efficiency of dislocation density reduction during heteroepitaxial growth of diamond

for detector applications. *Applied Physics Letters*, 2013. **103**(15): p. 151905. DOI: 10.1063/1.4824330.

51. Oliver Klein, Michael Mayr, Martin Fischer, Stefan Gsell, and Matthias Schreck; Propagation and annihilation of threading dislocations during off-axis growth of heteroepitaxial diamond films. *Diamond and Related Materials*, 2016. **65**: p. 53-58. DOI: 10.1016/j.diamond.2016.01.024.
52. A.T. Blumenau, Thomas Frauenheim, Sven Öberg, B. Willems, and Gustaaf van Tendeloo; Dislocation Structures in Diamond: Density-Functional Based Modelling and High-Resolution Electron Microscopy. *Defect and Diffusion Forum*, 2004. **226-228**: p. 11-30. DOI: 10.4028/www.scientific.net/DDF.226-228.11.
53. N. Fujita, A. T. Blumenau, R. Jones, S. Öberg, and P. R. Briddon; Core reconstructions of the 〈100〉 edge dislocation in single crystal CVD diamond. *physica status solidi (a)*, 2007. **204**(7): p. 2211-2215. DOI: 10.1002/pssa.200675444.
54. Christopher I. Pakes, Jose A. Garrido, and Hiroshi Kawarada; Diamond surface conductivity: Properties, devices, and sensors. *MRS Bulletin*, 2014. **39**(06): p. 542-548. DOI: 10.1557/mrs.2014.95.
55. M. Kaukonen, P. K. Sitch, G. Jungnickel, R. M. Nieminen, Sami Pöykkö, D. Porezag, and Th Frauenheim; Effect of N and B doping on the growth of CVD diamond (100):H(2×1) surfaces. *Physical Review B*, 1998. **57**(16): p. 9965-9970. DOI: 10.1103/PhysRevB.57.9965.
56. J. Achard, F. Silva, O. Brinza, A. Tallaire, and A. Gicquel; Coupled effect of nitrogen addition and surface temperature on the morphology and the kinetics of thick CVD diamond single crystals. *Diamond and Related Materials*, 2007. **16**(4–7): p. 685-689. DOI: 10.1016/j.diamond.2006.09.012.
57. A. Tallaire, A. T. Collins, D. Charles, J. Achard, R. Sussmann, A. Gicquel, M. E. Newton, A. M. Edmonds, and R. J. Cruddace; Characterisation of high-quality thick single-crystal diamond grown by CVD with a low nitrogen addition. *Diamond and Related Materials*, 2006. **15**(10): p. 1700-1707. DOI: 10.1016/j.diamond.2006.02.005.
58. F. K. de Theije, J. J. Schermer, and W. J. P. van Enckevort; Effects of nitrogen impurities on the CVD growth of diamond: step bunching in theory and experiment. *Diamond and Related Materials*, 2000. **9**(8): p. 1439-1449. DOI: 10.1016/s0925-9635(00)00261-2.
59. S. Dunst, H. Sternschulte, and M. Schreck; Growth rate enhancement by nitrogen in diamond chemical vapor deposition---a catalytic effect. *Applied Physics Letters*, 2009. **94**(22): p. 224101. DOI: 10.1063/1.3143631.
60. Michael Mayr, Christian Stehl, Martin Fischer, Stefan Gsell, and Matthias Schreck; Correlation between surface morphology and defect structure of heteroepitaxial diamond grown on off-axis substrates. *physica status solidi (a)*, 2014: p. 2257-2263. DOI: 10.1002/pssa.201431210.
61. N. F. Mott; Metal-insulator transitions. *Philosophical Magazine Part B*, 1984. **50**(2): p. 161-167. DOI: 10.1080/13642818408238834.
62. E. Bustarret, E. Gheeraert, and K. Watanabe; Optical and electronic properties of heavily boron-doped homo-epitaxial diamond. *physica status solidi (a)*, 2003. **199**(1): p. 9-18. DOI: 10.1002/pssa.200303819.
63. V. A. Sidorov and E. A. Ekimov; Superconductivity in diamond. *Diamond and Related Materials*, 2010. **19**(5-6): p. 351-357. DOI: 10.1016/j.diamond.2009.12.002.
64. Yoshihiko Takano, Masanori Nagao, Isao Sakaguchi, Minoru Tachiki, Takeshi Hatano, Kensaku Kobayashi, Hitoshi Umezawa, and Hiroshi Kawarada; Superconductivity in diamond thin films well above liquid helium temperature. *Applied Physics Letters*, 2004. **85**(14): p. 2851-2853. DOI: 10.1063/1.1802389.
65. J. P. Lagrange, A. Deneuville, and E. Gheeraert; Activation energy in low compensated homoepitaxial boron-doped diamond films. *Diamond and Related Materials*, 1998. **7**(9): p. 1390-1393. DOI: 10.1016/s0925-9635(98)00225-8.
66. H. El-Hajj, A. Denisenko, A. Kaiser, R. S. Balmer, and E. Kohn; Diamond MISFET based on boron delta-doped channel. *Diamond and Related Materials*, 2008. **17**(7–10): p. 1259-1263. DOI: 10.1016/j.diamond.2008.02.015.
67. E. F. Schubert, R. F. Kopf, J. M. Kuo, H. S. Luftman, and P. A. Garbinski; Spatial resolution of the capacitance-voltage profiling technique on semiconductors with quantum confinement. *Applied Physics Letters*, 1990. **57**(5): p. 497-499. DOI: 10.1063/1.103632.

68. H. El-Hajj, A. Denisenko, A. Bergmaier, G. Dollinger, M. Kubovic, and E. Kohn; Characteristics of boron δ-doped diamond for electronic applications. *Diamond and Related Materials*, 2008. **17**(4–5): p. 409-414. DOI: 10.1016/j.diamond.2007.12.030.
69. Alexandre Fiori, Julien Pernot, Etienne Gheeraert, and Etienne Bustarret; Simulations of carrier confinement in boron δ-doped diamond devices. *physica status solidi (a)*, 2010. **207**(9): p. 2084-2087. DOI: 10.1002/pssa.201000062.
70. P. N. Volpe, N. Tranchant, J. C. Arnault, S. Saada, F. Jomard, and P. Bergonzo; Ultra-sharp boron interfaces for delta doped diamond structures. *physica status solidi (RRL)*, 2012. **6**(2): p. 59-61. DOI: 10.1002/pssr.201105480.
71. Jan Isberg; *Transport Properties of Electrons and Holes in Diamond*, in *CVD Diamond for Electronic Devices and Sensors*, 2009, John Wiley & Sons, Ltd.
72. Rolf Sauer; *Chapter 8 Luminescence from optical defects and impurities in CVD diamond*, in *Semiconductors and Semimetals*, E.N. Christoph and R. Juergen, Editors, 2003, Elsevier.
73. R. Erz, W. Dötter, K. Jung, and H. Ehrhardt; Investigation of boron and hydrogen concentrations in p-type diamond films by infrared spectroscopy. *Diamond and Related Materials*, 1995. **4**(4): p. 469-472. DOI: 10.1016/0925-9635(94)05320-0.
74. Hyunjung Kim, M. Grimsditch, T. R. Anthony, A. K. Ramdas, and S. Rodriguez; Infrared and Raman Spectroscopy of Acceptors in Diamond: Boron Impurities. *physica status solidi (a)*, 2000. **181**(1): p. 51-58. DOI: 10.1002/1521-396x(200009)181:1<51::aid-pssa51>3.0.co;2-o.
75. G. Faggio, G. Messina, S. Santangelo, G. Prestopino, I. Ciancaglioni, and M. Marinelli; Raman scattering in boron-doped single-crystal diamond used to fabricate Schottky diode detectors. *Journal of Quantitative Spectroscopy and Radiative Transfer*, 2012. **113**(18): p. 2476-2481. DOI: 10.1016/j.jqsrt.2012.06.012.
76. Steven Prawer and Robert J. Nemanich; Raman spectroscopy of diamond and doped diamond. *Philosophical Transactions of the Royal Society of London A: Mathematical, Physical and Engineering Sciences*, 2004. **362**(1824): p. 2537-2565. DOI: 10.1098/rsta.2004.1451.
77. H. Kawarada, H. Matsuyama, Y. Yokota, T. Sogi, A. Yamaguchi, and A. Hiraki; Excitonic recombination radiation in undoped and boron-doped chemical-vapor-deposited diamonds. *Physical Review B*, 1993. **47**(7): p. 3633-3637. DOI: 10.1103/PhysRevB.47.3633.
78. J. Barjon, T. Tillocher, N. Habka, O. Brinza, J. Achard, R. Issaoui, F. Silva, C. Mer, and P. Bergonzo; Boron acceptor concentration in diamond from excitonic recombination intensities. *Physical Review B*, 2011. **83**(7): p. 073201. DOI: 10.1103/PhysRevB.83.073201.
79. E. Kohn and A. Denisenko; *Doped Diamond Electron Devices*, in *CVD Diamond for Electronic Devices and Sensors*, 2009, John Wiley & Sons, Ltd.
80. F. Brunet, P. Germi, M. Pernet, A. Deneuville, E. Gheeraert, F. Laugier, M. Burdin, and G. Rolland; The effect of boron doping on the lattice parameter of homoepitaxial diamond films. *Diamond and Related Materials*, 1998. **7**(6): p. 869-873. DOI: 10.1016/s0925-9635(97)00316-6.
81. F. Brunet, P. Germi, M. Pernet, A. Deneuville, E. Gheeraert, F. Laugier, M. Burdin, and G. Rolland; Microstructure evolution of boron doped homoepitaxial diamond films. *Journal of Applied Physics*, 1998. **83**(1): p. 181-186. DOI: 10.1063/1.366671.
82. P. Muret, P. N. Volpe, J. Pernot, and F. Omnès; Hole traps profile and physical properties of deep levels in various homoepitaxial diamond films studied by isothermal and deep level transient spectroscopies. *Diamond and Related Materials*, 2011. **20**(5–6): p. 722-725. DOI: 10.1016/j.diamond.2011.03.013.
83. Isao Sakaguchi, Mikka Nishitani-Gamo, Kian Ping Loh, Hajime Haneda, Shunichi Hishita, and Toshihiro Ando; Silicon incorporation into chemical vapor deposition diamond: A role of oxygen. *Applied Physics Letters*, 1997. **71**(5): p. 629-631. DOI: 10.1063/1.119812.
84. M. Kadri, D. Araujo, M. Wade, A. Deneuville, and E. Bustarret; Effect of oxygen on the cathodoluminescence signal from excitons, impurities and structural defects in homoepitaxial (100) diamond films. *Diamond and Related Materials*, 2005. **14**(3–7): p. 566-569. DOI: 10.1016/j.diamond.2004.10.018.
85. Peter K. Bachmann, Dieter Leers, and Hans Lydtin; Towards a general concept of diamond chemical vapour deposition. *Diamond and Related Materials*, 1991. **1**(1): p. 1-12. DOI: 10.1016/0925-9635(91)90005-u.
86. Elke Neu, Martin Fischer, Stefan Gsell, Matthias Schreck, and Christoph Becher; Fluorescence and polarization spectroscopy of single silicon vacancy centers in heteroepitaxial nanodiamonds on iridium. *Physical Review B*, 2011. **84**(20): p. 205211. DOI: 10.1103/PhysRevB.84.205211.

87. S. Jin, W. Zhu, T. Siegrist, T. H. Tiefel, G. W. Kammlott, J. E. Graebner, and M. McCormack; Anisotropy in diamond etching with molten cerium. *Applied Physics Letters*, 1994. **65**(21): p. 2675-2677. DOI: 10.1063/1.112599.
88. Wook-Seong Lee, Young-Joon Baik, Kwang Yong Eun, and Duk-Yong Yoon; Metallographic etching of polycrystalline diamond films by reaction with metal. *Diamond and Related Materials*, 1995. **4**(7): p. 989-995. DOI: 10.1016/0925-9635(95)00271-5.
89. C. L. Cheng, H. C. Chang, J. C. Lin, K. J. Song, and J. K. Wang; Direct Observation of Hydrogen Etching Anisotropy on Diamond Single Crystal Surfaces. *Physical Review Letters*, 1997. **78**(19): p. 3713-3716. DOI: 10.1103/PhysRevLett.78.3713.
90. Kazushi Hayashi, Sadanori Yamanaka, Hideyo Okushi, and Koji Kajimura; Stepped growth and etching of (001) diamond. *Diamond and Related Materials*, 1996. **5**(9): p. 1002-1005. DOI: 10.1016/0925-9635(95)00470-X.
91. R. E. Rawles, S. F. Komarov, R. Gat, W. G. Morris, J. B. Hudson, and M. P. D'Evelyn; Mechanism of surface smoothing of diamond by a hydrogen plasma. *Diamond and Related Materials*, 1997. **6**(5–7): p. 791-795. DOI: 10.1016/S0925-9635(96)00623-1.
92. Naesung Lee and Andrzej Badzian; Effect of misorientation angles on the surface morphologies of (001) homoepitaxial diamond thin films. *Applied Physics Letters*, 1995. **66**(17): p. 2203-2205. DOI: 10.1063/1.113947.
93. Brian D. Thoms, Michael S. Owens, James E. Butler, and Clifford Spiro; Production and characterization of smooth, hydrogen-terminated diamond C(100). *Applied Physics Letters*, 1994. **65**(23): p. 2957-2959. DOI: 10.1063/1.112503.
94. C. C. Battaile, D. J. Srolovitz, I. I. Oleinik, D. G. Pettifor, A. P. Sutton, S. J. Harris, and J. E. Butler; Etching effects during the chemical vapor deposition of (100) diamond. *The Journal of Chemical Physics*, 1999. **111**(9): p. 4291-4299. DOI: 10.1063/1.479727.
95. G. S. Sandhu and W. K. Chu; Reactive ion etching of diamond. *Applied Physics Letters*, 1989. **55**(5): p. 437-438. DOI: 10.1063/1.101890.
96. A. Joshi and R. Nimmagadda; Erosion of diamond films and graphite in oxygen plasma. *Journal of Materials Research*, 1991. **6**(07): p. 1484-1490. DOI: doi:10.1557/JMR.1991.1484.
97. R. Ramesham and B. H. Loo; Air-Microwave Plasma Etching of Polycrystalline Diamond Thin Films. *Journal of The Electrochemical Society*, 1992. **139**(7): p. 1988-1993. DOI: 10.1149/1.2069533.
98. Timothy J. Whetten, Angela A. Armstead, Thomas A. Grzybowski, and Arthur L. Ruoff; Etching of diamond with argon and oxygen ion beams. *Journal of Vacuum Science & Technology A*, 1984. **2**(2): p. 477-480. DOI: 10.1116/1.572598.
99. N. N. Efremow, M. W. Geis, D. C. Flanders, G. A. Lincoln, and N. P. Economou; Ion-beam-assisted etching of diamond. *Journal of Vacuum Science & Technology B*, 1985. **3**(1): p. 416-418. DOI: 10.1116/1.583276.
100. Toshihiro Ando, Kazuo Yamamoto, Motohiko Ishii, Mutsukazu Kamo, and Yoichiro Sato; Vapour-phase oxidation of diamond surfaces in O2 studied by diffuse reflectance Fourier-transform infrared and temperture-programmed desorption spectroscopy. *Journal of the Chemical Society, Faraday Transactions*, 1993. **89**(19): p. 3635-3640. DOI: 10.1039/ft9938903635.
101. E. van Veenendaal, P. van Beurden, W. J. P. van Enckevort, E. Vlieg, J. van Suchtelen, and M. Elwenspoek; Monte Carlo study of kinetic smoothing during dissolution and etching of the Kossel (100) and silicon (111) surfaces. *Journal of Applied Physics*, 2000. **88**(8): p. 4595-4604. DOI: 10.1063/1.1289812.
102. J. Achard, A. Tallaire, V. Mille, M. Naamoun, O. Brinza, A. Boussadi, L. William, and A. Gicquel; Improvement of dislocation density in thick CVD single crystal diamond films by coupling H_2/O_2 plasma etching and chemo-mechanical or ICP treatment of HPHT substrates. *physica status solidi (a)*, 2014: p. n/a-n/a. DOI: 10.1002/pssa.201431181.
103. M. Naamoun, A. Tallaire, F. Silva, J. Achard, P. Doppelt, and A. Gicquel; Etch-pit formation mechanism induced on HPHT and CVD diamond single crystals by H_2/O_2 plasma etching treatment. *physica status solidi (a)*, 2012. **209**(9): p. 1715-1720. DOI: 10.1002/pssa.201200069.
104. David B. Williams and C. Barry Carter; *Transmission Electron Microscopy - A Textbook for Materials Science*, 1st ed. Vol. 1, 2009, Springer US.
105. Cláudio Miguel Silva Nico; *Niobium oxides and niobates physical properties*, in *Department of Physics*, 2015, Universidade de Aveiro.

106. Mitsui Tadashi, Sekiguchi Takashi, Fujita Daisuke, and Koguchi Nobuyuki; Comparison between Electron Beam and Near-Field Light on the Luminescence Excitation of GaAs/AlGaAs Semiconductor Quantum Dots. *Japanese Journal of Applied Physics*, 2005. **44**(4R): p. 1820. DOI: 10.1143/JJAP.44.1820.
107. H. Kawarada and A. Yamaguchi; Excitonic recombination radiation as characterization of diamonds using cathodoluminescence. *Diamond and Related Materials*, 1993. **2**(2–4): p. 100-105. DOI: 10.1016/0925-9635(93)90038-4.
108. H. Sternschulte, J. Horseling, T. Albrecht, K. Thonke, and R. Sauer; Characterization of doped and undoped CVD-diamond films by cathodoluminescence. *Diamond and Related Materials*, 1996. **5**(6–8): p. 585-588. DOI: 10.1016/0925-9635(95)00400-9.
109. J. Barjon, M. A. Pinault, T. Kociniewski, F. Jomard, and J. Chevallier; Cathodoluminescence as a tool to determine the phosphorus concentration in diamond. *physica status solidi (a)*, 2007. **204**(9): p. 2965-2970. DOI: 10.1002/pssa.200776324.
110. C. Baron, M. Wade, A. Deneuville, F. Jomard, and J. Chevallier; Cathodoluminescence of highly and heavily boron doped (100) homoepitaxial diamond films. *Diamond and Related Materials*, 2006. **15**(4-8): p. 597-601. DOI: 10.1016/j.diamond.2006.01.015.

2 Gas phase studies during *in situ* boron-doping of diamond on Ir/YSZ/Si(001)

2.1 Introduction

Diamond is well-known for its outstanding properties, being the material of choice for high-end applications such as cutting of hard materials, tribology, radiation detection, electroanalysis, bio-sensing, high-power high-frequency switching, deep UV emission, quantum computing [1-6].

Among the most critical factors that still limit the widespread application of diamond are 1) the controlled growth of diamond with the desired properties, *e.g.* a well-defined doping level and 2) the availability of high-quality, large-area diamond substrates.

Even large-grain polycrystalline diamond substrates with the highest (structural and optical) quality suffer from the presence of some grain boundaries, which deteriorate charge transport properties and from the strong generic variation of boron incorporation with the crystallographic orientation of the growth surface [7]. Single crystals from the high-pressure, high-temperature (HPHT) synthesis or homoepitaxial layers grown on top can meet quality requirements [8], but not with technologically relevant sample size. A promising strategy in the quest for large area diamond single crystals is heteroepitaxial growth.

Significant progress has been made in the field of heteroepitaxial growth since the introduction of Ir as a substrate for high density nucleation of epitaxial diamond crystals by bias enhanced nucleation (BEN) [9-13]. This has allowed, under appropriate microwave plasma-enhanced CVD (MWPCVD) conditions, the formation of cm^2 large, dislocation-rich diamond single crystals (*i.e.* low mosaic spread) which can already be used in high-end applications as radiation detectors or as neutron monochromators [1, 14]. Further improvement of the heteroepitaxial diamond material is a challenging topic of current research, which will enable further technological applications. Therefore significant effort has been devoted into understanding and reducing the density of defects in the crystals, namely dislocations [13, 15-17].

The quality and the properties of diamond crystals grown by MWPCVD depend heavily not only on the substrate, but equally on the growth environment, as described in chapter 1. The 1) necessity to grow thick films with unspoiled single crystalline quality in an economically feasible time and 2) the necessity to adopt different strategies to accelerate the mutual interaction and annihilation of the dislocations are paramount. The former point (*i.e.* growing thick and fast) involves the selection of appropriate growth conditions, with particular attention to gas mixture and plasma chemistry around the substrate. In short, the controlled growth environment and the interaction of different species present in the plasma are crucial for the synthesis of high-quality diamond crystals with the desired electrical and optical properties. The interaction of chemical species in the plasma and the effect on the grown diamond films are the subject of study in this chapter.

Doping atoms or, more generally speaking, impurities in the gas phase can modify CVD diamond growth and thus, besides the simple incorporation of dopants in the lattice, their specific influence on growth and potential mutual interaction of impurity atoms are of interest. Furthermore, handling B in the CVD reactor to produce precise and constant doping concentrations over the whole thickness remains a challenge, and therefore needs investigation. This is very important for the fabrication of solid-state devices with optimum performance and is especially critical to produce δ-doping profiles [18, 19].

Last, but not least, in a number of former doping studies strong memory effects[1] and a high sensitivity of the doping efficiency to the presence of gases like oxygen have been reported [20, 21]. In all these cases a variation of the boron concentration in the gas phase is only one possible explanation, among other alternatives.

In a first step, in this work we focussed on the monitoring of impurities (namely B) added to the gas phase by optical emission spectroscopy (OES), in order to quantify potential memory effects in the CVD chamber and elucidate interactions between dopant-containing precursors and other gas phase components, such as O and N. Later we studied the interaction of B and N in the plasma during growth and its effect on the growth rate, again with aid of OES and light reflectance interferometry (LRI).

2.1.1 Optical emission spectroscopy (OES)

Optical emission spectroscopy (OES) is one of the oldest and most popular methods of plasma monitoring. Fundamentally, OES is a measure of the optical radiation emitted from the plasma species. Since emissions can emanate from reactants as well as products, OES measurements are most often used to obtain the average optical intensity at particular wavelengths. By setting an optical spectrometer to monitor the intensity at a wavelength associated with a particular reactant or by-product species, OES serves as a non-invasive, real-time plasma monitoring tool [22]. In contrast to absorption measurements, the technique suffers from the drawback of a very limited quantifiability due to very complex and normally uncontrollable excitation channels (*i.e.* direct excitation from the ground state, excitation into higher levels which radiatively cascade into the level of interest, and excitation from long-lived metastable atoms in the plasma). In some cases this problem can be addressed by the method of actinometry [23].

In the present studies we use OES as a semi-quantitative tool to detect the presence of impurities or dopants in the gas phase during diamond growth (see **Figure 2-1**), to monitor the correlation of their emission signal with the precursor concentration in the feed gas, and to detect potential chemical interactions between different components in the gas phase.

---

[1] *I.e.* when former processes influence subsequent processes by changing the environment in the reactor.

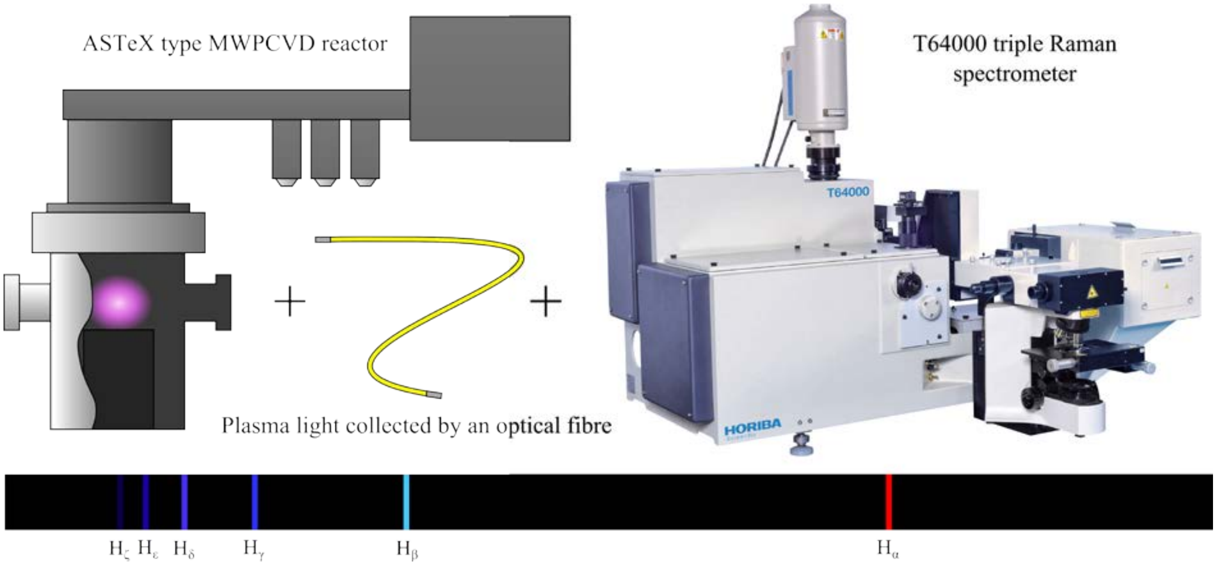

Figure 2-1: Schematics of the optical emission spectroscopy (OES) setup used in this work. The light emitted from the plasma during MWPCVD growth is collected through a quartz window by an optical fibre, and fed into the entrance slit of the T64000 triple Raman spectrometer for analysis. On the bottom part, a representation of the spectrum produced by atomic hydrogen with its Balmer lines is shown.

The signature of boron in the plasma, a band at 433.16 nm corresponding to the $A^1\Pi - X^1\Sigma$ system, stems from the emission of BH that is formed after the decomposition of a boron-containing gas such as diborane, B_2H_6, or trimethylborane (TMB for short), $B(CH_3)_3$, and as a result of "H-shifting" reactions of different species: $BH_x + H \rightleftharpoons BH_{x-1} + H_2$, $x = 1...3$ [24-26]. It is believed that BH is an energetically more favourable doping agent than BH_3 and BH_2, thus driving boron incorporation into the diamond lattice [26].

Nitrogen is detected from the emission of CN radicals with a prominent band of the $B^2\Sigma - X^2\Sigma$ system at 388.30 nm [27]. Former studies have shown that the CN signal scales linearly with $[N_2]_{\text{feedgas}}$ addition but it is only weakly dependent on the $[CH_4]_{\text{feedgas}}$ [28].

2.1.2 Laser reflectance interferometry (LRI)

LRI is an optical method that takes advantage of the interference phenomenon of light to enable the measurement of film thicknesses [29]. When a monochromatic light (*e.g.* from a laser) is directed towards a transparent thin film (see **Figure 2-2**), part is reflected at the surface (beam 1), and part is transmitted through the film (beam 2). The transmitted portion of light is eventually reflected back at the interface with a reflective substrate and leaves the film having travelled a different distance. This distance corresponds to an optical path difference (OPD) between the two beams, which is equal to $2dn_2 \cos\theta_2$, with *d* being the film thickness [30]. The OPD can change the phase relations between the two outgoing waves, *i.e.* constructive interference will occur whenever the phase difference is a multiple *m* of the wavelength λ of the incident light, which allows the determination of the thickness from the following equation [30]:

$$d = \frac{m\lambda}{2n_2 \cos\theta_2} = \frac{m\lambda}{2n_2 \cos\left[\sin^{-1}\left(\frac{\sin\theta_1}{n_2}\right)\right]} \tag{2.1.1}$$

In the case of quasi-normal incidence, *i.e.* $\theta_1 \approx 0$, the equation above simplifies to:

$$d \approx \frac{m\lambda}{2n_2 - \theta_1^2/n_2^2} \overset{\theta_1=0}{=} \frac{m\lambda}{2n_2} \tag{2.1.2}$$

By measuring over a time t the intensity $I_{\mathrm{LRI}}(t)$ of the light leaving the sample during diamond growth, the thickness $d(t)$ of the film can be determined by counting the number of maxima $m(t)$ of the measured oscillating pattern. Once the thickness is obtained, the growth rate $\Delta d/\Delta t$ can be calculated.

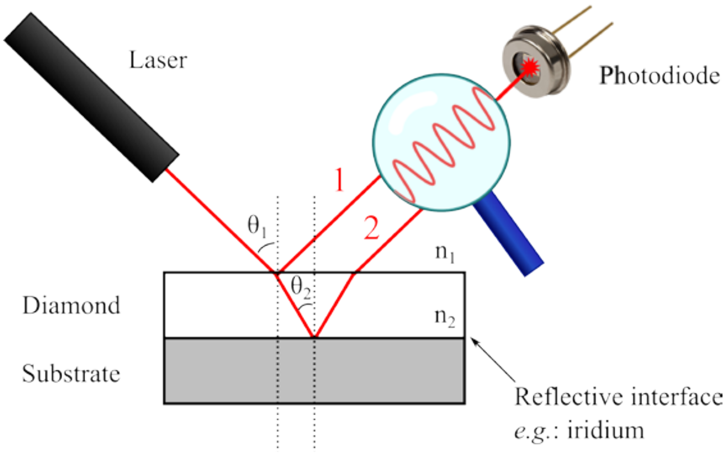

Figure 2-2: Schematics of the laser reflectance interferometry (LRI) setup.

2.2 Experimental

2.2.1 Sample preparation

All diamond films were grown on Ir/YSZ/Si(001) using BEN for the generation of diamond nuclei. For the preparation of the substrate, first a several ten nm thick layer of yttria-stabilised zirconia (YSZ) was deposited on a 3 mm thick, 4° off-axis Si(001) wafer by pulsed laser deposition (PLD) as described in ref. [31]. An iridium layer was then grown by e-beam evaporation at 650 °C (see ref. [32]). The BEN process was carried out in a MWPCVD reactor using an atmosphere of 3% CH_4 in H_2 and a bias voltage of −300 V. An intrinsic diamond layer of ~1 µm thickness was grown on the nucleated Ir/YSZ/Si(001) stack using a microwave power of 2 kW at 40 mbar in an atmosphere of 1.5% CH_4 in H_2 with 100 ppm N_2.

Subsequently, diamond growth was continued under variable conditions in one of two similar (identical vacuum chamber and microwave cavity) ASTeX type MWPCVD reactors, depending on the experiment. The reactor dedicated for B-doping with a separate gas line exclusive for TMB is referred to as “reactor #1”, while the other (which has a low B background and is used for growth of undoped diamond) is referred to as “reactor #2”. Base growth conditions were two: a) low pressure growth at 50 mbar, 2% CH_4 in H_2 at 720-750 °C and b) high pressure growth at 100 mbar, 4-5% CH_4 in H_2 at ~900 °C. The microwave power was adjusted to keep the temperature values comparable. Because reactor #1 has a heated stage (sample holder), it only needed 1100-1200 W, while reactor #2 needed 2100-2500 W to compensate for the use of a cooled stage. Detailed parameters will be mentioned where relevant.

The gas precursors used included purified H_2, CH_4, CO_2, trimethylborane (TMB) and N_2. With a typical total gas flow of 400 sccm the gas exchange time τ_{95} was estimated to be ~10 min (*i.e.*, after this time, over 95% of the initial gas volume was exchanged).

2.2.2 Measurement conditions

For the OES measurements the light emitted from the plasma was collected by an optical fibre and transferred to the T64000 triple Raman spectrometer. In the triple additive configuration the specified maximum resolution of this instrument is ~0.004 nm at 500 nm. To determine the detection threshold for BH in the plasma we tested different spectrometer modes and identified the single mode using a 1800 mm^{-1} diffraction grating and 30-50 µm slit width, corresponding to a spectral resolution of 0.03-0.04 nm, as optimum configuration. The emission intensities of the BH ($A^1\Pi - X^1\Sigma$ system at 433.16 nm) and CN ($B^2\Sigma - X^2\Sigma$ system at 388.30 nm [27]) species were normalised relative to the H_γ line (434.05 nm) of the Balmer series.

During the deposition process the growth rate was monitored *in situ* by laser reflectance interferometry (LRI) using a HeNe laser, a mechanical chopper, and lock-in technique.

The B concentration in the samples was evaluated using cathodoluminescence (CL), according to a method described in section 1.6.1 and in the literature [33, 34]. CL was performed in high vacuum (~10^{-6} mbar) at liquid nitrogen temperature. Excitation was done by a 7 keV electron beam with a spot size of ~1 mm. The light was guided from the exit window by optical elements on an optical table towards the entrance slit (with variable opening width) of the T64000 spectrometer, operating in single mode with a 600 mm^{-1} grating.

2.3 Results and discussion

2.3.1 Detection of boron in the gas phase

The addition of TMB to the gas mixture leads to the formation of BH species in the CVD plasma. In a first step, we investigated the relationship between BH emission intensity and TMB concentration in the gas phase by systematically varying the concentration of TMB in the feed gas and measuring the BH emission intensity. In this way, we aimed to establish optimum conditions for the detection of B in the gas using our OES setup, and to achieve the highest possible sensitivity. **Figure 2-3** (a) shows the spectral region between 432.9 nm and 434.2 nm which contains the H_γ Balmer line of atomic hydrogen at 434.05 nm and the BH emission band at 433.16 nm. By operating the spectrometer in the triple additive mode (highest resolution) the narrow BH band can be decomposed into several individual lines. However, it turned out that the higher resolution did not yield a higher sensitivity (*e.g.* by better separating individual BH peaks from the background emission). Instead it only reduced the signal-to-noise ratio. For this reason, the optimum spectral resolution was found to be 0.04 nm. Under this condition, the intensity of the BH peak was found to scale linearly with the TMB precursor concentration in the feed gas (**Figure 2-3** (b)), with a detection threshold for B in the gas phase equivalent to ~1-3 ppm TMB.

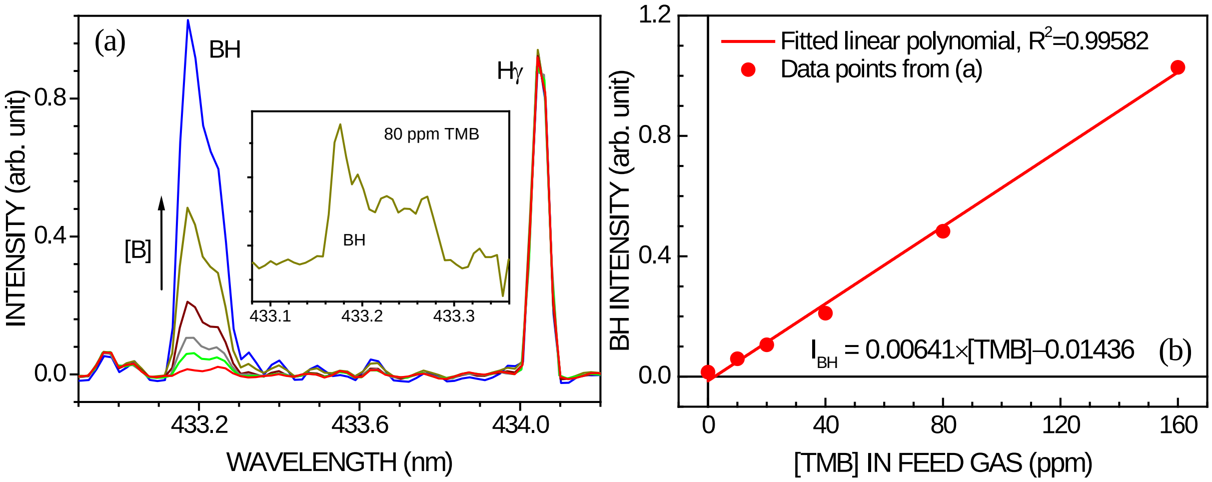

Figure 2-3: (a) Variation of the OE spectra in the wavelength region that contains the BH emission and the H_γ Balmer line with increasing TMB concentration in the feed gas (spectral resolution: 0.04 nm, $CH_4/H_2 = 2\%$, total flow rate: 400 sccm, 50 mbar, 1100 W microwave power). The spectra are normalised to a constant height of H_γ which showed a scatter in absolute intensity of less than 8%. The inset graph shows the BH system taken with higher resolution (0.01 nm). (b) Normalised BH emission *versus* TMB concentration in the feed gas.

The linear correlation between precursor concentration in the feed gas and the BH signal observed in the present OES measurements suggests that the OES signal of the BH species may be used as a semi-quantitative tool to study the memory effects, the influence of oxygen and the interaction between different gas phase species in a systematic way.

2.3.2 Interaction of the boron precursor with the reactor environment

In a CVD setup deposition does not only occur on the sample, but adsorption and desorption processes can also involve substrate holder, heater and the reactor walls. This adsorption/desorption kinetics will change when the precursor concentration is varied in the gas phase, which is necessary, for example, when preparing samples with defined doping profiles. Knowledge of the typical time constants of the deposition system is therefore of high relevance. The maximum change is obtained when a reactor is restarted after a profound cleaning. This situation is simulated in the following experiments.

The basic concept was to first clean the sample holder from carbon/boron deposits, and then perform an OES monitoring of the BH signal evolution during simulated growth conditions with a high TMB concentration in the feed gas. Afterwards the same procedure was repeated without the cleaning step. In both cases the BH emission signal was measured against time and plotted in **Figure 2-4** (a, b), respectively.

In order to estimate the time constants of the deposition system, a few considerations were made: 1) under normal process conditions, the working pressure in the reactor is controlled downstream by a regulated exhaust pumping system which counter-balances the flow of feedstock gases into the chamber; 2) the feedstock gas composition consists of more than 90% hydrogen, which is mostly not consumed, and so the flow of gas being extracted from the chamber is approximately identical to the flow of feed gas; 3) the feed gas is assumed to instantly form a homogeneous mixture with the gas in the chamber, because of the relatively small chamber volume (*ca.* 8 L), low pressure and high gas flow rate; 4) the difference in temperature between the gas mixture in the reactor and the feed gas is neglected. Under these conditions, a simple dilution model for the gas mixture in the reactor can be deduced:

$$c(t) = c_{\text{in}} + (c_0 - c_{\text{in}}) e^{-t/\tau} \tag{2.3.1}$$

where $c(t)$ is the concentration of the solute (*e.g.* TMB in H_2) at a given time *t*, c_0 is the initial solute concentration in the chamber (*i.e.* right before dilution starts) and c_{in} is the concentration of solute in the feed gas. The gas exchange time τ is given by:

$$\tau = \frac{\text{chamber volume} \times \text{working pressure}}{\text{ambient pressure} \times \text{total flow rate}}. \tag{2.3.2}$$

This exchange time, which corresponds to a decrease/dilution factor of e^{-1}, was estimated to be around 4 min for our reactor at present conditions (*i.e.* 100 sccm, 50 mbar). From the same equations, 90% of the gas is exchanged after ~9 min. However, upon analysis of the BH emission intensity in **Figure 2-4** (a), which shows the increase of the BH emission signal after a growth process was started with 1000 ppm TMB in the feed gas, we observed that it took ~7 hours instead of a few minutes for the BH signal to reach saturation level. This suggests that the clean parts of the reactor act as a sink for the boron precursor, until they are fully covered and adsorption and desorption are in an equilibrium. In a second, consecutive run, displayed in **Figure 2-4** (b), the rise time decreased to ~2 hours, which is a further evidence of having boron deposited on the inner parts of the reactor after the first run, leading to a quicker saturation and attainment of equilibrium.

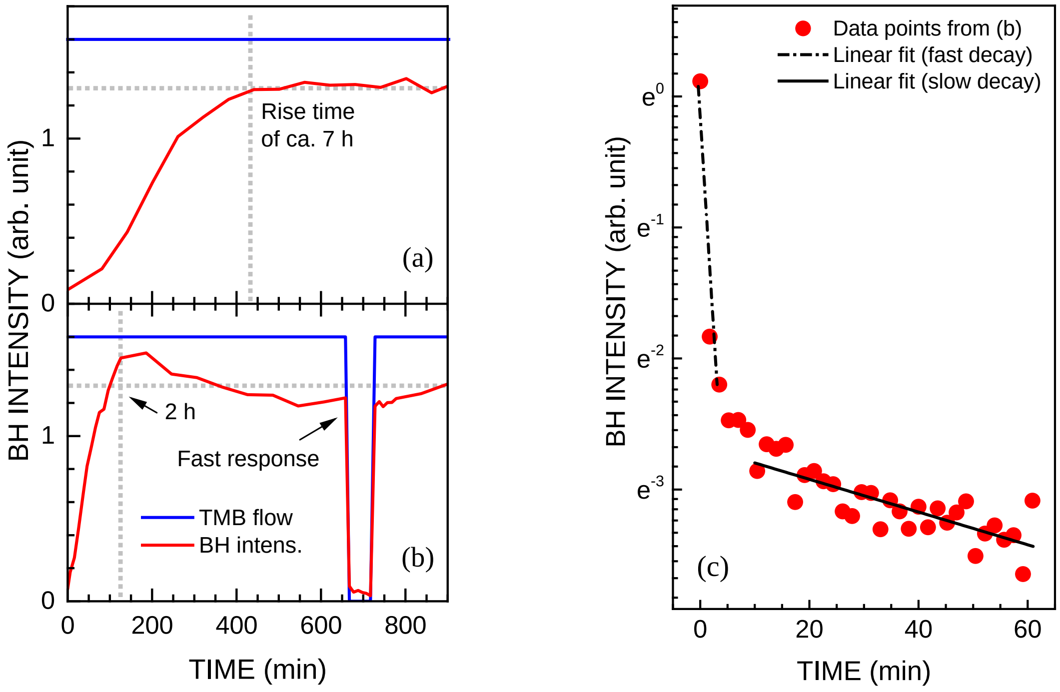

Figure 2-4: (a) Temporal development of the BH emission signal after the CVD reactor had been opened and cleaned. (b) Consecutive experiment under the same conditions. ([TMB] = 1000 ppm, $CH_4/H_2 = 2\%$, total flow rate: 100 sccm). The blue line shows the TMB flow. In (b) the TMB flow was interrupted for 1 hour and this period is shown in (c).

In **Figure 2-4** (b) the profile also shows the reaction after a sudden switch-off of the TMB addition, and the measured BH emission intensity is plotted in semi-logarithmic scale in **Figure 2-4** (c). There is a fast component with a time constant $\tau = 1.5$ min, that is less than half the pure gas exchange time estimated previously, and a slow component with $\tau = 80$ min. This behaviour can be explained by the fact that the reactor components, including the growing diamond film, first extract (or “pump”) boron from the gas phase, leading to a fast decay where the BH emission intensity decreased sharply by nearly one order of magnitude within less than 5 min. At a certain boron concentration the pumping by the reactor components changes its sign, *i.e.* boron is now released to the gas phase, thus giving rise to the slow decay component.

After a subsequent B doping growth process of 5 hours, a consecutive run without TMB in the feed gas for 20 hours reduced the BH intensity to a few ppm, close to our detection limit. This observation suggests that the release of boron by the contaminated parts in the reactor develops an even slower decay after prolonged process time. As a consequence, severe memory effects limit the possibility to realise steep concentration profiles or to grow superstructures consisting of alternating layers of high and low boron concentration.

There are different approaches which may help minimising this problem, including a complete redesign of the reactor. However, none of them can completely avoid it. In the following, we will explore a strategy to influence the memory effects by modifying the feed gas composition.

2.3.3 Interaction of oxygen with boron in the gas phase

Addition of oxygen during *in situ* B doping is known to reduce the incorporation efficiency drastically [20, 21] thus providing an interesting concept for the controlled reduction of memory effects and the preparation of steeper doping profiles. A *priori*, the reduction of the doping efficiency does not give any information about whether the interaction of B and O occurs in the gas phase or at the growth surface. In order to investigate these effects, we designed OES experiments to monitor the interaction of B with O in the gas phase.

Growth conditions were simulated in reactor #1 with the concomitant addition of TMB and CO_2 to the gas phase as, respectively, B and O precursors. The TMB concentration was fixed, while the CO_2 concentration was systematically varied and the BH emission monitored by OES. In the present experiments CO_2 was used instead of O_2 for safer handling. As CO_2 supplies O as well as C, the CH_4 concentration was adjusted (reduced) to compensate for the additional source of carbon. This results in the addition of CO_2 effectively translating into an equivalent addition of O_2 when $\left[CH_4\right]$ is kept constant. According to the basic idea of Bachmann's C-H-O diagram [35] (**Figure 1-18**) the specific nature of the precursors is irrelevant and only the atomic ratios matter.

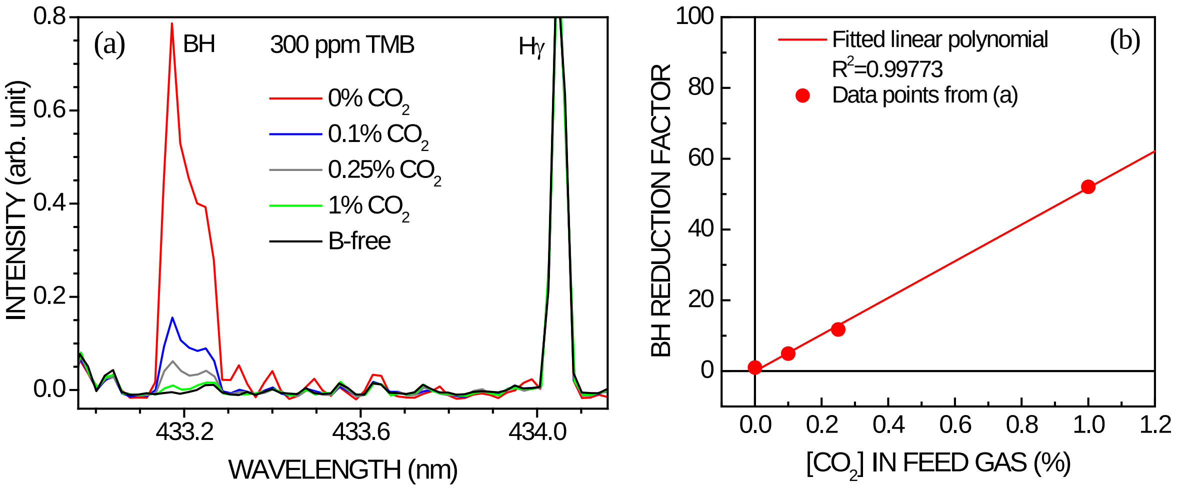

Figure 2-5: (a) OE spectra of the BH emission intensity with increasing CO_2 concentration for a TMB concentration of 300 ppm in the feed gas ($C/H_2 = 2\%$, variable $[CH_4]$ and $[CO_2]$, total flow rate: 200 sccm). (b) Reduction factor of the BH intensity versus CO_2 concentration in the feed gas and a linear fit of the data points. The highest data point at 1% CO_2 corresponds to a gas composition on the CO line of Bachmann's C-H-O diagram, *i.e.* $C{:}O = 1$ (see **Figure 2-7**).

The spectra in **Figure 2-5** (a) show the evolution of the BH emission with increasing concentration of CO_2 in the gas phase. The relationship between the BH emission intensity and CO_2 concentration is shown in **Figure 2-5** (b). These results show that CO_2 reduces the BH emission signal dramatically. From the linear correlation a reduction factor $I_{BH}(0)/I_{BH}([CO_2]) = [CO_2] \times 5200$ was deduced, *i.e.* for 1% CO_2 (equivalent to $O/C = 100\%$) the BH signal decreases by a factor of 52.

Two sets of diamond films have been grown with and without CO_2 addition in order to analyse the influence on the incorporation into the films. The B incorporation was determined by cathodoluminescence. In set 1, the B concentration in the films grown using only the boron background in the chamber (equivalent to 1-3 ppm TMB) was reduced by a factor of 13, from $8.8\times10^{17}\,\mathrm{cm}^{-3}$ to $7\times10^{16}\,\mathrm{cm}^{-3}$, when 0.25% CO_2 was added in the gas phase. In the second set 20 ppm TMB was used. Addition of 0.5% CO_2 reduced B concentration in the grown film from 2.2×10^{19} cm^{-3} to $1\times10^{18}\,\mathrm{cm}^{-3}$, *i.e.* by a factor of 22. Within experimental errors both values fit quite well to the relationship found for the reduction factor of the BH emission with CO_2 addition.

As a consequence, we conclude that the reduction of B incorporation into the diamond with addition of oxygen to the feed gas can be attributed to pure gas-phase effects, presumably through the formation of H_xBO ($x = 1,2$) compounds [36]. It is important to highlight this observation, since a completely different behaviour involving the interaction of B with N will be described later in section 2.3.6.

Our result has to be compared with a work by Omnés *et al.* [20] who reported a reduction of B incorporation by a factor of 100 with 0.25% of O_2 added to the gas phase for 1% CH_4, which corresponds to $O/C = 50\%$. Such reduction factor is 4-5 times higher than our calibration curve predicts. A decrease by more than two orders of magnitude has very recently been found for extreme O/C ratios of up to 1000% (*i.e.* 10 times more O than C) [21]. Such a strong suppression would provide a very efficient tool for the preparation of steep doping profiles, as required for δ-doping. However, the reported gas mixture is far away from the CO line towards the oxygen corner of Bachmann's C-H-O diagram. The mixture is even beyond the CO_2 line, which corresponds to an etching region where no growth should take place (see **Figure 2-7** (b)). Since the authors still report a small but positive deposition rate, it is currently difficult to make a final assessment of their findings and compare them with our observations, as variations among reported results may arise from differences in process parameters and conditions inherent to each reactor.

2.3.4 Retention of a constant growth rate under oxygen addition

Apart from reducing the incorporation of impurities in diamond, particularly of B, addition of O to the gas phase may lead to a significant reduction of the growth rate, which is often undesired. Irrespectively of the nature of the specific precursor, oxygen in the gas phase of a microwave discharge will always react with carbon and hydrogen to form predominantly CO and CO_2 or OH and H_2O. The most abundant species is typically CO [37]. Since CO is not supposed to contribute to the growth directly, the concentration of active growth species should decrease on oxygen addition, thus leading to slower growth. This follows the relationship illustrated in the Bachmann's C-H-O diagram in **Figure 1-18**. Preliminary observations of this effect had been made during routine experiments using oxygen.

In order to investigate this problem in a more systematic way and to establish a clearer relationship between oxygen concentration, concentration of growth species in the gas phase and growth rate, 3 different parameter sets representing different directions (or line scans) through Bachmann's C-H-O parameter space were defined (see **Table 2-1**):

1. Parameter set "A": effective O_2 addition (*i.e.* substitution of H by O). In this configuration the total amount of C is kept constant, while the total amount of O is increased. The assumption is that most O atoms will react with a C atom, producing CO and depleting the growth atmosphere of growth species, CH_x;
2. Parameter set "B": addition of CO_2 (*i.e.* substitution of H by CO_2). In this configuration the total amount of C increases by half the amount of O, and so only half of the added amount of O is assumed to convert growth species into inert CO;
3. Parameter set "C": effective CO addition (*i.e.* substitution of H by CO). In this configuration the total amount of C increases by the same amount as O. Thus, every added oxygen atom could be converted to CO without changing the concentration of active growth species, *i.e.*: $[\mathrm{C}]_{\mathrm{active}} = [\mathrm{C}]_{\mathrm{total}} - [\mathrm{O}]_{\mathrm{total}}$.

The term "effective" is adopted due to the fact that neither O_2 nor CO are available in our equipment as source gases that can be added directly to the feed gas mixture, but only CO_2. This required that the concentration of the different gas precursors (H_2, CH_4 and CO_2) were properly adjusted in order to achieve the correct atomic ratios for each case. **Table 2-1** shows the adjusted flow rates for CO_2 and CH_4 to achieve the growth regimes, for comparable O/C ratios.

Table 2-1: Summary of the different $([CO_2]/[CH_4])_{\mathrm{feedgas}}$ ratios used in this work to achieve the different growth regimes, "A", "B" and "C" (also plotted in **Figure 2-7**). Units are in percentage of total gas flow (400 sccm), *e.g.*, typical conditions without oxygen (*i.e.* 0% O/C) consist of 0% $[CO_2]_{\mathrm{feedgas}}$ and 4% $[CH_4]_{\mathrm{feedgas}}$ (16 sccm).

O/C ratio	**0%**	**25%**	**50%**	**75%**
„A": O addition	0/4	0.5/3.5	1/3	1.5/2.5
„B": CO_2 addition	0/4	0.57/4	1.33/4	2.4/4
„C": CO addition	0/4	0.66/4.6	1.93/5.8	5.88/9.8

These 3 parameter sets are displayed accordingly in the C-H-O diagram in **Figure 2-7** for clarity. Following the red line (parameter set "A") should lead to increasingly slower growth until, eventually, etching starts to take place. Following the green line (parameter set "B") should also lead to increasingly slower growth and eventually etching, but for a higher concentration of atomic oxygen compared to “A”. Following the blue line (parameter set “C”) should maintain a stable growth rate. For stable growth of epitaxial diamond by MWPCVD the C/H ratio is also important, and one should not expect the growth rate to be maintained when a large fraction of H is substituted by another element, since atomic hydrogen drives diamond growth. However, we chose moderate parameters where the fraction of H was never below ~94%.

In a first step, growth conditions were reproduced using both parameter sets “B” and “C”, with simultaneous *in situ* growth rate measurement by LRI. The results are shown in **Figure 2-6** (a). For increasing O/C ratio, the growth rate decreases upon CO_2 addition, while it stays constant for effective CO addition. **Figure 2-6** (b) shows the actual CH_4 concentrations used in the process to keep the growth rate constant when increasing the O/C ratio. The experimental values fit very well in the analytical curve representing the amount of CH_4 that needs to be added to the gas phase to counter-balance the increased CO_2 content, for the effective CO regime.

Our results confirm very nicely the initial assumptions regarding the C-H-O chemistry: addition of oxygen leads to the formation of inactive CO, which reduces the concentration of active growth species, CH_x, thus leading to slower growth. The initial (oxygen-free) growth rate can be restored by increasing the amount of atomic carbon in the process gas to compensate for the extra oxygen, thus bringing the concentration of CH_x back to its original level.

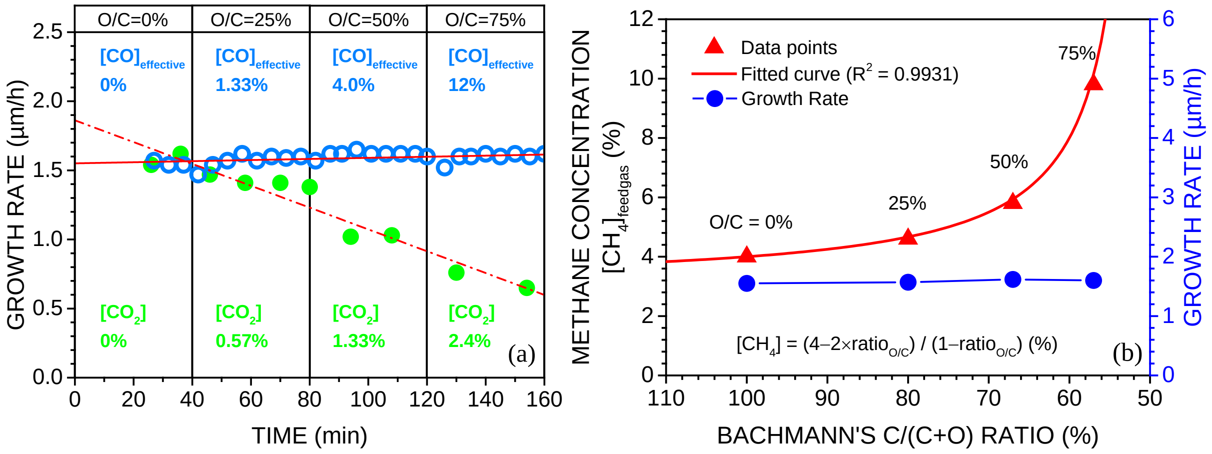

Figure 2-6: (a) Change in growth rate induced by both addition of CO_2 (green circles, parameter set “B” from **Table 2-1**) and effective addition of CO (blue open circles, parameter set “C”). (b) Calibration curve for the parameter set “C” to maintain a constant growth rate for a base $[CH_4]_{feedgas}$ of 4%. It defines the amount of CH_4 (and therefore of CO_2) that has to be added in the feed gas for a desired O/C ratio in the “effective CO addition” regime.

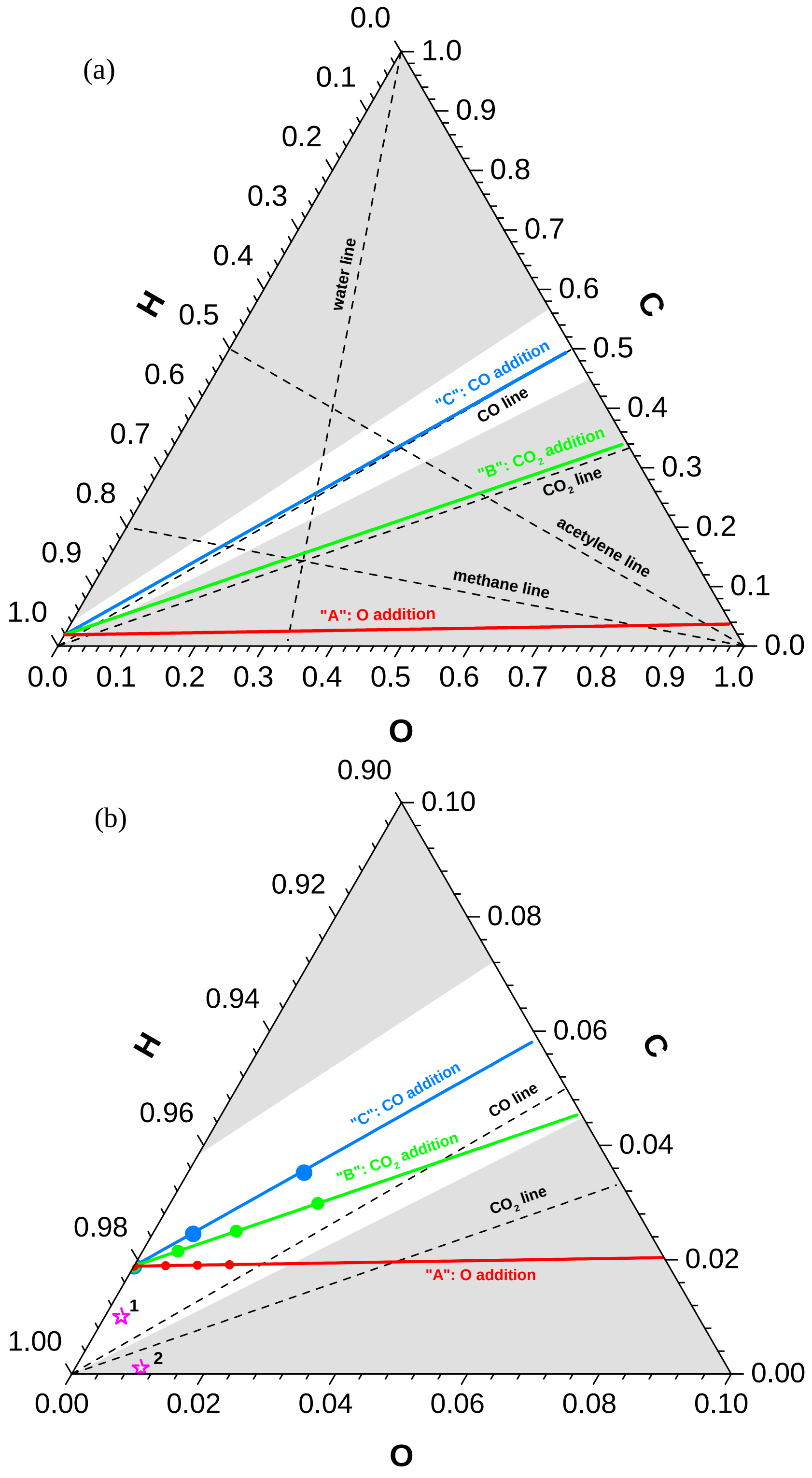

Figure 2-7: Bachmann's C-H-O diagram showing the growth regimes listed in **Table 2-1**. In (b) only a small portion of the full diagram displayed in (a) is shown, in order to highlight the specific parameters from sets "A", "B" and "C", together with two parameter sets from the literature: point 1 from Omnés *et al*. [20] (1% CH_4 and 0.25% O_2 in H_2); point 2 from Volpe *et al*. [21] (0.2% CH_4 and 1% O_2 in H_2).

2.3.5 Interaction of oxygen with boron in the gas phase under different growth regimes

In the previous section it was observed that the growth rate of diamond can be maintained constant upon addition of oxygen when the carbon concentration was increased simultaneously by the same amount, so that effectively CO was added. This approach apparently guaranteed that the concentration of active growth species stayed constant. However, previously, addition of oxygen to the gas phase was proposed as a strategy to better control B incorporation in diamond, since it was found to interact with B-containing species in the gas. This gives rise to an important question: is the reduction of B incorporation with O addition still possible when simultaneously trying to preserve the growth rate? Presumably, in the case of effective CO addition (parameter set "C") formation of CO would compete with formation of H_xBO $(x=1,2)$ compounds. We set out to investigate this problem.

In section 2.3.3 it was shown that the suppression of the optical emission of BH scales linearly with $[CO_2]_{feedgas}$, with experiments done in a low pressure regime in reactor #1 and with conservation of the total C concentration (equivalent to the regime of effective O addition). Here the same concept was applied again, *i.e.* monitoring the BH signal emission by OES with increasing O concentration in the gas phase, but for varying conditions. Experiments were performed in a high pressure regime to be comparable to the conditions used for the growth rate experiments in the previous section. The two extreme cases, effective O addition (parameter set "A") and effective CO addition (parameter set "C"), were compared for the same TMB concentration in the feed gas. The results of the measured spectra are shown in **Figure 2-8**.

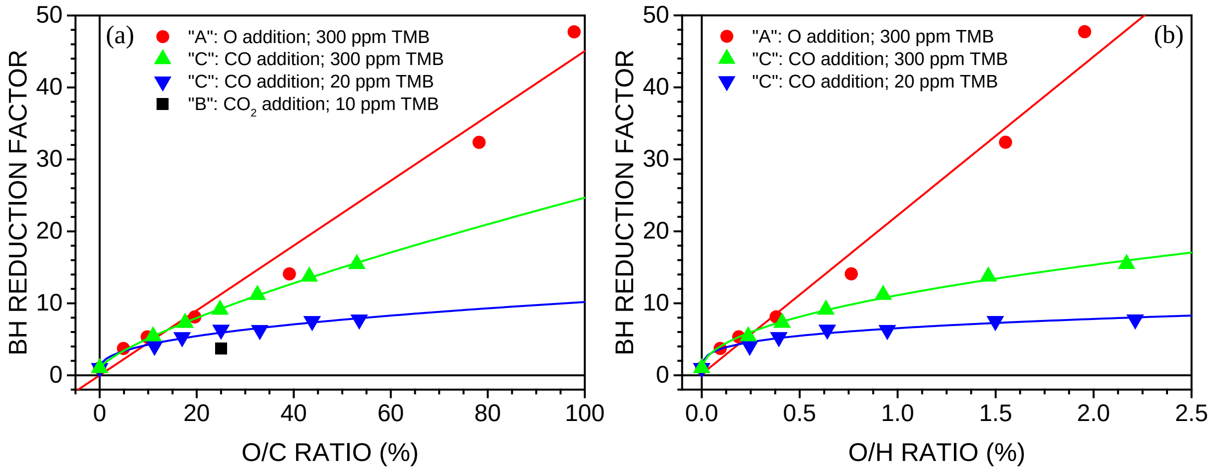

Figure 2-8: Reduction in BH emission *vs.* (a) O/C and (b) O/H ratios in the gas phase for parameter set "A" in red, for parameter set "C" in green and blue, and for parameter set "B" (1 data point for $O/C = 25\%$) in black. (see **Table 2-1** for more details).

In **Figure 2-8** the reduction factor of the BH signal is presented in two ways: in (a) as a function of O/C ratio and in (b) as a function of O/H ratio. The former case is comparable to **Figure 2-5** (b), highlighting the dependence of BH emission on the concentration of "free" oxygen[2], while the

---

[2] It should be understood by „free oxygen" any oxygen-containing species able to neutralise BH species in the gas, unlike CO which is inert.

latter case highlights the dependence of the BH emission on the total concentration of oxygen. The first observation from these results is that the linear relationship between the BH reduction factor and $\mathrm{O/C}$ ratio given by the red data points in **Figure 2-8** (effective addition of O), nicely matches the result previously obtained at lower pressure (see section 2.3.3). We interpret this in terms of a negligible pressure dependency. However, when the growth regime is switched to effective addition of CO (green data points in **Figure 2-8**) the BH reduction factor is significantly lower and the behaviour is non-linear. This indicates that the formation of CO is preferred over formation of $\mathrm{H}_x\mathrm{BO}$ $(x = 1, 2)$ compounds, and the concentration of BH species is not strongly affected.

The BH reduction factor was also observed to be dependent on the absolute B concentration in the gas, from comparison between the green and blue data sets in **Figure 2-8**. When the TMB concentration is reduced by more than an order of magnitude (from 300 to 20 ppm), not only is the BH attenuation weaker, but it also saturates earlier, becoming more insensitive to increasing amounts of oxygen. This suggests that with smaller B background levels, the attenuation of BH emission will flatten to a constant factor and not increase with increasing $\mathrm{O/C}$ ratio, rendering the strategy of oxygen addition to control B incorporation ineffective when the growth rate is to be preserved.

It is clear from **Figure 2-8**, therefore, that the BH emission intensity is only strongly reduced when only oxygen is added, which is what the parameter set “A” defines by keeping the total amount of atomic carbon constant in the gas mixture. This regime has, however, the drawback of decreasing the growth rate. Consequently, by extension, reducing B incorporation in diamond by adding O to the gas phase has a practical limit which is related to the C-H-O diagram (**Figure 2-7**): B incorporation can be lowered continuously until a point is reached where diamond stops growing. If the concentration of free atomic O is increased further, diamond growth will shift towards an etching regime. An example of this situation is the extreme parameters used by Volpe *et al.* shown in **Figure 2-7** (b) by a star with the label “2”. Despite such extreme parameters they still reported a positive growth rate of ~0.15 µm/h, which is somewhat surprising and apparently incongruent in comparison with our observations.

2.3.6 Interaction of nitrogen and boron in the gas phase

Another important element related to diamond growth is nitrogen. Nitrogen at trace levels of a few ppm can accelerate diamond growth by up to one order of magnitude [38-40] and still plays an important role in understanding the mechanisms of diamond growth and impurity incorporation. The absolute growth rate enhancement factor crucially depends on the deposition parameters, particularly the substrate temperature and the gas pressure. Since both boron and nitrogen can be simultaneously present in the growth environment due to contamination, gas leak or intentionally, any possible interaction between the two elements is of interest and remains unclear up to this day, despite earlier work with polycrystalline diamond [41].

In order to check for interaction between boron- and nitrogen-containing species in the gas phase, OE spectra of the plasma before and after addition of TMB to a nitrogen-containing gas mixture, and before and after addition of N_2 to a boron-containing mixture, have been recorded under typical growth conditions. In the first case OE spectra were recorded with lower resolution, to encompass the H_γ, BH and CN signals. When only the BH emission was of interest, higher resolution was used. The spectra are shown in **Figure 2-9**, respectively (a) and (b). Only the extreme cases of a whole series of different N_2 and TMB concentrations are shown. They indicate a negligible interaction of the two species in the gas phase up to concentrations which normally yield high doping (in the case of boron) or which already accelerate growth significantly (in the case of nitrogen).

A completely different behaviour is observed when the growth rate is studied. In deposition experiments on (001)-oriented heteroepitaxial diamond films at low pressure (50 mbar, 2% CH_4 in H_2, 1100 W microwave power and a substrate temperature of ~800 °C) in reactor #2 (nominally boron-free), addition of 100 ppm of N_2 accelerates growth by a factor of ~2. For the same experimental conditions in reactor #1 (boron background level equivalent to ~1-3 ppm TMB), the change in growth rate measured by LRI when 100 ppm N_2 were added was negligible (less than 10%). No enhancement was observed also with samples grown with 300 ppm N_2 at ~720 °C. This preliminary result already indicates that the action of nitrogen on the growth rate is strongly modified by the presence of boron.

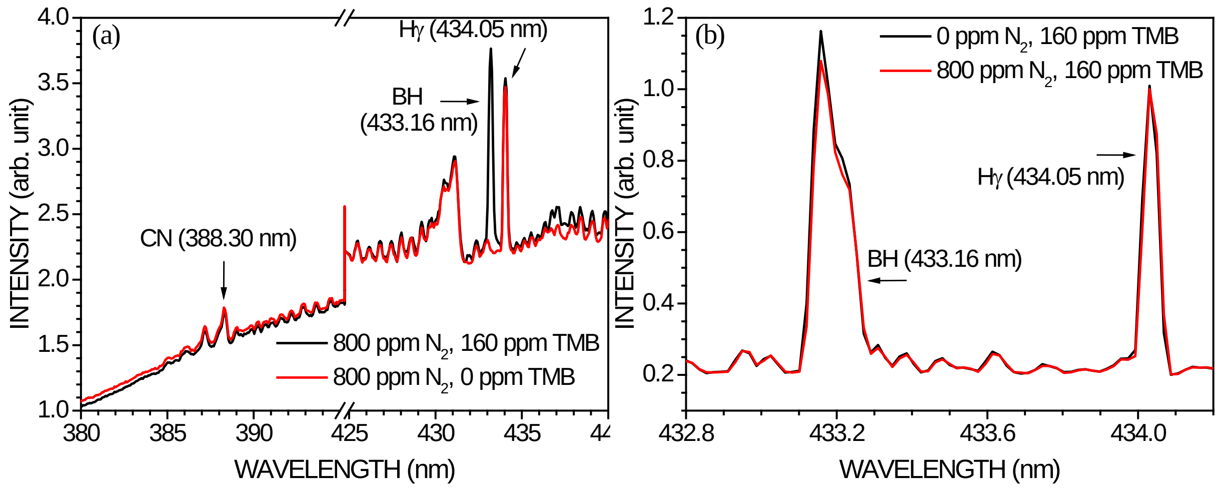

Figure 2-9: (a) OE spectra of the CN peak at 388 nm and the BH emission region before (red curve) and after (black curve) addition of 160 ppm TMB (spectral resolution: 0.23 nm). (b) Zoomed region of the BH peak including the H_γ line before (black curve) and after (red curve) addition of 800 ppm N_2 (spectral resolution: 0.04 nm). Experiments performed at low pressure (50 mbar).

This initial observation is partially in contrast to a report by Ramamurti *et al.* [42] who grew B-doped single crystals in a high pressure regime (160-220 mbar, 4-6% CH_4 in H_2). They found that 10 ppm B_2H_6 significantly decreased the growth rate, but a variation of N_2 between 2.5 and 550 ppm still caused acceleration by a factor of 2.6. Our OES results in **Figure 2-9** also rule out the formation of B-N compounds in the gas phase, as proposed by Hartmann *et al.* [41]. Since fundamental growth processes vary strongly with pressure and temperature [41, 43], further detailed experiments were required to clarify the mechanism.

2.3.7 Effect of B contamination on the growth rate enhancement by N_2

The preliminary growth rate observations described in the previous section, where N_2 added to the gas phase did not develop its catalytic effect on the growth rate of diamond in a boron-contaminated reactor, led us to investigate the problem further and more systematically. Here we want to examine how strong the effect of B contamination on the growth rate enhancement by N is, and see if this effect can be restored despite the B contamination.

In a first step, *in situ* growth rate measurements were performed using the two reactors, #1 (with a typical boron background of ~1-3 ppm) and #2 (nominally boron-free), by increasing $[N_2]_{\text{feedgas}}$ up to 2000 ppm and without any further addition of boron. The results are displayed in **Figure 2-10**.

The blue curve in **Figure 2-10** shows the variation of the growth rate upon nitrogen addition in the nominally boron-free reactor #2. Surprisingly, the growth rate is unchanged up to 150 ppm, and then it increases steeply above this threshold. This result contradicts former experiments. In contrast (see red curve), in the reactor #1 no acceleration occurs up to the highest nitrogen concentration of 2000 ppm.

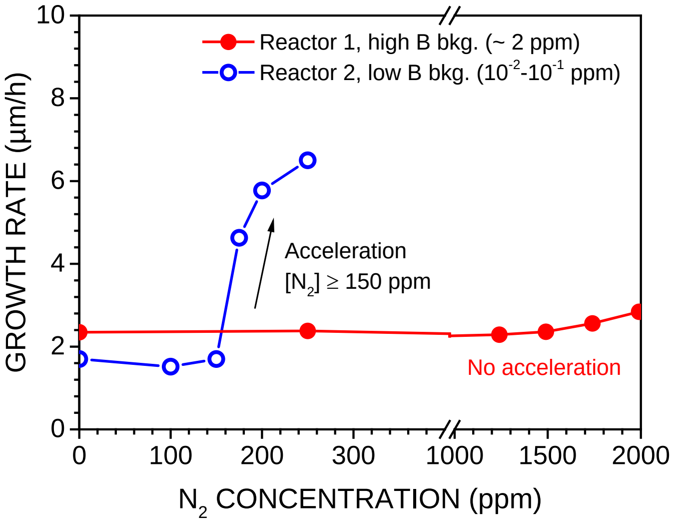

Figure 2-10: *In situ* growth rate measurements in reactors #1 and #2 without intentional boron addition.

The boron background in reactor #1 is high, because it is regularly used to grow boron-doped diamond. The concentration depends on the previous processes, and it was estimated to be around ~2 ppm at the time of these experiments, which is also the sensitivity limit for the detection of BH in the plasma by OES under our conditions. In reactor #2 the contamination level is well below the detection limit of OES. However, the results above suggest that boron might also be present in this reactor. In order to clarify this point, cathodoluminescence (CL) measurements of a diamond sample grown in reactor #2 were performed, yielding a boron dopant concentration in the low 10^{16} cm^{-3} range. From this value a B background concentration of 0.01-0.1 ppm was estimated. We interpret this result as a first hint that a minor B contamination below 0.1 ppm could be sufficient to cancel the growth acceleration for nitrogen additions in the range up to 150 ppm.

The most obvious proof of an interaction between nitrogen and boron would be a direct mutual influence in the gas phase. However, this has already been excluded from previous experiments (see section 2.3.6), in which no cross sensitivity in the emission signals was detected: CN emission didn’t change by TMB addition and the BH emission was insensitive to nitrogen addition.

As a consequence, systematic exploration of potential interactions would require growth rate measurements with controlled variation of nitrogen and boron. However, these are hampered by the fact that in the reactor dedicated to doping studies the background contamination already cancels the nitrogen effect completely, so that any further controlled TMB addition would only worsen the situation. In reactor #2, TMB addition was neither foreseen nor would it have allowed a controlled setting of B concentrations in the sub-ppm level, due to strong memory effects (as discussed in section 2.3.2). We have therefore chosen the strategy to control the B concentration in the gas phase by addition of oxygen. This concept is based on the previously shown observation that oxygen strongly neutralises boron in the gas phase under certain conditions, as deduced from the BH optical emission signal and from the lower boron concentration of the simultaneously grown diamond layers (see sections 2.3.3-2.3.5). However, in order for this concept to work, it is necessary that oxygen and nitrogen do not mutually interact in the gas phase, as this would complicate the experiment and reduce the significance of the results. Thus, this point had to be clarified first.

2.3.8 Interaction of N and O in the gas phase

It is known from sections 2.3.3-2.3.5 that O neutralises B in the gas phase during growth of diamond by MWPCVD, however a potential interaction between oxygen and nitrogen in the gas phase still needs to be investigated. For this purpose, new OES measurements under typical growth conditions were carried out.

An experiment was performed in the following way: for a constant concentration of $[N_2]_{feedgas} = 1750$ ppm, different quantities of CO_2 were admixed into the feed gas (parameter set “B” in **Table 2-1**) under the same high pressure regime (100 mbar) as before, while the emission intensity of CN species at 388.3 nm was monitored by OES. Using CO_2 addition instead of effective O_2 addition or effective CO addition is important here, because it establishes a compromise between having enough free oxygen and having enough “free carbon” (*i.e.* carbon in the form of growth species), which are necessary for the formation of CN.

Figure 2-11 shows the temporal development of the CN emission at 388.3 nm while $[CO_2]_{feedgas}$ was varied. Even for higher fractions of oxygen in the gas phase the CN stays completely unchanged. Likewise, the decreasing fraction of active growth species, which comes by using parameter set “B”, did not seem to affect the CN intensity. Therefore, we took these results as a strong hint that oxygen does not have a direct impact on the nitrogen in the gas phase. This enables oxygen being used to reduce the boron concentration in the gas phase in a controlled way without additional side-effects, which is a crucial prerequisite for a systematic of the influence of boron on the nitrogen-induced growth acceleration. The observed growth rates during the process (also displayed in **Figure**

2-11), which were monitored by LRI in parallel with OES, were already a preliminary confirmation that this is indeed the case. But more detailed investigations were carried out, as shown next.

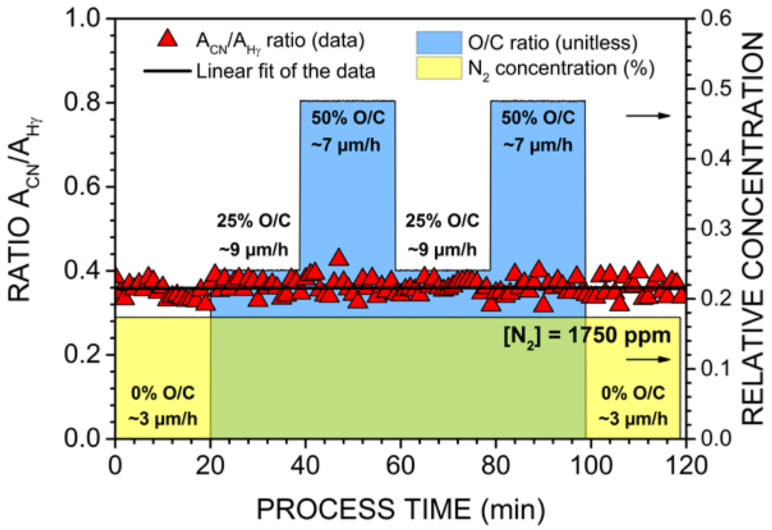

Figure 2-11: Optical emission intensity of CN for a constant $[N_2]_{\text{feedgas}}$ concentration of 1750 ppm and different O/C ratios according to parameter set "B" from **Table 2-1**. The intensity of the CN emission at 388.3 nm remained constant throughout the experiment, despite increasing the total amount of oxygen up to 2.66%. The growth rate measured *in situ* is also given for each parameter window.

2.3.9 Controlling the nitrogen-induced growth acceleration via oxygen addition

Here we carry on with a more systematic evaluation of the strategy to (re)activate the nitrogen-induced growth rate enhancement of diamond in a B-rich atmosphere, by adding oxygen to the gas phase during growth.

Modification of the nitrogen-induced growth acceleration by controlled addition of oxygen was first investigated in reactor #2 with low boron background. Two growth processes were carried out with increasing N content in the gas phase: in the first process no oxygen was added, while in the second process 50% O/C was added according to parameter set "C" from **Table 2-1** (*i.e.* effective CO addition), in order to keep the same base growth rate in both cases. The results are shown in **Figure 2-12**.

The step-like behaviour in the growth rate *vs.* nitrogen concentration in an oxygen-free environment, as already displayed in **Figure 2-10**, was modified quite significantly upon addition of oxygen to the gas phase: the step has completely disappeared, and for all applied nitrogen concentrations an increase in growth rate was observed. At 200 ppm the growth rates were nearly identical. Since effective addition of CO (parameter set "C" from **Table 2-1**) was chosen to keep the concentration of growth species constant, this behaviour indicates that after overcoming the threshold all nitrogen atoms present in the gas phase develop the same effect.

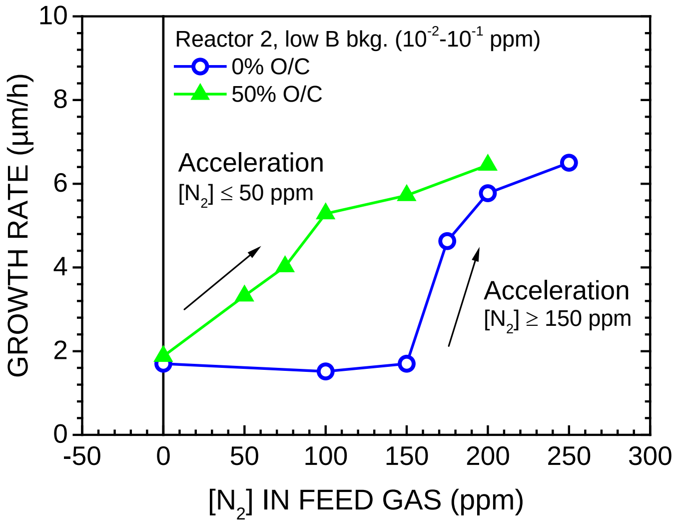

Figure 2-12: Growth rate enhancement by N_2 with and without oxygen addition in reactor #2 in the high pressure regime (100 mbar), following parameter set “C” from **Table 2-1**.

Further similar experiments were carried out in reactor #1, *i.e.*, in the regime of high boron concentrations. In order to have a better control over the real boron content in the gas phase, several runs with defined TMB flow rates of 1, 3, and 6 ppm were performed. Oxygen was added by CO_2 addition (parameter set “B” from **Table 2-1**), because preliminary experiments with effective CO addition (parameter set “C”) showed that not enough free oxygen existed in the gas phase to reduce the B background to a level where growth acceleration by nitrogen could be observed. Under such conditions, our maximum available N_2 flow was not sufficient.

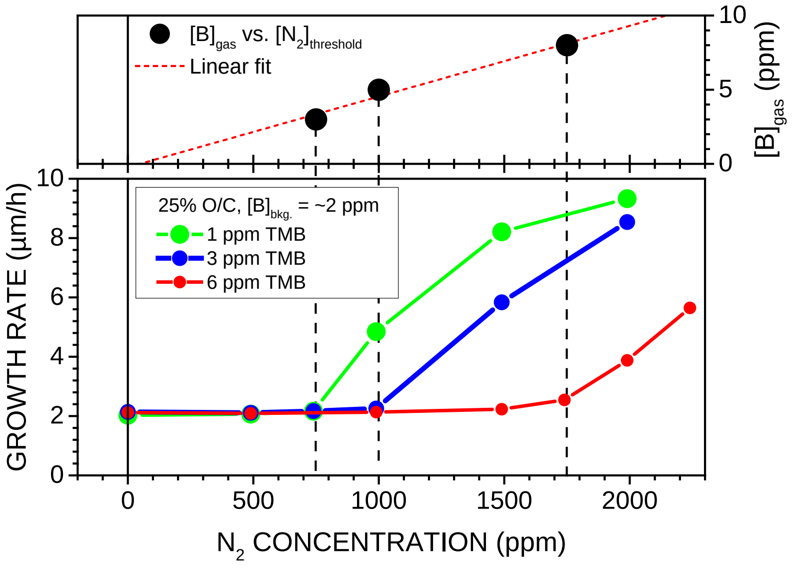

Figure 2-13: Growth experiments in reactor #1 (B background of ~2 ppm). For 3 different $[B]_{feedgas}$ the growth rate was measured *vs.* $[N_2]_{feedgas}$ for $O/C = 25\%$ and $[CH_4] = 4\%$ (parameter set “B” from **Table 2-1**). The upper part of the figure shows the relationship between the total $[B]_{gas} = [B]_{feedgas} + [B]_{bkg.}$ and the threshold values of $[N_2]_{feedgas}$.

Figure 2-13 summarises the results of the 3 runs in which the growth rate was measured *vs.* the nitrogen addition at a fixed O/C ratio of 25%. All the curves display a complete insensitivity at nitrogen levels of few hundred ppm, followed then by an increase at defined threshold values. The slopes of the curves above the threshold are similar, in contrast to the behaviour in reactor #2.

In the upper part of **Figure 2-13**, the boron concentration (taking into account the ~2 ppm contribution from the background contamination) is plotted *vs.* the nitrogen concentration at the threshold. The resulting linear relationship demonstrates how the growth rate enhancement by nitrogen can be switched on in a boron-containing gas phase by addition of oxygen in a controlled way.

The experiments in both reactors allow a clear discrimination of two states: standard and accelerated growth. The transition between each growth regime is marked by a threshold value. Its systematic variation suggests the existence of a critical ratio between boron and nitrogen atoms in the gas phase. We estimated this number from the experiments in the two concentration regimes, independently, in the following way:

Several samples grown in reactor #2 contained boron in concentrations of around $3\times10^{16}\ \text{cm}^{-3}$. For the estimation of the gas phase concentration during film deposition, the incorporation efficiency, *i.e.*, $[B/C]_{solid}/[B/C]_{gas}$, has to be known. Growth of several samples in this low B concentration range and subsequent analysis by CL yielded a large scatter ranging from 2% to 30%. For the present estimation a realistic incorporation efficiency of 10% is assumed, and thus we obtain a gas phase concentration of 0.07 ppm. From the step in the growth rate at 150 ppm N_2 (see **Figure 2-12**) we could then deduce a critical $[N_2]/[B]$ ratio at the threshold for nitrogen-induced growth acceleration of $\sim 2\times10^3$.

In reactor #1, defined quantities of TMB and N_2 were fed into the chamber. However, the threshold was only accessible when sufficient oxygen was present. As a consequence, the reduction factor from **Figure 2-8** (determined for 10 ppm TMB) had to be included in the evaluation. The linear relationship between boron concentration and nitrogen concentration at the threshold (see **Figure 2-13**) provided nearly identical values for all three runs. With a reduction factor of 3.7, estimated from **Figure 2-8**, a ratio of $[N_2]/[B]\cong 850$ was derived.

Taking into account the large uncertainty of the factors included in the calculation, we concluded that the presence of roughly one boron atom is sufficient to cancel the effect of more than 1000 nitrogen atoms in the gas phase.

Our previous experiments revealed essentially no interaction between nitrogen and boron in the gas phase, suggesting that surface processes are responsible for the observed dependence of nitrogen-induced growth rate acceleration on the $[N_2]/[B]$ ratio. The basic mechanisms of growth rate enhancement by nitrogen without any additional interacting impurities, like in the present experiments, are still not fully understood. In a proposed mechanism (described in section 1.4.2) for the catalytic effect of N on the growth rate, extra surface electrons supplied by the incorporated nitrogen facilitate the direct bonding of CH_2 radicals in sp^3 configuration [44]. However, in a more recent publication it was suggested that nitrogen adsorbs at the surface where it catalyses the incorporation of many hydrocarbon species in the neighbourhood [28]. During adsorption it competes with other hydrocarbon radicals for adsorption sites. Based on the latter model, our findings suggest that N and B either compete for adsorption sites or coadsorb, neutralising the catalytic action of nitrogen in this way, whereas, based on the former model, the growth mechanism is controlled by a charge compensation effect between electron and holes from, respectively, incorporated N and B.

Boron is present in our experiments in much lower concentrations in the gas phase. However, its incorporation efficiency of ~0.1-1 is significantly higher than for nitrogen: ~10^{-4} to 10^{-3} [45-47]. Jin and Moustakas explain this behaviour simply in terms of differences in the bonding energy $E_{\text{C-C}}$, $E_{\text{C-N}}$ and $E_{\text{C-B}}$, which vary as 83, 73, and 89 kcal mol^{-1} [45]. They assume that the condensation rate $\Re$, *e.g.* for nitrogen, scales with $E_{\text{C-N}}$ like:

$$\Re \sim \exp\left(\frac{E_{\text{C-N}}}{RT}\right). \tag{2.3.3}$$

At 1000 K the ratio of $\Re$ for N and B is $\sim 3\times10^{-4}$. Differences in the activation and dissociation in the gas phase, especially for the stable N_2 triple bond, should contribute further modifications. In spite of all uncertainties, this simple estimation suggests that the ratio between the area densities of B and N species adsorbed at the surface could be close to unity at the threshold of growth acceleration, which yields an important clue to the underlying growth mechanisms.

2.3.10 Incorporated N and B before and after growth acceleration

In order to confirm if indeed the incorporated N/B ratio in the films is close to unity, several samples were grown with varying $[\text{N}_2]/[\text{B}]$ ratio in the gas phase, chosen so that the final measured growth rates were either slightly below or slightly above the growth rate enhancement threshold. The samples were then characterised by Elastic Recoil Detection Analysis (ERDA) [48] for the quantification of incorporated N and B in the films. The results are shown in **Figure 2-14**.

The figure below shows the averaged growth rate measured *in situ* by LRI during the last minutes of growth of 5 samples, together with their respective N/B ratio measured by ERDA. The points corresponding to 2000 ppm $[\text{N}_2]_{\text{feedgas}}$ are the average of two samples which were just above the growth acceleration threshold. The other samples were just below. As the nitrogen concentration in the feed gas increased, so did the growth rate and the incorporated N/B ratio. For the lowest $[\text{N}_2]_{\text{feedgas}}$ of 500 ppm the N/B ratio was in its lowest value of 0.97±0.28, while for 2000 ppm $[\text{N}_2]_{\text{feedgas}}$ the N/B ratio was 1.58±0.21. It can be seen that, as predicted by our gas phase studies, the incorporated N/B ratio is indeed close to unity, with an averaged value of 1.88±0.35. Experimental errors and scatter considered, we can say with certainty that the threshold ratio of incorporated N to B, at which diamond growth switches from standard to catalysed by N, lies between 1 and 2. This result is a remarkable finding and very important for the understanding of doping and (impurity-assisted) diamond growth from an atomistic point of view. It will motivate further research into the chemistry taking place on the diamond surface during deposition, in order to understand, for example, if N and B simply compete for adsorption sites or if the growth acceleration is assisted by surface electrons, as discussed earlier.

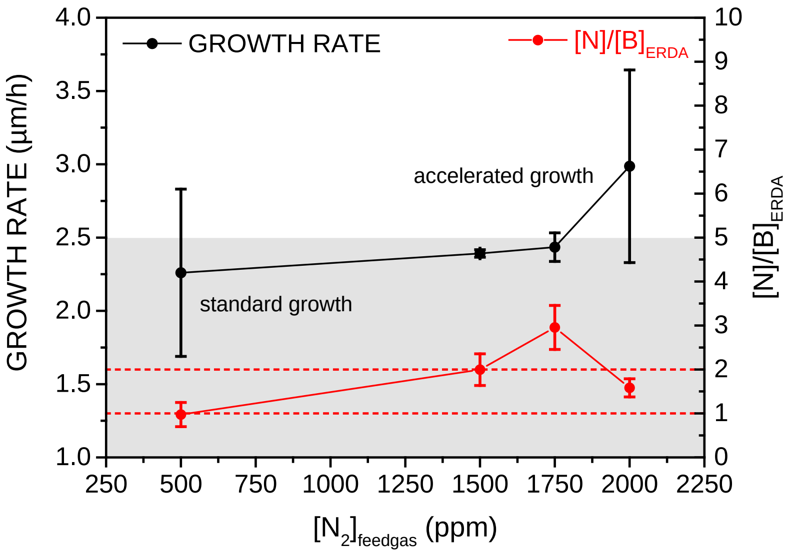

Figure 2-14: Growth rate (black points) and corresponding incorporated N/B ratio (red points) in diamond as a function of the N_2 concentration in the feed gas. The grey and white areas separate the standard growth regime from accelerated growth regime, respectively. The samples were grown with a high B background of roughly 1-3 ppm, which was fixed by adding 1 ppm TMB to the already existing B background contamination, and adding 4% CH_4 and CO_2 to a ratio of 26.1% O/C.

We would like to thank Dr Andreas Bergmaier from the *Institut für Angewandte Physik und Messtechnik (LRT2)* in Munich for his efforts in performing ERDA of our samples just in time for the conclusion of this thesis.

2.4 Conclusion and final remarks

The present work showed that OES, though not being a quantitative method for the measurement of particle densities, can yield important information about the crucial processes during *in situ* boron doping. The BH emission peak was found to scale linearly with the TMB concentration in the gas phase.

By monitoring the BH emission, the response time for the boron concentration in the gas phase after switching the TMB addition could be deduced. After a complete switch off, a fast decay by one order of magnitude with a time constant of less than half the gas exchange time of the reactor was followed by a very slow decay about 20 times higher than the gas exchange time. This behaviour gives rise to pronounced memory effects that hamper any attempt to achieve precise doping levels or to produce steep doping profiles in the same MWPCVD reactor.

Several reports in literature have described a reduction of the incorporation coefficient for boron due to the presence of oxygen in the gas phase. Here we have shown that this reduction can be explained comprehensively and quantitatively by gas phase processes, ruling out surface-related processes. The results support the concept of using oxygen for the realisation of steeper doping profiles under appropriate conditions. We also showed that BH reduction by O addition is insensitive to variations in the process pressure from 50 to 100 mbar, but very sensitive to the gas composition, namely to the O/C ratio. We evidenced that addition of oxygen has a weaker effect on the BH intensity when the concentration of active growth species is preserved through effective CO addition. In contrast, addition of oxygen has a much stronger effect on the BH intensity when growth species are consumed through effective O_2 addition. These variations due to process parameters can explain the different reduction factors reported in the literature.

Use of oxygen is, however, not without side-effects. For the purpose of using oxygen to have better control of B incorporation in reactors suffering from strong memory effects, it is necessary to have a high O/C ratio, of which a high amount of atomic oxygen is not in the form of inactive CO molecules, but free to abstract boron from its active compounds. This was demonstrated to be achievable when effective O_2 addition to the gas phase is chosen, *e.g.* by adding CH_4 and CO_2 for a given O/C ratio so that the total $[C]_{gas}$ remains constant (parameter set “A”) or, to a lesser degree, when effective CO_2 is added (parameter set “B”). However, this was shown, with the help of LRI, to cause a strong reduction of the growth rate. Preserving the growth rate, however, required an effective addition of CO, *e.g.* by adding CO_2 for a given O/C ratio and increasing $[CH_4]_{feedgas}$ to compensate for the excess oxygen. This procedure led to a significantly smaller BH attenuation and to a much weaker dependence on the O/C ratio. The attenuation factor is virtually constant for smaller $[B]$ values, despite increasing O/C. As a consequence, the use of oxygen as a strategy to reduce B incorporation does work, but under limited conditions. The lowest concentrations of incorporated B can only be achieved at very low growth rates. Attempting further reduction will lead to etching of the diamond.

Next in this work it was shown here for the first time that growth rate enhancement by N_2 addition to the process gas is severely hampered by the presence of boron. The effect is completely suppressed by boron in ppm levels. At lower boron concentrations a step-like behaviour was observed, *i.e.*, the nitrogen is initially inactive before it sharply develops its effect above a threshold concentration. We showed that the lack of interaction between nitrogen and oxygen in the gas phase could allow the use of the latter to reduce the B/N ratio in the plasma and allow nitrogen to deploy its catalytic effect on the growth rate.

In the reactor with low boron background (much less than 1 ppm) an O/C ratio of 50% ensured that the growth rate reacted immediately upon nitrogen addition. In the reactor with a typical background of 1-3 ppm, addition of oxygen caused the appearance of a threshold for nitrogen concentrations above which growth acceleration started abruptly, whereas before addition of oxygen no growth rate enhancement could be observed up to 2000 ppm $[N_2]_{feedgas}$. The value of the observed threshold upon oxygen addition (in the order of 1000 ppm N_2) scales linearly with the boron concentration in the gas phase, indicating a clear dependence of the growth rate on the N/B in the gas. We roughly estimated based on the individual incorporation efficiencies of B and N that the growth acceleration threshold coincides with an incorporation ratio $\mathrm{N/B} \cong 1$.

From ERD analysis of samples grown with controlled addition of N_2 and B in the gas phase, in such a way that the growth rates measured *in situ* by LRI were either just below or just above the acceleration threshold defined by the $\left([\mathrm{N_2}]/[\mathrm{B}]\right)_{\mathrm{gas}}$ ratio previously found, we confirmed that the incorporated $\mathrm{N/B}$ ratio is indeed close to unity. This result immediately suggests the simple idea that B and N could coadsorb at the surface and then incorporate into the diamond lattice as BN pairs. Due to the structural identity of diamond and cubic BN, with a lattice misfit of only 1.4%, this mechanism seems very plausible [49] and future experiments by FTIR or HRTEM should be carried out to investigate the presence of BN pairs in CVD-grown diamond.

In addition, our findings may represent a further piece for the still incomplete puzzle of growth rate enhancement by nitrogen. Even 20 years after its discovery, and despite its high technological relevance, a generally accepted mechanism which explains all phenomena is still to be presented.

Finally, we would like to point out that the present results can now yield a conclusive explanation for former observations of retarded growth acceleration by nitrogen. In addition, they provide an extremely sensitive procedure (ppb range) to check for low levels of boron contamination in CVD reactors, by performing *in situ* growth rate measurements with nitrogen addition and using the above mentioned $\mathrm{N/B}$ relationship to estimate the B background level.

References

1. Takeshi Kondo, Yasuaki Einaga, Bulusu V. Sarada, Tata N. Rao, Donald A. Tryk, and Akira Fujishima; Homoepitaxial Single-Crystal Boron-Doped Diamond Electrodes for Electroanalysis. *Journal of The Electrochemical Society*, 2002. **149**(6): p. E179-E184. DOI: 10.1149/1.1471548.
2. T. van der Sar, Z. H. Wang, M. S. Blok, H. Bernien, T. H. Taminiau, D. M. Toyli, D. A. Lidar, D. D. Awschalom, R. Hanson, and V. V. Dobrovitski; Decoherence-protected quantum gates for a hybrid solid-state spin register. *Nature*, 2012. **484**(7392): p. 82-86. DOI: 10.1038/nature10900.
3. D. J. Twitchen, A. J. Whitehead, S. E. Coe, J. Isberg, J. Hammersberg, T. Wikstrom, and E. Johansson; High-voltage single-crystal diamond diodes. *Electron Devices, IEEE Transactions on*, 2004. **51**(5): p. 826-828. DOI: 10.1109/TED.2004.826867.
4. Toshiharu Makino, Norio Tokuda, Hiromitsu Kato, Shokichi Kanno, Satoshi Yamasaki, and Hideyo Okushi; Electrical and light-emitting properties of homoepitaxial diamond p–i–n junction. *physica status solidi (a)*, 2008. **205**(9): p. 2200-2206. DOI: 10.1002/pssa.200879717.
5. Ken Haenen, Andrada Lazea, Miloš Nesládek, and Satoshi Koizumi; Rectifying properties and photoresponse of CVD diamond p(i)n-junctions. *physica status solidi (RRL)*, 2009. **3**(6): p. 208-210. DOI: 10.1002/pssr.200903155.
6. P. Muret, P. N. Volpe, T. N. Tran-Thi, J. Pernot, C. Hoarau, F. Omnès, and T. Teraji; Schottky diode architectures on p-type diamond for fast switching, high forward current density and high breakdown field rectifiers. *Diamond and Related Materials*, 2011. **20**(3): p. 285-289. DOI: 10.1016/j.diamond.2011.01.008.
7. N. R. Wilson, S. L. Clewes, M. E. Newton, P. R. Unwin, and J. V. Macpherson; Impact of grain-dependent boron uptake on the electrochemical and electrical properties of polycrystalline boron doped diamond electrodes. *Journal of Physical Chemistry B*, 2006. **110**(11): p. 5639-5646. DOI: 10.1021/jp0547616.

8. Jan Isberg, Johan Hammersberg, Erik Johansson, Tobias Wikström, Daniel J. Twitchen, Andrew J. Whitehead, Steven E. Coe, and Geoffrey A. Scarsbrook; High Carrier Mobility in Single-Crystal Plasma-Deposited Diamond. *Science*, 2002. **297**(5587): p. 1670-1672. DOI: 10.1126/science.1074374.
9. M. Schreck, F. Hörmann, H. Roll, J. K. N. Lindner, and B. Stritzker; Diamond nucleation on iridium buffer layers and subsequent textured growth: A route for the realization of single-crystal diamond films. *Applied Physics Letters*, 2001. **78**(2): p. 192-194. DOI: 10.1063/1.1337648.
10. M. Fischer, R. Brescia, S. Gsell, M. Schreck, T. Brugger, T. Greber, J. Osterwalder, and B. Stritzker; Growth of twin-free heteroepitaxial diamond on Ir/YSZ/Si(111). *Journal of Applied Physics*, 2008. **104**(12): p. 123531-5. DOI: 10.1063/1.3019046.
11. Kazuki Ohtsuka, Hideo Fukuda, Kazuhiro Suzuki, and Atsuhito Sawabe; Fabrication of Epitaxial Diamond Thin Film on Iridium. *Japanese Journal of Applied Physics*, 1997. **36**(Copyright (C) 1997 Publication Board, Japanese Journal of Applied Physics): p. L1214. DOI: 10.1143/JJAP.36.L1214.
12. Kazuhiro Suzuki, Hideo Fukuda, Takatoshi Yamada, and Atsuhito Sawabe; Epitaxially grown free-standing diamond platelet. *Diamond and Related Materials*, 2001. **10**(12): p. 2153-2156. DOI: 10.1016/s0925-9635(01)00497-6.
13. S. Washiyama, S. Mita, K. Suzuki, and A. Sawabe; Coalescence of Epitaxial Lateral Overgrowth-Diamond on Stripe-Patterned Nucleation on Ir/MgO(001). *Applied Physics Express*, 2011. **4**(9): p. 095502. DOI: 10.1143/apex.4.095502.
14. A. K. Freund, S. Gsell, M. Fischer, M. Schreck, K. H. Andersen, P. Courtois, G. Borchert, and M. Skoulatos; Diamond mosaic crystals for neutron instrumentation: First experimental results. *Nuclear Instruments and Methods in Physics Research Section A: Accelerators, Spectrometers, Detectors and Associated Equipment*, 2011. **634**(1, Supplement): p. S28-S36. DOI: 10.1016/j.nima.2010.05.043.
15. M. Fischer, S. Gsell, M. Schreck, and A. Bergmaier; Growth sector dependence and mechanism of stress formation in epitaxial diamond growth. *Applied Physics Letters*, 2012. **100**(4): p. 041906-3. DOI: 10.1063/1.3679611.
16. C. Stehl, M. Fischer, S. Gsell, E. Berdermann, M. S. Rahman, M. Traeger, O. Klein, and M. Schreck; Efficiency of dislocation density reduction during heteroepitaxial growth of diamond for detector applications. *Applied Physics Letters*, 2013. **103**(15): p. 151905. DOI: 10.1063/1.4824330.
17. Michael Mayr, Martin Fischer, Oliver Klein, Stefan Gsell, and Matthias Schreck; Interaction between surface structures and threading dislocations during epitaxial diamond growth. *physica status solidi (a)*, 2015. **212**(11): p. 2480-2486. DOI: 10.1002/pssa.201532243.
18. Robert Edgington, Syunsuke Sato, Yuichiro Ishiyama, Richard Morris, Richard B. Jackman, and Hiroshi Kawarada; Growth and electrical characterisation of delta-doped boron layers on (111) diamond surfaces. *Journal of Applied Physics*, 2012. **111**(3): p. 033710-7. DOI: 10.1063/1.3682760.
19. P. N. Volpe, N. Tranchant, J. C. Arnault, S. Saada, F. Jomard, and P. Bergonzo; Ultra-sharp boron interfaces for delta doped diamond structures. *physica status solidi (RRL)*, 2012. **6**(2): p. 59-61. DOI: 10.1002/pssr.201105480.
20. Franck Omnès, Pierre Muret, Pierre-Nicolas Volpe, Mamadou Wade, Julien Pernot, and François Jomard; Study of boron doping in MPCVD grown homoepitaxial diamond layers based on cathodoluminescence spectroscopy, secondary ion mass spectroscopy and capacitance-voltage measurements. *Diamond and Related Materials*, 2011. **20**(7): p. 912-916. DOI: 10.1016/j.diamond.2011.05.010.
21. Pierre-Nicolas Volpe, Jean-Charles Arnault, Nicolas Tranchant, Gauthier Chicot, Julien Pernot, François Jomard, and Philippe Bergonzo; Boron incorporation issues in diamond when TMB is used as precursor: Toward extreme doping levels. *Diamond and Related Materials*, 2012. **22**(0): p. 136-141. DOI: 10.1016/j.diamond.2011.12.019.
22. Gary S. May and Costas J. Spanos; *Process Monitoring*, in *Fundamentals of Semiconductor Manufacturing and Process Control*, 2006, John Wiley & Sons, Inc.
23. A. Gicquel, N. Derkaoui, C. Rond, F. Benedic, G. Cicala, D. Moneger, and K. Hassouni; Quantitative analysis of diamond deposition reactor efficiency. *Chemical Physics*, 2012. **398**(0): p. 239-247. DOI: 10.1016/j.chemphys.2011.08.022.

24. J. W. C. Johns, F. A. Grimm, and R. F. Porter; On the spectrum of BH in the near ultraviolet. *Journal of Molecular Spectroscopy*, 1967. **22**(1–4): p. 435-451. DOI: 10.1016/0022-2852(67)90190-7.
25. Dane W. Comerford, Andrew Cheesman, Thomas P. F. Carpenter, David M. E. Davies, Neil A. Fox, Rebecca S. Sage, James A. Smith, Michael N. R. Ashfold, and Yuri A. Mankelevich; Experimental and Modeling Studies of B Atom Number Density Distributions in Hot Filament Activated B_2H_6/H_2 and $B_2H_6/CH_4/H_2$ Gas Mixtures. *The Journal of Physical Chemistry A*, 2006. **110**(9): p. 2868-2875. DOI: 10.1021/jp053455p.
26. Qi Liang, Joseph G. Harrison, and Yogesh K. Vohra; Modeling of nitrogen/diborane/methane/hydrogen plasma for nanocrystalline diamond growth: Comparison with experimental data. *Diamond and Related Materials*, 2008. **17**(12): p. 2067-2070. DOI: 10.1016/j.diamond.2008.07.001.
27. R.W.B. Pearse and A.G. Gaydon; *The identification of molecular spectra*, 1st ed., 1976, Chapman & Hall.
28. S. Dunst, H. Sternschulte, and M. Schreck; Growth rate enhancement by nitrogen in diamond chemical vapor deposition---a catalytic effect. *Applied Physics Letters*, 2009. **94**(22): p. 224101. DOI: 10.1063/1.3143631.
29. Kazuhiko Ishikawa, Hitomi Yamano, Ki-ichiro Kagawa, Katsuhiko Asada, Koichi Iwata, and Masahiro Ueda; Measurement of thickness of a thin film by means of laser interference at many incident angles. *Optics and Lasers in Engineering*, 2004. **41**(1): p. 19-29. DOI: 10.1016/S0143-8166(02)00146-X.
30. Francis A. Jenkins and Harvey E. White; *Fundamentals of Optics*, 4th ed., 2001, McGraw-Hill Education.
31. S. Gsell, M. Fischer, Th. Bauer, M. Schreck, and B. Stritzker; Yttria-stabilized zirconia films of different composition as buffer layers for the deposition of epitaxial diamond/Ir layers on Si(001). *Diamond and Related Materials*, 2006. **15**(4–8): p. 479-485. DOI: 10.1016/j.diamond.2005.10.041.
32. M. Fischer, S. Gsell, M. Schreck, R. Brescia, and B. Stritzker; Preparation of 4-inch Ir/YSZ/Si(001) substrates for the large-area deposition of single-crystal diamond. *Diamond and Related Materials*, 2008. **17**(7–10): p. 1035-1038. DOI: 10.1016/j.diamond.2008.02.028.
33. J. Barjon, T. Tillocher, N. Habka, O. Brinza, J. Achard, R. Issaoui, F. Silva, C. Mer, and P. Bergonzo; Boron acceptor concentration in diamond from excitonic recombination intensities. *Physical Review B*, 2011. **83**(7): p. 073201. DOI: 10.1103/PhysRevB.83.073201.
34. C. Baron, M. Wade, A. Deneuville, F. Jomard, and J. Chevallier; Cathodoluminescence of highly and heavily boron doped (100) homoepitaxial diamond films. *Diamond and Related Materials*, 2006. **15**(4-8): p. 597-601. DOI: 10.1016/j.diamond.2006.01.015.
35. Peter K. Bachmann, Dieter Leers, and Hans Lydtin; Towards a general concept of diamond chemical vapour deposition. *Diamond and Related Materials*, 1991. **1**(1): p. 1-12. DOI: 10.1016/0925-9635(91)90005-u.
36. Yuri A. Mankelevich, Michael N. R. Ashfold, Dane W. Comerford, Jie Ma, and James C. Richley; Boron doping: B/H/C/O gas-phase chemistry; H atom density dependences on pressure and wire temperature; puzzles regarding the gas-surface mechanism. *Thin Solid Films*, 2011. **519**(14): p. 4421-4425. DOI: 10.1016/j.tsf.2011.01.328.
37. R. Beckmann, B. Sobisch, and W. Kulisch; On the gas-phase mechanisms in MWCVD and HFCVD diamond deposition. *Diamond and Related Materials*, 1995. **4**(4): p. 256-260. DOI: 10.1016/0925-9635(94)05243-3.
38. J. Achard, F. Silva, O. Brinza, A. Tallaire, and A. Gicquel; Coupled effect of nitrogen addition and surface temperature on the morphology and the kinetics of thick CVD diamond single crystals. *Diamond and Related Materials*, 2007. **16**(4–7): p. 685-689. DOI: 10.1016/j.diamond.2006.09.012.
39. A. Tallaire, A. T. Collins, D. Charles, J. Achard, R. Sussmann, A. Gicquel, M. E. Newton, A. M. Edmonds, and R. J. Cruddace; Characterisation of high-quality thick single-crystal diamond grown by CVD with a low nitrogen addition. *Diamond and Related Materials*, 2006. **15**(10): p. 1700-1707. DOI: 10.1016/j.diamond.2006.02.005.
40. F. K. de Theije, J. J. Schermer, and W. J. P. van Enckevort; Effects of nitrogen impurities on the CVD growth of diamond: step bunching in theory and experiment. *Diamond and Related Materials*, 2000. **9**(8): p. 1439-1449. DOI: 10.1016/s0925-9635(00)00261-2.

41. P. Hartmann, R. Haubner, and B. Lux; Effects of simultaneous boron and nitrogen addition on hot-filament CVD diamond growth. *Diamond and Related Materials*, 1997. **6**(2–4): p. 456-462. DOI: 10.1016/S0925-9635(96)00636-X.

42. R. Ramamurti, M. Becker, T. Schuelke, T. A. Grotjohn, D. K. Reinhard, and J. Asmussen; Deposition of thick boron-doped homoepitaxial single crystal diamond by microwave plasma chemical vapor deposition. *Diamond and Related Materials*, 2009. **18**(5–8): p. 704-706. DOI: 10.1016/j.diamond.2009.01.031.

43. H. Sternschulte, T. Bauer, M. Schreck, and B. Stritzker; Comparison of MWPCVD diamond growth at low and high process gas pressures. *Diamond and Related Materials*, 2006. **15**(4–8): p. 542-547. DOI: 10.1016/j.diamond.2006.01.010.

44. M. Kaukonen, P. K. Sitch, G. Jungnickel, R. M. Nieminen, Sami Pöykkö, D. Porezag, and Th Frauenheim; Effect of N and B doping on the growth of CVD diamond (100):H(2×1) surfaces. *Physical Review B*, 1998. **57**(16): p. 9965-9970. DOI: 10.1103/PhysRevB.57.9965.

45. S. Jin and T. D. Moustakas; Effect of nitrogen on the growth of diamond films. *Applied Physics Letters*, 1994. **65**(4): p. 403-405. DOI: 10.1063/1.112315.

46. R. Samlenski, C. Haug, R. Brenn, C. Wild, R. Locher, and P. Koidl; Incorporation of nitrogen in chemical vapor deposition diamond. *Applied Physics Letters*, 1995. **67**(19): p. 2798-2800. DOI: 10.1063/1.114788.

47. J. Stiegler, A. Bergmaier, J. Michler, S. Laufer, G. Dollinger, and E. Blank; The effect of nitrogen on low temperature growth of diamond films. *Thin Solid Films*, 1999. **352**(1–2): p. 29-40. DOI: 10.1016/S0040-6090(99)00285-0.

48. Jorge Tirira, Yves Serruys, and Patrick Trocellier; *Forward Recoil Spectrometry - Applications to Hydrogen Determination in Solids*, 1st ed., 1996, Springer US.

49. Xiaobing Liu, Xiaopeng Jia, Zhuangfei Zhang, Ming Zhao, Wei Guo, Guofeng Huang, and Hong-an Ma; Synthesis and Characterization of New “BCN” Diamond under High Pressure and High Temperature Conditions. *Crystal Growth & Design*, 2011. **11**(4): p. 1006-1014. DOI: 10.1021/cg100945n.

3 Analysis of B-doped heteroepitaxial diamond films: structure and defects

3.1 Overview

In the previous chapter, special focus was given to the growth environment and to aspects related to the plasma chemistry, which affect both growth (*i.e.* stability and deposition rate) and doping (*i.e.* control of impurities, namely B). Here in this chapter the attention is shifted to the properties of the grown crystals, namely of heavily B-doped films. The following work is divided into 3 main sections:

- 3.2 Measurements of boron incorporation in highly stressed heteroepitaxial diamond layers;
- 3.3 Visualisation of dislocations by etch-pit formation on heteroepitaxial diamond;
- 3.4 Direct imaging of boron segregation at dislocations in heteroepitaxial B-doped diamond.

Of main concern in 3.2 is the achievement of highly to heavily B-doped heteroepitaxial diamond films by *in situ* B-doping with TMB (trimethylborane) during MWPCVD, while keeping conditions that preserve single crystallinity, monitored by X-ray diffraction (XRD) measurements. The determination of the B doping level was investigated by several techniques and the results were compared. The very particular stress state of heteroepitaxial B-doped diamond films grown under the chosen conditions required a more careful and detailed approach than what is usually reported in the literature, as will be shown.

In section 3.3 the work focuses on the analysis of dislocations in the grown diamond films. The reduction of the dislocation density in heteroepitaxial diamond is a topic of major importance. Systematic studies on the reduction of dislocation density require, first of all, simple and reliable quantitative measurements of their density. Therefore, here we investigated the etch-pit formation method by varying etch parameters and measuring densities and shapes of the etch-pits formed on the surface of the diamond.

Finally, in section 3.4 dislocations in heavily B-doped heteroepitaxial diamond films are directly investigated with transmission electron microscopy (TEM) and other auxiliary techniques. Of particular importance is the relationship between dislocation and etch-pit, the type and orientation of the dislocations in the B-doped films compared to what is observed in undoped diamond, and the local features of the dislocations in a B-rich environment. Understanding how dislocations are generated, how they propagate and how they mutually interact is essential for the development of efficient strategies to reduce dislocation densities in the films.

3.2 Measurements of boron incorporation in highly stressed heteroepitaxial diamond layers

3.2.1 Introduction

Boron-doping is a fundamental capability that enables the application of diamond as high-end electronic and electrochemical devices. Without B-doping, the fabrication of diamond-based transistors, diodes and electrodes [1-11] to take advantage of the superb properties of diamond, would not be possible under practical conditions. Therefore, much work has been done around single- and polycrystalline B-doped diamond, such as the investigation of the effects that B precursors have in the gas phase during CVD [12, 13], their influence on growth [14-16], structure/crystallography [17-19] and generation of defects [20-24], and the effects of B incorporation on the electrical properties [25-31] of the grown crystals. However, little is known about B-doping of heteroepitaxial diamond films grown on Ir. Furthermore, there is a genuine possibility for the unique properties of diamond grown on Ir/YSZ/Si(001), namely the high density of threading dislocations, to reveal interactions with dopants which are not easily observable in homoepitaxial and polycrystalline films. Thus, this section is dedicated to the study of boron doping of heteroepitaxial diamond films by adding TMB (trimethylborane) as precursor to the process gas [32].

In this work B-doped diamond films of several µm thickness were grown by MWPCVD. High-resolution X-ray diffraction (HRXRD) and cathodoluminescence (CL) were used to evaluate structure, strain/stress and doping/composition of the films. It is shown that especially for the temperature range favourable for twin suppression a complete analysis of the strain tensor is required to extract the biaxial stress and the expansion of the lattice cell due to B atom incorporation. In light of the particular stress state of diamond films grown heteroepitaxially on Ir/YSZ/Si(001), several techniques for the quantification of B in the diamond (CL, SIMS and XRD) were compared and improved upon.

3.2.2 Formation of intrinsic stress by effective climb of dislocations

The optical and electronic properties of materials grown epitaxially on a lattice-mismatched substrate are strongly affected by processes of stress relaxation, which generally occur through the generation of misfit dislocations at the layer/substrate interface [33, 34]. Usually, this process requires that dislocations move into the crystal. However, the energy barrier against dislocation motion in certain crystals, such as $Al_xGa_{1-x}N$ and diamond inhibits this process. Instead, relaxation can occur via inclination of threading dislocations with respect to their original direction during growth, a process termed “effective climb” [34, 35]. The energy barrier for the inclination of dislocations in the crystal is overcome after a certain critical thickness, and is facilitated by surface roughness [34]. According to Romanov *et al.*, a possible mechanism of crystal growth with inclined dislocation may include directional surface diffusion and incorporation of adatoms at the intersection of the growing surface with pre-existing threading dislocations. **Figure 3-1** shows a sketch of the two basic processes of dislocation motion.

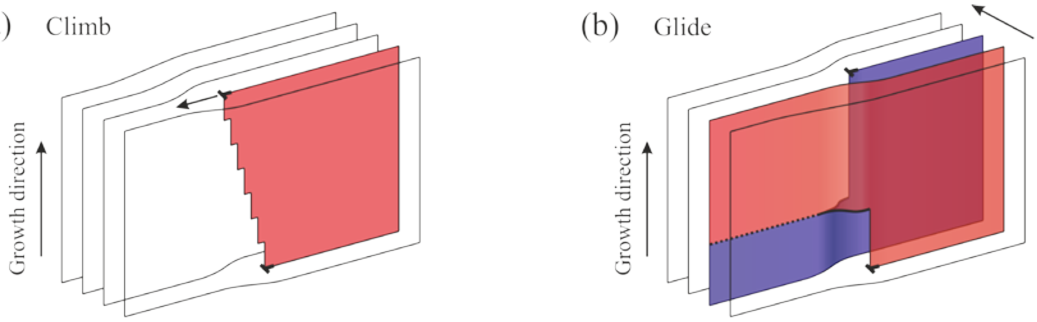

Figure 3-1: Sketch representing the two basic motion processes of dislocations. (a) In the climb process the extra lattice plane (red) moves further into the crystal (direction of the arrow) or out of the crystal (opposite to the arrow) along its plane, while (b) in the glide process the extra lattice plane (red) exchanges position with a neighbouring plane (blue).

In a recent publication by our group [35], it was shown that the stress state in heteroepitaxial diamond films with high dislocation densities can be controlled by varying the deposition temperature: the films display compressive biaxial[1] stress after growth at lower temperatures and tensile biaxial stress after growth at higher temperatures. In contrast to the example of stress relaxation in $Al_xGa_{1-x}N$ described before, here the tilt of the dislocation also creates growth stress. The stress in films with lower dislocation densities was found to be less sensitive to the deposition temperature. This implies that the growth temperature, which controls both chemistry and kinetics of film growth, causes the threading dislocations intersecting the surface to bend inwards or outwards, leading to compressive or tensile biaxial stress, respectively.

3.2.3 Experimental

3.2.3.1 Sample preparation

All diamond films were grown on Ir/YSZ/Si(001) using bias-enhanced nucleation (BEN) for the generation of diamond nuclei in a dedicated reactor, here labelled as “reactor #3”. For the preparation of the substrate, first a several ten nm thick layer of yttria-stabilised zirconia (YSZ) was deposited on a 3 mm thick, 4° off-axis Si(001) wafer by pulsed laser deposition (PLD) as described in [36]. An iridium layer was then grown by e-beam evaporation at 650 °C according to [37]. The BEN process was carried out in a MWPCVD reactor using an atmosphere of 3% CH_4 in H_2 and a bias voltage of −300 V. An intrinsic diamond layer of ~1 µm thickness was grown on the nucleated Ir/YSZ/Si(001) stack using a microwave power of 2 kW at 40 mbar in an atmosphere of 1.5% CH_4 in

---

[1] The two perpendicular in-plane strain components are equal.

H_2 with 100 ppm N_2. Subsequently a 5±0.5 µm thick B-doped layer was grown in a different CVD reactor (reactor #1) with 1.1 kW of microwave power at 50 mbar, and a substrate temperature of 720-750 °C in an atmosphere of 2% CH_4 in H_2 adding different amounts (0 to 240 ppm) of trimethylborane (TMB) as B-containing precursor.

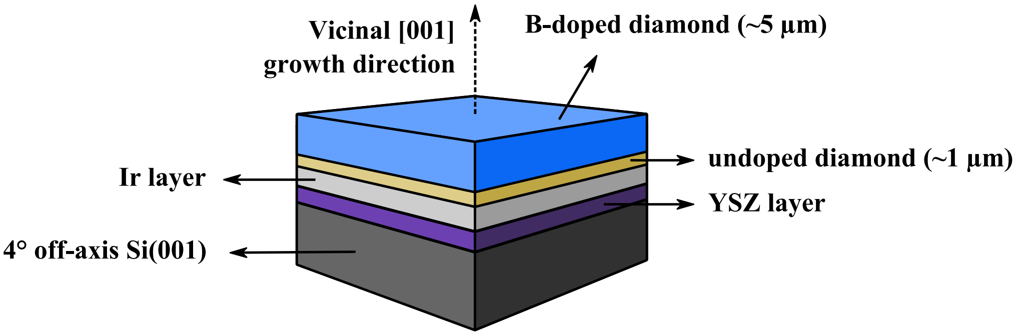

Figure 3-2: Illustrative sketch of the multilayer sample structure used in this section. The area of the substrates was 1×1 cm^2.

3.2.3.2 Measurement conditions

The thickness of the samples produced in this section was measured *ex situ* by white light interference using the T64000 triple Raman spectrometer setup. This technique takes advantage of the highly reflective Ir layer under the diamond and the low absorption and scattering of light from the thin diamond layers. By measuring the intensity of the light reflected by the sample over a wide wavelength range and counting the number of maxima from the oscillating pattern, the film thickness *d* can be calculated from [38]:

$$d = \frac{m}{2\left(\lambda_1^{-1} - \lambda_2^{-1}\right)\sqrt{n^2 - (\sin\theta)^2}} \tag{3.2.1}$$

where *m* is the number of maxima within a given wavelength interval, λ_1 is the wavelength from the 0th maximum in the interval, λ_2 is the wavelength from the mth maximum in the interval, *n* is the refraction index of diamond (~2.42) and θ is the light incidence angle, which was set to 0.

Optical microscopy and atomic force microscopy (AFM) were used to evaluate the surface of the samples before and after growth of B-doped diamond.

The B concentration in the samples was evaluated using cathodoluminescence (CL), according to a method described in section 1.6.1 and in the literature [39, 40]. The relationship between B concentration in the film and BE^{TO} peak position [40] is more adequate to high/heavy B-doping levels than the BE^{TO}/FE^{TO} peak ratio *vs.* $[B]$ method. CL was performed in high vacuum (~10^{-6} mbar) at liquid nitrogen temperature. Excitation was done by a 7 keV electron beam with a spot size of ~1 mm. The light was guided from the exit window by optical elements on an optical table towards the entrance slit (with variable opening width) of the T64000 spectrometer, operating in single mode with a 600 mm^{-1} grating.

For secondary ion mass spectroscopy (SIMS) [41] an ATOMIKA setup with an oxygen sputter gun operating at 5 keV was used. The incidence angle of the ion beam was 45° and the sputtered ions were analysed by a quadrupole mass filter. For intensity calibration, B-implanted diamond samples with peak B concentrations of 9.15×10^{16} cm^{-3}, 9.15×10^{18} cm^{-3} and 9.15×10^{20} cm^{-3} were previously prepared. The parameters for ion implantation were obtained after *SRIM* [2] (Stopping and Range of Ions in Matter) simulations: for an incidence angle of 7°, implantation energies in the range of 100 keV were used. After optimising our SIMS setup for B-doped diamond, we established a detection sensitivity level down to ~10^{18} cm^{-3} and a RSF (relative sensitivity factor)[3] for B in single crystal diamond of 1.99×10^{21} cm^{-3}.

3.2.4 Results and discussion

In order to investigate B-doping of heteroepitaxial diamond on Ir/YSZ/Si(001) in a systematic way, a series of 8 samples were grown following the structure displayed in **Figure 3-2**, with addition of TMB concentrations increased from 0 to 240 ppm to the gas phase. The growth conditions were established after an initial survey of parameters using several test samples/substrates, until stable growth conditions were found. Due to the limitations of reactor #1, which is dedicated for B-doping experiments, growth conditions were chosen at low pressure (50 mbar) in order to have a plasma ball large enough to cover the 1×1 cm^2 samples with the available MW power. The remaining optimised parameters (temperature, methane concentration, etc.) are described above in section 3.2.3.

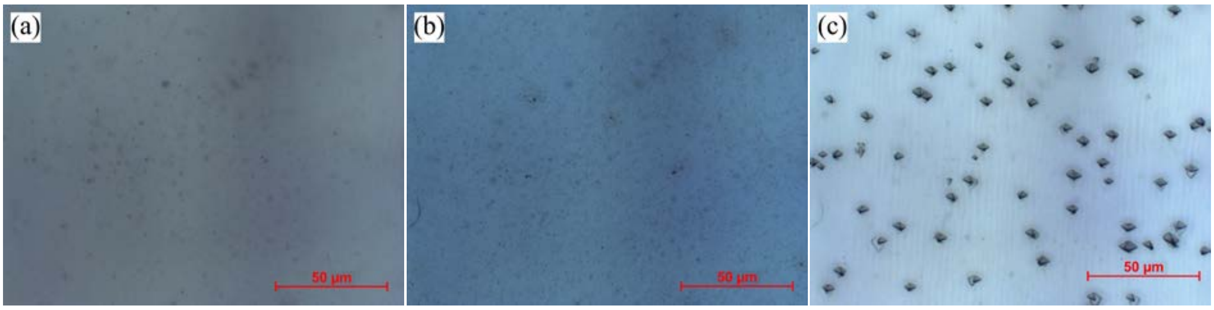

Figure 3-3: Optical microscope images of different B-doped diamond samples. (a) Sample grown without intentional B added to the gas phase (*i.e.* 0 ppm TMB; doping from background B of previous processes). (b) Sample grown with 240 ppm TMB added to the gas phase. Very high B concentrations roughen the surface. (c) Sample grown at higher temperature, doped from background B concentration, showing twins.

An immediate assessment of the diamond quality after growth is done by looking at the smoothness of the surface by naked eye. A glossy, smooth surface is a first hint of epitaxial growth.

---

[2] Website: http://www.srim.org/

[3] The count ratio of ^{11}B to ^{12}C multiplied by the RSF yields the actual B concentration in the diamond.

Samples grown under unsuitable conditions tend to show a matt surface due to polycrystalline growth and/or the formation of twins, particularly at the edges. The most critical parameter under B-doping conditions was found to be the temperature. Twinning was the main problem, occurring above ~750 °C and imposing a rather narrow temperature range for stable growth: roughly 700-740 °C. In **Figure 3-3** photographs of selected samples are shown.

AFM micrographs of several grown B-doped films were taken in order to evaluate their surface morphology and roughness. The results of representative samples are shown in **Figure 3-4**. The typical sample (~5 µm thick) prepared by the B-doping experiments in this section is shown in **Figure 3-4** (c). In (a, b) the pre-existing diamond layers from the post-nucleation growth step were grown further, up to ~85-90 µm thick, in reactor #3 (*i.e.* no B-doping). In (b) a B-doped layer was grown on top of the thick undoped layer.

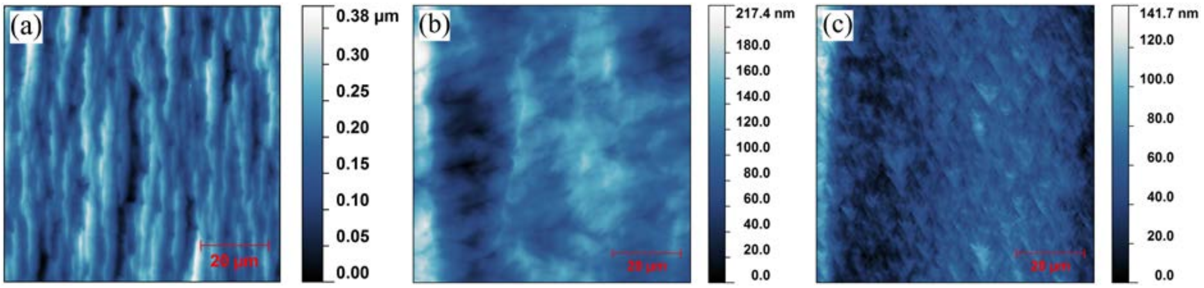

Figure 3-4: AFM micrographs showing distinct morphologies between undoped and B-doped heteroepitaxial diamond films. (a) Undoped sample (~90 µm thick) grown with 100 ppm $\mathrm{N_2}$ in the gas phase. $R_{\mathrm{RMS}} = 57.6\,\mathrm{nm}$. (b) B-doped layer (~5 µm thick) grown with 150-300 ppm TMB in the gas phase on a ~85 µm thick intrinsic substrate grown with 100 ppm $\mathrm{N_2}$ in the gas phase. $R_{\mathrm{RMS}} = 33.4\,\mathrm{nm}$. (c) B-doped layer (~5 µm thick) grown with 150-300 ppm TMB. $R_{\mathrm{RMS}} = 18.9\,\mathrm{nm}$.

The thick, undoped heteroepitaxial film displayed in **Figure 3-4** (a) shows a characteristic surface [42] with well-defined microstructures consisting of 1) terrace regions with a tilt towards the crystallographic (001) plane and 2) riser regions with increased tilt angle away from (001). They are aligned along the $[-110]$ axis for off-axis tilt of the substrate towards $[110]$ [43]. In **Figure 3-4** (b) a B-doped layer was grown on top of a thick undoped film identical to (a). It can be seen that the terrace/riser structure almost completely vanished. **Figure 3-4** (c) shows the morphology after growth of a B-doped layer on a thin substrate, presenting a smoother surface with triangular features very distinct from the terrace/riser structure. Therefore, the morphology shown in **Figure 3-4** (b) can be understood as a transition from (a) to (c), with the conclusion that the step bunching induced by nitrogen is reversed by boron.

To check the structural properties, the mosaic spread of the B-doped diamond samples was measured by XRD. The full width at half maximum (FWHM) from ω and ϕ scans (*i.e.* tilt and twist) were taken, respectively, from the (004) and (311) reflections, and plotted in **Figure 3-5**.

It can be seen that with increasing boron concentration in the gas phase, the tilt (blue curve) has worsened, while the twist (red curve) has improved. This is a contrasting result to the tendency observed with undoped films, *i.e.* both tilt and twist are expected to decrease with increasing film thickness, as shown in **Figure 1-10**. In the B-doping case here, the thickness is similar in all samples and thus an undoped layer would have displayed effectively unchanged tilt and twist.

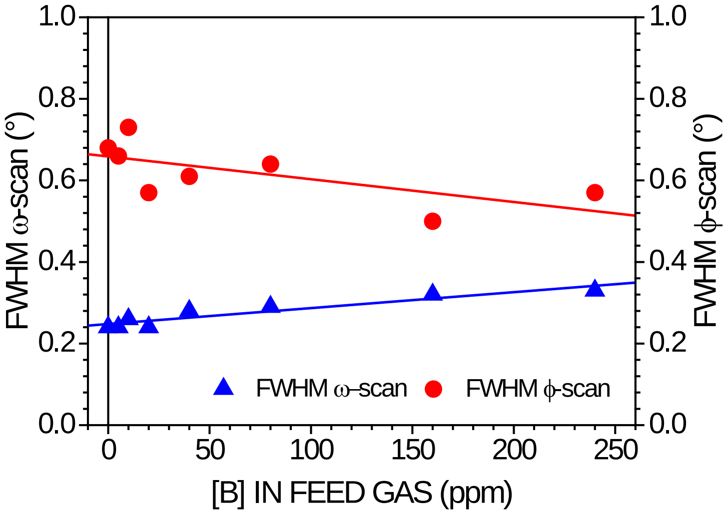

Figure 3-5: Full width at half maximum (FWHM) from rocking curves (tilt) and azimuthal scans (twist) as a function of TMB concentration in the feed gas.

This dependence of the mosaic spread on the B concentration suggests that there are other forces interfering with the texture improvement during growth, rather than pure growth/coalescence mechanisms (as described in section 1.3.2). We attribute the improvement of the twist and the worsening of the tilt with increasing B concentration to the following mechanism:

1) When the film growth process starts, TMB is introduced into the process gas and boron is incorporated into the diamond lattice, causing its expansion. Assuming that initially growth occurs in a pseudomorphic way, the B-doped layer adopts the in-plane lattice constant of the undoped substrate and the diamond cell experiences a tetragonal distortion;
2) During pseudomorphic growth, the elastic energy stored in the strained layer increases with its thickness. In materials which allow glide of dislocations at deposition temperature, nucleation and insertion of dislocations which relax the elastic deformation becomes energetically favourable [44]. Since gliding of dislocations in diamond is frozen at the present deposition temperatures, we speculate that the relaxation occurs by the effective climb of dislocations, as described in [34] for $Al_xGa_{1-x}N$, in such a way that the polar and azimuthal mosaic spread (*i.e.* tilt and twist) in the film change.

XRD is a high precision method for the measurement of lattice constants and lattice deformation. Boron incorporation increases the lattice parameter, but a detectable influence requires a doping level of $>10^{19}$ cm^{-3} [18]. For homoepitaxial layers, frequently the assumption of pseudomorphic growth (see **Figure 3-6** (a)) is made to simplify measurement and data evaluation, since only the strained lattice parameter perpendicular to the surface is measured [18]. With increasing doping level and thickness of the strained layer, partial or full relaxation (**Figure 3-6** (c)) by insertion of misfit dislocations, or by climb of dislocations, becomes energetically favourable. In heterosubstrates, the difference in coefficient of thermal expansion (CTE) between the materials adds a further stress component (see **Figure 1-8**). Additionally, as shown in a recent publication, in heteroepitaxial diamond films intrinsic stress with an absolute value of several GPa and positive or negative sign can develop [35]. As a consequence, additional measurements of asymmetric reflections are necessary to enable a full analysis of the strain tensor of the epitaxial layer. The derived stress tensor is then decomposed into a biaxial and a hydrostatic component, with the latter resulting from the incorporation of boron. This extra stress component in the film is illustrated in **Figure 3-6** (b).

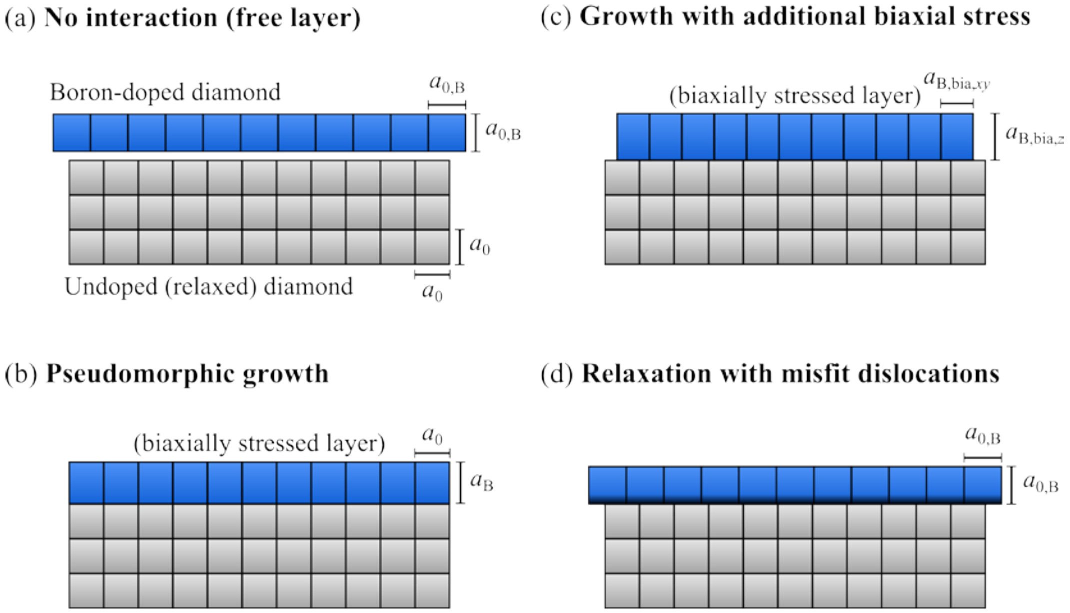

Figure 3-6: Illustration of different stress states of a heavily B-doped film grown on intrinsic (and relaxed) diamond, showing: (a) Fully relaxed B-doped without interacting with the substrate; (b) pseudomorphic growth, where the in-plane lattice constant of the grown layer is inherited from the substrate causing biaxial stress; (c) growth with additional compressive biaxial stress, where the in-plane lattice constant is smaller than in the pseudomorphic state; (d) fully relaxed film after insertion of misfit dislocations.

For the measurement of the strain tensor, rotational symmetry in the surface plane was assumed ignoring the slight off-axis angle. ε_{zz} and $\varepsilon_{xx} = \varepsilon_{yy}$ were extracted from θ-2θ scans of the diamond (004) and (311) reflections. With the stiffness tensor $\underline{\underline{C}}$ of diamond the components of the stress tensor are calculated from:

$$\underline{\sigma} = \underline{\underline{C}} \cdot \underline{\varepsilon} \tag{3.2.2}$$

The stress tensor can be decomposed into a sum of a hydrostatic component,

$$\underline{\sigma}_{\text{hydro}} = \begin{bmatrix} \sigma_{zz} & 0 & 0 \\ 0 & \sigma_{zz} & 0 \\ 0 & 0 & \sigma_{zz} \end{bmatrix} \tag{3.2.3}$$

and a biaxial component,

$$\underline{\sigma}_{\text{bia}} = \begin{bmatrix} \sigma_{xx} - \sigma_{zz} & 0 & 0 \\ 0 & \sigma_{yy} - \sigma_{zz} & 0 \\ 0 & 0 & 0 \end{bmatrix}. \tag{3.2.4}$$

Applying this method, we proceeded with a more thorough analysis of the stress components of the heteroepitaxial B-doped films from XRD measurements. First, the biaxial stress component was measured for various samples grown under the same base conditions, but with increasing deposition temperature. Later, both the biaxial and the hydrostatic stress components of samples grown with increasing B concentration in the gas phase were extracted and analysed.

Figure 3-7 shows the temperature dependence of the biaxial stress σ_{xx} of heteroepitaxial diamond layers grown in reactor #1 (high B background) without intentional boron addition, as well as of samples grown with 100 ppm N_2 added to the gas phase, in what was an attempt to suppress twin formation. At low temperatures, intrinsic compressive stress was found to build up during growth. With increasing deposition temperature its absolute value drops and turns from compressive to tensile, an identical behaviour to the one found for experiments at 200 mbar without boron [35].

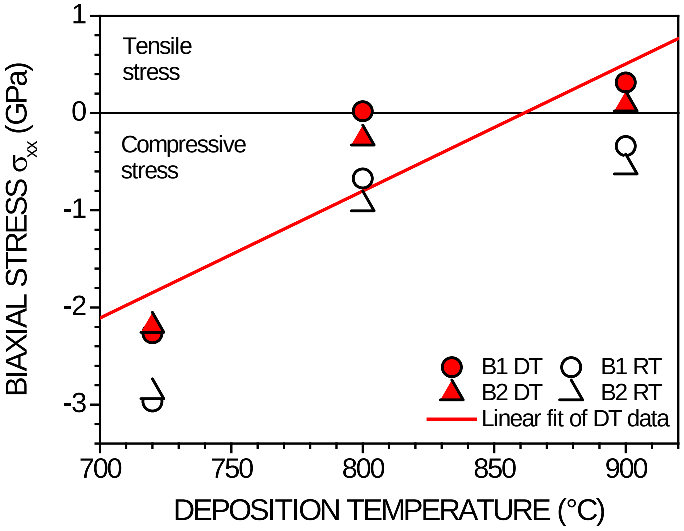

Figure 3-7: Biaxial stress in 6 heteroepitaxial diamond films grown in reactor #1 (high B background of ~2-3 ppm) at 50 mbar, 2% CH_4 in H_2 and 1100 W microwave power. Contrary to the samples from the "B1" set, the "B2" ones were grown with added 100 ppm N_2 for comparison. Room temperature (RT) values are as measured and deposition temperature (DT) values are calculated from the difference in CTE's. The DT values are equivalent to the intrinsic stress induced by growth process alone.

In principle, **Figure 3-7** recommends deposition above 800 °C in order to minimise generation of intrinsic stress. However, suppression of twins and non-epitaxial crystallites is much more effective at lower temperature, as shown in **Figure 3-3**. Even with nitrogen addition for the "B2" samples, no morphological differences were observed when compared with set "B1", probably because the catalytic effect of nitrogen on the growth rate was neutralised by the background B contamination, as discussed in chapter 2. Without the nitrogen-induced modification of the growth surface (see **Figure 3-4**), suppression of twins becomes ineffective. Since the intention is to have uncompensated B-doped samples without twins, it was only logical to focus this doping study on conditions without nitrogen, thus requiring growth at lower temperature.

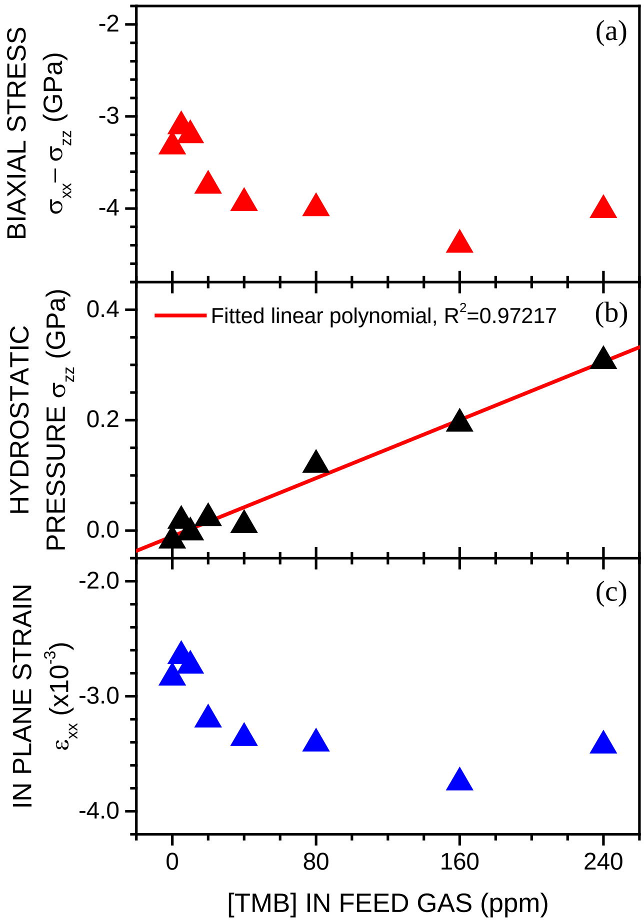

Figure 3-8: Components of the stress tensor: (a) biaxial component and (b) hydrostatic component due to B incorporation-induced lattice expansion *vs.* TMB concentration in the feed gas. (c) Variation of the in-plane strain component with the TMB concentration in the gas phase.

Figure 3-8 summarises the variation of (a) the biaxial stress $\sigma_{xx} = \sigma_{yy}$, (b) the hydrostatic stress σ_{zz} and (c) the in-plane strain component ε_{xx} with the B precursor concentration in the feed gas. It is observed that the biaxial compressive stress of −3 GPa increases slightly with increasing boron concentration. In order to assess this observation, one has to recall the mechanism of "effective climb" of dislocations suggested for the generation of intrinsic stress in epitaxial diamond growth [35]: the bending of dislocations, caused by a modification of the crystal growth at the intersection point of the dislocation with the surface, generates compressive or tensile stress. As described for GaN in [45], doping atoms can influence this process. In that specific case, silicon worked as an anti-surfactant, modifying the dislocation bending.

In our case, subsequent XRD measurements from B-doped layers grown on thick intrinsic layers, such as those shown in **Figure 3-4** (a, b), have shown that stress formation is strongly reduced when compared with the thin layers displayed above. This supports the hypothesis that the dislocations play a crucial role, since the thin material possesses a much higher dislocation density (see **Figure 1-12**) [46]. Secondly, the presence of boron did not cancel or counterbalance the formation of compressive stress. Instead, the biaxial stress values even increased by ~30%. The expansion of the lattice cell by boron, even for pseudomorphic growth, creates a contribution to the biaxial stress. Thus, it is more meaningful to discuss the in plane strain, ε_{xx}. As shown in **Figure 3-8**, the absolute value of ε_{xx} increases, meaning that the generation of new lattice cells at the growth surface due to dislocation bending is slightly enforced by the boron.

Continuing the analysis of the results shown in **Figure 3-8**, it can be seen that the hydrostatic stress increases linearly with increasing TMB concentration, indicating that the concentration of B atoms incorporated in the films increases with increasing TMB concentration in the gas. In order to estimate the B-doping level, $[\mathrm{B}]$, we applied Vegard's law [18] (equation (3.2.5)) to the measured hydrostatic strain, $\varepsilon_{\mathrm{hydro}}$, and summarised the results in **Figure 3-10** together with the B doping concentration deduced from other techniques.

$$[\mathrm{B}] = \frac{\varepsilon_{\mathrm{hydro}}[\mathrm{C}]r_{\mathrm{C}}}{r_{\mathrm{B}} - r_{\mathrm{C}}} \tag{3.2.5}$$

In the equation above, $[\mathrm{C}]$ is the density of carbon atoms in the diamond (1.77×10^{23} cm^{-3}), r_{C} is the covalent radius of the C atoms (0.077 nm), r_{B} is the covalent radius of the B atoms (0.088 nm) and $\varepsilon_{\mathrm{hydro}}$ is the hydrostatic strain component (*i.e.* the relative change of the lattice parameter, $\Delta a/a$, only due to hydrostatic stress).

The incorporation of boron was further investigated by SIMS and CL in order to compare with the values obtained by XRD. Each of these methods has its specific limitations in terms of accuracy, sensitivity and concentration range in which it can be applied. SIMS often turns out to be a technique used as a reference for others, because of its accuracy, and because it requires the use of calibrated samples with precisely known atomic composition. Likewise, in this work SIMS was mainly used as a reference for CL and XRD measurements of B incorporation in the diamond films.

In the CL analysis of B-doped diamond films, which was described in section 1.6.1, a contribution of stress to the peak shift has to be taken into account, since stress alone shifts the exciton-related peaks by ~0.01 eV per GPa, as reported by Naka *et al.* [47], which would significantly affect the estimation of the boron concentration in the diamond from this technique.

In order to address the stress-induced shift of the BE$^{\mathrm{TO}}$ peak, two samples were grown in reactor #1 without intentional B added to the feed gas, at different deposition temperatures, and then measured by CL. By changing the deposition temperature, the strength of the biaxial stress can be chosen (as shown in **Figure 3-7**), and a peak shift in the CL spectra can then be quantified. The result is shown in **Figure 3-9** (a).

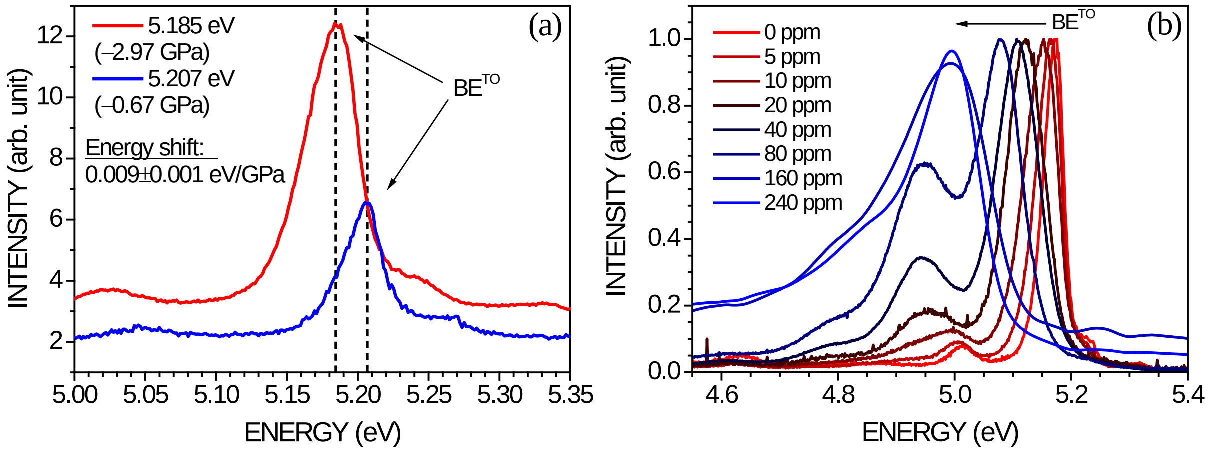

Figure 3-9: (a) CL spectra of two heteroepitaxial diamond films grown with unintentional B-doping from background contamination, at different temperatures, $CH_4/H_2 = 2\%$ and total flow rate of 200 sccm. Growth at 720 °C and at 800 °C resulted in a compressive stress of, respectively, −2.97 and −0.67 GPa at room temperature, as deduced from XRD measurements. An energy shift of 0.01 eV GPa^{-1} was deduced, which is in agreement with a former report by Naka *et al.* [47]. (b) CL spectra of B-doped samples grown with increasing TMB concentration in the gas phase. The shift of the boron-bound exciton peak BE^{TO} to lower energies is caused by increasing doping concentration.

By varying the biaxial stress in the B-doped films we have found the same stress-dependent peak shift previously reported by Naka *et al.* of ~0.01 eV GPa^{-1}. This relationship highlights the importance of knowing precisely the stress state of the B-doped films measured by CL, as well the importance of accurately calibrating the spectrometer: a variation of 0.01 eV caused by error or by 1 GPa in the film can lead to the estimation of B concentration being wrong by up to a factor of ~5 for a doping level of $\sim 10^{20}$ cm^{-3}, according to the BE^{TO} peak shift method [40]. This error increases with increasing B concentration.

Once the adequate conditions for the estimation of B in the film by CL were established, and once the stress state of each sample was known, we proceeded with the CL measurement of a series of B-doped samples grown with increasing TMB in the feed gas, in order to properly correlate the precursor concentration in the gas phase with the actual B acceptor concentration in the films. Their relationship is termed incorporation or doping efficiency (DE) [15]. The results are summarised in **Figure 3-10**.

An average doping efficiency of 20% was obtained, with the rough trend that it decreases with increasing boron concentration. This observation is similar to [15] but opposite to [17]. In this context, the differences among reported DE values can be partially explained by setup-specific parameters, such as different decay times of the gas precursors, as well different “pumping” behaviour by the chamber and the sample during growth (as studied in section 2.3.2), leading to B/C ratios which may significantly differ from the ratio in the feed gas.

Finally, **Figure 3-10** compares the B incorporation efficiency and the estimated $[B]$ in the films from all the techniques used throughout this study of B-doping of heteroepitaxial diamond. While SIMS is suited for any B concentration within the detection range (and as long as the correct RSF for B atoms in diamond is known from calibration), both CL and XRD have limitations. XRD depends upon a detectable expansion of the lattice, which is only caused by B starting at concentrations of $\sim 10^{20}$ cm^{-3}. Furthermore, the hydrostatic stress component must be extracted. The reliable determination of B in the film from CL spectra requires the application of the correct technique, either for low/medium or for high/heavy doping. In the latter case, reliable results can only be obtained when the stress state of the measured film is known, which may involve extra, more laborious XRD/stress tensor analysis.

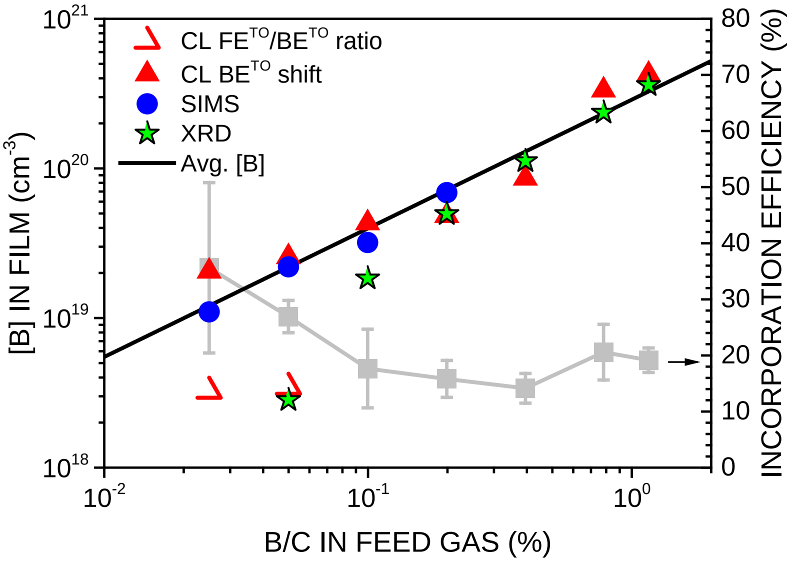

Figure 3-10: Boron concentration evaluated by several techniques for films grown at 720 °C. The procedure described for XRD is reliable above 10^{20} cm^{-3}, while the method from the FE^{TO}/BE^{TO} ratio resulted in underestimated values for the boron concentration in the films, as this technique is limited to $[B] < 10^{19}$ cm^{-3}, according to [39]. On the other hand, the BE^{TO} peak shift method proved reliable for the evaluated doping range. The black line is a linear fit of the averaged $[B]$ from all techniques, excluding the first XRD data point and the two data points from the CL ratio technique. The doping efficiency for each sample is shown in grey in the right axis.

The results summarised in **Figure 3-10** provide a guide for the selection of the most appropriate techniques for the measurement of B incorporation in different concentration ranges. Moreover, they allow for a more careful selection of growth/doping parameters for the preparation of films with the desired doping level, which is of particular importance for device fabrication.

In chapter 2 we have shown that B in the gas phase plays a role during diamond growth by neutralising the effect of N on the growth rate, a mechanism that is either related to surface chemistry or to the actual incorporation of the dopant. Here, we have shown that B also plays a role in changing the surface characteristics towards a smoother morphology, away from step bunching. With increasing TMB concentration in the gas phase, and therefore increasing B incorporation, changes in the mosaic spread as well as in biaxial stress were observed in our heteroepitaxial films of high dislocation density. We speculate that the particular characteristics of the B-doped film surface during growth, as well as the uptake of B and lattice expansion, may provide the conditions for enhanced "effective climb" of dislocations and increased stress. We do not exclude the possibility that preferential B incorporation occurs at these defects, which might have implications not only for the propagation of the dislocations, but also for the incorporation efficiency. In light of these observations, the backdrop for the upcoming studies was established.

Dislocations are expected to have an important influence on the electronic properties of devices, and thus, reliable concepts to derive quantitative values for the dislocation densities are required. In the upcoming section we focus attention on the identification of dislocations in the films by etching techniques.

3.3 Visualisation of dislocations by etch-pit formation on heteroepitaxial diamond

3.3.1 Introduction

A well-known technique in crystallography is the analysis of etch-pits formed on the crystal surface due to preferential etching of defect sites, namely dislocations [48]. Etch-pit formation on diamond has been employed mainly as a tool to estimate the dislocation density on grown crystals, and more recently to try to identify different types of dislocations from the shape and size distribution of the etch-pits [49-52].

Most of the etch-pit/dislocation studies focus on homoepitaxial films, usually undoped [49, 50, 52-54]. Here we want to investigate etch-pit formation and identification of dislocations in heavily B-doped, heteroepitaxial diamond grown on iridium. Several applications require high-quality B-doped diamond either as the active surface (*e.g.* in electrochemistry) or as substrate for electronic devices (*e.g.* in diamond-based Schottky rectifiers) and, therefore, the density of defects has to be kept as low as possible. Before strategies for the reduction of defects and dislocations can be employed, it is imperative to understand how they form, propagate and interact. For this purpose, simple and reliable techniques for the correct identification of the type of defect must be established, and selective etching is arguably the simplest, because it doesn't involve laborious and time-consuming sample preparation steps as, for example, in TEM analysis. Understanding how different etch conditions affect the formation of etch-pits is the focus here.

As most of the existing reports on etch-pit formation on diamond focus only on high pressure conditions (~200 mbar) and still significant variations in terms of etch-pit shapes/types exist, the aim of the present etching experiments is to survey a broader parameter range to find conditions for reproducible etch-pit formation for a reliable quantification of the dislocation density. Furthermore, a survey of parameters may highlight conditions which yield additional information, *e.g.* on the type of dislocations. For example, Sangwal in his book "Etching of Crystals" [48] mentions that etchant and etching conditions can control whether all types of dislocations are etched and whether the different types (*e.g.* screw- or edge-type) lead to etch-pits with distinct shape.

In the present study, preferential etching of undoped and B-doped diamond films was done in the MWPCVD reactors #1, #2 and #3 using different gas compositions (pure H_2, H_2+CO_2, H_2+TMB) and different plasma conditions (*i.e.* pressure and temperature). Undoped and heavily B-doped samples were etched in parallel to look for different etching behaviour.

3.3.2 Experimental

The study of etch-pit formation has a few requirements for maintaining reliability and accuracy of the results. First, it is necessary to select samples with an appropriate density of dislocations: high enough to provide a high count of etch-pits per area, and therefore increased accuracy, and low enough to minimise overlapping of etch-pits, which would lead to miscount and difficulties in the analysis of their shape. For this reason, a suitable density of dislocations was selected by defining the appropriate thickness for the heteroepitaxial diamond substrates. Following the relationship described in section 1.4.1 (see **Figure 1-12**), samples of several 10 µm thickness are expected to contain dislocations in the upper $10^8\,\mathrm{cm}^{-2}$ range, which we have found to be a suitable density for reliable etch-pit analysis. Thus, we have chosen to work with samples of intrinsic diamond layers with a thickness between 30 to 110 µm, as illustrated in **Figure 3-11** (a).

Another important aspect of this work is the comparison between etch-pit formation on the undoped diamond with etch-pit formation on B-doped diamond, in order to investigate potential differences in etching behaviour which could be attributed to segregation of B atoms along the dislocation lines. For this purpose, B-doped layers of *ca.* 8 µm thickness were grown on some of the 30-100 µm thick intrinsic layers (see **Figure 3-11** (b)), so that etching could be simultaneously performed on B-doped and undoped samples with comparable thicknesses.

Last but not least, the aspect of gas composition plays a major role in the selective etching of dislocations, and one of the purposes of this work was to gain a better understanding and control over this parameter. For this reason, different gas mixtures have been chosen: 1) pure H_2; 2) $H_2 + CO_2$ and 3) $H_2 + \mathrm{TMB}$. Pure hydrogen is expected to produce the lowest etch rates and lower selectivity. Oxygen, on the other hand, is expected to etch diamond faster and to promote enhanced selectivity, according to previous reports. The selection of TMB for etching arose from the observation that, during a routine growth process of B-doped films, strong etch-pit formation was observed after CH_4 was switched off while the plasma remained ignited for some time before the process ended. The process gas contained hydrogen and TMB.

Due to this preliminary observation, etching experiments with pure hydrogen and $H_2 + CO_2$ had to be performed in boron-free reactors (#2 and #3) to avoid misleading results. Etching experiments under high B background were performed in reactor #1.

As described in section 1.5.3, most relevant for etch-pit formation is to have a much higher removal rate at the dislocations relative to the removal rate on the pristine surface. Therefore, the most important aspects of this study focussed on 1) identifying which recipe yields the most reliable etch-pit formation to identify dislocations and 2) identifying whether one can distinguish different types of dislocations (*e.g.* edge-type, mixed-type, pure screw-type), according to the shape and/or size of the etch-pits and which gas mixture is best suited for this purpose. Due to the different etch rates the process time and the parameters had to be adapted for each gas mixture in order to obtain etch-pits which could be studied and compared. The base etching conditions are summarised in **Table 3-1**.

Data evaluation of the etching experiments comprised shape, size (size distribution) and the absolute etch-pit densities.

The visualisation and counting of etch-pits was done manually from SEM and/or AFM micrographs taken from each sample, with aid of a *MATLAB* program to mark and count etch-pits that were visually identifiable. The results are summarised in tables and collected all together in the end a final graph (**Figure 3-16**).

Analysis of the shape of the etch-pits was done by AFM (atomic force microscopy) in section 3.3.3.5. The measured surface profiles of the etched samples were then treated with the software *Gwyddion* in order to extract the angle of the etch-pit facets.

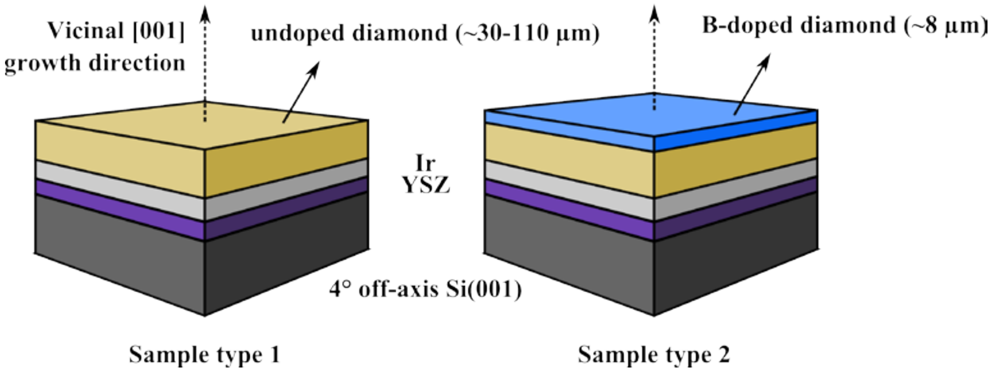

Figure 3-11: Schematic illustration of both undoped (left) and B-doped (right) samples used for the etching experiments. The samples were prepared as described in section 3.2.3.1, with thicker intrinsic layers. The B-doped layers were grown on top at 100 mbar, 5% CH_4 in H_2, 200 ppm TMB for 2 hours.

Table 3-1: General etching conditions used throughout this work for the different gas compositions.

Gas composition	**Pure H_2**	**$H_2 + CO_2$**		**$H_2 + B_{bkg.}$**
Reactor	#2	#2	#3	#1
Pressure	50 mbar	50 mbar	150 mbar	50 mbar
Temperature	~740 °C	~740 °C	700-1100 °C	~740 °C
Total gas flow	400 sccm	400 sccm	500 sccm	400 sccm
Boron background	0.01-0.1 ppm	0.01-0.1 ppm	~0.006 ppm	> 1 ppm

3.3.3 Results and discussion

3.3.3.1 Hydrogen etching: base condition

Two experimental runs were performed where pairs of B-doped and undoped samples, (a, b) and (c, d), were plasma-etched at 50 mbar in a pure hydrogen gas phase. Different thicknesses and etching times were tested in order to evaluate the best conditions. SEM images of each sample after etching are shown in **Figure 3-12**. The etch parameters and the etch-pit counts are summarised in **Table 3-2**.

Table 3-2: Data summary of the plasma etching experiments at 50 mbar in pure H_2 in reactor #2. The etch-pits were counted manually from the images shown in **Figure 3-12**.

Sample	**(a)**	**(b)**	**(c)**	**(d)**
Type	undoped	B-doped	undoped	B-doped
Total thickness	33 µm	40 µm	109 µm	108 µm
Etching time	1 h	1 h	4 h	4 h
Etch-pit density	$6.5\times10^{8}\ cm^{-2}$	$1.1\times10^{9}\ cm^{-2}$	$3.5\times10^{8}\ cm^{-2}$	$2.9\times10^{8}\ cm^{-2}$
Lateral size	~25 nm	50-100 nm	50-100 nm	50-100 nm

The SEM images below show that etching in pure H_2 produced black spots on the surface of the samples. These are etch-pits. With the exception of **Figure 3-12** (a), the etch-pit size and distribution on the surface are similar in all other images, with a certain fraction of clustered etch-pits arranged in lines, which are interpreted as residues of former grain boundaries. The etch-pits on the undoped sample (a) are smaller and difficult to interpret. The etch-pits on the B-doped sample in **Figure 3-12** (b) are the most clear. There, one can see that they have a defined shape, similar to a trapezoid aligned along the $[110]$ off-axis direction (green arrow). This shape corresponds in fact to inverted square pyramids with their base plane inclined towards $[110]$. A detailed analysis in section 3.3.3.5 will show that the asymmetric shape can be explained quantitatively by the off-axis angle. Perhaps the most striking result of etching under pure H_2 is that after 4 h the lateral size of the etch-pits (*ca.* 50-100 nm) did not increase significantly, but an overall roughening was observed. In the single case of the undoped sample etched for 1 h the pits were smaller and difficult to pinpoint, making the etch-pit density estimation unreliable. In contrast, the 4 h etching processes produced similar results in terms of size, shape and density of etch-pits for undoped and B-doped samples. We speculate that this difference is due to the softer hydrogen etching process involving a certain nucleation stage, which delays etch-pit formation and requires longer etching time, whereas in the B-doped sample this nucleation is facilitated by the presence of B. As consequence, etch-pit formation under pure H_2 requires a longer process time. After 4 h both types of sample produced equivalent results, as shown in **Table 3-2**.

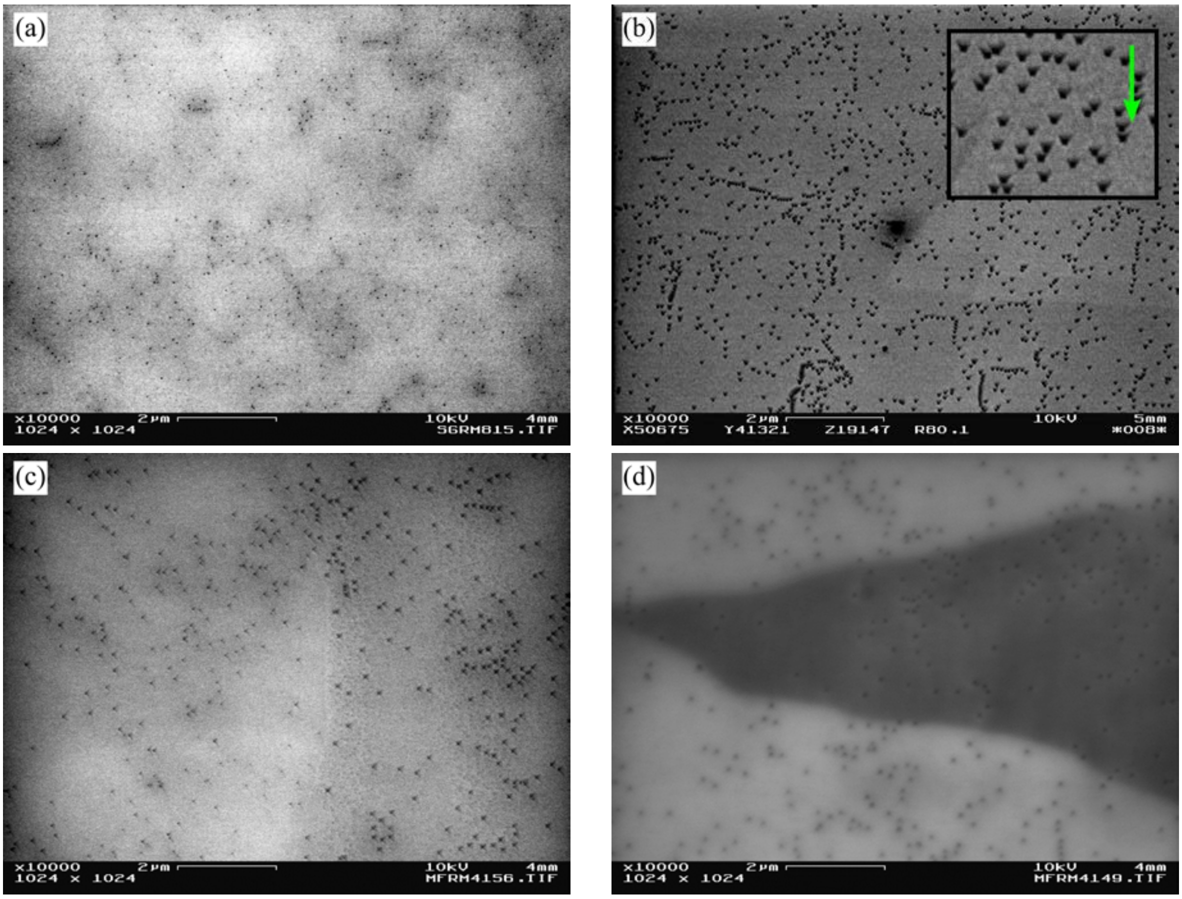

Figure 3-12: SEM images of (a, c) undoped and (b, d) B-doped samples etched in pure H_2 for (a, b) 1 hour and for (c, d) 4 hours. The arrow in (b) shows the $\left[110\right]$ off-axis direction.

3.3.3.2 Hydrogen and CO_2 etching

As pointed out in chapter 2, oxygen gas is often added to the gas composition during diamond growth in order to improve the phase purity of the grown crystal with a stronger suppression of sp^2 carbon. Too much oxygen causes the process to switch to the etching regime, as illustrated by Bachmann's C-H-O diagram (**Figure 1-18**). Introduction of oxygen in the gas phase can enhance the formation of etch-pits [49, 50], and some studies have been performed on the evolution of etch-pit size and density with etching time, at high pressure (200 mbar). However, little has been discussed about the selection of appropriate etch parameters with oxygen and how they affect etch-pit formation. Here we explore etching conditions with different CO_2 concentrations on undoped and B-doped diamond, and for two different etching durations at 50 mbar. In a first step, simultaneous etching of 2 diamond samples (undoped and B-doped) was performed with 1% CO_2 in H_2 for 2 hours. The samples had been pre-etched with pure H_2 for 3 h, in order to evidence whether the etch-pits would simply continue to enlarge or if a different pattern would arise after CO_2 etching. The parameters and results are summarised in **Table 3-3**.

Table 3-3: Data summary of the plasma etching experiments at 50 mbar with 1% CO_2 in H_2 in reactor #2. The etch-pits were counted manually from the images shown in **Figure 3-13**.

Sample	**(a)**	**(b)**
Type	undoped	B-doped
Total thickness	40 µm	40 µm
Etching time	2 h	2 h
Etch-pit density	$3.1\times10^{8}\ \text{cm}^{-2}$	$7.7\times10^{8}\ \text{cm}^{-2}$
Lateral size	up to ~1 µm	~500 nm

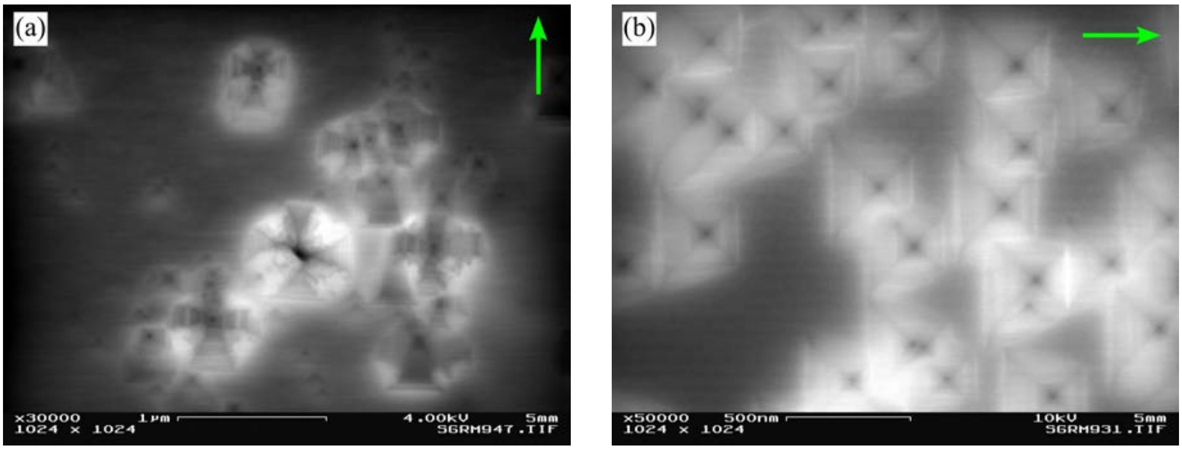

Figure 3-13: SEM images of (a, b) undoped and B-doped samples etched for 2 h with 1% CO_2 in H_2 in reactor #2. Both samples had been previously etched with pure H_2 for 3 h. The green arrows show the $[110]$ off-axis direction.

In this etching experiment a quite distinct result was obtained compared to the previous etching in pure H_2. The first obvious difference is the size of the etch-pits, which are significantly larger than before. The second obvious difference is that, while on the B-doped sample only etch-pits aligned along $\langle 110\rangle$ with uniform size distribution were formed, on the undoped sample large 8-fold structures can be distinguished from the small $\langle 110\rangle$ ones. Since both samples had been previously H_2-etched for 3 h, it appears that on the B-doped sample the etch-pits simply continued to develop homogeneously across the surface, whereas on the undoped sample selectivity took place with only a portion of the etch-pits developing into large 8-fold structures, while the others remained 4-fold. From a total etch-pit density of 3.1×10^{8} cm^{-2}, about half had the 8-fold shape. A possible explanation for this intriguing result could relate to differences in the type of the involved dislocations, as suggested by Sangwal [48]. Focussed ion beam (FIB) lamella taken at different etch-pits for a TEM analysis could reveal if such a correlation exists. Unfortunately, this analysis was not possible in the framework of this thesis.

In a second step, the CO_2 concentration was raised from 1% to 3%. All relevant process parameters are summarised in **Table 3-4**, including the results from the etch-pit analysis. The pairs of sample (a, b) and (c, d) had been previously subjected to pure H_2 etching. **Figure 3-14** shows SEM images of the sample surfaces after etching.

Table 3-4: Data summary of the plasma etching experiments at 50 mbar in reactor #2 with 3% CO_2 in H_2. The total amount of etch-pits was counted manually from the images shown in **Figure 3-14**.

Sample	**(a)**	**(b)**	**(c)**	**(d)**	**(e)**	**(f)**
Type	undoped	B-doped	undoped	B-doped	undoped	B-doped
Total thickness	108 µm	109 µm	40 µm	40 µm	35 µm	40 µm
Etching time	1 h	1 h	1 h	1 h	2 h	2 h
Etch-pit density (cm^{-2})	2.16×10^{8}	2.56×10^{8}	4.2×10^{8}	6.3×10^{8}	3.7×10^{8}	1.2×10^{8}
Lateral size	up to ~2 µm	up to ~500 nm	up to ~1 µm	up to ~300 nm	up to ~2 µm	up to ~1 µm

The most evident result of these 3 etching experiments with 3% CO_2 is the prominent formation of 2 types of etch-pits: new 4-fold pits with edges aligned along $\langle 100\rangle$ seen in **Figure 3-14** (a-d) and variations of 8-fold etch-pits, seen in (a, e, f), which could be understood as a superposition of the 4-fold $\langle 110\rangle$-type with the 4-fold $\langle 100\rangle$-type. The samples etched for 1 h (a-d) reveal a combination of small $\langle 110\rangle$ pits alongside larger rotated etch-pits, showing again that the combination of both pure H_2 and then CO_2 etching may enhance selectivity.

Another clear observation after these etching experiments is the different behaviour between undoped and B-doped samples. The etching pattern on the B-doped samples appears much smoother and more well-defined, especially the inner facets of the big $\langle 100\rangle$ etch-pits, indicating that incorporated B plays a certain role in etch-pit formation.

Looking more carefully, on the undoped samples the $\langle 100\rangle$ pits are actually composed of 8 facets, 4 which are flat (oriented along the $[110]$ direction), and 4 which are rough (oriented along the $[100]$ direction). The true shape is rather an asymmetric octagon. The B-doped samples show the same trend, although less pronounced and without roughening. With longer etching time, only 8-fold structures are distinguishable on both the undoped and B-doped samples, *i.e.* **Figure 3-14** (e, f), together with an overall surface roughening.

The amount of large $\langle 100\rangle$ etch-pits relative to the small $\langle 110\rangle$ ones, on the samples where both appeared, was generally small: roughly less than 10%, but with too much uncertainty to enable conclusive statements. Nevertheless, the final etch-pit densities (including all types and sizes) of all the samples are comparable ($\sim 10^{8}$ cm^{-2}) and fairly close to the dislocation density for heteroepitaxial diamond films on Ir later reported by our group [46] (**Figure 1-12**), despite differences in growth and etching conditions. This is a positive outcome concerning reliability.

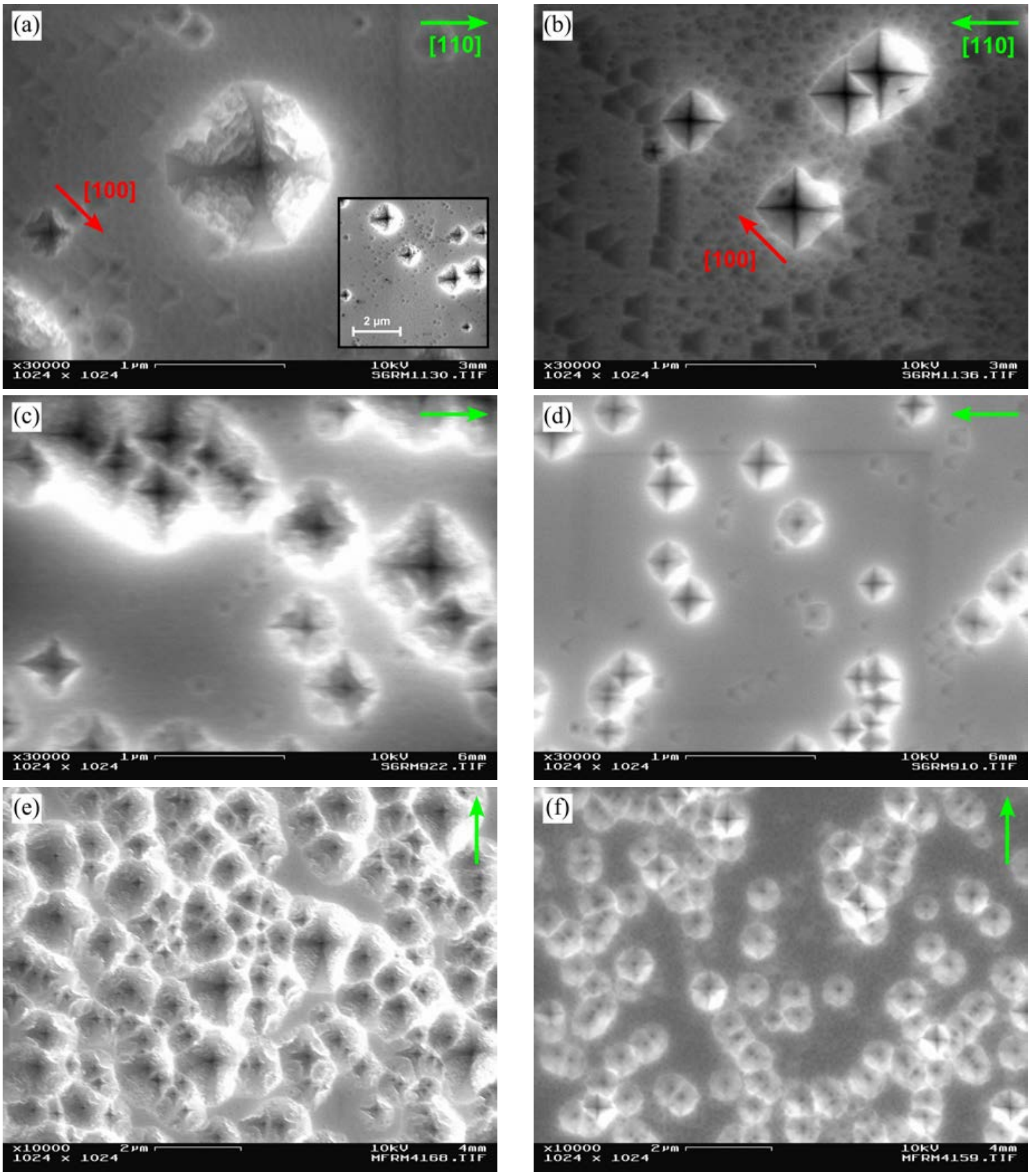

Figure 3-14: SEM images of (left) undoped and (right) B-doped samples etched at 50 mbar in reactor #2 with 3% CO_2 in H_2. Samples (a-d) were etched for 1 h under these conditions and pre-etched in H_2, while samples (e, f) were etched for 2 h without pre-etching. The green arrows show the $[110]$ off-axis direction. See text for further details.

3.3.3.3 Etching with a high B background

As mentioned earlier, we have observed etch-pit formation after a routine growth process in reactor #1 (dedicated to B-doping) where the CH_4 flow was accidentally stopped some time before the plasma was switched off. This outcome led to the question of whether B enhances etching in a similar way to oxygen. Our previous observation that boron neutralises the catalytic effect of nitrogen on the growth rate (discussed in section 2.3.7), presumably by "upsetting" the nitrogen-modified chemistry on the diamond surface, could be an indication that B might also play a role in selectively etching defects when combined with hydrogen. Therefore we went on to perform several etching experiments with addition of TMB to the gas phase in the highly B-contaminated reactor #1 to look for enhanced etch-pit formation.

Two etching experiments were carried out, again by simultaneously etching undoped and B-doped samples of comparable thicknesses. For each process a different B background concentration was selected by introducing TMB in the feed gas in various amounts. The etching conditions and results are summarised in **Table 3-5**. SEM images of the samples after etching are shown in **Figure 3-15**.

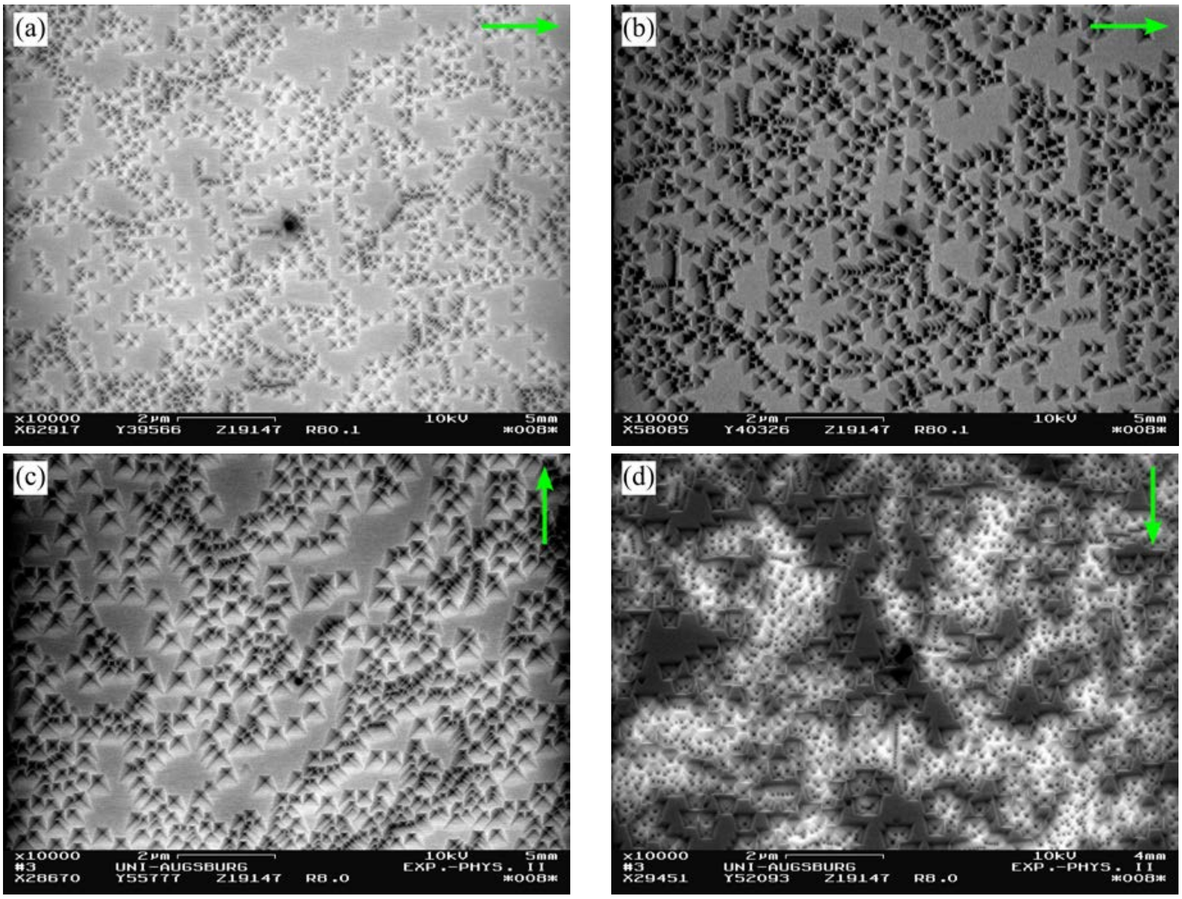

Figure 3-15: SEM images of (left) undoped and (right) B-doped samples etched at 50 mbar in reactor #1 (B background equivalent to ~1-3 ppm TMB). Samples (a, b) were etched without addition of TMB, samples (c, d) were etched with addition of 200 ppm TMB. See **Table 3-5** for details. The green arrows show the $[110]$ off-axis direction.

Table 3-5: Data summary of the etching experiments at 50 mbar in reactor #1 (B background of ~1-3 ppm TMB) with further addition of TMB. The total amount of etch-pits was counted from the images in **Figure 3-15**.

Sample	**(a)**	**(b)**	**(c)**	**(d)**
Type	undoped	B-doped	undoped	B-doped
Total thickness	40 µm	40 µm	40 µm	40 µm
Etching time	1 h	1 h	1 h	1 h
$[TMB]_{feedgas}$	0	0	200	200
Etch-pit density (cm^{-2})	1.34×10^9	1.03×10^9	7.83×10^8	1.23×10^9
Lateral size	~270 nm	~360 nm	~450 nm	~450 nm

Etching with high concentrations of B in the gas phase produced noticeable differences relative to the previous methods. In a high B background the samples were etched faster than with pure H_2, and the formed etch-pits have clear, uniform size distribution and shape (trapezoidal, aligned along the [110] off-axis direction). With high B background both undoped and B-doped samples appear to be etched in a similar way, revealing identical features, in a strong contrast to CO_2 etching. Also noticeable is the higher average etch-pit count (~10^9 cm^{-2}), which is in even better agreement with [46].

Interestingly, increasing the B background by 2 orders of magnitude, from ~1-3 to ~200 ppm did not produce significant differences between the etched samples, *i.e.* pairs (a, b) and (c, d) in the figure above, apart from a slight increase in the etch-pit size, which led to overlapping and a higher electronic contrast in the SEM micrograph of sample (d). This is attributed to the increased surface roughness, and to the fact that the heavily B-doped layer has higher electrical conductivity and darker contrast relative to the undoped layer.

These etching experiments with high B background have shown quite clearly that B does have an effect on the selective etching of defects, enhancing the action of hydrogen alone. Compared with the other parameters and conditions tried in this work, it proved to be the most reproducible for etch-pit count.

3.3.3.4 Summary of etch-pit densities for various etching conditions

The etch experiments performed above (from section 3.3.3.1 to 3.3.3.3) resulted in formation of etch-pits with different shape, orientation and in different quantities, depending on the etching condition used, and whether the sample was undoped or B-doped. The obtained etch-pit densities are summarised in **Figure 3-16** together with the results from [46].

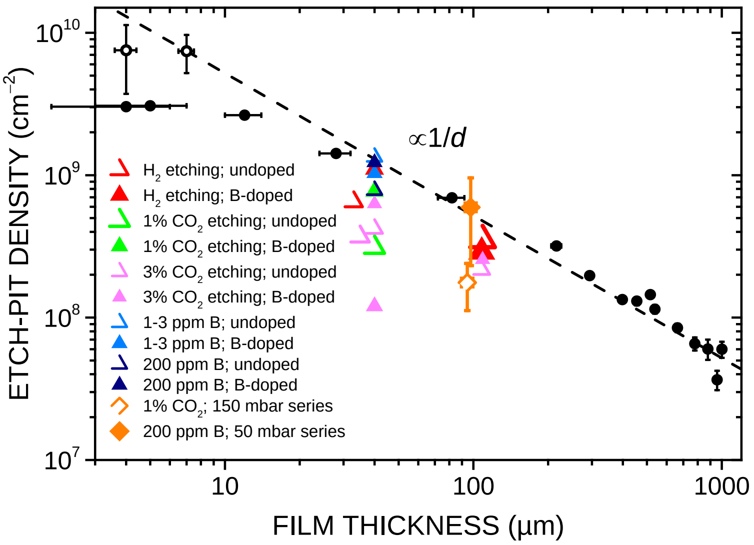

Figure 3-16: Etch-pit densities from various samples etched under the listed conditions. The black data points and curve are reproduced from [46]. The two orange data points from 150 mbar and 50 mbar series are explained in the upcoming section 3.3.3.6.

3.3.3.5 Orientation and shape of etch-pits (AFM analysis)

In this section a further analysis of the shape and orientation of the etch-pits formed on the etched samples studied above was carried out. Two main types of etch-pits were observed:

- $\langle 110\rangle$ etch-pits: inverted square pyramids with edges parallel to $[110]$ and $[-110]$;
- $\langle 100\rangle$ etch-pits: inverted square pyramids with edges parallel to $[100]$ and $[010]$.

From the SEM pictures all etch-pits appear stretched along the $[110]$ off-axis direction, giving an asymmetric appearance, and no information on the facet angles can be derived. Thus, in order to determine the crystallographic orientation of the side faces of the pyramids and to clarify the reason for their distortion, AFM analysis of etched samples containing the types of etch-pit described above was performed. Representative images of selected samples are shown in **Figure 3-17** .

For the measurement of the angle χ of the pyramid faces, defined relative to the surface plane, AFM line scans were performed along each edge direction of the etch-pits, *i.e.* along $[110]$ and $[-110]$ for the $\langle 110\rangle$ etch-pits, and along $[100]$ and $[010]$ for the $\langle 100\rangle$ etch-pits, intersecting at the tip of the pyramid. Several etch-pits on several samples were measured and the results averaged. They are summarised in **Table 3-6**.

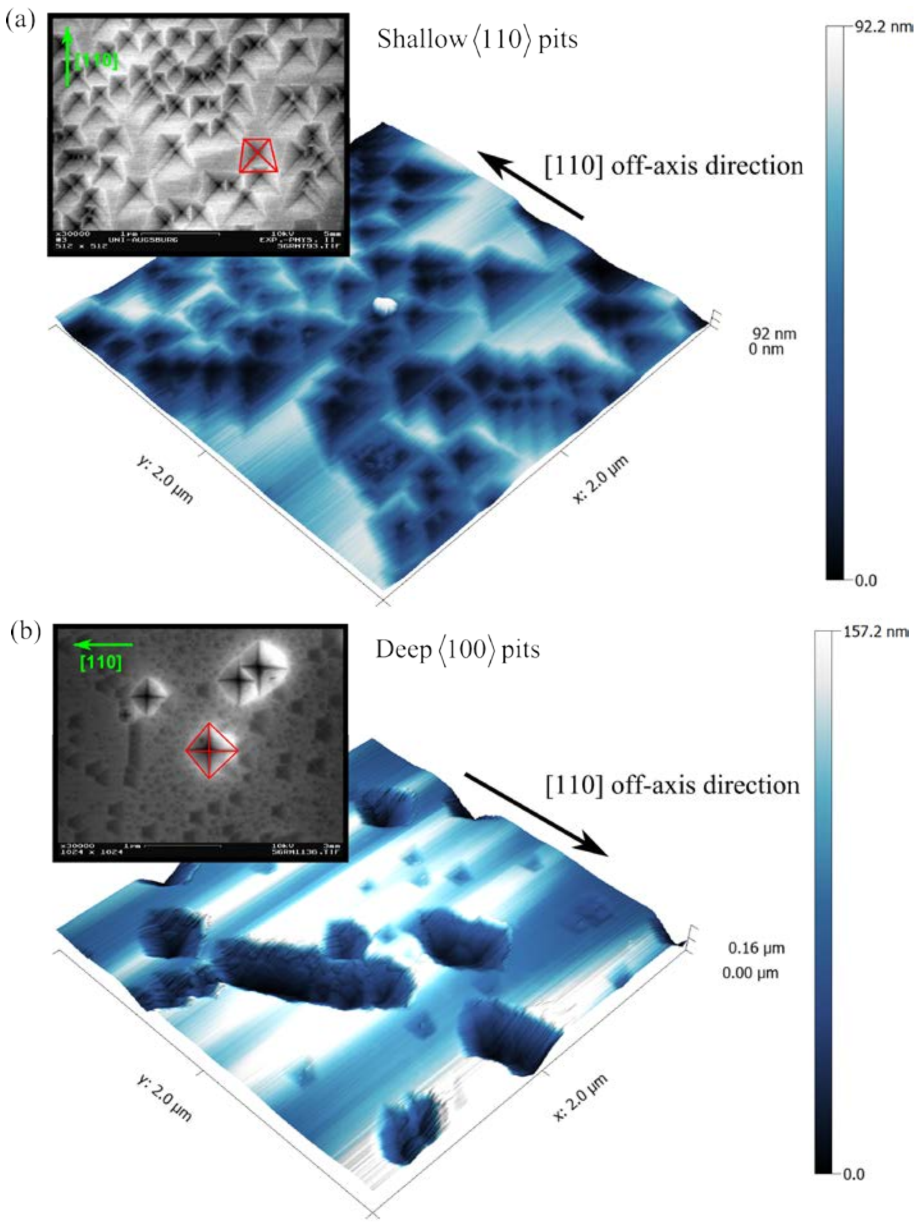

Figure 3-17: AFM scans showing diamond films etched for 1 h at 50 mbar with (a) 200 ppm TMB and (b) 3% CO_2 in H_2. In the inset, their respective SEM micrographs are shown. The green arrow indicates the $\left[110\right]$ off-axis direction.

From the AFM scans, the first observed difference between the two types of etch-pit is in their facet angles. The $\langle 110\rangle$ pits were found to be much shallower than the $\langle 100\rangle$ ones, with average facet angle of 14±5°, while the latter type resulted in 48±3°. We attribute this result to the etch-pits having different etch velocities along the main directions (see **Figure 1-19**), with the $\langle 100\rangle$ pits possessing a faster normal component. Furthermore, the measured angles are very close to defined crystallographic planes, as shown in **Table 3-6**, which poses the question of whether they are arbitrary or preferential. A more detailed analysis of this issue will be presented in section 3.3.3.6.

After a careful analysis of the facet angles of the $\langle 110\rangle$ etch-pits, it was found that the average angle difference[4] between the two facets along the $[110]$ off-axis direction has a value very close to the nominal off-axis angle of 4° (±1°). On the other hand, the average angle difference between the other two facets (perpendicular to the off-axis direction) is around 0° on average. A similar inclination along the off-axis direction was also observed with the $\langle 100\rangle$ etch-pits, with two adjacent facets being shallower than the other two, proportionally to the off-axis angle. This result is coherent with the possibility of the etch-pit facets being defined crystallographic planes, because they are symmetric relative to the $[001]$ direction instead of the surface normal. Consequently, the elongated shape of the etch-pits along the $[110]$ off-axis direction has a simple geometrical reason, instead of being caused by tilted dislocations, as observed in other materials [48]. To support this conclusion, it was recently found that dislocations in undoped heteroepitaxial diamond are tilted away from $[001]$ direction [55], while dislocations in heavily B-doped heteroepitaxial diamond strictly follow $[001]$, as will be shown in section 3.4. However, in all samples etched here, undoped and heavily B-doped, the asymmetry of the etch-pits can be attributed exclusively to the off-axis angle.

Table 3-6: Summary of the etch-pit shapes found with the experiments described above.

Etch-pit type and orientation	Facet angle χ	Nearest crystallographic planes	Etch conditions
$\langle 110\rangle$	14±5°	$\{113\}\ldots\{115\}$	50 mbar, 200 ppm TMB in H_2
$\langle 100\rangle$	48±3°	$\{011\}$	50 mbar, 3% CO_2 in H_2

The demonstration that the asymmetry of the etch-pits are caused by the off-axis angle is illustrated in **Figure 3-18**.

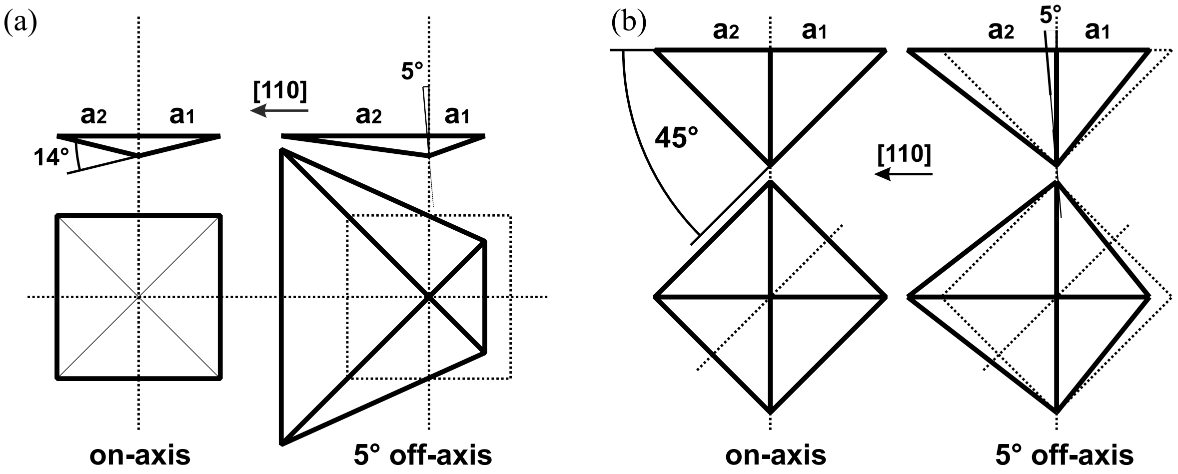

Figure 3-18: Sketch of the (a) shallow $\langle 110\rangle$ etch-pits and (b) deep $\langle 100\rangle$ etch-pits with approximate facet angles χ relative to the vicinal (001) surface with off-axis tilt towards $[110]$. A small off-axis angle of ~5° is enough to cause a shallow etch-pit such as (a) to appear strongly asymmetric. The $\langle 110\rangle$-type pits are in fact

---

[4] That is, $|\chi_1| - (|\chi_1| + |\chi_2|)/2 \cong \text{O.A.}$

inverted square-based pyramids with a tilted base plane. The same principle applies to the $\langle 100 \rangle$-type etch-pits, which acquire a less pronounced asymmetry, in a kite-like shape, due to their steeper facet angles. The formation of asymmetric etch-pits was also observed on off-axis SiC [56].

Considering **Figure 3-18**, assuming that two opposite facets of an etch-pit make an angle 2θ, for an etch-pit on an exact (001) surface its normal $[001]$ bisects the 2θ angle. The angle θ is therefore complementary to the facet angle χ, as defined before. Under these conditions, if the etch-pit is now tilted by an angle φ, so that φ is the angle of the bisection relative to the axis normal to the surface, the projection of the two facets on the surface plane, a_1 and a_2, are related by the following equation:

$$\frac{a_2 - a_1}{a_2 + a_1} = \frac{\cot(\chi - \varphi) - \cot(\chi + \varphi)}{\cot(\chi - \varphi) + \cot(\chi + \varphi)} \tag{3.3.1}$$

This relationship, plotted in **Figure 3-19**, gives the asymmetry of the etch-pits when they are tilted by a certain angle φ for every angle of the facets with the surface normal. The values are only meaningful between 0 (symmetric, $a_2 = a_1$) and 1 (totally asymmetric, $a_1 = 0$ or $a_2 = 0$), *i.e.* the range within which an etch-pit is visible on the surface. Besides being a purely analytical expression for the shape of the etch-pits, equation (3.3.1) also contains an important piece of information: the higher the off-axis angle, the closer the etch-pit facets must be to 45° in order to be visible on the surface. For example, for 1° off-axis surface, etch-pits with a facet angle down to 1° will still be visible; for 20° off-axis surface, etch-pits must have at least 20° in order to be visible. **Figure 3-19** shows exactly this point: for each off-axis angle, the curve shows which χ values are allowed (visible). This fact poses constraints to the etching parameters, depending on the surface characteristics. The best strategy is, therefore, to avoid conditions which produce shallow pits.

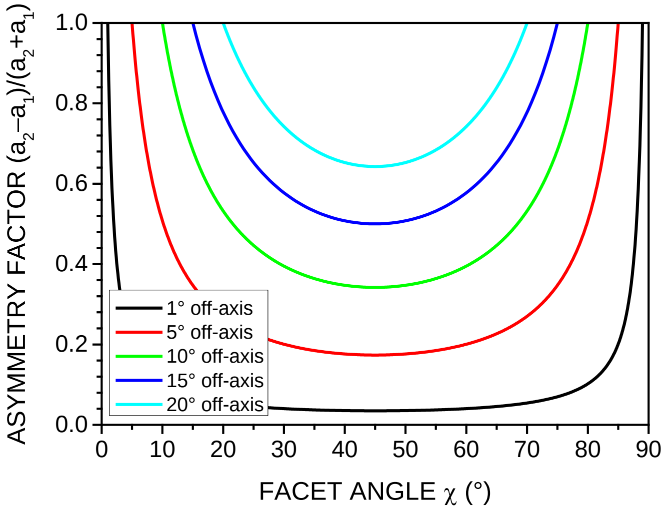

Figure 3-19: Asymmetry factor for different tilt (off-axis) angles, φ, for all possible facet inclinations, χ. A value of 0 corresponds to a perfectly symmetric (square) etch-pit, while values equal to 1 correspond to totally asymmetric etch-pits (one facet is perpendicular to the surface).

3.3.3.6 *Dependence of etch-pit shape on process temperature*

Apart from investigating etch-pit formation by varying the gas composition, further experiments were carried out to look for temperature- and pressure-dependent behaviour on the formation and shape of the etch-pits. Two experimental series at different etching regimes were explored:

a) Etching at 50 mbar with 200 ppm TMB in H_2 in reactor #1 (the same conditions used in section 3.3.3.3), at different temperatures (between 650-925 °C), for 1 hour;

b) Etching at 150 mbar with 1% CO_2 in H_2 in reactor #3 (no B background), at different temperatures (between 700-1100 °C), for 20 minutes.

The samples used in each experimental series were grown for 2 hours with 100 ppm N_2 added to the process gas, with 10% CH_4 in H_2, followed by 30 min growth without N_2, to a total thickness of ~100±5 µm thick. The structure remains the same[5] as "sample type 1" in **Figure 3-11**. The samples were then etched under the conditions described above, followed by AFM measurements of their surface profiles. Several etch-pits per sample were selected for line scans parallel and perpendicular to the off-axis direction. The angles of the facets were then averaged and plotted as a function of the temperature in **Figure 3-21**.

The two extreme samples from the 150 mbar series can be seen in **Figure 3-20**.

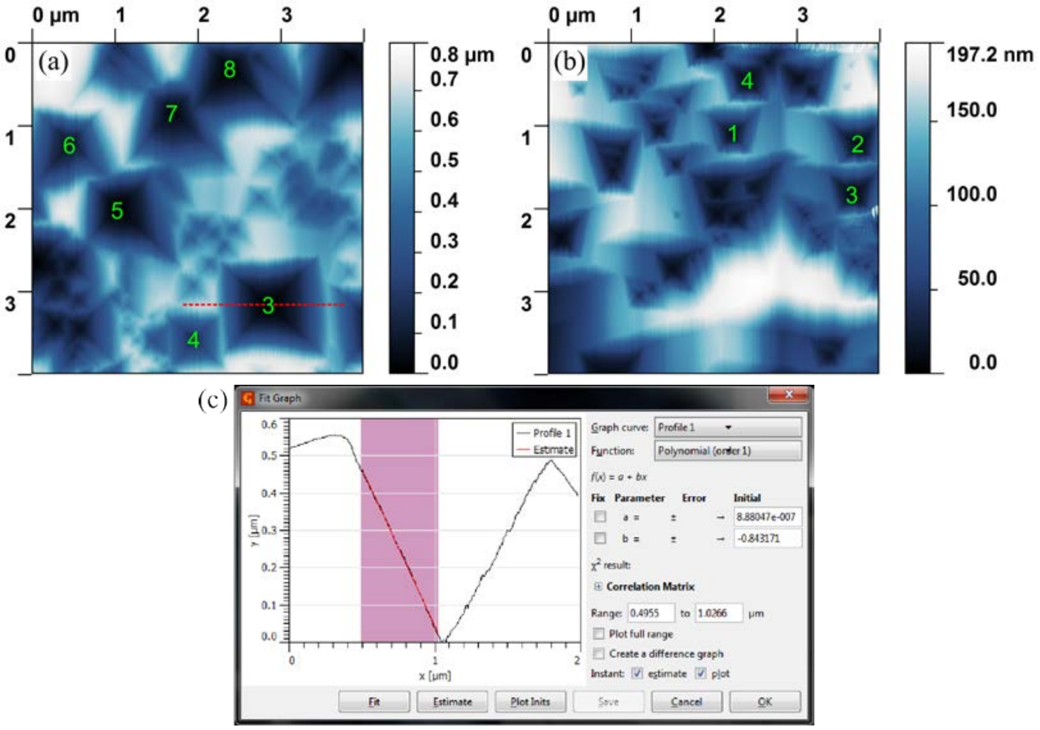

Graph curve: Profile 1

Function: Polynomial (order 1)

$f(x) = a + bx$

Fix	Parameter	Error	Initial
☐	a =	±	→ 8.88047e-007
☐	b =	±	→ -0.843171

χ^2 result:

⊞ Correlation Matrix

Range: 0.4955 to 1.0266 µm

☐ Plot full range

☐ Create a difference graph

Instant: ☑ estimate ☑ plot

Figure 3-20: AFM images of the etched samples from the 150 mbar series, etched respectively at (a) 700 °C and (b) 1100 °C. An illustrative line scan of the etch-pit 3 from (a) is shown in (c).

---

[5] The substrates used for the etching series a) and b) were, respectively, 4° and 6° off-axis along [110].

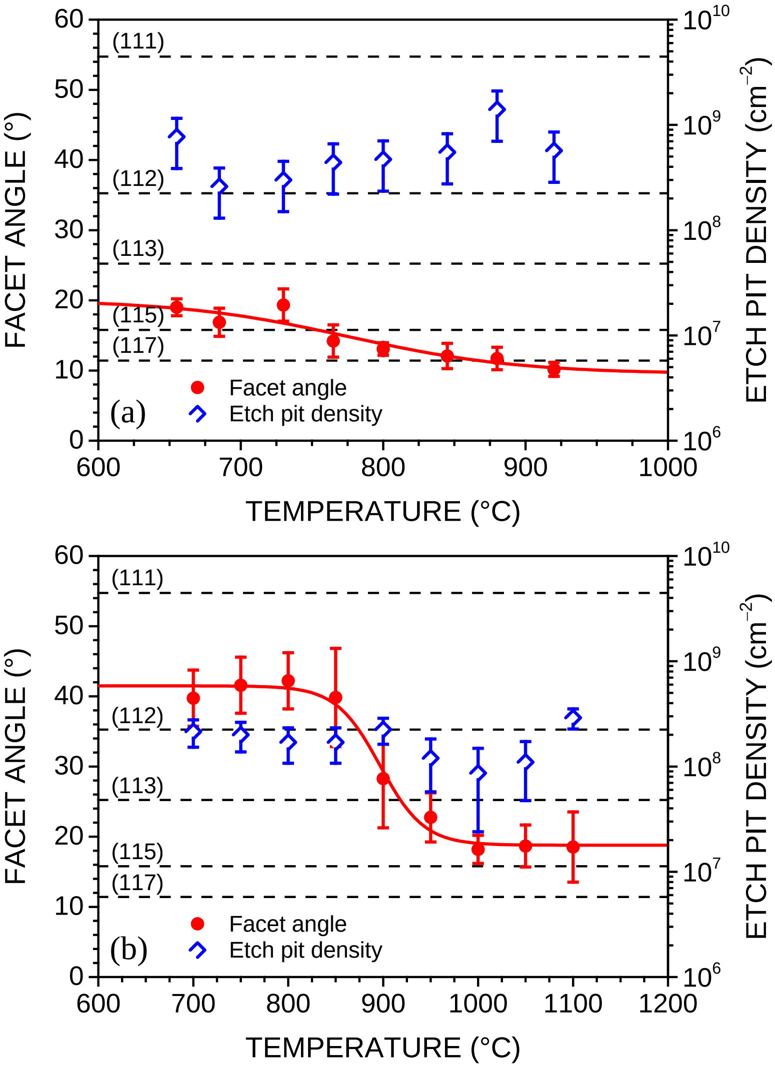

Figure 3-21: Temperature dependence of the facet angle of the etch-pits (left axis) and the etch-pit density (right axis) at (a) 50 mbar, 200 ppm TMB in H_2 for 1 hour; and (b) 150 mbar, 1% CO_2 in H_2 for 20 minutes. The facet angle *vs.* temperature curves were fitted to a sigmoid-type function, yielding $R^2 = 0.8739$ for (a) and $R^2 = 0.9884$ for (b).

One can see from the results above, that for very different pressure regimes there is a clear temperature-dependent trend for etch-pit formation: the higher the temperature, the shallower the etch-pits. Whereas at 50 mbar the facet angle varied within roughly 10° between 650 and 925 °C, at 150 mbar the facet angle varied by roughly 25° between 700 and 1100 °C. In the 50 mbar case it is hardly possible to make a statement concerning having defined crystallographic facets instead of arbitrary angles, due to the inaccuracies involved in the measurements. But the 150 mbar etching regime showed a quite remarkable result: a sharp transition at about 900 °C (see **Figure 3-21**) from near $\langle 112 \rangle$ to near $\langle 115 \rangle$ facet angles, which is further evidence of etch-pits exposing defined crystallographic facets. Such transition is more difficult to observe in the 50 mbar case due to experimental uncertainties, and due to the higher index facets being closer to each other. However, a faint transition can still be distinguished.

Our results have to be compared with a report by J. Achard *et al.* [49] where it was found that etch-pits are comprised of $\{113\}$ facets, and that evolution of $\{111\}$ facets was prohibited by the stability criterion for etch-pit formation (equation (1.5.1)). However, their chosen etch parameters were restricted to ~850 °C at 200 mbar with 2% O_2/H_2 in the gas phase. Considering our temperature series at 150 mbar, which has conditions more comparable[6] to the above report, we have shown that, 1) in fact, the exposure of $\{113\}$ facets is not a universal property of etch-pits formed by O_2/H_2 plasma etching; 2) the conditions for the evolution of $\{113\}$ facets are the narrowest; 3) the evolution of either lower or higher index planes can be stabilised by the appropriate process temperatures. Furthermore, considering also our temperature series at 50 mbar, we have shown that process pressure plays a significant role in defining the range of allowed crystallographic facets which can develop in the etch-pits. At 50 mbar $\{113\}$ facets are not formed.

Comparing the etching with 1% CO_2 at 150 mbar with the 50 mbar case from section 3.3.3.2 at ~740 °C, there is an evident difference in terms of etch-pit shape: at 150 mbar all etch-pits are inverted square pyramids aligned along $[110]$, while in the 50 mbar case sparse, 8-fold etch-pits developed on the undoped sample alongside pre-existing, smaller $[110]$ etch-pits from the previous pure H_2 etching step. The first conclusion from this observation is that etch-pit shape is also a function of pressure. The second conclusion is that the selectivity of the etch process is also controlled by the process pressure, *i.e.* different types of dislocations may only result in the formation of etch-pits with distinguishable features at specific pressure ranges.

Reports on GaN and SiC show a clear correlation between etch-pit size and type of dislocation [57, 58]. The formation of larger pits is attributed to dislocations having a larger Burgers vector and, therefore, higher elastic energy[7] than smaller ones. In diamond, since typically the Burgers vectors belong to the $a/2\langle 110\rangle$ family, the most likely cause for different shapes and sizes is the orientation of the dislocation line relative to its Burgers vector, *i.e.* whether the dislocation is pure edge-, pure screw-, or mixed-type. In a recent report, Sawabe *et al.* [59] correlate etch-pit facet angles on heteroepitaxial diamond with dislocation type. In general, 45° mixed-type dislocations produced larger etch-pits than pure edge dislocations, which is consistent with the above discussion. However, only four etch-pits were analysed, which adds to the uncertainty of the results.

Still on the two temperature-dependent series presented here, the different gas composition between the 50 mbar and the 150 mbar etching series, *i.e.* the former with TMB and the latter with CO_2, must also not be neglected. It is clear from **Figure 3-22** and **Figure 3-20** that the process with TMB leads to an earlier loss of selectivity as the process temperature increases, pointing to stronger

---

[6] The etch conditions of the above report are comparable in terms of pressure and temperature, but the choice of gas composition results in a more aggressive etching, because of the relative amount of O/H in the gas phase. The concentration of atomic oxygen in our process is 4 times lower.

[7] The elastic energy of a dislocation is directly proportional to the square of the Burgers vector.

overall etching. This finding further supports that B in the gas phase enhances etching, as first described in section 3.3.3.3.

It was found as a general trend in all cases that as the temperature increases, the surface roughens. Nevertheless, within the investigated temperature ranges, and considering all the experimental and statistical errors involved, the etch-pit densities remained fairly stable, *i.e.* within a single order of magnitude (see **Figure 3-21**). The averaged results are plotted together with the previous etch-pit data in **Figure 3-16** (orange data points).

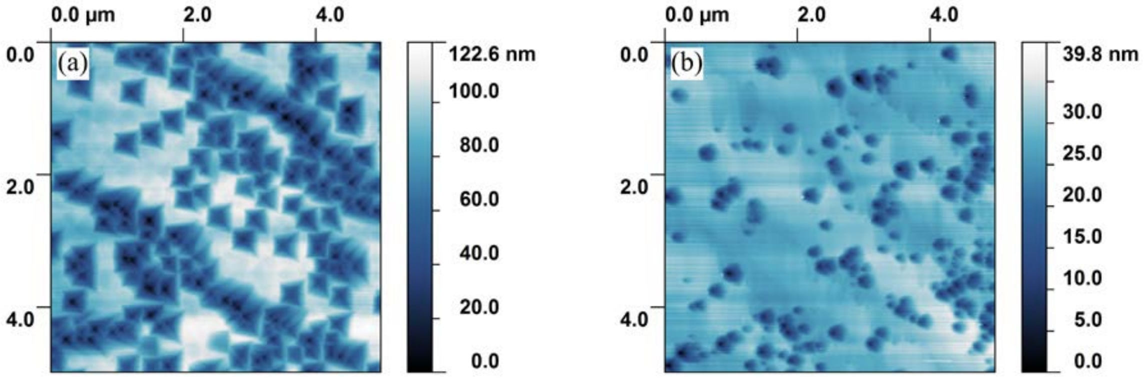

Figure 3-22: AFM pictures of samples etched at 50 mbar with 200 ppm TMB in H_2, respectively at (a) 665 °C and (b) 920 °C. From low to high temperature there seems to be an increased overall etching of the surface, causing the etch-pits to be less pronounced, leading to lower etch selectivity.

After the broad survey of etching parameters presented here for the identification of dislocations in heteroepitaxial diamond films, we proceeded with a deeper investigation of dislocations present in our B-doped films, in order to understand their local features, the influence that B has on their formation/propagation, and to confirm their correlation with etch-pits. These studies are presented in the following.

3.4 Direct imaging of boron segregation at dislocations in heteroepitaxial B-doped diamond

3.4.1 Introduction

High density of dislocations, which is inherent to heteroepitaxial diamond, is expected to strongly influence the transport of charge carriers in the material by acting as scattering or trapping centres, and to influence as well the incorporation and distribution of dopants, as observed in other semiconductors [60-63]. Boron-doping of diamond, which is particularly important for the fabrication of diamond-based electronic devices (as discussed in more detail in chapter 5), is known to reduce charge carrier mobility (**Figure 1-15**) and to induce lattice expansion and introduction of misfit dislocations [24] when incorporated in very high concentrations, as discussed in section 3.2. However, a more detailed picture of the local environment of B dopants in the lattice is still lacking. The knowledge of how B incorporation is affected by the dislocations present in the diamond, and equally the knowledge of how dislocations are influenced by this dopant, are important aspects for the understanding of the properties of the material and for its future improvement, and therefore need to be investigated.

In a recent work, the distribution of boron dopants in HPHT diamond was found to significantly influence the superconducting properties of B-doped diamond [64, 65]. Previous studies by S. Turner *et al.* have also shown that defects such as twin boundaries and stacking faults in B-doped diamond can be enriched with boron [20], due to the relaxation of the local lattice parameter at these locations [22]. As dislocations are characterised by having a strain field around their cores, which could then facilitate B incorporation in a similar way as the defects mentioned above, the dislocation-rich nature of heteroepitaxial diamond offers the ideal conditions for the study of how this dopant interacts with dislocations. The results of such investigation may provide further insights into growth, doping and into the mechanisms of dislocation propagation, which may ultimately influence device performance.

For this purpose, a thin heavily B-doped diamond layer was grown by MWPCVD homoepitaxially on an undoped heteroepitaxial diamond substrate grown on the Ir/YSZ/Si(001) stack. In a first step, the density and nature of the dislocations in the film was investigated by conventional TEM and weak-beam, dark-field transmission electron microscopy (WBDF TEM) techniques. Threading dislocations propagating from the substrate through the B-doped layer, as well as new dislocations formed at the interface between the two layers, were analysed. A correlation between threading dislocations and etch-pits formed on the surface was also established. In a subsequent step, the presence and distribution of boron in the film was studied using a combination of annular dark-field (high-resolution) scanning transmission electron microscopy (ADF-STEM) and spatially resolved electron energy-loss spectroscopy (STEM-EELS), performed with a state-of-the-art aberration-corrected TEM instrument at the University of Antwerp.

3.4.2 Experimental

This work was a result of a close collaboration with the group of Dr. Stuart Turner from the University of Antwerp. Heteroepitaxial diamond samples were prepared in our facilities and the TEM sample preparation and characterisation were performed in Antwerp.

3.4.2.1 Sample growth

The diamond samples were grown by MWPCVD in two steps on top of a Ir/YSZ/Si(001) substrate with an off-axis angle of 6° towards the $\left[-110\right]$ direction. The first step consisted in growing a ~1 mm thick diamond (the first half with 20 ppm N_2 added to the gas phase and the second half without), as illustrated in **Figure 3-23** (a). Next, the Ir/YSZ/Si(001) was removed from the diamond sample and its dislocation-rich backside was mechanically polished (several tens of microns of diamond were removed), followed by cleaning in hydrogen plasma (**Figure 3-23** (b)). Subsequently, a 1-2 µm thick heavily B-doped layer was grown by MWPCVD on this side of the diamond, with addition of 980 ppm trimethylborane (TMB) to the gas phase and 2% CH_4 , *i.e.* $[B/C]_{gas} = 42763$ ppm (**Figure 3-23** (c)). The backside was chosen as growth substrate for the B-doping process in order to guarantee a higher number of dislocations in the electron transmittable area of the TEM samples. Finally, a short hydrogen plasma etching step was carried out to produce etch-pits on the diamond surface.

The preparation of the Ir/YSZ/Si(001) substrate followed standard procedures described before in this chapter (see section 3.2.3.1).

3.4.2.2 Sample preparation and TEM experiments

The samples for TEM investigation were prepared using a focussed ion beam lift-out procedure, carried out in a FEI Helios FIB/SEM instrument. In order to view etch-pits in plan-view, the samples were cut relatively close to the film surface, as illustrated in **Figure 3-23** (d). For the study of single dislocations in plan-view, FIB plan-view lamellae were sliced from deeper into the B-doped diamond film (approximately 500 nm into the film).

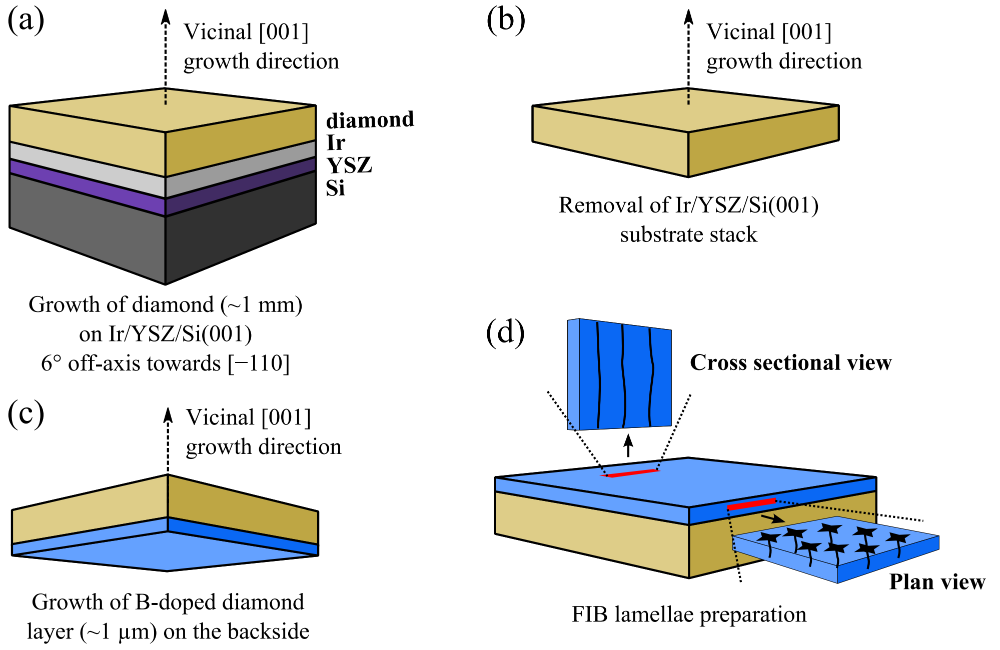

Figure 3-23: Illustration of the sample preparation: (a-c) sample growth steps. (d) Diagram showing the plan-view and cross-sectional FIB preparation geometries.

Bright-field (BF) and WBDF TEM images were acquired in a FEI Tecnai microscope operated at 200 kV. Aberration-corrected high-resolution TEM imaging was performed in a FEI Titan "cubed" microscope operated at 300 kV and equipped with both TEM and STEM aberration correctors. Aberration-corrected TEM imaging was performed under negative C_s conditions (C_s tuned to −12 μm). Aberration corrected ADF-STEM imaging was performed in the same microscope, operated at 300 kV. The convergence semi-angle α was 21 mrad, the ADF inner acceptance angle β and EELS acceptance angles were both 28 mrad. Quantification of B/C (boron-to-carbon) ratios was performed with the Gatan Digital Micrograph (DM) software package, using Hartree-Slater cross sections. Fourier filtering of the high-resolution images was performed by masking the lattice reflections in a Fourier transform pattern, and then back-transforming it to yield the filtered image. This filtering was also performed with the digital micrograph (DM) software package.

3.4.3 Results and discussion

First a general survey of the B-doped sample was performed by taking BF-TEM and STEM images of the prepared lamellae in plan-view and cross section. They are shown in **Figure 3-24** (a-c).

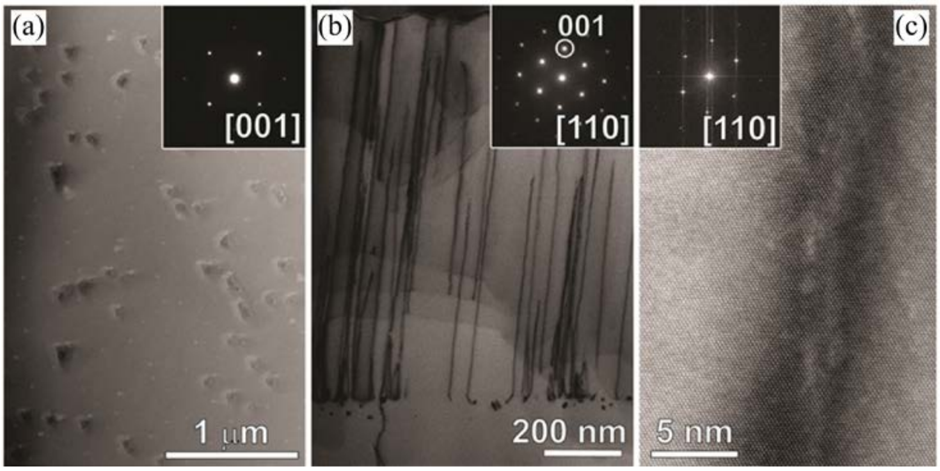

Figure 3-24: (a) Plan-view TEM image overview showing etch-pits at the surface. (b) Cross-sectional TEM image overview showing dislocations in the film. (c) HR ADF-STEM cross-sectional image taken along the $[110]$ zone axis showing a single dislocation. The diffraction patterns in the inset of each image confirm their orientation and the single crystallinity of the samples.

Figure 3-24 (a) is a plan-view overview image of a dislocation-rich sample, showing etch-pits on the surface which were generated after a short H_2 plasma etching step under high B background from the reactor. Each etch-pit is expected to be associated with a threading dislocation.

In **Figure 3-24** (b) an overview BF-TEM image of the diamond film in cross-section is displayed. The diffraction pattern in the inset confirms that the material is monocrystalline diamond viewed along the $[110]$ zone axis. The interface between the undoped diamond substrate and the B-doped layer can be seen at the lower part of the image, lying close to the (001) plane. Looking more closely, the diffraction pattern demonstrates that, in fact, as a result of the (nominal) 6° off-axis angle of the Si growth substrate, the additional tilt typically occurring at the diamond/Ir interface [66] and the further polishing step, the $[001]$ growth direction is slightly tilted with respect to the interface between the two layers by approximately 7-8°. Many dislocations (dark-contrast lines) can be seen arising mostly from the interface. They are visibly parallel, following the $[001]$ direction and the majority of them threads all the way through the entire film thickness of the film.

In **Figure 3-24** (c), a bright-field high-resolution scanning transmission electron microscopy image shows a single dislocation in cross section. It is clear from the image that, at an atomic level, the dislocation is not straight, displaying rather a local wavy structure while keeping an overall $[001]$ direction.

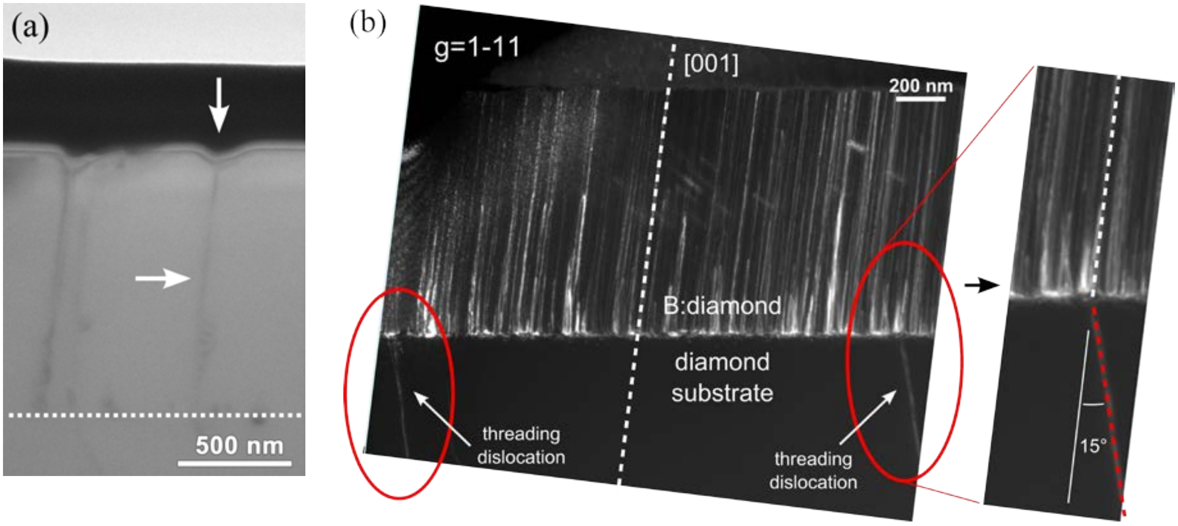

Figure 3-25: Cross-sectional TEM images of the interface between the undoped diamond substrate and the B-doped layer, highlighting: (a) threading dislocations in the B-doped diamond ending at etch-pits. Note also the asymmetry of the etch-pit, which is in accordance with the model from **Figure 3-18** considering a tilt of 7-8°; (b) threading dislocations from the undoped substrate (grown with 20 ppm N_2) propagating through the B-doped layer. Several dislocations generated at the interface formed closed loops with adjacent dislocations and ceased to propagate before reaching the surface.

Figure 3-25 shows cross-sectional (a) BF and (b) WBDF images of dislocation-rich samples. In the first image, two dislocations can be seen arising at the surface (one starting at the interface, the other one threading through from the substrate), each one ending at an etch-pit. This is a clear confirmation that etch-pits are indeed formed where dislocations are present, supporting the previous etch-pit investigations in section 3.3. In **Figure 3-25** (b), individual dislocations can be seen more clearly. Many of them are generated at the interface between the undoped diamond substrate and the B-doped layer. Some dislocations propagate through from the substrate, changing their direction once in the B-doped layer, from ~15° to 0° relative to the $[001]$ direction. Many dislocations thread through to the surface, while others, which appear to originate in pairs, form closed loops and cease to propagate.

The formation of new dislocations at the interface can be attributed here to two major facts: 1) polishing-induced defects generated prior to deposition of the B-doped layer and 2) lattice mismatch between the undoped substrate and the heavily B-doped layer. The pronounced tilting of dislocations away from $[001]$ direction in heteroepitaxial diamond grown on off-axis substrates with addition of several 10 ppm N_2, similar to the present substrate, was also reported by our group in another publication [55]. In that report, nitrogen-free growth on off-axis substrates was also studied, albeit the dislocations in the samples showed smaller inclinations and a pronounced variation in tilt angles. Here we now find a third variant, where despite the appreciable off-axis angle during growth of the B-doped layer, the dislocations strictly followed the crystallographic $[001]$ direction.

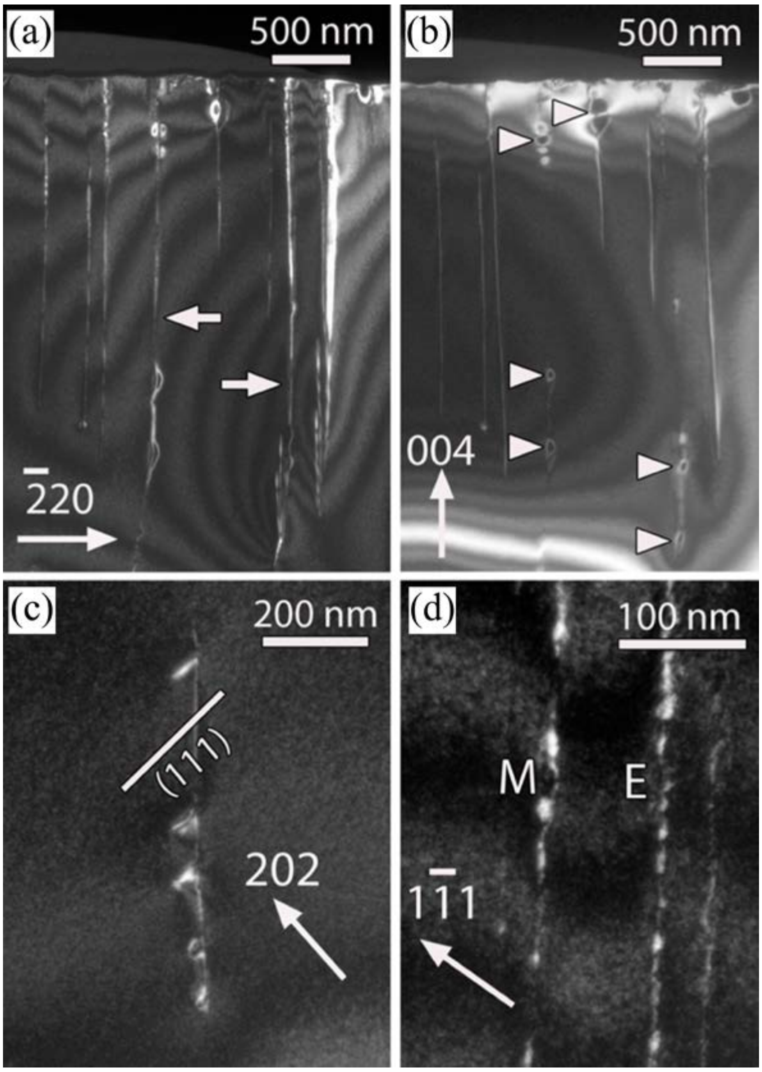

Figure 3-26: Weak-beam dark-field TEM characterisation of the $[001]$ dislocations in FIB lamella cut along (110) (a, b, d) and along (010) (c). In (a) and (b) images obtained with, respectively, $g = \bar{2}20$ and $g = 004$, are shown. Edge dislocations with $\vec{b} = a/2[1\bar{1}0]$ are marked by white arrows in (a). They are invisible with $g = 004$. The dislocations which are visible in (a) and also in (b) are 45° mixed dislocations (see supplementary information in section 7.1). Note in (b) the presence of loops (white arrowheads) on both edge- and 45° mixed-type dislocations. In (c) an image taken with $g = 202$ shows loops parallel to the projection of the trace of the (111) plane. This projection is indicated by a solid white line. In (d) an image taken with $g = 1\bar{1}1$ shows interrupted diffraction contrast on edge- "E" and 45° mixed-type "M" dislocations.

In order to study the nature of the dislocations present in the boron doped diamond film, weak-beam dark-field TEM technique was applied. With this technique, the Burgers vector of dislocations can be identified based on the invisibility criterion $\vec{g} \cdot \vec{b} = 0$, and also the near-core properties of the dislocations can be revealed. Typically, dislocations in CVD diamond have Burgers vectors $\vec{b} = a/2\langle 101\rangle$.

The presence of mixed-type and pure edge dislocations in diamond have already been reported in the literature [55, 67]. In the present study, different extinction conditions (see the details and acquired dark-field images as supplementary information in section 7.1) have shown that both edge- and 45° mixed-type dislocations with lines along $[001]$ are present in the B-doped film. They can be clearly seen in the WBDF images of a FIB lamella cut along the (110) plane, which were taken with $g = \bar{2}20$ and $g = 004$ and shown respectively in **Figure 3-26** (a, b). The 45° mixed-type dislocations appear in both images, while the pure edge-type ones only appear in (a). Upon a closer examination, some of the dislocations appear accompanied by loops, which are indicated by the white arrowheads in the WBDF image in **Figure 3-26** (b). In most cases, such loops display a diffraction contrast parallel to the projection of the trace of the $\{111\}$ planes of the diamond lattice, as shown in **Figure 3-26** (c) for a FIB lamella cut along the (010) plane. This indicates that the loops consist of planar defects lying in $\{111\}$ planes and probably caused by B incorporation. Taking a closer look at the dislocations using higher magnification (**Figure 3-26** (d)), a peculiar feature can be observed: both edge- and 45° mixed-type dislocation lines do not display a solid, uninterrupted diffraction contrast, but rather an intermittent one, which is attributed to clustered segregation of boron at the dislocations. The observation of edge- and 45° mixed-type dislocations along $[001]$ in this work is in agreement with a previous report by Gaukroger *et al.* on homoepitaxial diamond grown by MWPCVD [67]. Finally, the samples analysed by WBDF have yielded a dislocation density in the range of 2×10^{10} cm^{-2}, which is coherent with the fact that the dislocation-rich backside of the undoped diamond substrate was used, and with the observation that many new dislocations were generated at the interface between the undoped and B-doped layers.

In order to measure the distribution of boron incorporated in the B-doped diamond film, a combination of scanning transmission electron microscopy (STEM) and electron energy-loss spectroscopy (EELS) was adopted. In a first experiment, a single dislocation was scanned using spatially resolved EELS. In this technique, the fine electron probe is scanned over the sample, acquiring an EELS spectrum in every scanned point. Each acquired spectrum contained both the boron and the carbon K-edges. An ADF-STEM overview image of the studied dislocation is shown in **Figure 3-27** (a), while a typical EELS spectrum acquired from the sample is displayed in **Figure 3-27** (f).

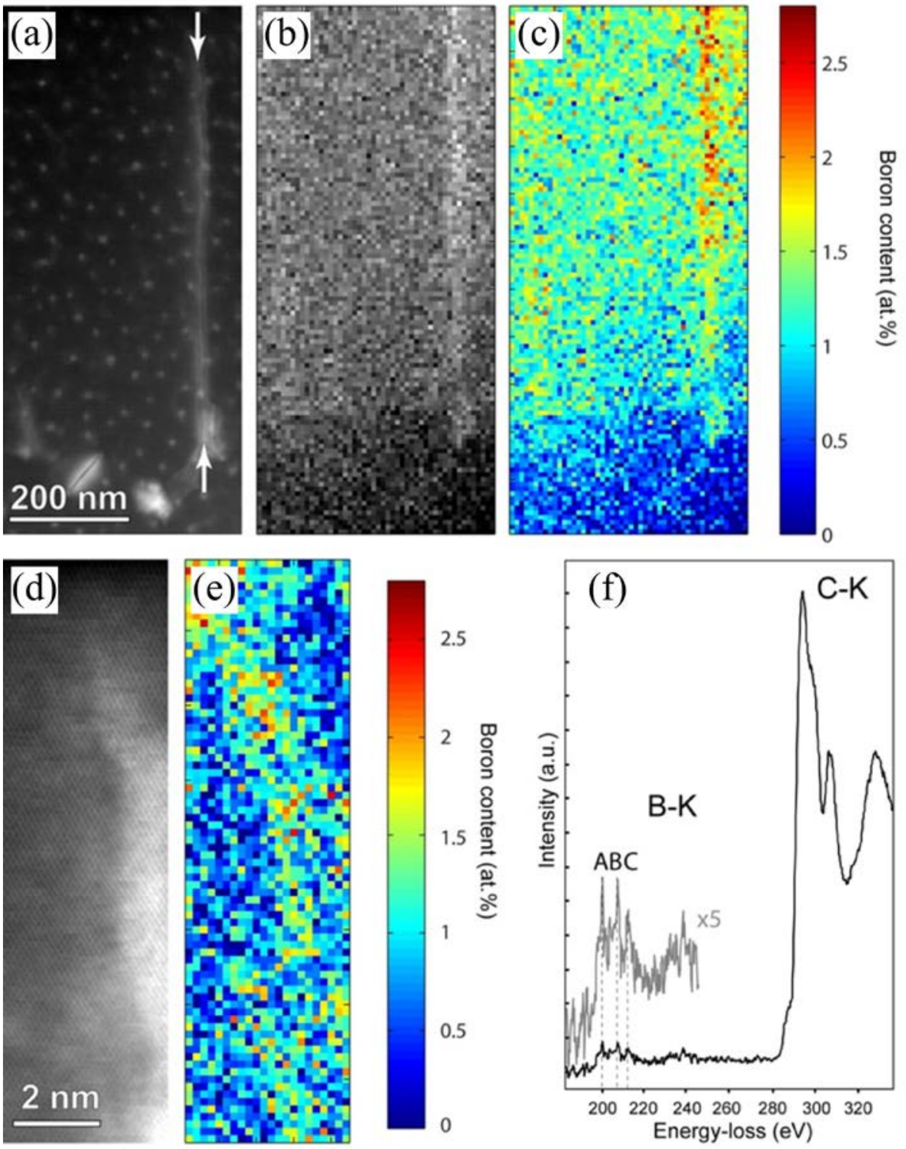

Figure 3-27: Detection of boron by EELS. (a) Overview ADF-STEM image showing a single dislocation indicated by the two arrows. (b) Boron K-edge map showing segregation of B at the dislocation. (c) Map of the B/C ratio in the dislocation showing boron enrichment up to 2.5 at.%. (d) HR ADF-STEM image of a single dislocation and its corresponding B/C ratio map shown in (e). The width of the B-enriched region is approximately 2 nm. (f) EELS spectrum from a pristine diamond area, showing the boron K-edge at 190 eV and the carbon K-edge at 285 eV.

Upon first inspection of the EELS spectrum, the presence of a strong carbon K-edge at 285 eV and also of a weak boron K-edge at around 190 eV becomes clear. The fine structure of the carbon K-edge is typical of diamond, with a large σ^* contribution at 292 eV. The small π^* contribution at 285 eV can be attributed mostly to surface amorphisation during sample preparation. However, a contribution from the dislocations cannot be excluded, as their cores may contain carbon with distorted and/or dangling bonds [20, 22]. The boron edge at 190 eV shows three distinct sub-peaks, A, B and C, which are typical signatures of tetrahedrally embedded boron in diamond, as will be discussed further below.

By integrating the intensity of the boron K-edge at each scanned point, a quantitative map of incorporated boron was produced, as shown in **Figure 3-27** (c). It can be seen that, even though a boron signal is measured across the whole B-doped diamond film, the dislocation itself shows a higher B concentration. A boron background signal of 1~1.5 at.% was measured, which is in good agreement with the expected[8] incorporated $\mathrm{B/C}$ ratio based on the process gas composition during growth, and taking into account the incorporation efficiency determined earlier in section 3.2.4. At the dislocation, the boron signal rises to approximately 2.5 at.%, although this number is expected to be much higher due to the fact that a single dislocation does not fill the full sample thickness, meaning that the EELS signal at the dislocation also carries a contribution from the background $\mathrm{B/C}$ ratio, which is lower.

Further measurements at higher resolution are presented in **Figure 3-27** (d, e). The STEM-EELS images show similar results as before: the projected $\mathrm{B/C}$ ratio along the dislocation can reach up to 2.5 at.%. The EELS map also allows the measurement of the width of the boron-rich dislocation, which was found to be ~2 nm. This result is in good agreement with the magnitude of strain field around the dislocation, which was measured later (**Figure 3-28** (e, f)). Finally, the high-resolution scan also confirms the observation from the previous dark-field images that the boron enrichment along the dislocation line is not constant, but rather intermittent.

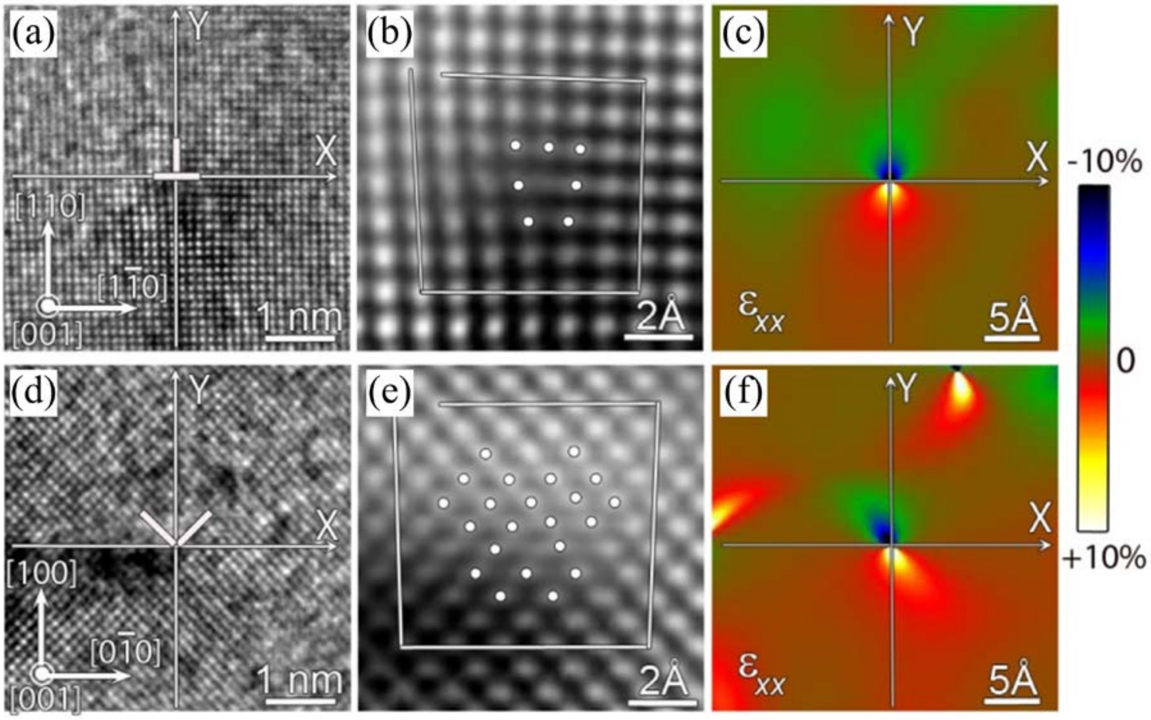

Figure 3-28: High-resolution characterisation of dislocations in the B-doped diamond film imaged in plan-view along the $[001]$ zone axis. Images (a-c) correspond to an edge-type dislocation, while images (d-f) correspond to a mixed-type dislocation. Images (a, d) are HRTEM images; (b, e) Fourier-filtered images of the respective cores; (c, f) GPA map of the dislocations showing the strain field around the core. The colour scale indicates the strain ε_{xx} and the origin of *x*-axis and *y*-axis was set at the core of the dislocation. The white dots in (b, e) indicate the atom column positions.

---

[8] $[\mathrm{B/C}]_{\mathrm{gas}} = 42763\ \mathrm{ppm}\ \times 20\%\ (\mathrm{incorporation\ efficiency}) \approx 0.9\%$.

Next, the two types of dislocations present in the B-doped diamond film were investigated at high-resolution. **Figure 3-28** (a) and (d) show aberration-corrected HRTEM images of, respectively, single edge- and 45° mixed-type dislocations, viewed along the $[001]$ zone axis (*i.e.* in plan-view). These images were taken under so-called negative C_s imaging conditions (C_s was set to $-12\ \mu m$). Under these conditions, enhanced contrast can be achieved for light elements by balancing a positive defocus to a negative spherical aberration coefficient [68]. HRTEM image simulations indicate that under this slight overfocus (close to the optimal Scherzer defocus of +6 nm), the carbon atomic columns in the structure can be imaged as white contrast on a dark background. From the knowledge of the contrast transfer of the microscope through image simulations, it was then possible to indicate the positions of the atomic columns in the images of **Figure 3-28** (a, d). By Fourier-filtering these images, the core of the dislocations was evidenced, as shown respectively in **Figure 3-28** (b, e).

Upon analysis of these images, it can be seen that the edge dislocation consists of a single extra $\{110\}$-type half-plane, which appears in **Figure 3-28** (a, b) inserted from the top. The structure of the core strongly resembles the zig-zagged $\langle 100 \rangle$ edge-type dislocation core reported by Fujita *et al.* [69]. The strain field surrounding this dislocation was mapped using the so-called geometrical phase analysis (GPA) approach, a method developed by Hÿtch *et al.* which allows a quantitative mapping of the variations of interatomic distances [70]. The GPA corresponding to the edge dislocation[9] is shown in **Figure 3-28** (c). There, the strain was defined relative to the bulk region away from the dislocation core, where the strain is assumed to be zero. The magnitude of the strain ε_{xx} is shown in the colour scale and the origin of the *x*-axis and *y*-axis was set at the core of the dislocation. It becomes clear from the image that the insertion of an extra $\{110\}$-type half plane induces compressive strain in the lattice, while tensile stress develops on the opposite side.

The second type of dislocation found in the film, the 45° mixed-type, was analysed in a similar manner as the previous. A high-resolution image of one exemplar is displayed in **Figure 3-28** (d). Upon analysis of the image, the differences from the edge-type dislocation become evident, even more so after Fourier-filtering (**Figure 3-28** (e)): the 45° mixed-type dislocation is characterised by two $\{110\}$-type half-planes, at an angle of 90° relative to each other, being inserted into the structure (from the top in the image) towards the dislocation core. To the best of our knowledge, this is the first direct visualisation of a mixed-type dislocation in diamond, and the observed structure appears to coincide well with predictions by Fujita *et al.* from density functional theory calculations [71]. The tensile and compressive strain fields surrounding the core of the 45°-type dislocation are shown in the GPA map of **Figure 3-28** (f), which results similar to the strain field observed for the edge-type dislocations when the visible distortion caused by neighbouring dislocations is considered.

In a final experiment, a single edge-type dislocation was investigated using spatially resolved EELS, in order to precisely locate the region of boron segregation with respect to the dislocation core. An edge-type dislocation was chosen for this analysis due to greater stability under electron irradiation than the mixed-type. **Figure 3-29** (a) shows an aberration-corrected ADF-STEM image of a single edge-type dislocation in plan-view, *i.e.* along the $[001]$ zone axis. The Fourier-filtered image in

---

[9] The GPA treatment was performed on raw data, not on the Fourier filtered data.

Figure 3-29 (b) highlights the insertion of an extra $\{110\}$-type half plane into the diamond lattice, from the right in the image. After ADF-STEM imaging, the region marked by the white rectangle in **Figure 3-29** (a) was fine-scanned for the simultaneous acquisition of an ADF-STEM image and an EELS map containing both the boron K- and the carbon K-edge. In this way, the exact location of the dislocation in the EELS map can be determined. **Figure 3-29** (c) shows a map of the boron distribution surrounding the dislocation, evidencing the boron enrichment close to the dislocation core as expected from the cross-sectional experiments. In **Figure 3-29** (d) the boron signal (green) is overlaid on top of the simultaneously acquired ADF-STEM data (purple), with a white "T" marking the position of the dislocation core. It becomes clear from this image that boron is not symmetrically distributed around the dislocation, but is rather segregated in the region of tensile strain (left side of the core in the images). This result is, however, not unexpected, since tensile strain may accommodate more easily the insertion of extra boron atoms either substitutionally or interstitially into the diamond lattice. A similar observation from EDX measurements of indium-enriched dislocations in InGaN has been recently reported by Horton *et al.* [72].

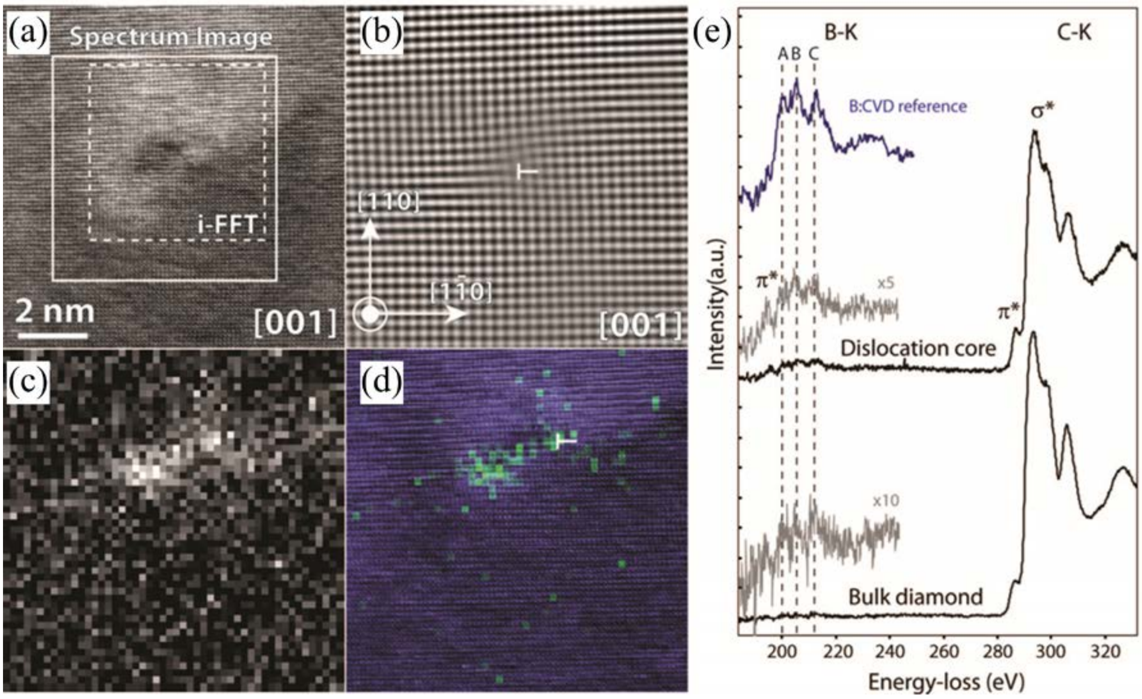

Figure 3-29: Spectroscopic investigation of a single edge-type dislocation. (a) Overview ADF-STEM image of a single edge dislocation; (b) Fourier-filtered image of the dislocation core (marked by a "T"), showing the insertion of an extra half-plane. (c) Boron K-edge (EELS) map showing boron enrichment close to the dislocation core. (d) Overlay of the boron K-edge map with a simultaneously acquired HAADF-STEM image. The dislocation core is highlighted by a "T". Boron (green colour) segregates in the region of tensile stress surrounding the dislocation. (e) EELS spectra containing the boron K- and carbon K-edges. The boron signal in the dislocation core is clearly higher than in the bulk. A fine structure reference for tetrahedrally embedded boron in diamond is plotted in blue.

Finally, interesting information can be derived from the fine structure of the boron K-edge at the dislocation core. In **Figure 3-29** (e), the two main curves in black show the boron K- and carbon K-edge averaged over two different spots: over the dislocation core and over a pristine region of the B-doped diamond film. A reference spectrum (top curve) was added for comparison. It shows the presence of three typical sub-peaks A, B and C, which have been previously measured in both CVD and HPHT B-doped diamond, and subsequently correlated with simulations from density functional theory in order to prove their correspondence with substitutionally embedded boron in diamond [21, 65, 73].

Upon analysis of the spectra from **Figure 3-29** (e), one can see that those three sub-peaks also appear in the spectrum acquired at the dislocation core, confirming that at least a certain amount of boron close to the core is embedded tetrahedrally. However, a clear π^* contribution was also measured at 194 eV, indicating that a significant amount of boron close to the dislocation core is present in a lower coordination. This increased π^* contribution has been observed before by EELS at twin and grain boundaries, and is most likely arising from a higher presence of dangling and distorted bonds at these locations.

3.5 Conclusion and final remarks

In the first part of this chapter, growth of heavily B-doped diamond was carried out and investigated. B-doping at 50 mbar indicated a certain modification of the growth surface, which was evidenced by the disappearance of the riser/terrace microstructure present on the undoped substrate which is caused by nitrogen in the gas phase inducing step-bunching. Boron reverses the step bunching and facilitates a smooth step-flow growth, thus leading to a smoother growth surface. The mosaic spread was found to depend upon B incorporation: with higher B-doping, an improvement of the twist and a worsening of the tilt were observed. The twist roughly followed the trend previously seen for undoped film growth, where an improvement occurs with increasing film thickness. For the tilt, we assume that even if the B-doped layer starts to grow in a pseudomorphic way, the increasing elastic energy stored in the layer with progressive film growth will reach a point where relaxation takes place with insertion of misfit dislocations, or the tilt of dislocations in such way that “effective climb” causes a reduction in stress. These processes apparently increase the polar angular spread (tilt) and reduce the azimuthal spread (twist). Deposition of heteroepitaxial diamond films at 50 mbar showed strong temperature dependence for the generation of intrinsic stress, similar to previous observations for deposition at 200 mbar. In the present work we focussed on boron doping at a low temperature of ~720 °C where the appearance of twins and non-epitaxial crystallites was minimised and the compressive stress was maximal. The deposition experiments showed that the generation of intrinsic stress is rather enhanced than reduced by the presence of boron. SIMS, CL, and XRD data were compared for the evaluation of the boron concentration in the film: 1) XRD was found to be a reliable method at heavy B concentrations, $[\mathrm{B}] \geq 10^{20}\ \mathrm{cm}^{-3}$, due to the lattice expansion effect caused by B-doping, but with the condition that the biaxial stress in the film is taken into consideration. This is a crucial point for dislocation-rich diamond films, as we have demonstrated, and it requires the measurement of both the perpendicular and the parallel lattice constants from θ-2θ scans of the diamond (004) and (311) reflections; 2) the CL peak-shift method was fairly reliable at high to heavy B concentrations, $[\mathrm{B}] \geq 10^{19}\ \mathrm{cm}^{-3}$; 3) the CL peak-ratio method was not reliable at high/heavy doping regimes, as expected from the report by Barjon *et al.* [39]. This method has its strength at much lower boron concentrations, which facilitates a sensitive detection of boron down to, at least, $[\mathrm{B}] \approx 10^{14}\ \mathrm{cm}^{-3}$; 4) SIMS is an accurate and widespread technique to measure $[\mathrm{B}]$ in diamond films, with reported sensitivity ranges down to 10^{14} B cm^{-3}. With our setup, the best achieved sensitivity was only down to $10^{18}\ \mathrm{cm}^{-3}$, which is still relatively high. This fact, added to the destructive nature of SIMS measurements, required complementary techniques such as CL, XRD and, as will be shown in chapters 4 and 5, electrochemical and electrical techniques. By combining the results of all methods, an incorporation efficiency of roughly 20% for the range of high-heavy B-doping was determined, with the trend that it decreases with increasing precursor concentration in the gas phase.

In the second part of this chapter, focus was given to the identification of dislocations from selective etching. Undoped and B-doped diamond films were simultaneously etched under different conditions (namely varied gas composition, pressure and temperature) and the etch-pits formed on the surface were analysed. It was observed that distinct types of etch-pits evolve on the surface when increasing the $\mathrm{CO_2}$ concentration from 1% to 3%. Together with etch-pits of the $\langle 110 \rangle$ type with edges aligned along $[110]$ and $[-110]$, larger etch-pits of the $\langle 100 \rangle$ type with edges aligned along $[100]$ and $[010]$ also appear, possessing not only larger lateral sizes, but also steeper facets. In the absence of $\mathrm{CO_2}$, etching with $\mathrm{H_2}$ also produced etch-pits, although much smaller, showing lower selectivity. On the other hand, etching with $\mathrm{H_2}$ under a high B background promoted a more pronounced selective etching on both undoped and B-doped diamond, and with more homogeneous size distribution and a single etch-pit type. To the best of our knowledge, etching under high B background was never reported prior to this work. It also yielded a somewhat higher etch-pit count compared with the other methods, reaching $\sim 10^{9}\ \mathrm{cm}^{-2}$ for a diamond film thickness of ~40 µm, compared with values in the lower to mid $\sim 10^{8}\ \mathrm{cm}^{-2}$ with $\mathrm{CO_2}$.

For the asymmetric shape of the etch-pits, the tilting of the dislocations caused by off-axis growth was initially considered as one possible reason, since reports in the literature describe such behaviour [48]. However, a careful analysis of the etch-pit profiles by AFM finally proved that their side-walls can be fully described by the planes belonging to the $[110],[-110]$ or $[100],[010]$ zone axis, respectively. Their asymmetry is a simple geometric effect caused by the macroscopic off-axis angle. The latter observation was particularly clear when etching undoped diamond at 150 mbar as a function of temperature. From 700 °C to 1100 °C, a fast switch from (112) to (115) facet angles was observed at ~950 °C. As a general trend, etching at higher pressure tends to produce steeper etch-pits than etching at lower pressure, while lower temperature promotes steeper etch-pits. The simultaneous appearance of different types of etch-pits for specific sets of etching parameters suggests the possibility of different types of dislocations giving rise to etch-pits differing in size and shape. Further investigation of this hypothesis, *e.g.* by preparing a FIB lamella at the position of each type of etch-pit for a subsequent TEM analysis, will be left for a future work.

After concluding a general survey of etching parameters for the selective etching of dislocations, the third and final part of this chapter was dedicated to the direct visualisation and analysis of dislocations in heavily B-doped films by TEM. For this part, a thin film of heavily B-doped diamond was grown on the backside of an undoped diamond layer initially grown on the typical Ir/YSZ/Si(001) substrate stack. FIB lamellae were then prepared for plan-view and cross section. In a first step, the density and nature of the dislocations in the film were investigated by conventional and weak-beam dark-field transmission electron microscopy techniques. Several important observations were made: 1) threading dislocations in the B-doped film are aligned along $[001]$, both edge- and 45° mixed-type type with $\vec{b} = a/2\langle 110\rangle$; 2) dislocations from the undoped substrate which had an angle of ~15° relative to $[001]$ switched to 0° once propagating through the B-doped layer; 3) many new dislocations were formed at the interface between the undoped diamond substrate and the B-doped layer, likely due to defects induced by mechanical polishing and due to stress caused by the lattice expansion of heavily B-doped diamond, leading to a dislocation density of 2×10^{10} cm^{-2}; 4) many of the new dislocations formed at the interface were in pairs which eventually closed to form loops, ceasing to propagate before reaching the surface of the ~1 µm thick film. This indicated that they are nucleated in pairs with opposite Burgers vector; 5) etch-pits were accurately correlated with dislocations threading to the surface, confirming the concept of selective etching of dislocations applied in the second part (section 3.3). After characterisation of the dislocations in the film, the presence and distribution of B in the sample was studied using a combination of annular dark-field scanning transmission electron microscopy and spatially resolved electron energy-loss spectroscopy, performed on a state-of-the-art aberration corrected TEM instrument. Using these tools, the B concentration, its spatial distribution and the local B environment in this type of dislocation-rich diamond hetero-epitaxial film was determined. Boron enrichment at dislocations was clearly evidenced, which was shown not to be uniform, but intermittent along the dislocation line. Investigation of a single edge-type dislocation revealed a segregation of boron in regions with a tensile strain field surrounding the edge-type dislocations. The fine structure of the B K-edge at the core of an edge-type dislocation showed that the boron is partially substitutionally incorporated into the diamond lattice, and partially present in a lower coordination (sp^2-like hybridisation).

References

1. A. Aleksov, A. Denisenko, M. Kunze, A. Vescan, A. Bergmaier, G. Dollinger, W. Ebert, and E. Kohn; Diamond diodes and transistors. *Semiconductor Science and Technology*, 2003. **18**(3): p. S59. DOI: 10.1088/0268-1242/18/3/308.
2. H. El-Hajj, A. Denisenko, A. Kaiser, R. S. Balmer, and E. Kohn; Diamond MISFET based on boron delta-doped channel. *Diamond and Related Materials*, 2008. **17**(7–10): p. 1259-1263. DOI: 10.1016/j.diamond.2008.02.015.
3. Hiromitsu Kato, Kazuhiro Oyama, Toshiharu Makino, Masahiko Ogura, Daisuke Takeuchi, and Satoshi Yamasaki; Diamond bipolar junction transistor device with phosphorus-doped

diamond base layer. *Diamond and Related Materials*, 2012. **27–28**(0): p. 19-22. DOI: 10.1016/j.diamond.2012.05.004.

4. Giancarlo Richard Salazar Banda, Yasuaki Einaga, and Carlos Alberto Martinez-Huitle; New Trends on the Boron-Doped Diamond Electrode: From Fundamental Studies to Applications. *International Journal of Electrochemistry*, 2012. **2012**. DOI: 10.1155/2012/548504.
5. H. Umezawa, T. Matsumoto, and S. I. Shikata; Diamond Metal-Semiconductor Field-Effect Transistor With Breakdown Voltage Over 1.5 kV. *Electron Device Letters, IEEE*, 2014. **35**(11): p. 1112-1114. DOI: 10.1109/led.2014.2356191.
6. A. Fiori, T. Teraji, and Y. Koide; Diamond Schottky diodes with ideality factors close to 1. *Applied Physics Letters*, 2014. **105**(13): p. 133515. DOI: 10.1063/1.4897315.
7. Hana Krysova, Zuzana Vlckova-Zivcova, Jan Barton, Vaclav Petrak, Milos Nesladek, Petr Cigler, and L. Kavan; Visible-Light Sensitization of Boron-Doped Nanocrystalline Diamond through Non-covalent Surface Modification. *Physical Chemistry Chemical Physics*, 2014. DOI: 10.1039/c4cp04148h.
8. Yasuaki Einaga, John S. Foord, and Greg M. Swain; Diamond electrodes: Diversity and maturity. *MRS Bulletin*, 2014. **39**(06): p. 525-532. DOI: 10.1557/mrs.2014.94.
9. Satoshi Yamasaki, Etienne Gheeraert, and Yasuo Koide; Doping and interface of homoepitaxial diamond for electronic applications. *MRS Bulletin*, 2014. **39**(06): p. 499-503. DOI: 10.1557/mrs.2014.100.
10. Sabine Szunerits, Christoph E. Nebel, and Robert J. Hamers; Surface functionalization and biological applications of CVD diamond. *MRS Bulletin*, 2014. **39**(06): p. 517-524. DOI: 10.1557/mrs.2014.99.
11. Roberta Caterino, Réka Csiki, Alina Lyuleeva, Jonas Pfisterer, Markus Wiesinger, Stoffel D. Janssens, Ken Haenen, Anna Cattani-Scholz, Martin Stutzmann, and Jose A. Garrido; Photocurrent Generation in Diamond Electrodes Modified with Reaction Centers. *ACS Applied Materials & Interfaces*, 2015. **7**(15): p. 8099-8107. DOI: 10.1021/acsami.5b00711.
12. Dane W. Comerford, Andrew Cheesman, Thomas P. F. Carpenter, David M. E. Davies, Neil A. Fox, Rebecca S. Sage, James A. Smith, Michael N. R. Ashfold, and Yuri A. Mankelevich; Experimental and Modeling Studies of B Atom Number Density Distributions in Hot Filament Activated B_2H_6/H_2 and $B_2H_6/CH_4/H_2$ Gas Mixtures. *The Journal of Physical Chemistry A*, 2006. **110**(9): p. 2868-2875. DOI: 10.1021/jp053455p.
13. Yuri A. Mankelevich, Michael N. R. Ashfold, Dane W. Comerford, Jie Ma, and James C. Richley; Boron doping: B/H/C/O gas-phase chemistry; H atom density dependences on pressure and wire temperature; puzzles regarding the gas-surface mechanism. *Thin Solid Films*, 2011. **519**(14): p. 4421-4425. DOI: 10.1016/j.tsf.2011.01.328.
14. Hideaki Maeda, Kyo Ohtsubo, Masanori Kameta, Takeyasu Saito, Katsuki Kusakabe, Shigeharu Morooka, and Tanemasa Asano; Growth behavior of boron-doped diamond in microwave plasma-assisted chemical vapor deposition using trimethylboron as the dopant source. *Diamond and Related Materials*, 1998. **7**(1): p. 88-95. DOI: 10.1016/s0925-9635(98)80001-0.
15. R. Issaoui, J. Achard, F. Silva, A. Tallaire, A. Tardieu, A. Gicquel, M. A. Pinault, and F. Jomard; Growth of thick heavily boron-doped diamond single crystals: Effect of microwave power density. *Applied Physics Letters*, 2010. **97**(18): p. 182101. DOI: 10.1063/1.3511449.
16. R. Issaoui, J. Achard, A. Tallaire, F. Silva, A. Gicquel, R. Bisaro, B. Servet, G. Garry, and J. Barjon; Evaluation of freestanding boron-doped diamond grown by chemical vapour deposition as substrates for vertical power electronic devices. *Applied Physics Letters*, 2012. **100**(12): p. 122109-4. DOI: 10.1063/1.3697568.
17. Koichi Ushizawa, Kenji Watanabe, Toshihiro Ando, Isao Sakaguchi, Mikka Nishitani-Gamo, Yoichiro Sato, and Hisao Kanda; Boron concentration dependence of Raman spectra on {100} and {111} facets of B-doped CVD diamond. *Diamond and Related Materials*, 1998. **7**(11–12): p. 1719-1722. DOI: 10.1016/s0925-9635(98)00296-9.
18. F. Brunet, P. Germi, M. Pernet, A. Deneuville, E. Gheeraert, F. Laugier, M. Burdin, and G. Rolland; The effect of boron doping on the lattice parameter of homoepitaxial diamond films. *Diamond and Related Materials*, 1998. **7**(6): p. 869-873. DOI: 10.1016/s0925-9635(97)00316-6.
19. F. Brunet, P. Germi, M. Pernet, A. Deneuville, E. Gheeraert, F. Laugier, M. Burdin, and G. Rolland; Microstructure evolution of boron doped homoepitaxial diamond films. *Journal of Applied Physics*, 1998. **83**(1): p. 181-186. DOI: 10.1063/1.366671.

20. Ying-Gang Lu, Stuart Turner, Johan Verbeeck, Stoffel D. Janssens, Patrick Wagner, Ken Haenen, and Gustaaf Van Tendeloo; Direct visualization of boron dopant distribution and coordination in individual chemical vapor deposition nanocrystalline B-doped diamond grains. *Applied Physics Letters*, 2012. **101**(4): p. 041907-4. DOI: 10.1063/1.4738885.
21. Stuart Turner, Ying-Gang Lu, Stoffel D. Janssens, Fabiana Da Pieve, Dirk Lamoen, Jo Verbeeck, Ken Haenen, Patrick Wagner, and Gustaaf Van Tendeloo; Local boron environment in B-doped nanocrystalline diamond films. *Nanoscale*, 2012. **4**(19): p. 5960-5964. DOI: 10.1039/c2nr31530k.
22. Ying-Gang Lu, Stuart Turner, Johan Verbeeck, Stoffel D. Janssens, Ken Haenen, and Gustaaf Van Tendeloo; Local bond length variations in boron-doped nanocrystalline diamond measured by spatially resolved electron energy-loss spectroscopy. *Applied Physics Letters*, 2013. **103**(3): p. 032105-5. DOI: 10.1063/1.4813842.
23. P. Ashcheulov, J. Sebera, A. Kovalenko, V. Petrak, F. Fendrych, M. Nesladek, A. Taylor, Z. V. Zivcova, O. Frank, L. Kavan, M. Dracinsky, P. Hubik, J. Vacik, I. Kraus, and I. Kratochvilova; Conductivity of boron-doped polycrystalline diamond films: influence of specific boron defects. *European Physical Journal B*, 2013. **86**(10). DOI: 10.1140/epjb/e2013-40528-x.
24. M. P. Alegre, D. Araújo, A. Fiori, J. C. Pinero, F. Lloret, M. P. Villar, P. Achatz, G. Chicot, E. Bustarret, and F. Jomard; Critical boron-doping levels for generation of dislocations in synthetic diamond. *Applied Physics Letters*, 2014. **105**(17): p. 173103. DOI: 10.1063/1.4900741.
25. H. Sternschulte, J. Horseling, T. Albrecht, K. Thonke, and R. Sauer; Characterization of doped and undoped CVD-diamond films by cathodoluminescence. *Diamond and Related Materials*, 1996. **5**(6–8): p. 585-588. DOI: 10.1016/0925-9635(95)00400-9.
26. M. Werner, R. Locher, W. Kohly, D. S. Holmes, S. Klose, and H. J. Fecht; The diamond Irvin curve. *Diamond and Related Materials*, 1997. **6**(2–4): p. 308-313. DOI: 10.1016/S0925-9635(96)00683-8.
27. J. P. Lagrange, A. Deneuville, and E. Gheeraert; Activation energy in low compensated homoepitaxial boron-doped diamond films. *Diamond and Related Materials*, 1998. **7**(9): p. 1390-1393. DOI: 10.1016/s0925-9635(98)00225-8.
28. Yoshihiro Yokota, Takeshi Tachibana, Koichi Miyata, Kazushi Hayashi, Koji Kobashi, Akimitsu Hatta, Toshimichi Ito, Akio Hiraki, and Yoshihiro Shintani; Cathodoluminescence of boron-doped heteroepitaxial diamond films on platinum. *Diamond and Related Materials*, 1999. **8**(8–9): p. 1587-1591. DOI: 10.1016/s0925-9635(99)00085-0.
29. P. Muret and M. Wade; Acceptor compensation by dislocations related defects in boron doped homoepitaxial diamond films from cathodoluminescence and Schottky diodes current voltage characteristics. *physica status solidi (a)*, 2006. **203**(12): p. 3142-3146. DOI: 10.1002/pssa.200671116.
30. J. Barjon, N. Habka, C. Mer, F. Jomard, J. Chevallier, and P. Bergonzo; Resistivity of boron doped diamond. *physica status solidi (RRL)*, 2009. **3**(6): p. 202-204. DOI: 10.1002/pssr.200903097.
31. J. Barjon, E. Chikoidze, F. Jomard, Y. Dumont, M. A. Pinault-Thaury, R. Issaoui, O. Brinza, J. Achard, and F. Silva; Homoepitaxial boron-doped diamond with very low compensation. *physica status solidi (a)*, 2012. **209**(9): p. 1750-1753. DOI: 10.1002/pssa.201200136.
32. J. Cifre, J. Puigdollers, M. C. Polo, and J. Esteve; Trimethylboron doping of CVD diamond thin films. *Diamond and Related Materials*, 1994. **3**(4–6): p. 628-631. DOI: 10.1016/0925-9635(94)90238-0.
33. L.B. Freund; Dislocation Mechanisms of Relaxation in Strained Epitaxial Films. *MRS Bulletin*, 1992. **17**(07): p. 52-60. DOI: 10.1557/S088376940004166X.
34. A. E. Romanov and J. S. Speck; Stress relaxation in mismatched layers due to threading dislocation inclination. *Applied Physics Letters*, 2003. **83**(13): p. 2569-2571. DOI: 10.1063/1.1613360.
35. M. Fischer, S. Gsell, M. Schreck, and A. Bergmaier; Growth sector dependence and mechanism of stress formation in epitaxial diamond growth. *Applied Physics Letters*, 2012. **100**(4): p. 041906-3. DOI: 10.1063/1.3679611.
36. S. Gsell, M. Fischer, Th. Bauer, M. Schreck, and B. Stritzker; Yttria-stabilized zirconia films of different composition as buffer layers for the deposition of epitaxial diamond/Ir layers on Si(001). *Diamond and Related Materials*, 2006. **15**(4–8): p. 479-485. DOI: 10.1016/j.diamond.2005.10.041.

37. M. Fischer, S. Gsell, M. Schreck, R. Brescia, and B. Stritzker; Preparation of 4-inch Ir/YSZ/Si(001) substrates for the large-area deposition of single-crystal diamond. *Diamond and Related Materials*, 2008. **17**(7–10): p. 1035-1038. DOI: 10.1016/j.diamond.2008.02.028.
38. Andrew Hind and Lisette Chomette; Application note: The determination of thin film thickness using reflectance spectroscopy. 2011.
39. J. Barjon, T. Tillocher, N. Habka, O. Brinza, J. Achard, R. Issaoui, F. Silva, C. Mer, and P. Bergonzo; Boron acceptor concentration in diamond from excitonic recombination intensities. *Physical Review B*, 2011. **83**(7): p. 073201. DOI: 10.1103/PhysRevB.83.073201.
40. C. Baron, M. Wade, A. Deneuville, F. Jomard, and J. Chevallier; Cathodoluminescence of highly and heavily boron doped (100) homoepitaxial diamond films. *Diamond and Related Materials*, 2006. **15**(4-8): p. 597-601. DOI: 10.1016/j.diamond.2006.01.015.
41. R. G. Wilson; SIMS quantification in Si, GaAs, and diamond - an update. *International Journal of Mass Spectrometry and Ion Processes*, 1995. **143**: p. 43-49. DOI: 10.1016/0168-1176(94)04136-u.
42. F. K. de Theije, J. J. Schermer, and W. J. P. van Enckevort; Effects of nitrogen impurities on the CVD growth of diamond: step bunching in theory and experiment. *Diamond and Related Materials*, 2000. **9**(8): p. 1439-1449. DOI: 10.1016/s0925-9635(00)00261-2.
43. Michael Mayr, Christian Stehl, Martin Fischer, Stefan Gsell, and Matthias Schreck; Correlation between surface morphology and defect structure of heteroepitaxial diamond grown on off-axis substrates. *physica status solidi (a)*, 2014: p. 2257-2263. DOI: 10.1002/pssa.201431210.
44. L. B. Freund and W. D. Nix; A critical thickness condition for a strained compliant substrate/epitaxial film system. *Applied Physics Letters*, 1996. **69**(2): p. 173-175. DOI: 10.1063/1.117362.
45. A. Dadgar, R. Clos, G. Strassburger, F. Schulze, P. Veit, T. Hempel, J. Bläsing, A. Krtschil, I. Daumiller, M. Kunze, A. Kaluza, A. Modlich, M. Kamp, A. Diez, J. Christen, and A. Krost; Strains and Stresses in GaN Heteroepitaxy - Sources and Control. *Advances in Solid State Physics*, 2004. **44**: p. 1254-1254. DOI: 10.1007/978-3-540-39970-4_24.
46. C. Stehl, M. Fischer, S. Gsell, E. Berdermann, M. S. Rahman, M. Traeger, O. Klein, and M. Schreck; Efficiency of dislocation density reduction during heteroepitaxial growth of diamond for detector applications. *Applied Physics Letters*, 2013. **103**(15): p. 151905. DOI: 10.1063/1.4824330.
47. N. Naka, J. Omachi, and M. Kuwata-Gonokami; Suppressed formation of electron-hole droplets in diamond under a strain field. *Physical Review B*, 2007. **76**(19): p. 193202. DOI: 10.1103/PhysRevB.76.193202.
48. Keshra Sangwal; *Etching of crystals*, 1st ed., Defects in solids, ed. S. Amelinckx and J. Nihoul, 1987, Elsevier Science Publishers B. V.
49. J. Achard, F. Silva, O. Brinza, X. Bonnin, V. Mille, R. Issaoui, M. Kasu, and A. Gicquel; Identification of etch-pit crystallographic faces induced on diamond surface by H_2/O_2 etching plasma treatment. *physica status solidi (a)*, 2009. **206**(9): p. 1949-1954. DOI: 10.1002/pssa.200982210.
50. M. Naamoun, A. Tallaire, F. Silva, J. Achard, P. Doppelt, and A. Gicquel; Etch-pit formation mechanism induced on HPHT and CVD diamond single crystals by H_2/O_2 plasma etching treatment. *physica status solidi (a)*, 2012. **209**(9): p. 1715-1720. DOI: 10.1002/pssa.201200069.
51. Michael Mayr, Martin Fischer, Oliver Klein, Stefan Gsell, and Matthias Schreck; Interaction between surface structures and threading dislocations during epitaxial diamond growth. *physica status solidi (a)*, 2015. **212**(11): p. 2480-2486. DOI: 10.1002/pssa.201532243.
52. Nobuteru Tsubouchi, Y. Mokuno, and S. Shikata; Characterizations of etch pits formed on single crystal diamond surface using oxygen/hydrogen plasma surface treatment. *Diamond and Related Materials*, 2015. DOI: 10.1016/j.diamond.2015.08.012.
53. O. A. Ivanov, A. B. Muchnikov, V. V. Chernov, S. A. Bogdanov, A. L. Vikharev, and J. E. Butler; Experimental study of hydrogen plasma etching of (100) single crystal diamond in a MPACVD reactor. *Materials Letters*, 2015. **151**: p. 115-118. DOI: 10.1016/j.matlet.2015.03.073.
54. A. Tallaire, J. Barjon, O. Brinza, J. Achard, F. Silva, V. Mille, R. Issaoui, A. Tardieu, and A. Gicquel; Dislocations and impurities introduced from etch-pits at the epitaxial growth resumption of diamond. *Diamond and Related Materials*, 2011. **20**(7): p. 875-881. DOI: 10.1016/j.diamond.2011.04.015.

55. Oliver Klein, Michael Mayr, Martin Fischer, Stefan Gsell, and Matthias Schreck; Propagation and annihilation of threading dislocations during off-axis growth of heteroepitaxial diamond films. *Diamond and Related Materials*, 2016. **65**: p. 53-58. DOI: 10.1016/j.diamond.2016.01.024.

56. D. Siche, D. Klimm, T. Hölzel, and A. Wohlfart; Reproducible defect etching of SiC single crystals. *Journal of Crystal Growth*, 2004. **270**(1–2): p. 1-6. DOI: 10.1016/j.jcrysgro.2004.05.098.

57. S. A. Sakwe, R. Müller, and P. J. Wellmann; Optimization of KOH etching parameters for quantitative defect recognition in n- and p-type doped SiC. *Journal of Crystal Growth*, 2006. **289**(2): p. 520-526. DOI: 10.1016/j.jcrysgro.2005.11.096.

58. I. Y. Knoke, P. Berwian, E. Meissner, J. Friedrich, H. P. Strunk, and G. Müller; Selective etching of dislocations in GaN grown by low-pressure solution growth. *Journal of Crystal Growth*, 2010. **312**(20): p. 3040-3045. DOI: 10.1016/j.jcrysgro.2010.07.011.

59. K. Ichikawa, H. Kodama, K. Suzuki, and A. Sawabe; Dislocation in heteroepitaxial diamond visualized by hydrogen plasma etching. *Thin Solid Films*, 2016. **600**: p. 142-145. DOI: 10.1016/j.tsf.2016.01.009.

60. S. Hashimoto, Y. Yoshizumi, T. Tanabe, and M. Kiyama; High-purity GaN epitaxial layers for power devices on low-dislocation-density GaN substrates. *Journal of Crystal Growth*, 2007. **298**(0): p. 871-874. DOI: 10.1016/j.jcrysgro.2006.10.117.

61. L. McCarthy, I. Smorchkova, H. Xing, P. Fini, S. Keller, J. Speck, S. P. DenBaars, M. J. W. Rodwell, and U. K. Mishra; Effect of threading dislocations on AlGaN/GaN heterojunction bipolar transistors. *Applied Physics Letters*, 2001. **78**(15): p. 2235-2237. DOI: 10.1063/1.1358358.

62. H. Idrissi, G. Regula, M. Lancin, J. Douin, and B. Pichaud; Study of Shockley partial dislocation mobility in highly N-doped 4H-SiC by cantilever bending. *physica status solidi (c)*, 2005. **2**(6): p. 1998-2003. DOI: 10.1002/pssc.200460544.

63. H. Idrissi, B. Pichaud, G. Regula, and M. Lancin; 30° Si(g) partial dislocation mobility in nitrogen-doped 4H-SiC. *Journal of Applied Physics*, 2007. **101**(11): p. 113533. DOI: 10.1063/1.2745266.

64. Gufei Zhang, Stuart Turner, Evgeny A. Ekimov, Johan Vanacken, Matias Timmermans, Tomás Samuely, Vladimir A. Sidorov, Sergei M. Stishov, Yinggang Lu, Bart Deloof, Bart Goderis, Gustaaf Van Tendeloo, Joris Van de Vondel, and Victor V. Moshchalkov; Global and Local Superconductivity in Boron-Doped Granular Diamond. *Advanced Materials*, 2014. **26**(13): p. 2034-2040. DOI: 10.1002/adma.201304667.

65. Ying-Gang Lu, Stuart Turner, E. A. Ekimov, Jo Verbeeck, and Gustaaf Van Tendeloo; Boron-rich inclusions and boron distribution in HPHT polycrystalline superconducting diamond. *Carbon*, 2015. **86**: p. 156-162. DOI: 10.1016/j.carbon.2015.01.034.

66. S. Gsell, M. Schreck, and B. Stritzker; Crystal tilting of diamond heteroepitaxially grown on vicinal Ir/$SrTiO_3$(001). *Journal of Applied Physics*, 2004. **96**(3): p. 1413-1417. DOI: 10.1063/1.1766098.

67. M. P. Gaukroger, P. M. Martineau, M. J. Crowder, I. Friel, S. D. Williams, and D. J. Twitchen; X-ray topography studies of dislocations in single crystal CVD diamond. *Diamond and Related Materials*, 2008. **17**(3): p. 262-269. DOI: 10.1016/j.diamond.2007.12.036.

68. C. L. Jia, M. Lentzen, and K. Urban; Atomic-Resolution Imaging of Oxygen in Perovskite Ceramics. *Science*, 2003. **299**(5608): p. 870-873. DOI: 10.1126/science.1079121.

69. N. Fujita, A. T. Blumenau, R. Jones, S. Öberg, and P. R. Briddon; Core reconstructions of the 〈100〉 edge dislocation in single crystal CVD diamond. *physica status solidi (a)*, 2007. **204**(7): p. 2211-2215. DOI: 10.1002/pssa.200675444.

70. M. J. Hÿtch, E. Snoeck, and R. Kilaas; Quantitative measurement of displacement and strain fields from HREM micrographs. *Ultramicroscopy*, 1998. **74**(3): p. 131-146. DOI: 10.1016/S0304-3991(98)00035-7.

71. N. Fujita, A. T. Blumenau, R. Jones, S. Öberg, and P. R. Briddon; Theoretical studies on 〈100〉 dislocations in single crystal CVD diamond. *physica status solidi (a)*, 2006. **203**(12): p. 3070-3075. DOI: 10.1002/pssa.200671102.

72. Matthew K. Horton, Sneha Rhode, Suman-Lata Sahonta, Menno J. Kappers, Sarah J. Haigh, Timothy J. Pennycook, Colin J. Humphreys, Rajiv O. Dusane, and Michelle A. Moram; Segregation of In to Dislocations in InGaN. *Nano Letters*, 2015. **15**(2): p. 923-930. DOI: 10.1021/nl5036513.

73. Steffen Heyer, Wiebke Janssen, Stuart Turner, Ying-Gang Lu, Weng Siang Yeap, Jo Verbeeck, Ken Haenen, and Anke Krueger; Toward Deep Blue Nano Hope Diamonds: Heavily Boron-Doped Diamond Nanoparticles. *ACS Nano*, 2014. **8**(6): p. 5757-5764. DOI: 10.1021/nn500573x.

4 Electrochemical characterisation of highly boron-doped heteroepitaxial diamond

4.1 Introduction

In this chapter we turn to the investigation of the electrochemical properties of B-doped diamond heteroepitaxially grown on Ir/YSZ/Si(001). Highly conductive B-doped diamond (BDD) has been shown to be an excellent electrode, not only due to its robustness and chemical inertness, but also due to its inherent resistance to fouling, wide potential window for water splitting, low resistance and low background current [1-4]. Electrochemistry became in recent times one of the most dominant, if not the biggest field of application of BDD, for example in electro-organic synthesis [5, 6], electroanalytical sensing [7, 8] and wastewater treatment [9-12].

Despite the inherent qualities of diamond, mostly polycrystalline (highly defective) BDD electrodes have been investigated. Their electrochemical properties can be affected by various factors, such as 1) different B incorporation at different facets of the grains, 2) heterogeneous distribution of the surface density of states and local conductivity, 3) presence of sp^2 carbon and other impurity aggregates at grain boundaries and 4) other surface defects [13-16]. Especially for applications that require high sensitivity (low background current) and high selectivity (with a very well defined surface), the use of high-quality BDD single crystals becomes necessary. However, diamond single crystals suffer from the major technological disadvantage of being limited in size and being costly, which are the main reasons for the widespread use of polycrystalline BDD.

Homoepitaxial single crystal BDDs have been generally grown on HPHT diamond single crystals of various surface orientations by MWPCVD and several studies on their electrochemical properties have been reported [17-21]. Single crystal BDD provides a significantly lower background current and is less prone to fouling from adsorption, making it a more superior electrode material than polycrystalline diamond, which is the most common and easily available in large areas. Kondo *et al.* studied (111)- and (001)-oriented single crystal BDDs with $[\mathrm{B}]$ (B-doping concentration levels) of, respectively, $2\times10^{19}\,\mathrm{cm}^{-3}$ and $2\times10^{18}\,\mathrm{cm}^{-3}$. Apparent outer-sphere electron transfer was observed for various redox systems, except for $\mathrm{Fe(CN)}_6^{3-/4-}$ on the (001) surface, which was attributed to the high-quality diamond surface not possessing specific chemical sites necessary to catalyse the redox reaction for this particular mediator [17]. Ramesham *et al.* also observed similar phenomena by investigating the electrochemical properties of (001)-oriented BDD in $\mathrm{Fe(CN)}_6^{3-/4-}$, showing reversible but sluggish kinetics [18]. Lagemaat *et al.* also investigated oxidised (001)- and (011)-oriented single crystal diamond, and attributed the observed reversible electron transfer kinetics to surface states distributed in the bandgap. The flatband potential differed significantly on these two orientations, a result attributed to the relative coverage of the surface by hydroxyl (C−OH) or carbonyl (C=O) groups [19]. Pleskov *et al.* compared homoepitaxial BDD single crystal with polycrystalline BDD, showing that both exhibited similar kinetic and impedance characteristics in a $\mathrm{Ce}^{3+/4+}$ redox couple. The electrochemical behaviour of the polycrystalline BDD was also reported to be more strongly influenced by the polycrystalline nature of the material and of the surface, rather than by disordered carbon present at the grain boundaries [20]. They also investigated single crystal BDD grown by the HPHT method, and observed that differences in electrochemical properties between different crystallographic facets were mainly due to different acceptor (boron) concentrations in the growth sectors associated with the facets, resulting from their different boron incorporation efficiency during synthesis. In other words, they showed that conductivity plays a major role in the electrochemical behaviour of the BDD electrodes [21].

Although high-quality BDD single crystals with excellent electrochemical properties have already been demonstrated and subjected to a considerable amount of research, it follows a technological route possessing a major drawback of not yet being able to provide electrodes with large areas (*e.g.* several cm^2), which is a necessity from an economical point of view. Polycrystalline BDD, on the other hand, can be produced in large areas, but suffer from the poor quality inherent to its defective polycrystalline nature. Heteroepitaxial BDD grown on Ir/YSZ/Si(001) has, however, the potential to “bridge” the two types of materials and allow single crystal performance (well-defined and homogeneous surface) with competitive dimensions and a much lower density of defects than the polycrystalline counterpart. Heteroepitaxial BDD has the potential to be a very suitable and better alternative to both single- and polycrystalline BDD for special electrochemical applications, and yet, there are no studies reporting the electrochemical properties of heteroepitaxial BDD electrodes prior to the work described in this chapter.

Therefore, in this work a few heteroepitaxial BDD electrodes were prepared and subjected to a comprehensive electrochemical characterisation, performed in close collaboration with the group of Prof. Dr John S. Foord from the Department of Chemistry at the University of Oxford. The study presented here is the first on such kind of diamond, and the results were compared directly with the performance of polycrystalline BDD electrodes with similar characteristics, as well as with published results on BDD single crystal electrodes. The electrodes were characterised by cyclic voltammetry (CV), impedance spectroscopy (EIS), as well as by scanning electrochemical microscopy (SECM). Two different redox mediators, $\mathrm{Fe(CN)}_6^{3-/4-}$ and $\mathrm{Ru(NH_3)}_6^{3+/2+}$, were used to evaluate the heterogeneous transfer rate constant from peak-peak separation in CV and EIS data, and used also for the measurement of approach curves and SECM maps. Additional studies involving more complex electrochemical processes using methyl viologen (MV) and anthraquinone (AQDS) were also carried out. To finalise, the electrochemical activity of the electrodes was further studied by Pt deposition onto the diamond surfaces, complementing the results obtained by SECM.

Overall, the obtained results were very positive and make a clear statement about the potential and advantages of using heteroepitaxy on Ir/YSZ/Si(001) to produce high-quality, highly conductive diamond electrodes, especially for sensing applications, but also for bulk electrochemical processes.

4.2 Electrochemistry: the basics

Electrochemistry concerns the study of chemical reactions at the interface between a metallic or semiconducting electrode and a conducting solution, *i.e.* the electrolyte. The flow of electric charge through this junction characterises the chemical reactions taking place (either oxidation or reduction of chemical species). This field of research has gained special focus in the last decades, and even more nowadays, because of the many opened possibilities for energy conversion and storage (batteries, fuel cells, super capacitors, solar cells, etc.), electroanalysis (sensing), electrochemical production of bulk chemicals, water purification, etc. Comprehensive information on electrochemistry and much of what is presented in this chapter can be found in [22-25]. In the scope of this thesis the semiconductor-electrolyte interface is of interest, requiring the establishment of basic principles of electrochemistry, which will follow.

4.2.1 The electrochemical cell

An electrochemical cell is the environment where electrochemistry takes place. It consists of at least two solid electrodes, metallic or semiconducting, inserted into an electrically conductive, liquid medium, *i.e.* the electrolyte. Typical electrodes consist of noble metals such as Pt and Au, as well as non-metals such as graphite, glassy carbon and diamond. Typical electrolytes are aqueous solutions of ionic salts: chlorides (*e.g.* KCl), nitrates (*e.g.* KNO_3) and sulphates (*e.g.* $CuSO_4$), which may contain active redox species. Non-aqueous electrolytes are also used.

When an electrode is placed inside the solution, the difference in chemical potential will drive the flow of electrons from one phase to the other until equilibrium is reached, giving rise to a characteristic potential difference. When two electrodes are inserted in the solution, a potential difference between them can then be measured, and it will be characteristic of the chemical reactions (the so-called half reactions) taking place at both electrodes. This concept describes a simple electrochemical cell (see **Figure 4-1**).

Having the potential at both electrodes variable is not very useful for electrochemical experiments, and so a reference is necessary. Reference electrodes exist for this purpose, being the *standard hydrogen electrode* (SHE) universally accepted. Its potential lies at approximately −4.5 eV below the vacuum level (*i.e.* the energy of a free, stationary electron in vacuum) and is defined as 0 V. Widely used reference electrodes, such as the *silver-silver chloride* (Ag/AgCl) and the *saturated calomel electrode* (SCE), have their potential referenced to the SHE: 0.197 V and 0.242 V respectively. The two-electrode configuration, comprising the reference electrode (RE) and the working electrode (WE), is useful in the field of potentiometry, where the measured potential at the WE can be related to the concentration of analytes.

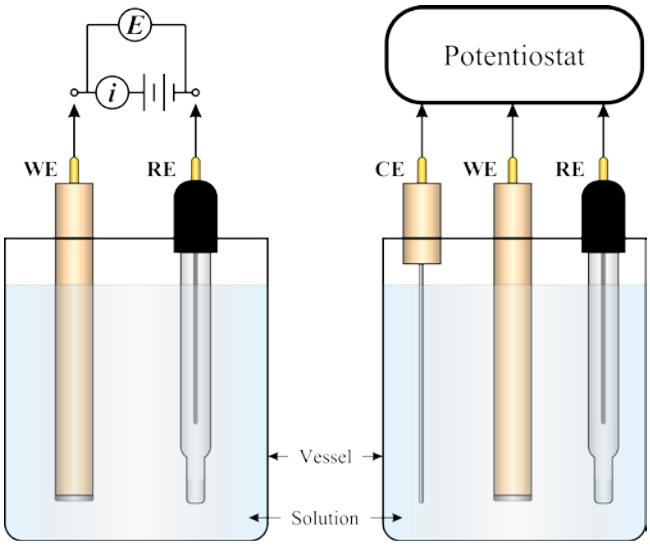

Figure 4-1: Schematic representation of two electrochemical cells with (left) two- and (right) three-electrode configuration.

However, when the study of the electrochemical cell's behaviour under current flow is important (such as for batteries), the two-electrode configuration is not very well suited, because of the complexity in interpreting a coupled current-voltage profile which is very sensitive to the chemical processes occurring at the electrodes and to the flow of charge across the electrolyte. For this reason, a third electrode, the counter electrode (CE), is added to the electrochemical cell (see **Figure 4-1**), and the circuitry around is modified: now 1) the potential of the WE of interest is measured against the RE, under the condition of *zero* current flow through RE. 2) The current flow is measured between WE and CE. This operation is done under the control of a potentiostat, described in more detail in section 4.4.1.

With the three-electrode configuration, the current flow at the WE can be intimately linked to the chemistry and charge transport processes occurring at its vicinity, and to the potential drop across this interfacial region. This setup opens up the possibility for more advanced techniques.

4.2.2 The double layer

Whenever a semiconductor is put in contact with an electrolyte, the difference between its Fermi level (chemical potential) E_F and the redox potential [26] E^0_redox of the electrolyte will drive the flow of electrons from the side with highest energy to lowest energy, until equilibrium is reached and both levels coincide (see **Figure 4-2**). The difference in density of states between the two phases will dictate which level will shift more than the other.

After equilibrium, an n-type semiconductor would have provided the electrolyte with majority carriers (electrons) and be left with its volume immediately close to the surface depleted of electrons, giving rise to a positive space charge. In an analogous way, a p-type semiconductor would have provided the electrolyte with holes and be left with a negative space charge. The charge imbalance with the formation of the depletion region changes the potential distribution at the interface (see **Figure 4-3**).

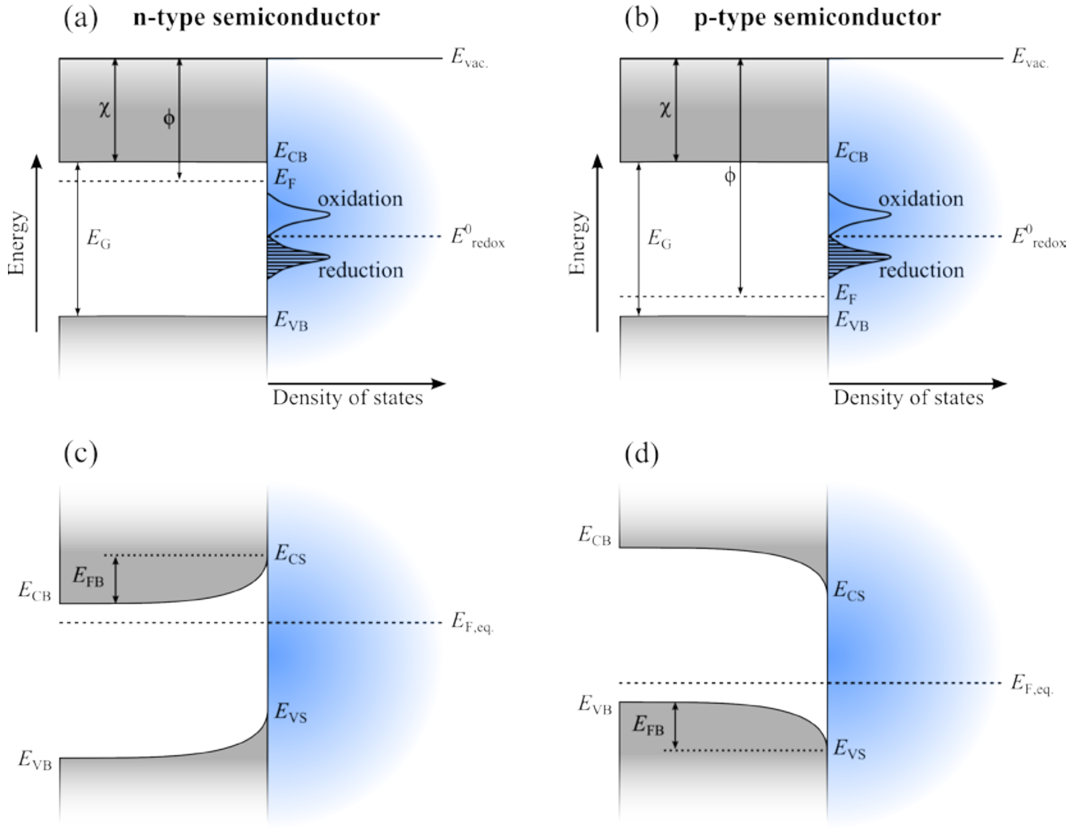

Figure 4-2: (a, b) Energy diagram relative to the vacuum level from, respectively, n-type and p-type semiconductors before equilibrium with the solution. (c, d) Energy levels after equilibrium [23].

The charged surface of the semiconductor affects the electrolyte side as well. A compact dipole layer of typically less than 1 Å, known as Helmholtz layer, is formed by solvent molecular dipoles (*e.g.* water) and solvated ions attracted to the surface. The remaining unbalanced charge leads to the formation of a diffuse layer, known as Gouy layer, where the charge distribution decreases exponentially towards the bulk of the liquid. Since most of the potential across the semiconductor-electrolyte junction drops within the space charge and the Helmholtz layers, provided that the electrolyte is concentrated enough, the electrical double layer can be modelled approximately by two capacitors, C_{SC} and C_H, in series (see **Figure 4-3**).

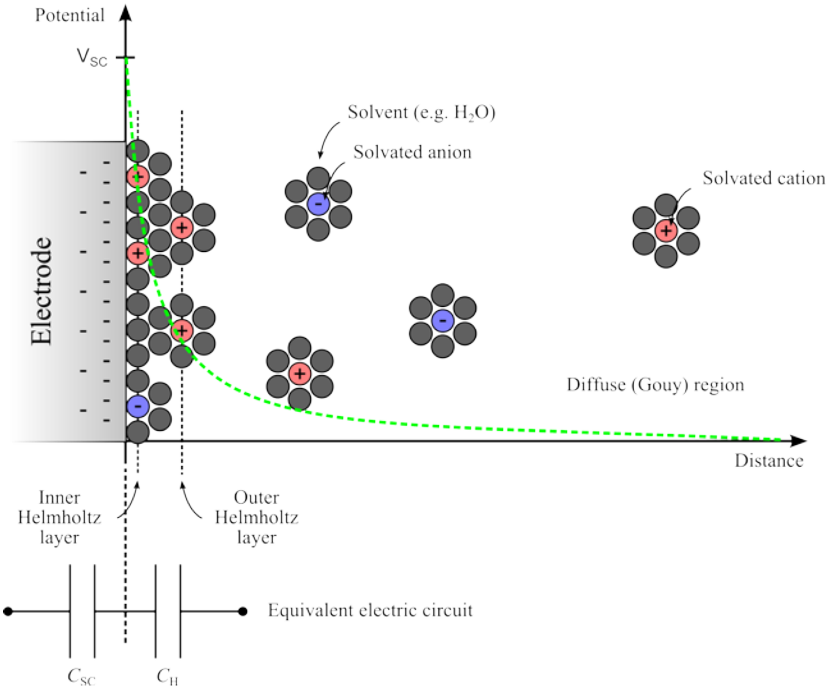

Figure 4-3: Sketch of the semiconductor-electrolyte junction (electrical double layer). The green curve represents the potential drop across the liquid.

There are two types of current flowing through a double layer in an electrochemical cell: faradaic and non-faradaic. Faradaic current flows as a result of charge transfer due to reduction or oxidation of chemical species, and is given by:

$$\frac{dQ}{dt} = \frac{d}{dt}(nFN) = nF\frac{dN}{dt} \tag{4.2.1}$$

where Q (C) is the charge that passes through the interface, t (s) is the time, n is the number of transferred electrons involved in the reaction, F (C mol^{-1}) is the Faraday constant and N (mol) is the molar number of redox species in the solution.

Non-faradaic current flows whenever there is a change in the potential drop across the solid-liquid interface, due to charging and discharging of the double layer capacitance.

4.3 Fundamental theories of electrochemistry

In this chapter fundamental theories of electrochemistry will be given to support the techniques and analyses implemented in the investigation of the electrochemical properties of B-doped diamond heteroepitaxially grown on Ir/YSZ/Si(001). The following content is mostly drawn from the “Handbook of Electrochemistry” [24] and from the book “Electrochemical Methods: Fundamentals and Applications” [25].

4.3.1 Electrochemical equilibrium and Nernst equation

In an electrochemical cell in equilibrium, *i.e.* where no current flows and constant potential is achieved, it is of interest to understand how the potential on the electrode relates to the concentration of chemical species in the cell. Consider the following reaction:

$$\mathrm{O} + ne^- \rightleftarrows \mathrm{R} \tag{4.3.1}$$

where O is the oxidised species, R is the reduced species and n is the number of electrons e^- exchanged between O and R. The relationship between the concentration of oxidised species $[\mathrm{O}]$, concentration of reduced species $[\mathrm{R}]$, and free energy ΔG (J mol^{-1}) is given as:

$$\Delta G = \Delta G^0 + RT \ln \frac{[\mathrm{R}]}{[\mathrm{O}]} \tag{4.3.2}$$

where R is the gas constant (8.3145 J mol^{-1} K^{-1}) and T (K) is the absolute temperature. The critical aspect of this equation is that the ratio of reduced to oxidised species can be related to the Gibbs free energy[1] change ΔG, from which the potential E (V) can be derived:

$$\Delta G = -nFE \tag{4.3.3}$$

Here, E is the maximum potential between two electrodes, also known as the open-circuit potential (OCP) or the equilibrium potential, which is present when no current is flowing through the cell, and F is the Faraday constant (9.6485×10^4 C mol^{-1}). If the reactant and product have unity activity, and E is for the reaction in the direction of reduction, *i.e.* left to right in equation (4.3.1), then equation (4.3.3) can be written as

$$\Delta G^0 = -nFE^0 \tag{4.3.4}$$

In this case the potential E^0 (V) is known as the *standard electrode potential* (or *standard potential*), and it relates to the *standard Gibbs free energy change* ΔG. It should be noted that due to the minus sign in equation (4.3.4), all spontaneous reactions (*i.e.*, with $\Delta G^0 < 0$) will have a positive standard electrode potential ($E^0 > 0$).

The mathematical expression describing the correlation between potential and concentration for a cell reaction is a central element of electrochemistry and is known as the *Nernst equation*, obtained by combining equations (4.3.2)-(4.3.4):

---

[1] The Gibbs free energy is a measure of electrochemical work [25].

$$E = E^0 + \frac{RT}{nF}\ln\frac{[\mathrm{O}]}{[\mathrm{R}]} \tag{4.3.5}$$

The Nernst equation solves the potential of an electrochemical cell containing a reversible system with fast kinetics and it is valid only at equilibrium and at the surface of the electrode:

$$E = E^{0'} + \frac{RT}{nF}\ln\frac{C_{\mathrm{O}}^{*}}{C_{\mathrm{R}}^{*}} \tag{4.3.6}$$

$$E = E^0 + \frac{RT}{nF}\ln\frac{a_{\mathrm{O}}}{a_{\mathrm{R}}} \tag{4.3.7}$$

where $E^{0'}$ (V) is the formal potential[2], E^0 (V) is the standard potential, C_j^* (mol L^{-1}) is the bulk concentration for the species j, and a (mol L^{-1}) is the activity. A common assumption is to ignore the activity coefficients, resulting in $E^0 = E^{0'}$. The formal potential in equation (4.3.6) accounts for the activity coefficients for the species O and R. The values for the formal potential (see chapter 18 in [24]) are dependent upon the nature of both the solvent and the supporting electrolyte.

4.3.2 Dynamic electrochemistry

The Nernst equation above readily predicts how the potential difference in an electrochemical cell in equilibrium (*i.e.* no net current flow) relates to the concentration of redox species in the solution. However, understanding the reaction kinetics of the chemical processes taking place during chemical change (*i.e.* under current flow), along with mass transport effects in the cell, is often desired.

For a non-spontaneous cell reaction to occur, an overpotential η (V), must be applied. The extent to which the reaction is driven beyond the equilibrium potential, $E_{\mathrm{eq.}}$ (V), is:

$$\eta = E - E_{\mathrm{eq.}} \tag{4.3.8}$$

One fundamental aim of dynamic electrochemical theory is to explain how the current flow relates to the applied overpotential.

4.3.2.1 Current, current density and charge transfer rate

Starting from Faraday's law, which correlates the total charge Q (C) passed through a cell to the amount of product N (mol):

---

[2] That is, the potential which is actually measured in an electrochemical cell.

$$Q = nFN \tag{4.3.9}$$

where n is the number of electrons transferred per mole of product, one can obtain a transfer rate from the calculation of the corresponding electric current i:

$$i = \frac{dQ}{dt} = nF\frac{dN}{dt} \Leftrightarrow \frac{dN}{dt} = \frac{i}{nF} \ (\text{mol s}^{-1}) \tag{4.3.10}$$

Chemical reactions can be either *homogeneous* or *heterogeneous*. The first type occurs in a single phase, and its rate is uniform everywhere in the volume where it occurs. *Heterogeneous reactions* occur at the electrode-solution interface, and they are characteristic of electrochemistry, being dependent upon the area A (cm^2) of the electrode, or the area of the phase boundary where the reaction occurs. Thus, the rate is more useful when normalised to the electrode area:

$$\frac{1}{A}\frac{dN}{dt} = \frac{i}{nFA} \ (\text{mol s}^{-1}\ \text{cm}^{-2}) \tag{4.3.11}$$

There are four major factors governing the reaction rate and current at electrodes: (i) mass transfer to the electrode surface; (ii) kinetics of electron transfer; (iii) preceding and subsequent reactions; (iv) surface reactions (adsorption, crystallisation). The slowest process will be the rate-determining step. When all of the processes leading to the reaction are fast, then only the electron transfer reaction becomes the limiting factor. The measurement of fast electron transfer rates can be, however, limited by the non-faradaic time constant of the electrode:

$$\tau = R_{\text{sol.}} C_{\text{H}} \tag{4.3.12}$$

where $R_{\text{sol.}}$ (Ω) is the series resistance of the solution and C_{H} (F) is the double layer capacitance. One way to minimise τ is to use the three-electrode configuration mentioned in section 4.2.1, which is often the case. In a potential sweep experiment (described in section 4.4.2) the output is the current, which accounts for both the faradaic and non-faradaic processes. Since the scan rate ν (V s^{-1}) is known, it is possible to calculate the non-faradaic current, i_{nf} (A) from:

$$i_{\text{nf}} = \nu C_{\text{H}} \tag{4.3.13}$$

4.3.2.2 Butler-Volmer equation

The *Butler-Volmer equation* is a simple phenomenological model to explain the flow of current in an electrochemical cell caused by an applied overpotential, assuming that there are no mass transfer limitations (*e.g.* depletion of chemical species near the electrode). This model is based on the idea that the reactant at the electrode is required to cross an energy barrier in order to be converted into reaction products, the magnitude of which depends on the applied potential. Using transition state theory [25], the behaviour of reaction kinetics can be predicted. If one considers again the simple reaction in equation (4.3.1), it can be re-written as follows (note: Butler-Volmer always assumes that $n=1$):

$$\mathrm{O}+e^{-}\underset{k_\mathrm{b}}{\overset{k_\mathrm{f}}{\rightleftarrows}}\mathrm{R} \tag{4.3.14}$$

where k_f (cm s^{-1}) and k_b (cm s^{-1}) are the rate constants for the forward (reduction) reaction and backward (oxidation) reactions, respectively. The overall current i (A) can be predicted by the Butler-Volmer equation as the difference between the cathodic (reduction) and anodic (oxidation) reactions, which are presented respectively as i_c and i_a in the equation below:

$$i=i_\mathrm{c}-i_\mathrm{a} \tag{4.3.15}$$

Both i_c and i_a are proportional to the respective rate constants and the concentration of the reacting species at the electrode surface as follows:

$$i_\mathrm{c}=FAk_\mathrm{f}C_\mathrm{O}(0,t) \tag{4.3.16}$$

$$i_\mathrm{a}=FAk_\mathrm{b}C_\mathrm{R}(0,t) \tag{4.3.17}$$

where F (C mol^{-1}) is the Faraday constant, A (cm^2) is the electrode area and $C_j(x,t)$ (mol cm^{-3}) is the concentration of species j measured at the electrode ($x=0$) at the time t (s). The rate constants of the forward and backward reactions can be written as a function of the *standard heterogeneous rate constant*, k_0 (cm s^{-1}), and the applied overpotential, according to the following expressions:

$$k_\mathrm{f}=k_0e^{-\alpha f\left(E-E^{0'}\right)} \tag{4.3.18}$$

$$k_\mathrm{b}=k_0e^{(1-\alpha)f\left(E-E^{0'}\right)} \tag{4.3.19}$$

where $f=F/RT$, and α is known as the *transfer coefficient*, which varies within $\left[0,1\right]$ and is usually estimated as 0.5. It relates to where the transition state is located along the reaction coordinate, which tends to be midway between reactants and products. See section 4.3.2.4 on *Marcus theory* for more details.

Based on the above equations, the net current flow at the electrode for an applied potential *E* can be described:

$$i = FAk_0\left[C_{\mathrm{O}}\left(0,t\right)e^{-\alpha\left(E-E^{0'}\right)} - C_{\mathrm{R}}\left(0,t\right)e^{(1-\alpha)f\left(E-E^{0'}\right)}\right] \tag{4.3.20}$$

When the electrochemical cell is in equilibrium, *i.e.* when the net current is zero, the exchange current i_0 can be obtained from $i_0 = i_{\mathrm{c}} = i_{\mathrm{a}}$ and the following equation can be deduced:

$$i_0 = FAk_0 C_{\mathrm{O}}^{*(1-\alpha)} C_{\mathrm{R}}^{*\,\alpha} \tag{4.3.21}$$

where C_j^* (mol cm^{-3}) is the bulk concentration of the *j* species. The value of i_0 can be obtained experimentally by extrapolation from Tafel plots ($\log\left|i\right|$ *vs.* η, also known as the *polarisation curve*). From equations (4.3.20) and (4.3.21) one arrives at the *current-overpotential equation*:

$$i = i_0\left[\frac{C_{\mathrm{O}}\left(0,t\right)}{C_{\mathrm{O}}^*}e^{-\alpha f\eta} - \frac{C_{\mathrm{R}}\left(0,t\right)}{C_{\mathrm{R}}^*}e^{(1-\alpha)f\eta}\right] \tag{4.3.22}$$

where $\eta = E - E^{0'}$ is the overpotential. Without mass transfer limitations, *i.e.* when the transport of species from the bulk to the electrode, and vice-versa, is efficient, $C_j / C_j^* \cong 1$ and equation (4.3.22) simplifies to the *Butler-Volmer equation*:

$$i = i_0\left[e^{-\alpha f\eta} - e^{(1-\alpha)f\eta}\right] \tag{4.3.22}$$

Although the Butler-Volmer equation allows the estimation of the current through an electrode in a well-stirred solution for a given overpotential, it is nevertheless a simplification and more of a qualitative measure of the dynamic behaviour of an electrochemical cell. Nowadays, detailed modelling of electrochemical reactions is normally based on modern theories of electron transfer, such as *Marcus theory* and *Marcus-Hush-Chidsey* formalisms. Some of their important concepts are presented in section 4.3.2.4.

4.3.2.3 Reversibility

Reversibility is a key concept when dealing with electrochemical reaction mechanisms. An electrochemical cell is considered chemically *reversible* if reversing the current through the cell reverses the cell reaction and no new reactions or side products appear.

An electrochemical cell is considered chemically *irreversible* if reversing the current leads to different electrode reactions and new side products. This is often the case if a solid falls out of solution or a gas is produced, as the solid or gaseous product may not be available to participate in the reverse reaction.

4.3.2.4 Microscopic theory of charge transfer

Section 4.3.2.2 dealt with a generalised theory of *heterogeneous electron-transfer kinetics* based on macroscopic concepts, in which the rate of the reaction was expressed in terms of the phenomenological parameters, k_0 and α. While useful in helping to organise the results of experimental studies and in providing information about reaction mechanisms, such approach does not predict how the kinetics are affected by factors such as the nature and structure of the reacting species, the solvent, the electrode material, and adsorbed layers on the electrode. To obtain this information it is necessary to apply a microscopic theory that describes how molecular structure and environment affect the electron-transfer process. Several authors, most notably Rudolf A. Marcus, who won a Nobel Prize in Chemistry for his achievements, devoted a great deal of effort to develop microscopic theories for electrochemistry. The *Marcus model* has been widely applied in electrochemical studies and has demonstrated the ability to make useful predictions about structural effects on kinetics with minimal computation.

To begin with, it is important to distinguish between *inner-sphere* and *outer-sphere* electron transfer reactions at electrodes (see **Figure 4-4**):

- The term "outer-sphere" refers to a reaction between two species in which the original coordination spheres are maintained in the activated complex, *i.e.*, there is no significant rearrangement of the chemical bonds and the electron transfer occurs from one primary bond system to another. In such case, the reactant and product do not interact strongly with the electrode surface, and they are generally at a distance of at least a solvent layer from the electrode. A typical example is the heterogeneous reduction of $\mathrm{Ru(NH_3)_6^{3+}}$, where the reactant at the electrode surface is essentially the same as in the bulk.
- In contrast, "inner-sphere" reactions occur in an activated complex where the ions share a ligand, requiring a significant rearrangement of the chemical bonds. Therefore, electron transfer takes place within a primary bond system. In an inner-sphere electrode reaction, there is a strong interaction of the reactant, intermediates, or products with the electrode; that is, such reactions involve specific adsorption of species involved in the

electrode reaction. For example, the reduction of oxygen in water and the oxidation of hydrogen on Pt are inner-sphere reactions. Consequently, outer-sphere reactions are less dependent on electrode material than inner-sphere ones.

Outer-sphere electron transfers can be treated in a more general way than inner-sphere processes, where specific chemistry and interactions are important. For this reason, the theory of outer-sphere electron transfer is much more highly developed, and the discussion that follows pertains to these kinds of reactions. However, in practical applications, such as in fuel cells and batteries, the more complicated inner-sphere reactions are important. A theory of these requires consideration of specific adsorption effects, as described in [25], chapter 13.

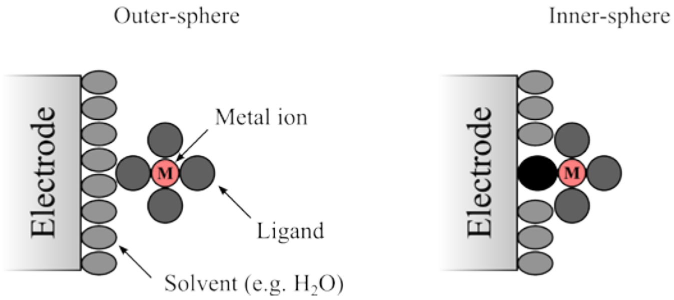

Figure 4-4: Outer-sphere and inner-sphere reactions. The diagram shows the heterogeneous reaction of a metal ion M surrounded by ligands. In the inner-sphere reaction, a ligand adsorbs on the electrode and bridges to the metal. Figure adapted from [25].

The main considerations in *Marcus theory* are the following:

a) A heterogeneous electron transfer from an electrode to a species O to form the product R is treated in the same theoretical context as the related homogeneous reduction of O to R by reaction with a suitable reductant $\mathrm{R'}$: $\mathrm{O + R' \rightarrow R + O'}$.
b) Electron-transfer reactions, whether homogeneous or heterogeneous, are radiationless electronic rearrangements of reacting species. Consequently, an electron must move from an initial state (on the electrode or in the reductant $\mathrm{R'}$) to a receiving state (in species O or on the electrode) of the same energy. This demand for *isoenergetic electron transfer* is a fundamental aspect with extensive consequences.
c) The configuration of reactants and products are assumed to remain unchanged during electron transfer, according to a principle which states that nuclear momenta and positions do not change on the time scale of electronic transitions.

Considering the standard free energy plot in **Figure 4-5** of species O and R as a function of reaction coordinate, the goal is to obtain an expression for the standard free energy of activation G^* as a function of structural parameters of the reactant, so that the rate constant can be calculated from transition state theory. The relationship will take the following form:

$$k_{\mathrm{f}} = K_{\mathrm{P,O}} \nu_{\mathrm{n}} \kappa_{\mathrm{el.}} \frac{\mathrm{k_B} T}{h} e^{-\Delta G^{*}/RT} \qquad (4.3.23)$$

where $K_{\mathrm{P,O}}$ (cm) is a *precursor equilibrium constant*, representing the ratio of the reactant concentration in the reactive position at the electrode (the precursor state) to the concentration in bulk solution, *i.e.* $C_{\mathrm{O,surf.}}/C_{\mathrm{O}}^{*}$; ν_{n} (s^{-1}) is the *nuclear frequency factor*, which represents the frequency of attempts on the energy barrier (generally associated with bond vibrations and solvent motion); $\kappa_{\mathrm{el.}}$ is an electron transmission coefficient (tunnelling probability) varying within $[0,1]$; $\mathrm{k_B}$ is Boltzmann's constant, T is the absolute temperature, h is the Planck constant and R is the ideal gas constant.

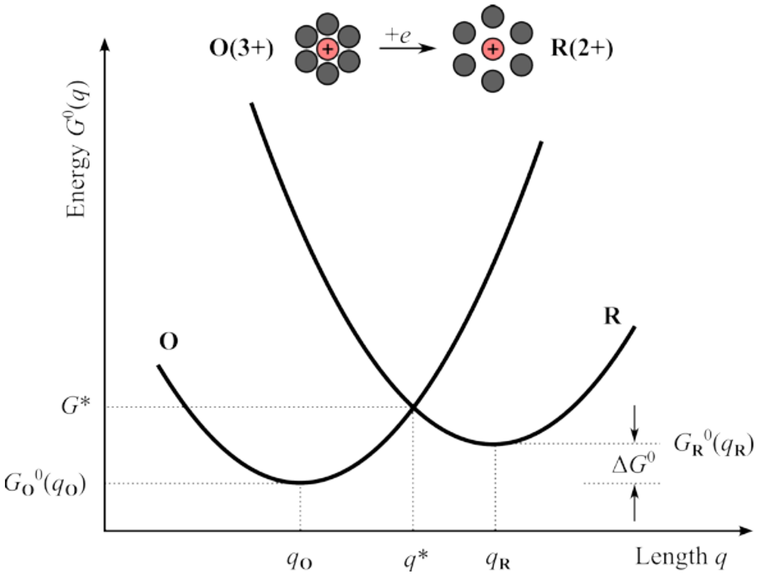

Figure 4-5: Standard free energy G^0 as a function of reaction coordinate q for an electron transfer reaction, such as $\mathrm{Ru(NH_3)_6^{3+}} + e^{-} \rightarrow \mathrm{Ru(NH_3)_6^{2+}}$. In the case of heterogeneous electron transfer, the curve for O is the sum of energies for species O and for an electron on the electrode at the Fermi level corresponding to a potential E. Then, $\Delta G^0 = F\left(E - E^0\right)$. The picture at the top is a general representation of structural changes that might accompany electron transfer. The changes in spacing of the six surrounding dots could represent, for example, changes in bond lengths within the electroactive species or the restructuring of the surrounding solvent shell. Figure adapted from [25].

Assuming that 1) the reactant O is centred at some fixed position with respect to the electrode (or in a bimolecular homogeneous reaction, the reactants being at a fixed distance from each other), and that 2) the standard free energies of O and R, G_{O}^{0} and G_{R}^{0}, depend quadratically on the reaction coordinate q:

$$G_{\mathrm{O}}^{0}(q) = (k/2)(q - q_{\mathrm{O}})^{2} \qquad (4.3.24)$$

$$G_{\mathrm{R}}^{0}\left(q\right)=\left(k/2\right)\left(q-q_{\mathrm{R}}\right)^{2}+\Delta G_{0} \qquad (4.3.25)$$

where k is a proportionality constant (*e.g.* force constant for a change in bond length). The other parameters are described in **Figure 4-5**. In that sketch, the molecules shown at the top are meant to represent the stable configurations of the reactants, for example, $\mathrm{Ru(NH_3)_6^{3+}}$ and $\mathrm{Ru(NH_3)_6^{2+}}$ as O and R, as well as to provide a view of the change in nuclear configuration upon reduction. The transition state is the position where O and R have the same configuration, denoted by the reaction coordinate q^{*}. According to the assumption c) described before, the reaction can only occur at this point. Therefore, the free energies at the transition state are given by:

$$G_{\mathrm{O}}^{0}(q^{*})=\left(k/2\right)\left(q^{*}-q_{\mathrm{O}}\right)^{2} \qquad (4.3.26)$$

$$G_{\mathrm{R}}^{0}\left(q^{*}\right)=\left(k/2\right)\left(q^{*}-q_{\mathrm{R}}\right)^{2}+\Delta G_{0} \qquad (4.3.27)$$

Since $G_{\mathrm{O}}^{0}\left(q^{*}\right)=G_{\mathrm{R}}^{0}\left(q^{*}\right)$, one arrives at:

$$q^{*}=\frac{\left(q_{\mathrm{R}}+q_{\mathrm{O}}\right)}{2}+\frac{\Delta G^{0}}{k\left(q_{\mathrm{R}}-q_{\mathrm{O}}\right)} \qquad (4.3.28)$$

The free energy of activation for reduction of O is given by:

$$\Delta G_{\mathrm{f}}^{*}=G_{\mathrm{O}}^{0}\left(q^{*}\right)-G_{\mathrm{O}}^{0}\left(q_{\mathrm{O}}\right)=G_{\mathrm{O}}^{0}\left(q^{*}\right) \qquad (4.3.29)$$

So, combining equations (4.3.26), (4.3.28) and (4.3.29) yields:

$$\Delta G_{\mathrm{f}}^{*}=\frac{\lambda}{4}\left(1+\frac{\Delta G^{0}}{\lambda}\right), \text{ with } \lambda=\left(k/2\right)\left(q_{\mathrm{R}}-q_{\mathrm{O}}\right)^{2} \qquad (4.3.30)$$

with λ being the *reorganisation energy* necessary to transform the nuclear configurations in the reactant and the solvent to those of the product state. Also, $\Delta G^{0}=F\left(E-E^{0}\right)$ for an electrode reaction.

There can be free energy contributions beyond those considered in the derivation described above. In general, they are energy changes involved in bringing the reactants and products from the average environment in the medium to the special environment where electron transfer occurs. Among them are the energy of ion pairing and the electrostatic work needed to reach the reactive position. Those terms were omitted for simplicity.

From equation (4.3.30) one can also determine the *transfer coefficient* α, first introduced for the Butler-Volmer equation, from:

$$\alpha = \frac{1}{F}\frac{\partial \Delta G_{\mathrm{f}}^{*}}{\partial E} = \frac{1}{2} + \frac{F\left(E - E^{0}\right)}{2\lambda} \tag{4.3.31}$$

From the above equation, the Marcus theory predicts not only that $\alpha = 0.5$ but also that it is potential-dependent, contrary to the classic Butler-Volmer theory which accounts for α as a constant.

Since it’s not in the scope of this thesis to dive too much into theories of electrochemistry, this is as far as this chapter goes in presenting the fundamentals of the Marcus theory. More details can be found in the references given in the beginning of the chapter.

4.3.3 Equations governing mass transfer

Apart from reaction kinetics, mass transport also has an important effect in controlling the performance of electrochemical cells under dynamic conditions. Since chemical species are created and destroyed at the electrode surface, transport of species within the cell must take place. For example, the Butler-Volmer equation derived before identifies the current flow as being dependent on the concentration of species at the electrode surface itself, so, unless the consumed reactants in this region are replenished, current flow cannot be sustained. Mass transport can often be the rate-limiting factor governing the overall behaviour in the electrochemical cell, since electron transfer occurs on a much shorter timescale.

Mass transfer in electrochemical reactions can generally follow three different pathways or combinations of: a) *migration*, referring to movement of charged particles in an electric field; b) *diffusion*, meaning the movement of species due to a concentration gradient; c) *convection*, correlating with the movement that may be induced in fluids, associated with density and temperature gradients or stirring operations.

The *Nernst-Planck* equation below correlates the flux of species j to migration, diffusion and convection in a single direction:

$$J_j\left(x\right) = -D_j\frac{\partial C_j\left(x\right)}{\partial x} - \frac{z_j F}{RT}D_j C_j\frac{\partial \phi\left(x\right)}{\partial x} + C_j v\left(x\right) \tag{4.3.32}$$

where $J_j\left(x\right)$ (mol cm^{-2} s^{-1}) is a one-dimensional flux for species j at distance x (cm) from the electrode; D_j (cm^{2} s^{-1}), z_j and C_j (mol cm^{-3}) are the diffusion coefficient, the charge, and the concentration for the species j, respectively; $v\left(x\right)$ (cm s^{-1}) is the rate with which a volume element moves in solution; $\partial C_j\left(x\right)/\partial x$ is the concentration gradient; and $\partial \phi\left(x\right)/\partial x$ is the potential gradient along the x-axis. In equation (4.3.32) the first term is concerned with the diffusion and is, in fact, Fick’s first law (see below). The second term accounts for the migration of the species in the solution, and the last term represents the convection of the solution.

In many electrochemical experiments migration is negligible, because the usually highly concentrated supporting electrolytes screen (*i.e.* dampen) the electric field in the bulk solution. Also, because the experiments are carried out in a stagnant solution, convection effects are negligible on short timescales. Under these circumstances, the main mode of transport of species to and from the bulk solution is by diffusion, induced by concentration gradients created by the electrochemical reaction.

Fick proposed two laws of diffusion in solution. These equations describe the relation between the flux J_j of a substance j and its concentration C_j (mol cm^{-3}) as a function of both time t (s) and position x (cm). The first law describes the flux as a function of a change in concentration with distance:

$$-J_j\left(x,t\right)=D_j\frac{\partial C_j\left(x,\mathrm{t}\right)}{\partial x} \tag{4.3.33}$$

The second law describes a change of concentration as a function of time t (s):

$$\frac{\partial C_j\left(x,t\right)}{\partial t}=-D_j\left[\frac{\partial^2 C_j\left(x,t\right)}{\partial x^2}\right] \tag{4.3.34}$$

Mass transfer occurs before charge transfer, and both processes are always occurring. The slower of the two is the rate-limiting step. If the applied potential is small enough, the charge transfer is slow and becomes the limiting factor, while mass transport becomes negligible. However, if the applied potential is high, the charge transfer is very fast and the mass transfer is the rate-limiting step. The *mass-transfer limited current* i_l, which is by definition independent of the potential, can be written in terms of a *mass-transfer coefficient* m (cm s^{-1}) in a similar way to the charge-transfer limited current (see section 4.3.2.1):

$$i_l=nFAmC^* \tag{4.3.35}$$

which can also be written in terms of the diffusion coefficient D (cm^2 s^{-1}) as:

$$i_l=\frac{nFADC^*}{\delta} \tag{4.3.36}$$

where $\delta=D/m$ (cm) and corresponds to the Nernst diffusion layer thickness.

It arrives from Fick’s second law that, for a planar electrode:

$$\delta=\sqrt{\pi Dt} \tag{4.3.37}$$

Combining equations (4.3.36) and (4.3.37) leads to the well-known *Cottrell equation*:

$$i(t) = \frac{nFAD_j^{1/2}C_j^*}{\pi^{1/2}t^{1/2}} \tag{4.3.38}$$

where n is the number of transferred electrons, F is the Faraday constant, A (cm^2) is the electrode area, D_j ($\mathrm{cm}^2\ \mathrm{s}^{-1}$) and C_j^* ($\mathrm{mol\ cm}^{-3}$) are, respectively, the diffusion coefficient and the bulk concentration of species j and t (s) is the time. The Cottrell equation enables many electrochemical techniques by relating the current in a directly proportional manner to the concentration of the electrochemically active species. It correctly predicts that the current should decay to zero with an inverse relationship to the square root of the time, a good example of mass transport limitation. In practice, capacitive charging on short timescales and natural convection on long timescales will lead to inaccuracies. Deviations from linearity in the plot of i vs. $t^{-1/2}$ sometimes also indicate that the redox event is correlated with other processes, such as association of a ligand, dissociation of a ligand, or a change in geometry. In practice, $t^{-1/2}$ is replaced by $(\text{scan rate})^{1/2}$ and the peak current i_p is used for analysis.

4.4 Electrochemical techniques

4.4.1 Potentiostat

Used in combination with an electrochemical cell, the purpose of a potentiostat [25, 27] is to maintain a constant potential difference between working electrode (WE) and reference electrode (RE). It does so through a high-impedance feedback loop involving the counter electrode (CE). The simplest scheme of a potentiostat is shown in **Figure 4-6**. There, the RE is connected to the inverting input of an operational amplifier; the WE is kept at ground potential, and the potential V_set between the non-inverting input and the ground becomes the potential difference between RE and WE. There is no potential difference between both inputs of the operational amplifier. The op-amp delivers the current through the counter electrode (CE) to keep the difference between V_RE and V_WE constant.

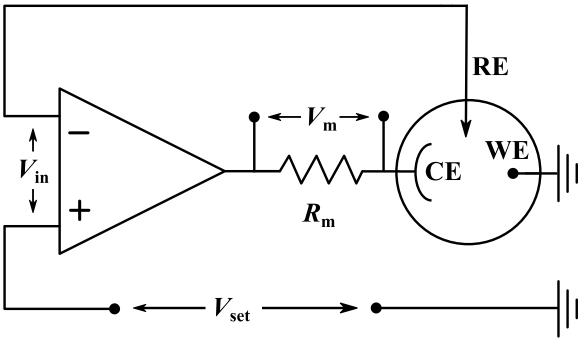

Figure 4-6: Schematic circuit of a potentiostat. The current flowing through the counter electrode causes the reference electrode to be at the same potential as V_set, with $V_\mathrm{in} = 0$. The current is then measured by the potential drop at R_m.

The potentiostat also requires a means to measure the current. One approach is to measure the potential drop across a resistor, shown in **Figure 4-6** as R_m. Another possible approach (not shown) is to use an additional circuit connected to the WE, a current follower, consisting of another operational amplifier. There, the WE is connected to the inverting input; the non-inverting input and the output are connected to ground; and a resistor connects the output to the inverting input. Thus, the output voltage is proportional to the input current by a scale factor determined by the resistor.

Alternatively, one can view the potentiostat as an active element whose job is to force through the working electrode whatever current that is required to achieve the desired potential at any time. Since the current and the potential are related functionally, that current is unique. Chemically, it is the flow of electrons needed to support the active electrochemical processes at rates consistent with the potential. Thus, the response from the potentiostat (the current) actually is the experimental observable.

In more complex apparatus, the potentiostat is connected to a function generator, which enables different types of experiments, including potential sweep measurements, which will be described in the following.

4.4.2 Potential sweep: Cyclic Voltammetry (CV)

The potential sweep technique [24] is a broadly used method in electrochemical studies. In this technique, the current through the WE (the response signal) is recorded while an applied potential (the excitation signal [28]) between WE and RE is varied linearly at a particular scan rate v (mV s^{-1}) between two values, E_1 and E_2. Normally, the chosen value for E_1 is the one at which no electrochemical activity exists, while E_2 is the value at which the reaction is mass-transfer controlled. In linear sweep voltammetry, the scan stops at E_2, whereas in cyclic voltammetry, the sweep direction is reversed when the potential reaches E_2 and the potential returned to E_1. This constitutes one cycle of the cyclic voltammogram. Multiple cycles may be recorded, for example, to study film formation or until the electrode is at a reproducible state.

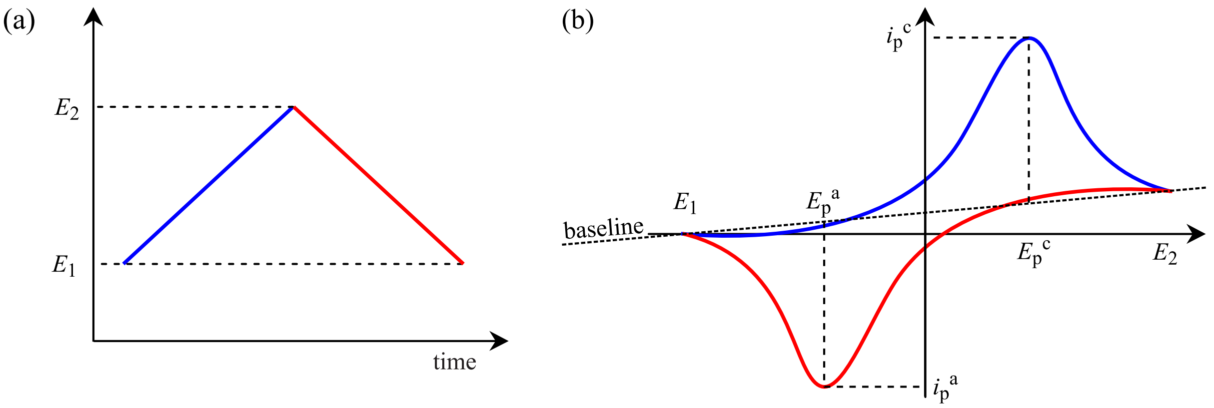

Figure 4-7: (a) Waveform used in classic cyclic voltammetry and (b) cyclic voltammogram (current-potential curve). This particular voltammogram depicts the behaviour of a reversible, diffusion-controlled system, with

symmetric anodic and cathodic peaks. At small potentials the redox reaction is limited by how fast charge-transfer occurs at the electrode, while at larger potentials the reaction is limited by how fast the redox species diffuse from the bulk towards the electrode, and vice-versa. The current peaks separate the two regimes.

Cyclic voltammetry is perhaps the most typical potential sweep method, and often the choice for the study of new electrochemical systems, since it allows a quick assessment of the reaction mechanisms, even when there are additional complications such as coupled homogeneous reactions, or surface adsorption, which can then be studied in more detail with other techniques. CV also provides quantitative information, as described next.

When looking at a system with cyclic voltammetry, it is useful first to carry out qualitative experiments. Typically, E_1, E_2, v (scan rate), pH and C_{O}^* (concentration) are varied systematically and the differences in the shape of the voltammogram are analysed. Points to note are the number of peaks present, their shape, their absolute value (current) and position (potential). By monitoring how each of them behaves, it is possible to derive mechanistic and kinetic information.

In a cyclic voltammogram, the magnitudes of the anodic peak potential $E_{\mathrm{p}}^{\mathrm{a}}$ and the cathodic peak potential $E_{\mathrm{p}}^{\mathrm{c}}$, along with their corresponding anodic peak current $i_{\mathrm{p}}^{\mathrm{a}}$ and cathodic peak current $i_{\mathrm{p}}^{\mathrm{c}}$, are important parameters (see **Figure 4-7**). In a redox couple reaction, if both species exchange electrons with the working electrode very fast, the system can be considered electrochemically reversible. The formal potential E^0 in this case is found at the centre, between $E_{\mathrm{p}}^{\mathrm{a}}$ and $E_{\mathrm{p}}^{\mathrm{c}}$:

$$E^0 = \frac{E_{\mathrm{p}}^{\mathrm{a}} + E_{\mathrm{p}}^{\mathrm{c}}}{2} \tag{4.4.1}$$

The peak-peak potential separation ΔE_{p} between $E_{\mathrm{p}}^{\mathrm{a}}$ and $E_{\mathrm{p}}^{\mathrm{c}}$ is dependent on the number of electrons n exchanged in the electrochemically reversible reactions, and can be expressed as follows:

$$\Delta E_{\mathrm{p}} = E_{\mathrm{p}}^{\mathrm{a}} - E_{\mathrm{p}}^{\mathrm{c}} \cong \frac{0.059}{n} \text{ (at 25 °C)} \tag{4.4.2}$$

Therefore, for a reversible one-electron transfer, ΔE_{p} should be about 0.059 V, which is independent of the scan rate v. However, if the system is irreversible due to slow electron transfer at the electrode surface, equation (4.4.2) is not applicable and the peak-peak separation will increase with increasing scan rate.

For a planar diffusion-controlled system, the peak current value can be estimated with the *Randles-Sevčik equation*:

$$i_{\mathrm{p}} = 0.4463 \frac{n^{3/2} F^{3/2}}{R^{1/2} T^{1/2}} A D_j^{1/2} C_j^* v^{1/2} \tag{4.4.3}$$

or

$$i_{\mathrm{p}} = 2.69 \times 10^5 n^{3/2} A D_j^{1/2} C_j^* v^{1/2} \qquad (4.4.4)$$

Since the number of transferred electrons n, the electrode area A and the diffusion coefficient D_j are all constants in a practical experiment, i_{p} is directly proportional to the bulk concentration C_j^* of species j in the solution and to the square root of the scan rate v. Once C is kept constant, i_{p} will only depend linearly on $v^{1/2}$. Note that equation (4.3.38) is analogous to equation (4.4.3) in that in the latter the current depends on $v^{1/2}$ while in the former it depends on $t^{-1/2}$.

The more an electrochemical system shifts from reversible to irreversible, *i.e.* from very fast to very slow electron transfer, the larger will be the peak-peak separation and the asymmetry between them. Ultimately, the reverse peak $i_{\mathrm{p}}^{\mathrm{a}}$ will disappear.

Potential sweep experiments are very sensitive to redox reactions involving adsorption of a reactant or a product. The cyclic voltammetry where both species O and R are adsorbed on the electrode surface is different to that when both are in solution, because there is no mass transport step to consider. The typical shape of a cyclic voltammogram for an ideal Nernstian electron transfer, with only short-range repulsive interactions between the adsorbates, consists of two symmetric peaks. The charges (the areas under the peaks) for oxidation and reduction are equal, as all the adsorbed species undergo reduction/oxidation. The current peaks and decays to zero because there is a fixed amount of reactant present.

In summary, a quick qualitative analysis of an electrochemical system can be done by looking at the peak-peak separation and peak heights in a cyclic voltammogram. One can quickly assess reversibility, transfer rates, adsorption, etc., as well as perform quantitative measurements with aid of special techniques which will be described next.

4.4.2.1 Nicholson's method

The mass transfer coefficient in linear sweep voltammetry and cyclic voltammetry is directly proportional to the square root of the potential scan rate, $v^{1/2}$, as expected from equations (4.4.3) and (4.3.35). In theory, by increasing v one can render a completely reversible (Nernstian) electrode reaction quasi-reversible, and even irreversible, in order to determine its kinetic parameters. In practice, this approach is limited by increasing non-faradaic currents at the double layer (due to charging and discharging) and increasing resistive potential drop in the solution.

A more straightforward method to extract kinetic parameters from a linear sweep voltammogram is possible for a one-step irreversible electron-transfer reaction at large (*e.g.* mm-sized) electrodes. The transfer coefficient α can be found from the slope of the linear dependence of the peak current *vs.* square root of the scan rate $(i_{\mathrm{p}} \text{ vs. } v^{1/2})$:

$$i_{\mathrm{p}} = 2.99 \times 10^5 \alpha^{1/2} A D^{1/2} C_j^* v^{1/2} \qquad (4.4.5)$$

Alternatively, the same parameter can be found from the difference between the peak-peak potential ΔE_{p} and the half-peak potential:

$$\alpha = \frac{47.7\ \mathrm{mV}}{\left|\Delta E_{\mathrm{p}} - E_{\mathrm{p}/2}\right|}\ \text{(at 25°C)} \tag{4.4.6}$$

where $E_{\mathrm{p}/2}$ is the potential where the current is half its peak value. The standard rate constant k_0 of a one-electron reduction reaction can then be found from:

$$\Delta E_{\mathrm{p}} = E^{0'} - \frac{RT}{\alpha F}\left(0.78 - \ln\frac{D_{\mathrm{O}}^{1/2}}{k_0} + 0.5\ln\frac{\alpha F v}{RT}\right) \tag{4.4.7}$$

where $E^{0'}$ is the formal potential and D_{O} is the diffusion coefficient of oxidised species.

Richard S. Nicholson developed a much simpler method to measure quasi-reversible kinetic parameters from voltammograms [29]. The only required experimental parameter is ΔE_{p} from equation (4.4.2). Nicholson has shown that ΔE_{p} is a function a single dimensionless kinetic parameter, so defined:

$$\psi = \frac{\left(D_{\mathrm{O}}/D_{\mathrm{R}}\right)^{\alpha/2} k_0}{\left(\pi D_{\mathrm{O}} v F/RT\right)^{1/2}} \tag{4.4.8}$$

After measuring ΔE_{p}, one can use **Table 4-1** to find the corresponding value of ψ and estimate k_0 . When the transfer coefficient α is within $]0.3, 0.7[$, which is most common for simple electron-transfer reactions, ΔE_{p} is essentially independent of α. Moreover, the diffusion coefficients of oxidised and reduced species are typically similar. Therefore $D_{\mathrm{O}}/D_{\mathrm{R}} \simeq 1$ and k_0 can be easily calculated from equation (4.4.8).

Table 4-1: Variation of ΔE_{p} with ψ at 25 °C [29].

ψ **from equation (4.4.8)**	ΔE_{p} (mV)
20	61
7	63
6	64
5	65
4	66
3	68
2	72
1	84
0.75	92
0.5	105
0.35	121
0.25	141
0.10	212

One very important condition for using this method safely is to take into account the resistive potential drop in the solution, which leads to higher ΔE_{p}, otherwise underestimated rate constants will be obtained. In fact, the more the cyclic voltammogram deviates from the simple quasi-reversible model (*e.g.* due to adsorption effects, high charging currents, etc.), the higher will be the error associated with Nicholson's method. Therefore, it may be safer to fit the entire voltammogram to the theory (*e.g.*, by using *DigiSim*®).

4.4.2.2 DigiSim simulation

Nowadays computational tools allow for more detailed analyses of the electrochemical data obtained with cyclic voltammetry. One of these tools is *DigiSim*®, developed by *Bioanalytical Systems Inc.*[30] This software is designed mainly for CV simulations and uses an implicit finite difference method to simulate any electrochemical mechanism that can be expressed in terms of single or multiple electron transfer reactions (recall the Butler-Volmer equation introduced earlier in section 3.3.2.2) and first- and second-order homogenous reactions.

To generate a theoretical curve using *DigiSim*®, it is necessary to select a model for the kinetics (*e.g.* Butler-Volmer, Marcus) involved in the desired electrochemical/homogeneous reactions, define certain conditions/constraints of the system and feed known values in, such as rate constants, diffusion coefficients, etc. The simulation results include concentration profiles of all species involved at any point in time, and current *vs.* time dependencies. The effects of the double layer charging and the resistive potential drop in solution can also be included.

Last but not least, *DigiSim*® can fit simulated data to imported experimental data and extract key parameters for the experimentalist, such as rate constants (k), transfer coefficients (α), etc.

4.4.3 Scanning Electrochemical Microscopy (SECM)

SECM is a scanning probe microscopy technique in which three-dimensional images of surfaces are obtained by scanning a small ultramicroelectrode (UME) tip (also referred to as the probe) across the working electrode (WE) surface and recording an appropriate electrical response. To understand the operation and response of the SECM, it is necessary to briefly review the behaviour of a very small probe in an electrochemical cell. For a more detailed discussion of UMEs than the one which will follow, consult reference [24], chapter 6.

If one considers a metallic UME (the cross section of a wire, laterally insulated) with a few μm in diameter, immersed in a solution containing an electrolyte and an electroactive species O; counter electrode (CE) and reference electrode (RE) also being present; then when a potential $E - E^{0'}$ sufficiently negative is applied to the UME, the reduction of O to R occurs on its surface at a diffusion-controlled rate, and a corresponding current is detected passing through the UME. This current decays as a diffusion layer of O builds up around the electrode, attaining rather quickly a steady-state value, $i_{\mathrm{T},\infty}$, which depends on the concentration C_{O}^{*} of O species and on its diffusion coefficient, D_{O}, and is given by:

$$i_{\mathrm{T},\infty} = 4nFD_{\mathrm{O}}C_{\mathrm{O}}^{*}r \tag{4.4.9}$$

where n is the number of electrons involved in the electrode reaction, F is the Faraday constant, and r is the radius of the UME. The steady-state current results from the constant flux of O species to the UME's surface driven by an expanding, essentially hemispherical, diffusion layer around it. In SECM it is the perturbation of the tip current, when the tip is brought to within a few tip diameters of a surface, which constitutes the SECM response.

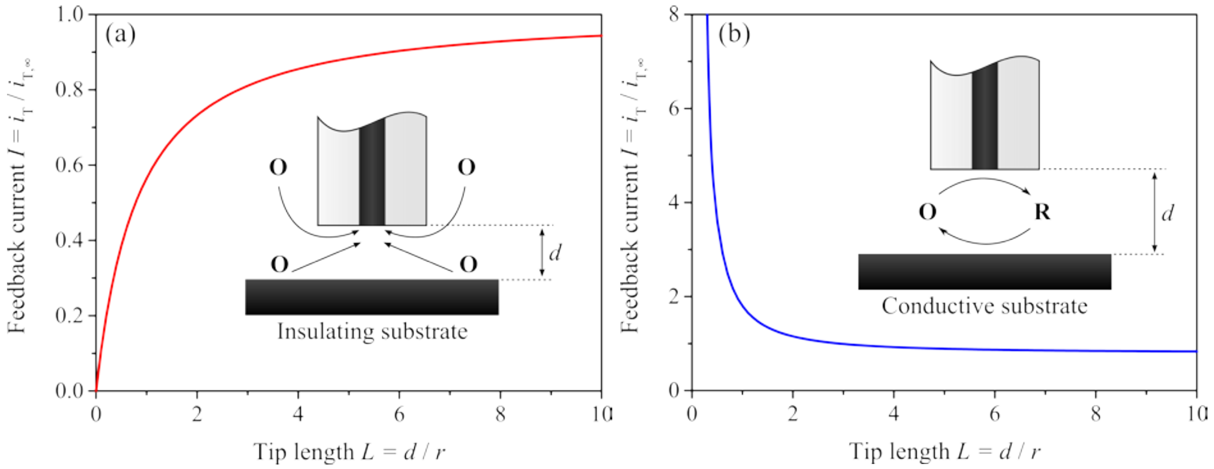

Figure 4-8: SECM approach curves on insulating (a) and conductive (b) substrates. Negative feedback is observed on an insulating substrate and positive feedback is observed on a conductive substrate.

Consider first when the tip is brought close to an insulating substrate, as shown in **Figure 4-8** (a). The steady-state current flowing through the tip, i_{T}, will now be smaller than $i_{\mathrm{T},\infty}$, because the insulating substrate partially hinders the diffusion of O from the bulk solution to the tip. Clearly, the closer the tip is to the insulating surface, the smaller i_{T} will be, up to the point when $i_{\mathrm{T}} \to 0$ as the tip-substrate separation *d* approaches 0. This effect is termed “negative feedback”. However, when the tip is close to a conductive substrate at which R can be oxidised back to O, an immediate source of O is established, which adds to contribution from the bulk. Oxidised species are more readily available to react again with the tip by diffusing back from the substrate, resulting in $i_{\mathrm{T}} > i_{\mathrm{T},\infty}$ as the tip gets nearer. This behaviour is termed “positive feedback” and is illustrated in **Figure 4-8** (b). Thus, the magnitude of i_{T} relative to $i_{\mathrm{T},\infty}$ is governed by the nature of the substrate (*i.e.* its electrical properties) and by the tip-substrate spacing (surface topography is therefore also a factor). The actual general situation can be more complicated than those two limiting cases described above, for example, when the rate of the reaction $\mathrm{R} \to \mathrm{O} + e^{-}$ on the substrate is governed by the kinetics of heterogeneous electron-transfer rather than by the rate of mass transfer (diffusion) of R to the substrate.

When the UME tip is scanned across the substrate surface at a constant height, an image of the local electrochemical activity can be obtained by monitoring the feedback current. The current image can be presented in grey scale, where high values of current are shown in light colours and small values as dark colours. The resolution attainable with SECM is largely governed by the tip size and the distance between tip and sample. With a very small diameter tip (*e.g.*, $\text{diameter} < 100\ \text{nm}$), scanning the tip in close proximity to the substrate surface (*e.g.*, 100 nm above the surface) and measuring the current becomes very difficult due to vibrations. For higher resolution, SECM must be carried out in constant current mode, as is often used with STM, where the distance is adjusted by a feedback loop to a *z*-piezo to maintain i_{T} constant. This method works when the sample is either all conductive or all insulating, as the piezo feedback can be set to counter a decrease in tip current by either moving the tip closer (conductor) or farther away (insulator). However, for samples containing both types of regions the vertical motion of the tip has to be modulated while $\partial i_{\mathrm{T}} / \partial z$ is monitored, in order to identify the type of response.

In any case, the most important aspect to retain about SECM is that it can provide a map of the electrochemical activity across an electrode surface, allowing the correlation of local features such as topography, conductivity, surface termination/functionalisation and other material properties, with the reactivity of the redox species in solution.

4.4.4 Electrochemical impedance spectroscopy (EIS)

EIS is a very powerful technique used to study dielectric properties of electrochemical systems through their treatment as equivalent electric circuits. From the measurement and subsequent non-linear regression of the system’s frequency-dependent complex impedance, its constituents (*e.g.* diffusion layers, interfaces) and related physical properties can be discriminated and quantified. In other words, depending on the specific contribution of each element to the total impedance, *i.e.*

whether more capacitive or more resistive, and on their particular response to the applied frequency spectrum, detailed information about charge transport across the system can be obtained. EIS is typically used in the study of corrosion, fuel cells, batteries, super capacitors, solar cells, etc. Comprehensive information on EIS can be found on [27, 31].

An impedance spectroscopy measurement requires applying an alternating voltage $V(t)=|\Delta V|\cos(\omega t)$ to the system – for example, between electrodes in an electrochemical cell – and measuring its current response $I(t)=|\Delta I|\cos(\omega t+\varphi)$, where φ is the phase difference between input voltage and output current. From the input voltage and the output current, the impedance *Z*, defined as $Z=V/I$ can be obtained. After a few mathematical considerations it results in $Z=|Z|e^{-i\varphi}$, with $|Z|=|\Delta V|/|\Delta I|$ being its magnitude and $i=\sqrt{-1}$ the imaginary unit. This measurement is performed for a wide range of frequencies, so that one obtains an impedance spectrum. Given that *Z* is a complex value, it can either be represented as $|Z|$ and φ or as $Z'=\mathrm{Re}(Z)$ and $Z''=\mathrm{Im}(Z)$ as a function of frequency, *i.e.* usually the ordinary frequency $f=\omega/2\pi$.

A very important condition for impedance spectroscopy is the consistency between the real and imaginary parts of the impedance, which is achieved when the Kramers-Kronig relations are satisfied [31]. They imply that the system's response to an input signal respects stability over time, linearity and causality. For this reason the system must remain in a quasi-steady state, driven by a low amplitude input signal (small perturbation), usually in the range of 10 mV.

With state-of-the-art equipment, much of the work involved in performing impedance spectroscopy is automatised and easily done through a simple software interface (which is usually provided with the commercial impedance analyser or potentiostat). Suppliers of such devices, *e.g. Gamry Instruments* and *Metrohm Autolab* go as far as to provide full support for data analysis, fitting and modelling, etc., as well as to consider special cases of impedance measurements. Other optional software tools include *ZView*®/*ZPlot*® [32] and *ZSimpWin* [33].

Apart from typical, well-known impedance elements, such as resistors, capacitors and inductors, a couple of other elements are worth of mention: the *constant phase element* (CPE) and the *Warburg impedance element* (W). The impedance response of electrodes rarely shows the ideal response expected for single electrochemical reactions. Instead, it typically reflects a distribution of reactivity that is commonly represented in equivalent electrical circuits as a CPE, which has an impedance contribution given by [27]:

$$Z_{\mathrm{CPE}}=\frac{1}{(i\omega)^{n}Q_{0}}\ (\Omega) \tag{4.4.10}$$

where *n* is unitless and ranges from 0 to 1, and Q_0 $(\mathrm{s}^n\Omega^{-1})$ is a parameter given in Farads only when $n=1$, *i.e.* when the impedance of a CPE simplifies to that of an ideal capacitor. At the other extreme, when $n=0$, Z_{CPE} simplifies to the impedance of a resistor, with Q_0 becoming a conductance value. Hence, the CPE can be understood as a leaking capacitor with a frequency-independent phase of $-(90\times n)^{\circ}$, and its behaviour is often attributed to surface heterogeneity or to continuously distributed time constants for charge-transfer reactions. An equivalent capacitance $C_{\mathrm{eq.}}$ (F) can be extracted from the CPE by [34]:

$$C_{\mathrm{eq.}} = \left(i\omega_{\max}\right)^{(n-1)} Q_0 \tag{4.4.11}$$

where $\omega_{\max}$ is the maximum point of the depressed semi-circle produced by the CPE in a *Nyquist plot* (*i.e.* Z'' vs. Z'). At that point the real part of the impedance is independent of *n*, and consequently $Z_{\mathrm{C,eq.}} = Z_{\mathrm{CPE}}$.

The Warburg impedance element W models a simple semi-infinite planar diffusion mechanism taking place in an electrochemical reaction. In stagnant environments, if natural convection can be ignored, the mass transport equation is reduced to Fick's second law, shown in equation (4.3.34). With semi-infinite boundary conditions defined, one can correlate the current generated by an oscillating potential-dependent concentration of species *C* at the electrode with the applied potential, and obtain the corresponding impedance [27]:

$$Z_{\mathrm{W}} = \frac{W}{\sqrt{i\omega}} \ (\Omega) \tag{4.4.12}$$

with *W* being the Warburg constant, which contains parameters pertaining to the diffusion process (presented in Section 4.3.3):

$$W = \frac{\pi\sqrt{2}}{nFAD^{1/2}C^{*}} \ (\Omega\ \mathrm{s}^{-1/2}) \tag{4.4.13}$$

The *Randles circuit* shown in **Figure 4-9** is a well-known model of a simple electrochemical system, consisting of a CPE representing the double layer, a charge transfer (parallel) resistance representing a faradaic (redox) reaction, a Warburg impedance element representing the diffusion of redox species towards the electrode, and a bulk (series) resistance.

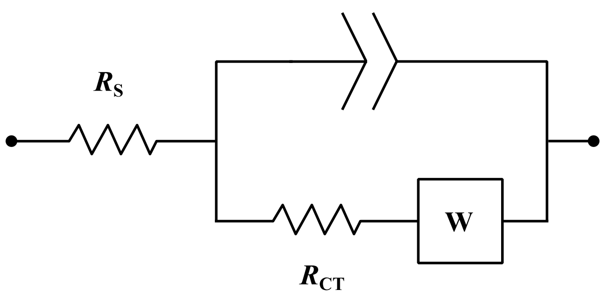

Figure 4-9: Randles circuit, consisting of a constant phase element (sometimes simplified to a capacitor C_{P}) representing the Helmholtz (double layer) capacitance, in parallel with a charge-transfer resistance R_{CT} in series

with a Warburg impedance element, to account for diffusion-limited charge transfer processes, and a series resistance R_S to account for the bulk electrode and electrolyte resistances.

In the particular case of a semiconductor-electrolyte interface, the existence of a space charge at the semiconductor surface introduces another capacitance source to C_P (see **Figure 4-3**), but as long as the electrolyte is conductive enough, $C_\mathrm{H} \gg C_\mathrm{SC}$ and consequently $C_\mathrm{P} \cong C_\mathrm{SC}$, as it is for the semiconductor-metal junction.

One particular case of impedance spectroscopy consists in superimposing a DC voltage, V_bias, on the input signal and measuring the capacitance of the system for a single frequency, assuming a pre-determined model or equivalent circuit, *e.g.* resistor-capacitor in series. The measurement is repeated for a range of DC values and plotted as $1/C^2$ *vs.* V_bias. It is particularly useful for the Mott-Schottky analysis described next, and is often referred to as C-V plot.

4.4.5 Mott-Schottky analysis

The Mott-Schottky analysis takes advantage of the C-V measurement capabilities of impedance analysers to allow the study of semiconductor-electrolyte and semiconductor-metal interfaces by means of the Mott-Schottky relationship [23, 35]:

$$\frac{1}{C_\mathrm{SC}^2} = \frac{2}{qN_\mathrm{A}\varepsilon_0\varepsilon_\mathrm{r}A^2}\left[\left(V_\mathrm{bias} - V_\mathrm{FB}\right) - \frac{\mathrm{k_B}T}{q}\right] \tag{4.4.14}$$

where C_SC (F) is the space-charge capacitance, q (C) is the electron's charge, N_A (m^{-3}) is the density of acceptors for a p-type semiconductor, ε_0 ($\mathrm{F\ m}^{-1}$) and ε_r (unitless) are, respectively, the vacuum dielectric permittivity and the relative dielectric permittivity of the electrode, A (m^2) is the electrode area in contact with the electrolyte, V_bias (V) is the applied potential, V_FB (V) is the flatband potential, $\mathrm{k_B}$ ($\mathrm{m^2\ kg\ s^{-2}\ K^{-1}}$) is Boltzmann's constant and T (K) is the absolute temperature. This equation is derived considering that a space charge at the semiconductor surface exists when a junction with another material is formed, such as with a metal or a conductive electrolyte. The space charge can be treated as a capacitor and the capacitance written as a function of the space charge (depletion layer) width, which depends on the potential drop across the junction [35].

A semiconductor-metal junction (also known as a Schottky diode) is relatively simple, because metals are highly conductive, electrons are abundant and free to move, and charge transfer is rapid. There are no diffusion mechanisms to account for, and the only capacitive element in the circuit, ideally speaking, is the space charge capacitance. Under these circumstances, a semiconductor-metal interface can be modelled by a simple RC circuit. Likewise, a semiconductor-liquid interface can be treated in a similar way when the electrolyte is made highly conductive and when it is devoid of redox mediators. Then, looking at the Randles circuit (**Figure 4-9**) as a reference, the charge-transfer resistance R_CT and the Warburg element W are, in this case, absent.

An accurate measurement of C_{SC} for the Mott-Schottky equation (4.4.14) can be done by performing Impedance Spectroscopy for a fixed frequency and varying the bias voltage. The experimental data can then be fitted with appropriate analysis software and the capacitance C_{SC} extracted. The density of acceptors N_{A} is obtained from the slope of $1/C_{\mathrm{SC}}^2$ *vs. V*. A straight line indicates that the depletion layer width changes according to the applied potential, as expected from a capacitive behaviour, and the Mott-Schottky relationship can be applied. Deviations from this linearity point to the presence of other effects in the junction, which may be due to other capacitive sources and/or non-capacitive behaviour from, *e.g.* contaminants on the surface or in the electrolyte. Such factors will have implications on the validity of the Mott-Schottky relationship for the extraction of C_{SC} and N_{A}.

4.5 Experimental

As mentioned earlier, this work was a result of a close collaboration with the group of Prof. Dr John S. Foord from the Department of Chemistry in the University of Oxford. Heteroepitaxial diamond samples were prepared in our facilities and the electrochemical measurements were performed in Oxford. The author of this thesis participated directly in the initial experimental characterisations, while the remaining work was completed by the Oxford team. The analysis and discussion of the results are the outcome of a collective effort.

4.5.1 Preparation of diamond electrodes

The heteroepitaxial B-doped diamond single crystals were grown on a Ir/YSZ/Si(001) substrate with a 4° off-axis angle towards [110]. The preparation of the substrate followed identical procedures to those described earlier in the previous chapters, and according to [36-38]. After the bias-enhanced nucleation (BEN) step, an intrinsic diamond film of ~80 µm in thickness was grown by MWPCVD with addition of 100 ppm N_2 to the gas phase, and followed by the growth of a boron-doped layer of around 3 µm thickness in a separate MWPCVD reactor. The feedstock gases consisted of 2% CH_4 in H_2 and 300 ppm trimethylborane (TMB). BDD deposition was conducted at 750 °C at 50 mbar and a microwave power of 1100 W. The final sample size was $\sim 8 \times 8\ \mathrm{mm}^2$ (see **Figure 4-10**).

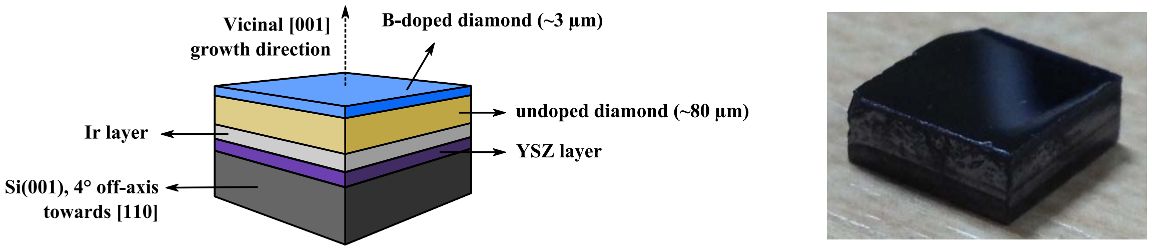

Figure 4-10: (left) Sketch of the multilayer sample structure. (right) Image of the actual sample.

In fact, two similar but not identical samples were produced and analysed: sample “A” with as-grown diamond layer and sample “B” with both layers polished after growth. The latter was not used until the studies presented in section 4.6.4.

Rocking curves measured by high-resolution X-ray diffraction showed a full width at half maximum (FWHM) of 0.15°, confirming the high crystalline quality of the heteroepitaxial diamond layer. The as-grown BDD film without polishing has a wavy surface structure with RMS roughness of 0.7 nm, which was reduced to below 0.12 nm after polishing, based on AFM measurements within a scan area of $1\times1\,\mu\text{m}^2$.

Freestanding polycrystalline BDD wafers with $[\text{B}] > 10^{20}\ \text{cm}^{-3}$ and $10\times10\times0.6\ \text{mm}^3$ were obtained from *Element Six Co*. The rough polycrystalline BDD was polished smooth to an RMS roughness of less than 3 nm, to be easily comparable with the smooth single crystalline BDD electrodes.

A similar cleaning process was carried out on all BDD samples before use. The electrodes were gently polished with alumina (1 µm and 0.3 µm) to remove most of the physically adsorbed impurities on the surface. All samples were subsequently cleaned with acetone in an ultrasonic bath to remove alumina residues, followed by rinsing in distilled water and finally blow-dried with N_2.

The BDD samples were mounted into a home-built PTFE cell with a circular area of around 0.454 cm^2 exposed to the electrolyte. Silver paste was applied from the four corners on the surface, around and to the Si backside of the heteroepitaxial samples, in order to form Ohmic contacts for the electrochemical experiments.

In order to assure reproducibility of the experiments, the samples were potential-cycled between −1.8 and 2.5 V for at least 20 sweeps in 0.1 M HNO_3, to promote a stable oxygenation of the diamond surface [4].

4.5.2 Characterisation techniques

All electrochemical experiments involving cyclic voltammetry (CV) were done at room temperature with a µ-AUTOLAB III potentiostat (PGSTAT128N, *Eco-Chemie*, Netherlands) running a GPES (Version 4.9) software. A standard three-electrode system consisting of the working electrode (sample), a *silver-silver chloride* (Ag/AgCl) reference electrode and a Pt wire counter electrode was employed.

Electrochemical impedance spectroscopy (EIS) measurements were operated on the same workstation with a Frequency Response Analysis (FRA) module of type III µ-Autolab. A modulation amplitude of 10 mV was applied and the frequency varied between 0.1 Hz and 500 kHz. The supplied FRA software was used for data conversion and analysis.

Scanning electrochemical microscopy (SECM) was carried out with a commercial CHI 900B setup. Instead of using the three-electrode configuration mentioned for the previous methods, a four-electrode configuration was introduced: the BDD working electrode, an Ag/AgCl reference electrode, a Pt wire counter electrode, and a fourth Pt microelectrode. It consists of a Pt wire sealed into a quartz capillary by the laser puller method. The electrode was delicately polished until the diameter of the wire was ~4 µm and the insulation radius $r_{\mathrm{quartz}}/r_{\mathrm{Pt}} < 5$. This probe electrode, positioned initially at 2 µm above the WE, was used to measure approach curves towards the diamond surface at a rate of 0.1 µm s^{-1}. Depending on whether the oxidised species leaving the probe, *e.g.* $\mathrm{Ru(NH_3)_6^{3+}}$, diffused to an electrochemically active or inactive site on the diamond surface, the current through the approaching probe showed, respectively, negative or positive feedback, as illustrated in **Figure 4-8**. In this current *vs.* distance plot, which carries information about electrochemical characteristics of the studied electrode [39], *L* corresponds to a "tip length", *i.e.* the distance *d* between the probe and the substrate normalised to the tip radius *r*, and *I* corresponds to the measured current $i_{\mathrm{T}}(L)$ normalised to the steady-state current $i_{\mathrm{T},\infty}$ far away from the substrate. By scanning the probe across the electrode surface at a fixed height and fixed scan rate of 2.5 µm s^{-1} (thanks to *x*-*y* positioning motors) while measuring the current through the probe using different mediator electrolytes, several maps of the electrochemical activity were traced.

Finally, SEM (scanning electron microscopy) characterisation was done using a Hitachi S530 SEM with acceleration voltage of 20 kV.

4.5.3 Chemicals

Hexaamineruthenium(III) chloride ($\mathrm{Ru(NH_3)_6Cl_3}$, 98%), potassium ferrocyanide ($\mathrm{K_4Fe(CN)_6}$, 98.5%), potassium ferricyanide ($\mathrm{K_3Fe(CN)_6}$, $>99.99\%$), methyl viologen (MV, 98%) and anthraquinone-2,6-disulfonate (2,6-AQDS, 90%, mixture of isomers) were obtained from *Sigma-Aldrich* and directly used as redox mediators in electrochemical experiments without any further purification. 0.1 M KCl was selected as a supporting electrolyte for $\mathrm{Ru(NH_3)_6^{3+}}$, $\mathrm{Fe(CN)_6^{4-}}$ and methyl viologen, and 0.1 M $\mathrm{HClO_4}$ was used for AQDS. All the solutions were prepared with *Milli-Q* water (>18 MΩ cm) and bubbled with nitrogen to remove dissolved oxygen before each measurement.

4.6 Results and discussion

4.6.1 CV and EIS characterisations

The electrochemical characterisation of the BDD electrodes started with cyclic voltammetry (CV) measurements in 0.1 M $\mathrm{HNO_3}$ to compare the potential window for water hydrolysis and the background current of the following samples:

- The heteroepitaxial sample "A" (as-grown surface);
- The polished/smooth polycrystalline sample;
- The as-grown rough polycrystalline sample.

Scans were performed from −1.8 to 2.5 V and the results are shown in **Figure 4-11**. Defining 200 µA cm^{-2} as the limiting current for the potential window, it can be seen that both polycrystalline samples present similar potential window of about 2.9 V, while the heteroepitaxial sample presents a higher value of about 3.3 V. In other words, the available potential window for electrochemical applications, such as for electrochemical sensing, provided by the heteroepitaxial diamond is significantly wider than that of polycrystalline diamond. In **Figure 4-11** (a), hydrogen evolution starts at a very negative potential on all samples, but is particularly strongly inhibited on the heteroepitaxial sample. A similar result has been reported by Kondo *et al.* [17] on homoepitaxial diamond. The authors attributed the greater width of the potential window to a much lower boron concentration, *i.e.* 2×10^{18} cm^{-3} in their case, which was about two orders of magnitude less than that of the polycrystalline diamond. In our study, the dopant concentration was estimated from the Mott-Schottky measurements discussed below, and has a value of $[\mathrm{B}]_{\mathrm{A}} = 1.4\times10^{20}\,\mathrm{cm}^{-3}$ for the heteroepitaxial sample and $[\mathrm{B}]_{\mathrm{poly}} = 9.5\times10^{20}\,\mathrm{cm}^{-3}$ for the polycrystalline samples. Although the former value is still lower than the latter, other polycrystalline diamond samples with comparable boron concentration (1.7×10^{20} cm^{-3}) shows a restricted potential window of around 2.5 V, measured in 0.1 M H_2SO_4 [17]. The conclusion is, therefore, that the difference in doping level plays a partial, if not minor, role in defining the potential window, and that other factors must be involved. Studies of the hydrogen evolution reaction on diamond [40] indicate that the rate-limiting step involves adsorption of H_3O^+ on the electrode surface. Presumably, the comparative lack of grain boundaries and surface defects on the heteroepitaxial diamond electrode's surface significantly impedes this adsorption process, leading to the enhanced potential window at cathodic potentials.

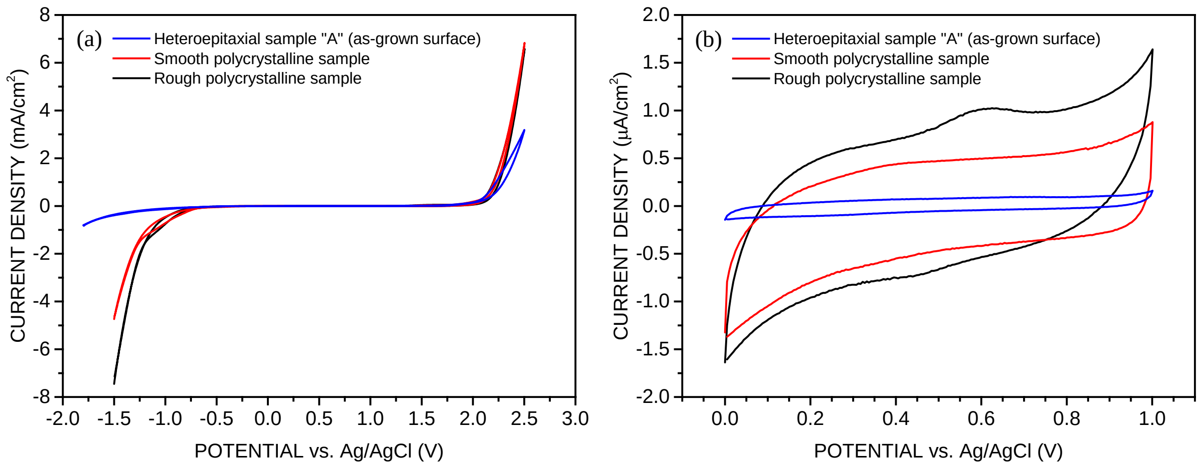

Figure 4-11: CVs of the tree different BDD electrodes, performed in 0.1 M HNO_3 at a scan rate of 100 mV s^{-1} showing (a) the potential window and (b) the background current.

Apart from the wider potential window, the heteroepitaxial BDD also exhibits an approximately 5 to 10 times lower background current than polycrystalline diamond, as presented in **Figure 4-11** (b). The background current is about 0.9 to 1.4 µA cm^{-2} for both polycrystalline samples throughout the measured potential range, which is in line with values reported in the literature [17, 41]. In contrast, the background current density of the heteroepitaxial sample is only around

0.13 µA cm^{-2}, a value comparable with observations on a hydrogen-terminated homoepitaxial diamond of lower boron concentration [17]. Thus, it is clear that not only the heteroepitaxial diamond electrode is superior than the polycrystalline electrodes, but also on par with high-quality homoepitaxial diamond electrodes, offering both low background current and wide potential window. The featureless background current of the heteroepitaxial sample is mainly due to a much lower double layer capacitance, caused by a ~6 times lower doping concentration, along with a comparatively lower density of electrically active defects. Furthermore, its surface has fewer active redox functionalities, which also contribute to the observed featureless profile. As for the two types of polycrystalline diamond electrodes, the as-grown rough diamond shows a slightly larger background current density compared to the polished one, probably due to a larger effective surface area. Again, these differences point to the advantages of using diamond single crystals in applications such as electrochemical sensors, where lower background currents can lead to enhanced detection limits.

The double layer capacitance was further evaluated by impedance spectroscopy measurements in 1 mM $\mathrm{Fe(CN)}_6^{3-/4-}$ and $\mathrm{Ru(NH_3)}_6^{3+/2+}$ in 0.1 M KCl. The measured results were fitted to the Randles circuit (see **Figure 4-9**). The results for ferrocyanide are shown in **Figure 4-12** and the extracted parameters for both ferrocyanide and RuHex are summarised in **Table 4-2**.

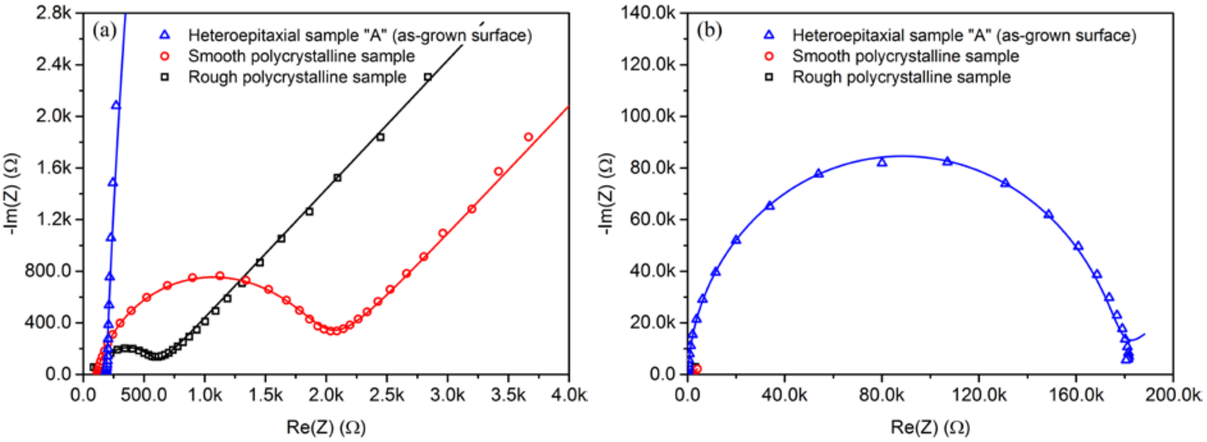

Figure 4-12: (a) Nyquist impedance plots of the diamond electrodes measured in 1 mM $\mathrm{Fe(CN)}_6^{3-/4-}$ in 1 M KCl. An expanded view of the data is shown in (b). The impedance data was fitted to the Randles circuit shown in **Figure 4-9**.

The curves in **Figure 4-12** show essentially two features in varying relative proportions: a semi-circle which contains the CPE and the charge-transfer resistance (kinetics region), and a straight line due to the Warburg impedance (diffusion region). Visually, the larger semi-circles already indicate larger charge-transfer resistance values, which were confirmed by fitting (see **Table 4-2**). The higher charge-transfer resistance for the heteroepitaxial diamond can be attributed, for both mediators, to its slightly lower doping level (and therefore lower conductivity). In the particular case of ferrocyanide, where the differences in charge-transfer resistance are larger, the more pristine surface of the heteroepitaxial diamond is likely also a factor.

The fitting of the impedance data shown above yielded significantly different capacitance values of ~0.7 µF and ~3 µF for, respectively, the heteroepitaxial and the smooth polycrystalline electrodes. Measurements done in $\mathrm{Ru(NH_3)_6^{3+/2+}}$ yielded similar values of, respectively ~0.6 µF and ~2 µF. The higher capacitance value of the polycrystalline sample is similar to those reported in the literature [2, 42]. This capacitance usually reflects the space charge capacitance C_{SC} at the semiconductor surface, as the double layer capacitance C_{H} at the electrode-electrolyte interface is usually an order of magnitude larger and can be neglected [43]. The capacitance difference between the different electrodes can be attributed to the different doping levels, as well as to variations of the surface O-/H-termination and to the presence of defects. More on this issue will be discussed below in the Mott-Schottky analysis.

The parameter *n* from the CPE in the equivalent circuit describes how close the interface (in this case, the solid-liquid junction) is to an ideal capacitor. The deviation from ideal behaviour is usually attributed to impurities/defects and to an inhomogeneous distribution of electrochemically active regions on the surface, leading to a frequency dispersion of the capacitance [44, 45]. The fitted equivalent circuit yielded $n = 0.97$ for the heteroepitaxial diamond and $n = 0.86$ for the smooth polycrystalline diamond, both in ferrocyanide, and $n = 0.96$ and $n = 0.59$ for the same electrodes in RuHex. The trend is the same with both mediators and it shows that the heteroepitaxial diamond electrode forms a more homogeneous junction with the solution, *i.e.* with respect to the electrochemical behaviour the surface is more homogeneous. This is attributed to the single crystal nature of the heteroepitaxial diamond, in which crystal growth is limited to one single type of growth sectors, in this case $\{001\}$. As a consequence, boron incorporation it not only quite homogeneous, but also the density of defective structures, *e.g.* with $\mathrm{sp^2}$ carbon, is minimised due to the absence of large-angle grain boundaries. The lower *n* obtained from the polycrystalline diamond reflects the fact that its surface contains different crystallographic facets with different boron concentration (and therefore different conductivity), as well as non-diamond phases and/or other defects on its grain boundary-rich surface [46, 47].

The series resistance R_{S} obtained from the fitting procedure resulted in very similar values, regardless of the mediator, with the two polycrystalline samples having practically the same values (~112 Ω) and the heteroepitaxial sample having slightly higher values (~200 Ω in average). These values originate from the resistance across the diamond films and from cables and electric contacts, since a highly conductive electrolyte (0.1 M KCl) was used. The higher resistance value of the heteroepitaxial sample is consistent with lower doping level, absence of conductive graphitic channels in the bulk, and to the indirect electric contact using silver paste/paint around the wafer. The series resistance was used to correct the potential drop, iR_{S}, in experiments later described, and to fit the data using *DigiSim*®. The impedance data measured with both mediators are generally consistent, despite some minor differences.

The electrochemical behaviour of the diamond electrodes was further examined by cyclic voltammetry with the outer-sphere and inner-sphere redox mediators, respectively $\mathrm{Ru(NH_3)_6^{3+}}$ and $\mathrm{Fe(CN)_6^{4-}}$. The first results are shown in **Figure 4-13** (a) and (b), respectively.

In the case of RuHex, both types of polycrystalline diamond show a similar peak position with approximately 95 mV peak-peak separation and comparable peak current densities for CV performed at 100 mV s^{-1}. The heteroepitaxial diamond shows, however, a ~30% lower peak current density and a much higher peak-peak separation of 171 mV, suggesting slower electron transfer kinetics on this electrode, likely due to the slightly lower doping level.

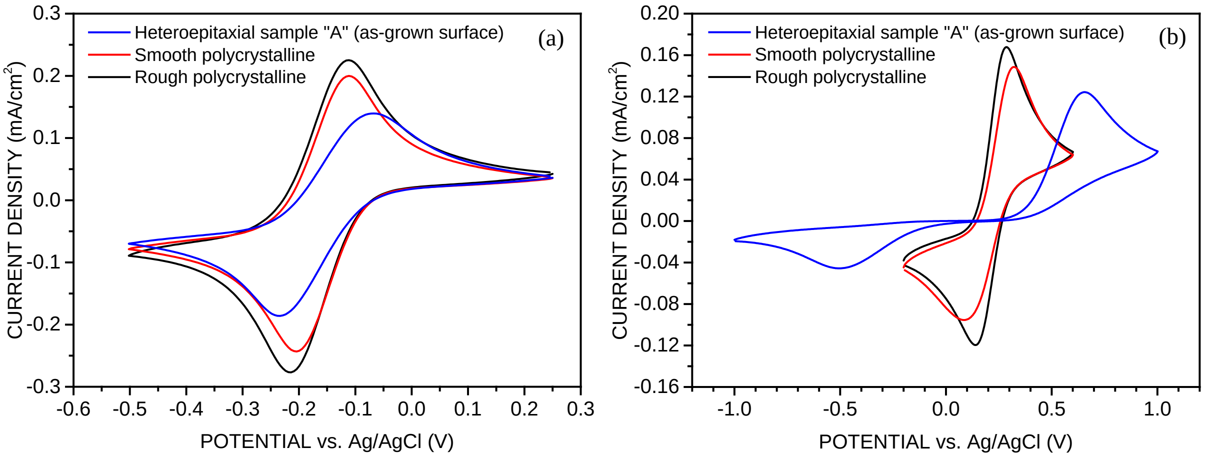

Figure 4-13: CVs of the different diamond electrodes performed in (a) 1 mM $Ru(NH_3)_6^{3+}$ in 0.1 M KCl at a scan rate of 100 mV s^{-1} and in (b) 1 mM $Fe(CN)_6^{4-}$ at 100 mV s^{-1}.

In the case of ferrocyanide, the performance of the two polycrystalline diamond electrodes resulted also very close, with similar peak-peak separation and peak current densities. However, the CV of the heteroepitaxial diamond showed a much larger peak-peak separation of ~1.2 V and lower peak current densities. This is a first indication of electron transfer being hindered on the heteroepitaxial diamond surface due to the higher material purity/quality when compared with the polycrystalline samples.

To deepen the analysis of their electrochemical behaviour, different scan rates were used in further CV measurements of the diamond electrodes, using the same mediator concentration. The results are shown in **Figure 4-14** (a). The peak current density is found to be proportional to the square root of the scan rate on all three electrodes, suggesting planar diffusion control and Nernstian behaviour. This result is in contrast to an observation on polycrystalline diamond with lower doping level [48], which exhibits a nonlinear relationship between the peak current density and the square root of scan rate.

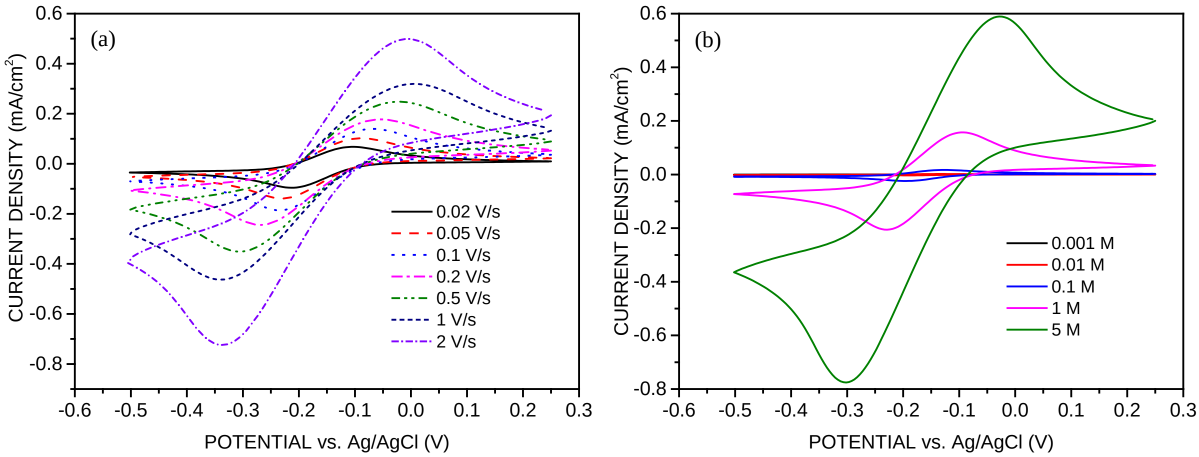

Figure 4-14: CVs of the heteroepitaxial sample "A" in (a) 1 mM $Ru(NH_3)_6^{3+}$ in 0.1 M KCl at different scan rates and (b) in different concentrations of $Ru(NH_3)_6^{3+}$ at a scan rate of 100 mV s^{-1}.

Table 4-2: Summary of the results using $Ru(NH_3)_6^{3+}$ and $Fe(CN)_6^{4-}$, highlighting the heterogeneous electron transfer rate constant k_0 calculated from the Nicholson method, *DigiSim*® and impedance spectroscopy fitting.

		$Ru(NH_3)_6^{2+/3+}$			**$Fe(CN)_6^{3-/4-}$**		
		Heteroepi. BDD "A"	**Smooth BDD**	**Rough BDD**	**Heteroepi. BDD "A"**	**Smooth BDD**	**Rough BDD**
	E_p (mV)	347(a)	209(a)	201(a)	-	234(b)	244(b)
Nicholson method	E_p (mV)(c)	260	99	110	-	219	211
	k_0 (µm s^{-1})	24.5	290	161	-	9.20	20.6
***DigiSim*® simulation**	k_0 (µm s^{-1})(d)	25.2	320	213	0.25	5.84	17.2
	α (unitless)	0.49	0.56	0.55	0.81	0.46	0.54
Impedance(e)	R_S (Ω)	213	112	112	189	112	123
	R_{CT} (Ω)	657	20.1	41.9	175×10^3	1.83×10^3	449
	Q_0 (s$^{\alpha}$MΩ^{-1})	0.868	132.8	137.3	0.854	7.77	3.69
	n_{CPE} (unitless)	0.96	0.59	0.61	0.97	0.86	0.91
	$C_{SC,\,eq.}$ (µF)(f)	0.637	2.19	4.76	0.741	3.08	1.87
	k_0 (µm s^{-1})(g)	17.8	583	280	0.067	6.43	26.2

(a) Values measured at a scan rate of 1.0 V s^{-1}.
(b) Values measured at a scan rate of 0.1 V s^{-1}.
(c) iR_S-corrected peak-peak separation values.
(d) k_0 acquired at a scan rate of 500 mV s^{-1}, 1 V s^{-1}, 2 V s^{-1} using *DigiSim*® fitting.
(e) Impedance characterisation performed at the formal (open circuit) potential in solutions containing either 1 mM $Ru(NH_3)_6^{3+/2+}$ or 0.5 mM $Fe(CN)_6^{4-}$ with 0.5 mM $Fe(CN)_6^{3-}$.
(f) $C_{SC,\,eq.}$ calculated using equation (4.4.11).
(g) k_0 calculated using equation (4.6.1).

Further CV measurements were carried out with the heteroepitaxial diamond electrode also for different concentrations of RuHex at a fixed scan rate of 100 mV s^{-1}, as shown in **Figure 4-14** (b). In a theoretical reversible diffusion-controlled model, the peak-peak separation isn't affected, regardless of the applied scan rate. However, this value is found to increase steeply at higher concentrations of $\mathrm{Ru(NH_3)_6^{3+}}$, indicating a contribution of the resistance of the diamond electrode to the voltammogram, especially at higher mediator concentrations. Therefore, it becomes necessary to correct the measured peak-peak separation by taking into account the series resistance.

The resistance values were then taken from the impedance measurements to correct the peak-peak separation using *DigiSim*® simulation, yielding iR_S-compensated peak-peak separation values of 260 mV, 99 mV and 110 mV, respectively for the heteroepitaxial, smooth poly- and rough polycrystalline diamond electrodes, measured in 1 mM $\mathrm{Ru(NH_3)_6^{3+}}$ at a scan rate of 1.0 V s^{-1} (see **Table 4-2**). After the correction, the peak-peak separation became fairly independent from the analyte concentration, pointing to quasi-reversible kinetics in all cases.

With the corrected peak-peak separation, the electron transfer rate k_0 was calculated based on the Nicholson method [29] and summarised in **Table 4-2**. With the smallest peak-peak separation, the smooth polycrystalline diamond exhibits the highest $k_0 = 290\ \mu\mathrm{m\ s^{-1}}$, while its rough counterpart shows a smaller $k_0 = 161\ \mu\mathrm{m\ s^{-1}}$, along with an approximately 10 mV higher compensated peak-peak separation. The heteroepitaxial sample yielded, however, $k_0 = 24.5\ \mu\mathrm{m\ s^{-1}}$, which is more than an order of magnitude smaller than the rate constant of the smooth polycrystalline diamond, a result attributed to the very high peak-peak separation, which indicates much slower kinetics on this electrode. Note the respective charge-transfer resistances, R_{CT}, measured previously by impedance spectroscopy (**Table 4-2**) and how they are coherent with the rate constants calculated by the Nicholson method, *i.e.* a higher k_0 corresponds to a lower R_{CT}. This agreement was also verified by the following method.

An alternative procedure to calculate the electron transfer rate constant k_0 was carried out using the commercial simulation software *DigiSim*® *3.03* from *Bioanalytical Systems Inc*. to fit the measured voltammograms. The model assumes a homogeneous electrode and semi-infinite planar diffusion. The series resistance R_S and the space charge capacitance C_{SC}, measured by EIS, were taken into account. The rate constants evaluated in $\mathrm{Ru(NH_3)_6^{3+}}$ for the heteroepitaxial and the smooth polycrystalline electrodes closely match the values obtained by the Nicholson method, showing that the appropriate iR_S-correction is crucial to validate Nicholson's kinetic evaluation model. Good agreement is also observed for the rate constants evaluated in $\mathrm{Fe(CN)_6^{4-}}$.

Apart from the two calculation approaches mentioned before, the rate constants were also determined from the electron transfer resistance obtained from impedance measurements, in both solutions of $\mathrm{Ru(NH_3)_6^{3+/2+}}$ and $\mathrm{Fe(CN)_6^{3-/4-}}$, using the following equation [49]:

$$k_0 = \frac{RT}{\left[n^2 F^2 A (C_{\mathrm{O}})^{\alpha} (C_{\mathrm{R}})^{(1-\alpha)} R_{\mathrm{CT}}\right]} \tag{4.6.1}$$

where R is the ideal gas constant, T is the temperature, n is the number of transferred electrons, F is the Faraday constant, A is the electrode surface area, C is the concentration of the analytes, α is the transfer coefficient and R_{CT} is the charge transfer resistance. The rate constants calculated in this way match also quite well the values calculated from the other two methods, despite a certain scatter in the impedance data and also uncertainties in the fitting of the Randle's equivalent model to the measured data.

Looking at **Table 4-2** in the case of RuHex, the calculated rate constant of the heteroepitaxial diamond electrode is slightly larger than what is reported for (001)-oriented homoepitaxial diamond with $[\mathrm{B}] = 2 \times 10^{18}\,\mathrm{cm}^{-3}$ [17], but an order of magnitude lower than that of a polycrystalline diamond with similar doping level [48]. The rate constants of our polycrystalline samples are in line with reported values for polycrystalline diamond electrodes with similar doping level [4, 48]. The fitted transfer coefficient α was found to be around 0.5 in most cases, indicating that the diamond behaves like a degenerate semiconductor, in contrast to $\alpha = 0$ for typical non-degenerate semiconductors [43]. $\mathrm{Ru(NH_3)_6^{3+}}$ is a typical outer-sphere electron transfer mediator, insensitive to surface functional groups or surface defects. The most influential factor on this type of mediator is the density of electronic states at the electrode near the formal potential of the redox mediator. Therefore, the heteroepitaxial diamond's lower rate constant is attributed to a lower density of states in the bandgap, due to a lower doping level [4].

Now, looking at the results obtained with ferrocyanide (see **Figure 4-13** (b)), the first noticeable difference between the polycrystalline electrodes and the heteroepitaxial one is the much larger peak-peak separation of ~1.2 V produced by the latter. The electron transfer rate k_0 was calculated by the various methods also used for RuHex (see **Table 4-2**), yielding consistent numbers. The rate constants calculated from equation (4.6.1) show the same trend and good agreement also in absolute values, except for the heteroepitaxial diamond, which yielded k_0 over one order of magnitude lower than the value obtained from *DigiSim*® simulation.

Comparing the different mediators, the rate constants for $\mathrm{Fe(CN)_6^{4-}}$ on all three electrodes are at least one order of magnitude lower than the values obtained with $\mathrm{Ru(NH_3)_6^{3+}}$. This is not without a good reason, given that ferrocyanide exhibits inner-sphere electron transfer on a carbon electrode, being very sensitive to adsorbates, to the presence of specific chemical sites, as well as to the surface termination, in order to catalyse the electron transfer. For example, the edge plane of sp^2 carbon has been shown to efficiently catalyse the electron transfer on glassy carbon or HOPG (highly oriented pyrolytic graphite) electrodes [50, 51]. That means the lack of sp^2 carbon impurities or crystallographic defects make the electron transfer with ferrocyanide strongly impeded on more perfect crystals such as the heteroepitaxial diamond. The heteroepitaxial electrode exhibits also a larger depletion layer due to its lower doping level, and this also contributes to the hindrance of charge transfer. The rate constant obtained with ferrocyanide for the heteroepitaxial sample is very similar to the typical value reported for homoepitaxially grown samples [17, 18, 41], indicating comparable electrochemical characteristics between the two. Because k_0 differs by two orders of magnitude between the heteroepitaxial sample and a polycrystalline sample of similar B-doping concentration

[17], the lower doping level compared to our polycrystalline samples is ruled out as the main cause for the slower rate constant. Instead, the lower transfer rate has to come from the absence of carbon impurities or defects on the heteroepitaxial electrode surface, together with a larger depletion layer, more than from a difference in bulk electrical conductivity. Finally, the comparison between the two, rough and smooth, polycrystalline samples shows that k_0 is lower for the latter, indicating that there is some removal of sp^2 carbon aggregates from the grain boundaries during the polishing process.

4.6.2 Mott-Schottky plot and energy diagram

Mott-Schottky (or capacitance-voltage) measurements of the heteroepitaxial sample “A” and of the smooth polycrystalline sample were carried out, in order to evaluate the acceptor density N_A in the diamond and the flatband potential V_FB at the semiconductor-electrolyte interface. The experiments were conducted using a solution of 0.1 M KCl at various frequencies (80 Hz, 250 Hz, 2.5 kHz and 250 kHz). The potential range was from −0.5 to 0.7 V, within which almost no faradaic current flows. In the Mott-Schottky analysis, a simple RC circuit is assumed as an equivalent electrical model of the double layer, and the measured parallel capacitance C_P (assumed to be the space charge capacitance) is plotted as C_P^{-2} versus applied potential, V_bias. The results are shown in **Figure 4-15**.

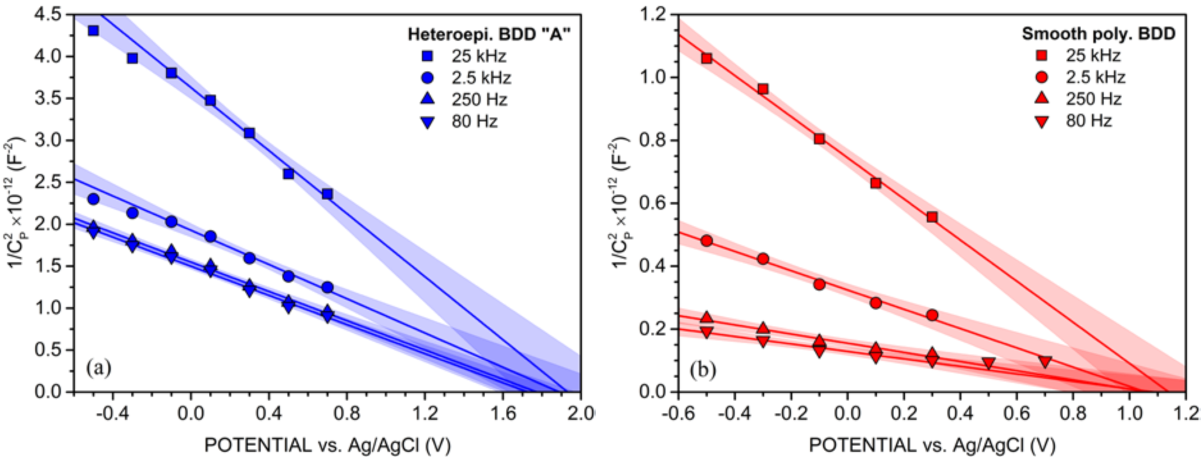

Figure 4-15: Mott-Schottky curves measured at various frequencies (a) for the heteroepitaxial diamond electrode “A” and (b) for the smooth polycrystalline electrode. The 95% confidence bands from the linear regressions are also shown.

Looking at the two groups of curves one observes a clear frequency dispersion of the capacitance C_P, since that the slopes and the intersections at $C_\mathrm{P}^{-2} = 0$ have a certain scatter. Such phenomenon has been reported for diamond and other semiconductors before [52, 53]. According to Pleskov *et al.* [20], it is attributed to: (1) the frequency dependence of dielectric relaxation in the space charge region; (2) the electrode surface roughness; (3) the slow ionisation of deep donor/acceptor levels in the space charge region; (4) the effect of surface states.

The curves measured at 80 and 250 Hz were chosen for the Mott-Schottky analysis. The carrier concentration N_A was calculated from equation (4.4.14), yielding in average $(1.4 \pm 0.1)\times 10^{20}$ cm^{-3} and $(9.5 \pm 1.0)\times 10^{20}$ cm^{-3} for, respectively, the heteroepitaxial and the polycrystalline diamond electrodes. The flatband potential V_FB, calculated from the intersection at $C_\mathrm{P}^{-2} = 0$ resulted in averaged values of 1.75±0.02 V and 1.08±0.02 V, respectively for those samples. These results show that the doping level (or conductivity) is not the only difference between the samples; the flatband potential values indicate a stronger band bending at the heteroepitaxial diamond surface than in the polycrystalline counterpart.

The calculated flatband potential assumes a potential-independent potential drop across the Helmholtz layer, which is true for typical non-degenerate semiconductors. For degenerate semiconductors with a high acceptor concentration, such as the samples studied here, the extrapolation value at the potential axis is shifted by [19, 54]:

$$\Delta V = \frac{q\varepsilon_0\varepsilon_\mathrm{r}N_\mathrm{A}}{2C_\mathrm{H}^2} \tag{4.6.2}$$

Given that C_H is usually much larger than C_SC, it is often neglected/undetected in the Mott-Schottky analysis [43], where only a single capacitive element is accounted for, such as in the simple RC circuit. Therefore, for the calculation above, a literature value of 20 µF cm^{-2} had to be assumed for C_H [4]. Offset values were then estimated to be −0.014 V for the heteroepitaxial diamond electrode and −0.093 V for the smooth polycrystalline one, leading to corrected flatband potential values of, respectively, 1.73 V and 0.99 V, which nevertheless fall either within or very close to the uncertainty of the original values. Such correction becomes even less important considering the frequency dispersion that affects the data and the uncertainty regarding the true value of C_H.

Despite the uncertainties concerning the absolute values, the flatband potential difference between the two samples is large, and knowing already that the samples possess distinct electrochemical behaviour under certain conditions, this result was worth of further analysis.

The flatband potential, E_FB, maps the energy of the valence band edge at the surface, E_VS, to the Fermi energy of the reference Ag/AgCl electrode in the chemical scale as follows:

$$E_\mathrm{VS} = E_\mathrm{FB} + E_\mathrm{VB} \tag{4.6.3}$$

where E_VB is the energy difference between the valence band in the neutral region of the semiconductor and the Fermi level.

Its sign and magnitude indicate the direction and extent of the band bending when the electrode is in equilibrium with the solution. Based on this relationship, an interfacial energy diagram at equilibrium with the redox solution is proposed in **Figure 4-16**.

The flatband potential of the smooth polycrystalline diamond is comparable to the reported value of 0.91 V *vs.* Ag/AgCl measured at 103 Hz in 0.5 M NaCl [42] and within the range of 0.45 to

1.00 V *vs.* SCE reported for polycrystalline diamond [4]. The measured V_{FB} of 1.73 V for the heteroepitaxial diamond is somewhat higher than the reported 1.2 V for homoepitaxial diamond [21], but much smaller than the typical potential of ~4.0 V for a heavily oxidised (001)-oriented homoepitaxial diamond with lower boron concentration [19]. This discrepancy is expected to arise from the shift of the band edge to lower energies (*i.e.* more positive potentials) due to the dipole character of oxygen-containing groups on the heavily oxidised diamond surface. All our samples went through the same potential cycling procedure in dilute nitric acid in order to oxygenate and stabilise the surface before the experiments. Therefore any difference has to be related to the distinct surface characteristics of each sample and to the bulk conductivity. There can be several factors contributing to the flatband potential values:

- The higher carrier concentration in the polycrystalline electrode may cause the Fermi level in the solution to move slightly (or slightly more) instead of being effectively fixed when the junction reaches equilibrium, leading to a smaller Fermi level shift in the diamond and, consequently, smaller V_{FB}.
- The heteroepitaxial sample has effectively a well-defined (001) surface with a homogeneous density of atoms, while the polycrystalline sample has a mixture of facets, each with their particular atomic density ($\rho_{(111)} > \rho_{(001)} > \rho_{(011)}$) and bond configuration. Therefore, even under the same oxygenation procedure the two surfaces will likely have different densities of carbonyl groups and, consequently, different polarities. In other words, the oxygen coverage will be inherently different in the two types of material.
- The polycrystalline diamond possesses a structurally more defective surface due to the grain boundaries, possibly with non-diamond phases intermixed, which could lead to different functional groups on the surface hindering a more effective oxygenation, and in fact introducing acceptor/donor levels in the bandgap which can lead to Fermi level pinning.

All factors considered, the results indicate that the heteroepitaxial diamond is more effectively oxygenated because it has a structurally more perfect and well-defined surface.

Although both types of diamond are heavily boron-doped, they still show diode-like rectifying behaviour at extreme overpotentials, depending on the charge carrier concentration. For example, for oxygen evolution above 2 V, the energy bands bend up and an accumulation layer appears at the interface. As a consequence, both types of diamond electrodes have shown fast kinetics for oxygen evolution (**Figure 4-11** (a)). For hydrogen evolution reaction (negative potential), the energy bands bend downwards and holes are almost depleted on the surface, so the electron transfer kinetics depend on the width of space charge region through which the electrons have to tunnel. As the depletion layer is influenced by the concentration of charge carriers in the bulk material, the less boron-doped heteroepitaxial diamond sample has shown a much lower current than polycrystalline diamond in our hydrolysis experiment shown in **Figure 4-11** (a).

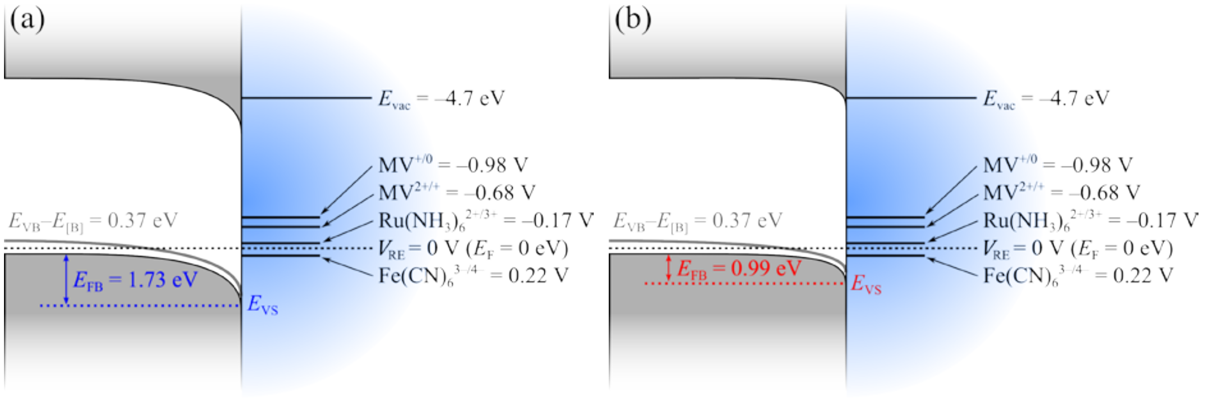

Figure 4-16: Proposed band diagrams based on the measured flatband potential from the Mott-Schottky analysis for (a) the heteroepitaxial diamond "A" ($[B] \cong 1.4 \times 10^{20}\,\text{cm}^{-3}$) and (b) the smooth polycrystalline diamond ($[B] \cong 9.5 \times 10^{20}\,\text{cm}^{-3}$).

4.6.3 Electrochemical characterisations of methyl viologen and AQDS

4.6.3.1 Electrochemical characterisation of methyl viologen

The electrochemical properties of the heteroepitaxial BDD "A" were further investigated with a more complex electrochemical process, the redox process of methyl viologen (MV), and compared against the smooth and polycrystalline BDD electrodes. The redox process of MV involves multi-step electron transfer and stripping[3] of precipitate. Methyl viologen exhibits two consecutive one-electron transfer processes [55, 56]:

$$MV^{2+} + e^- \rightleftarrows MV^+ \tag{4.6.4}$$

$$MV^+ + e^- \rightleftarrows MV^0 \tag{4.6.5}$$

Figure 4-17 presents cyclic voltammograms of each diamond electrode in 4 mM MV^{2+} at a scan rate of 100 mV s^{-1}. Both smooth and rough polycrystalline diamonds show a redox peak of around −0.68 V, corresponding to the electron transfer between MV^{2+} and MV^+. The cathodic peak at −1.1 V is related to the precipitation of the neutral MV^0 phase, and the asymmetric anodic peak at −0.9 V is attributed to the stripping of the MV^0 precipitate. The higher current observed on the rough polycrystalline diamond is likely partially caused by a larger effective surface area.

---

[3] Stripping means, in this context, the reverse process of depositing.

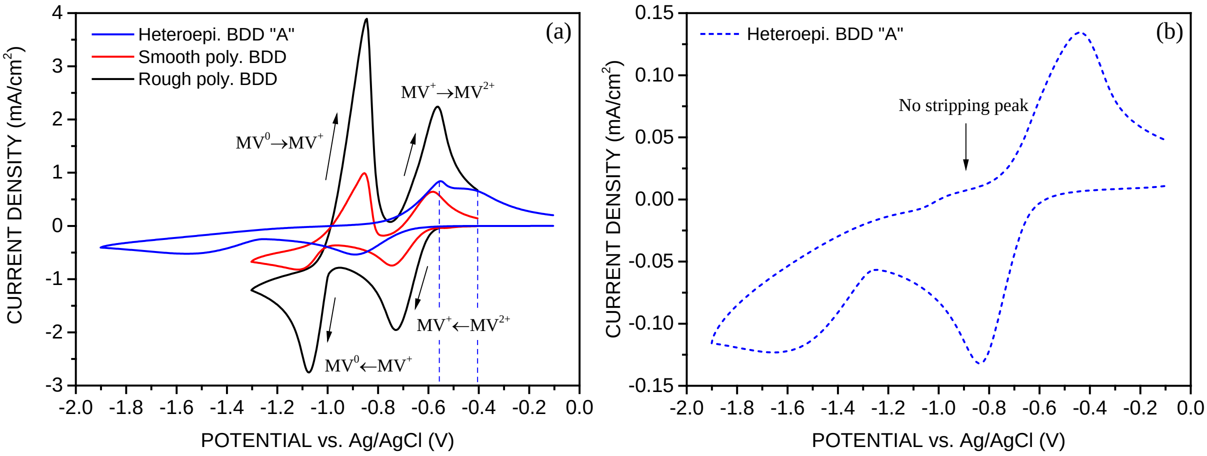

Figure 4-17: CVs of the three electrodes (heteroepitaxial single crystal “A”, smooth and rough polycrystalline diamond) with (a) 4 mM MV and (b) 1mM MV in 0.1 M KCl at a scan rate of 100 mV s^{-1}.

In contrast, the heteroepitaxial diamond shows a weak MV^0 precipitation peak at a very cathodic potential of −1.5 V, and absence of an expected stripping peak at −0.9 V. Instead, two anodic peaks are observed around −0.6 V, the typical potential for oxidation from MV$^+$ to MV^{2+}. At a lower MV concentration, as shown in **Figure 4-17** (b), only one anodic peak can be seen, while a stripping peak around −0.9 V remains absent. A similar behaviour has been observed on polycrystalline diamond, and is attributed to a comproportionation process described in equation (4.6.6) [57]. The peak at −0.6 V is attributed to the oxidation of MV$^+$ from comproportionation, and the peak at −0.4 V is attributed to the stripping of MV^0 directly to MV^{2+}. The onset of the comproportionation process depends on various aspects, such as analyte concentration and scan rate. Here, the comproportionation process seems to occur only at a higher concentration, 4 mM, and was found to be independent of the scan rate.

$$MV^0(s) + MV^{2+}(sol.) \rightleftarrows 2MV^+(sol.) \tag{4.6.6}$$

The absence of a stripping peak for MV^0 → MV$^+$ on the heteroepitaxial diamond is attributed to its lower doping level and to the lack of defect sites to catalyse the reaction. At the formal potential of MV$^{0/+}$, the energy bands bend downwards strongly, and the surface is depleted of majority carriers, *i.e.* holes. Under this condition, MV^{2+} can be reduced by receiving one electron from the electrode surface via tunnelling, but the supply of holes for the oxidation of MV^0 is more strongly inhibited until a larger overpotential is applied to reduce the potential barrier for charge transfer. In contrast, electrons can tunnel through the space charge region more easily in the polycrystalline diamond electrodes, due to a thinner depletion layer (from the higher doping level) and due to the weaker band bending from the (less effective) O-termination; the presence of a larger amount of surface states from the impurities/defects also facilitates the electron transfer process.

4.6.3.2 Electrochemical characterisation of AQDS

Diamond is known for its strong resistance to fouling by polar adsorbates, such as AQDS [58]. A thorough evaluation of the electrochemical properties of the heteroepitaxial diamond single crystal would not be complete without testing its resistance to fouling.

Cyclic voltammograms of the three electrodes (heteroepitaxial single crystal “A”, smooth polycrystalline and rough polycrystalline diamond) were conducted in 0.1 M $HClO_4$ supporting electrolyte, after potential cycling in 1 mM AQDS and physically rinsing with Milli-Q water to remove weakly adsorbed species. The results are shown in **Figure 4-18**.

Observing **Figure 4-18** (a), the rough BDD produced an overwhelmingly large background current in that specific potential cycling region, making any feature related to the adsorption of AQDS difficult to discern. Nevertheless, a couple of small and broad peaks appeared between 0.2 and 0.4 V. The smooth polycrystalline BDD, on the other hand, shows a pair of symmetric peaks with an almost zero peak-peak separation at −0.1 V, which can be seen in more detail in **Figure 4-18** (b). The peak current is observed to vary linearly with the scan rate, indicating that the electron process is adsorption-controlled on this material’s surface. The total charge transferred during the faradaic electron transfer process is integrated as 1.6×10^{-3} mC cm^{-2}, which is independent of the scan rate. This value corresponds to 7.53×10^{-12} mol of AQDS adsorbed on the surface, which means that approximately 6.4% of the surface is covered by the AQDS adsorbates, assuming a flat orientation for all AQDS molecules and a reported molecular area of 1.407 nm^2 [59]. The adsorption of AQDS, although very weak on the smooth polycrystalline diamond’s surface, is attributed here to the presence of a high density of surface defects caused by mechanical polishing [60]. The surface defects are acknowledged as the hosts for dipolar functionalities on the surface [61, 62], which are effectively absent in the heteroepitaxial diamond and which explains why it showed no adsorption peaks after careful rinsing. This result is coherent with the results of our previous experiments, supporting that the heteroepitaxial diamond electrode has a more pure surface and resistance to fouling.

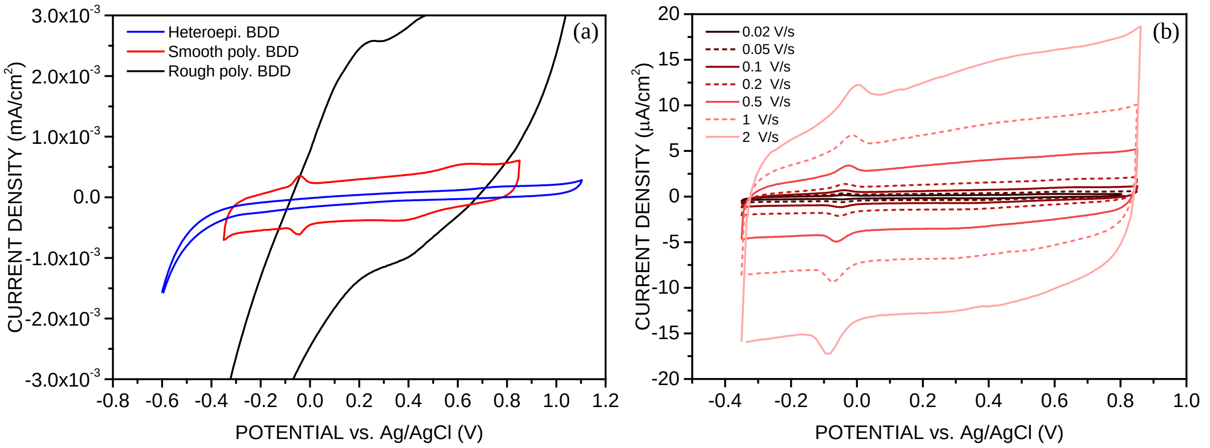

Figure 4-18: (a) CVs of each of the three electrodes in 0.1 M $HClO_4$ at a scan rate of 50 mV s^{-1} after previous CVs in 1 mM AQDS and rinsing. (b) Smooth polycrystalline diamond electrode in 0.1 M $HClO_4$ at different scan rates after CV in 1 mM AQDS and rinsing.

4.6.4 Electrochemical homogeneity and scanning electrochemical microscopy (SECM)

SECM was conducted in feedback mode in 1 mM $Ru(NH_3)_6^{3+}$ to examine the heterogeneous electrochemical activity of the diamond electrodes (smooth polycrystalline BDD and heteroepitaxial BDD “A”), which has been reported for polycrystalline and nanocrystalline diamond [48, 63] but not yet for heteroepitaxial diamond single crystals. This technique permits the visualisation of how electrochemically homogeneous the electrode surface is, which is closely correlated to its electrical properties (*e.g.* doping level) and presence of certain types of defects. During the SECM experiment, the platinum probe and the substrate were held at, respectively, −0.4 V and 0 V, corresponding to the reduction and oxidation potential of $Ru(NH_3)_6^{3+/2+}$. The resulting SECM images are shown in **Figure 4-19** (a, b).

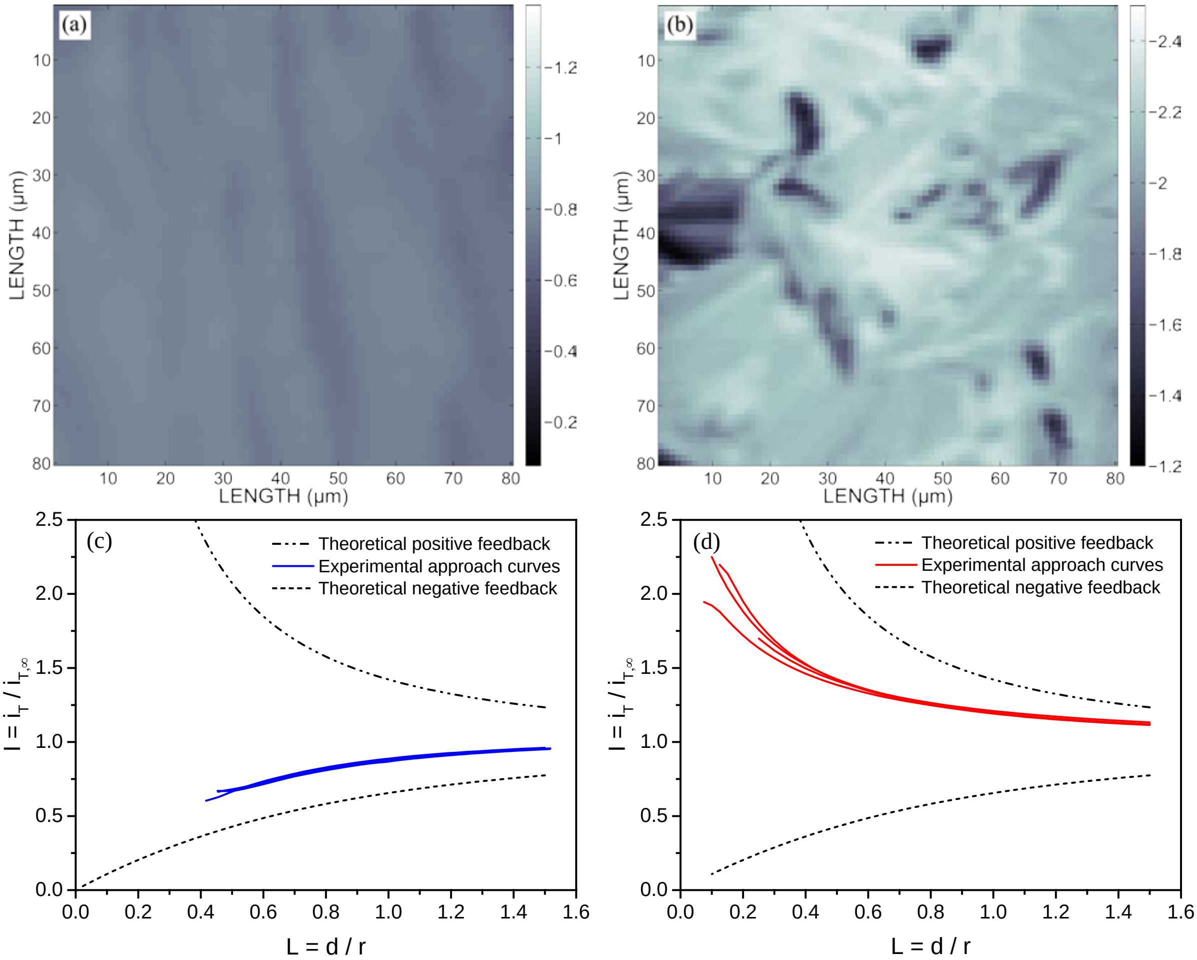

Figure 4-19: SECM of (a) heteroepitaxial BDD “A” *vs.* (b) smooth polycrystalline BDD in $Ru(NH_3)_6^{3+}$. Both maps are scaled to a current window of 1.3 nA. Below in (c) and (d), the approach curves taken at various spots on each corresponding sample are shown, together with theoretical positive and negative feedback curves.

The polished polycrystalline diamond shows an inhomogeneous distribution of high and low feedback current, indicating a heterogeneous electrochemical activity. Since this sample was polished down to a RMS roughness of less than 3 nm, topographic effects can be ruled out as an explanation for the observed inhomogeneity. The pattern of the electrochemical activity closely matches the distribution and shape of the diamond grains seen later by SEM (**Figure 4-23**). This heterogeneity is in line with similar observations on polycrystalline diamond of various doping levels, as well as on nanocrystalline diamond, from combined SECM and conductive AFM [48, 63]. It is attributed to different boron incorporation in different crystallographic facets and in grain boundaries. The positive feedback displayed by the corresponding approach curves in **Figure 4-19** (d) is consistent with finite charge transfer kinetics and quasi-reversible process.

Looking at the SECM image of the heteroepitaxial BDD displayed in **Figure 4-19** (a), a much more homogeneous feedback current ($I_{\text{A, min}} = -0.643$ nA, $I_{\text{A, max}} = -0.808$ nA) compared to the polycrystalline diamond ($I_{\text{poly, min}} = -1.25$ nA, $I_{\text{poly, max}} = -2.39$ nA) was observed, along with a general lack of “hot spots” of high electrochemical activity, as in the case of the polycrystalline sample. Also, the negative feedback displayed by the corresponding approach curves in **Figure 4-19** (c), which is consistent with slow charge transfer kinetics and an irreversible process, clearly distinguishes the character of the two samples: the polycrystalline electrode effectively reduces $\text{Ru(NH}_3)_6^{3+}$ back to $\text{Ru(NH}_3)_6^{2+}$, while the heteroepitaxial single crystal performs less efficiently. This is likely due to its lower and more homogeneous doping level, as well as the lack of defect-rich grain boundaries. Indeed, this observation is coherent with our findings in section 4.6.1, where a smaller k_0 (electron transfer rate constant) was determined for the reaction of $\text{Ru(NH}_3)_6^{3+/2+}$ on the heteroepitaxial BDD and attributed mainly to its lower conductivity, since RuHex is a simple outer-sphere mediator. The fitted ideality factor n of the CPE (constant phase element) in the impedance model also confirmed the higher homogeneity observed here.

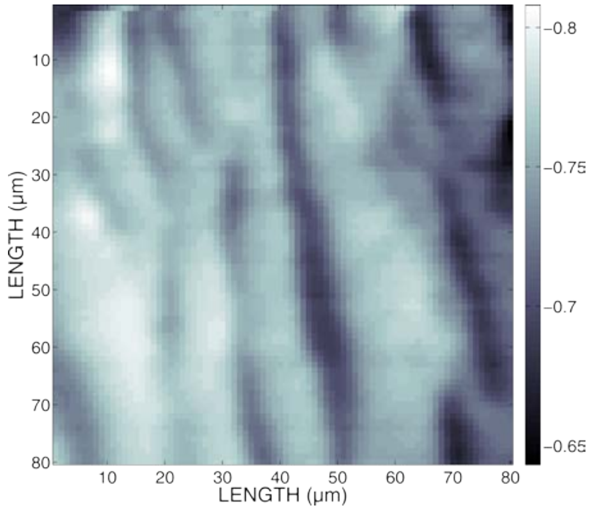

Figure 4-20: SECM of the heteroepitaxial BDD “A” (as-grown surface) in $\text{Ru(NH}_3)_6^{3+}$, within the measured current range from −0.808 to −0.643 nA. The same image rescaled to the polycrystalline BDD current range is displayed in **Figure 4-19** (a).

Despite the comparatively homogeneous surface of the heteroepitaxial BDD becoming evident with SECM, a slight variation of current is discernible at closer examination. Vertical stripes of lower and higher current can be seen forming a wavy structure when **Figure 4-19** (a) is rescaled to within the measured current range, as shown in **Figure 4-20**:

Although surpassing the polished polycrystalline BDD in homogeneity of its electrochemical activity, the heteroepitaxial BDD with as-grown surface is not in fact truly homogeneous. The picture above closely resembles the sample topography seen later by SEM (**Figure 4-23**). A closer analysis with AFM showed that despite a roughness RMS of ~0.7 nm being measured within a $1\times1\,\mu\text{m}^2$ scan area, topographical features of up to 100 nm in height could be seen within $20\times20\,\mu\text{m}^2$, a size[4] which is comparable to the observed SECM contrast pattern. Such surface features are expected to arise during growth of the diamond layers, as discussed before in chapters 1 and 3. To summarise, the topography of the as-grown heteroepitaxial BDD is caused by: 1) the nature of the substrate with its 4° tilt relative to the (001) plane, which leads to off-axis growth; 2) the use of nitrogen during growth of the 80 µm thick interlayer (see **Figure 4-10**), which promotes a characteristic step-like surface with terraces and risers; 3) the smoothing of such features during the growth of the B-doped layer on top. From the nature of the current feedback profiles (approach curves), one can see that the current response becomes more sensitive to variations of the distance (Δd) to the substrate when $d \to 0$, meaning that irregularities of the sample surface (topography) are also mapped and can account for the measured SECM features. Therefore, the natural topographic features of the as-grown heteroepitaxial BDD "A" resulted in a sample too rough for accurate SECM measurements.

In order to remove the effect of an irregular surface from the SECM analysis, the heteroepitaxial BDD "A" was subjected to chemical-mechanical polishing (CMP). The new surface resulted with a roughness RMS of ~0.12 nm, measured over an area of $1\times1\,\mu\text{m}^2$ by AFM.

With this sample now having a smooth surface, further SECM experiments were carried out to evaluate the electrochemical activity of the different electrodes by taking images on the same spot on each sample using two different redox mediators: $\text{Ru(NH}_3)_6^{3+}$ and Fe(CN)_6^{4-}. The resulting SECM images are shown in **Figure 4-21**. The probe and the substrate were held at the potential values listed in **Table 4-3**. A higher potential difference was applied between the heteroepitaxial BDD substrate and the probe, in order to compensate for the wider peak-peak separation compared to the polycrystalline BDD when ferrocyanide is used as mediator, as previously seen in **Figure 4-13**.

Table 4-3: Potential values used during the SECM experiments shown in **Figure 4-21**.

Sample	**$\text{Ru(NH}_3)_6^{3+}$**		**Fe(CN)_6^{4-}**	
	Probe	**Substrate**	**Probe**	**Substrate**
Smooth polycrystalline BDD	−0.4 V	0 V	0.4 V	0 V
Heteroepitaxial BDD "A"	−0.4 V	0 V	0.4 V	−0.3 V

---

[4] AFM measurement of a very similar sample across $80\times80\,\mu\text{m}^2$ resulted in a roughness RMS of ~35 nm.

The SECM images of the polycrystalline diamond in **Figure 4-21** (a, b) show very distinct behaviours, depending on whether $Ru(NH_3)_6^{3+}$ or $Fe(CN)_6^{4-}$ is used. In some regions, such as those marked with a square, the electrochemical response is similar with both mediators, whereas in other regions such as the ones marked with a circle and a hexagon, the responses are significantly different, if not the opposite. That is, an inactive feature with $Ru(NH_3)_6^{3+}$ becomes an active feature with $Fe(CN)_6^{4-}$, and vice-versa. These discrepancies have been observed before on nanocrystalline diamond, and were attributed to differences in the local structure of the double layer [63]. As discussed previously, $Ru(NH_3)_6^{3+/2+}$ is an outer-sphere electron transfer mediator, and the high electrochemical activity in the SECM image correlates with a high density of electronic states in that region of the surface. However, as an inner-sphere redox couple, the electron transfer of $Fe(CN)_6^{3-/4-}$ mostly depends on the surface termination and oxygen-containing functional groups instead of the local density of states. Hence, the SECM image in $Fe(CN)_6^{4-}$ is a map of surface termination, whereas the image in $Ru(NH_3)_6^{3+}$ is a map of the local electrical conductivity.

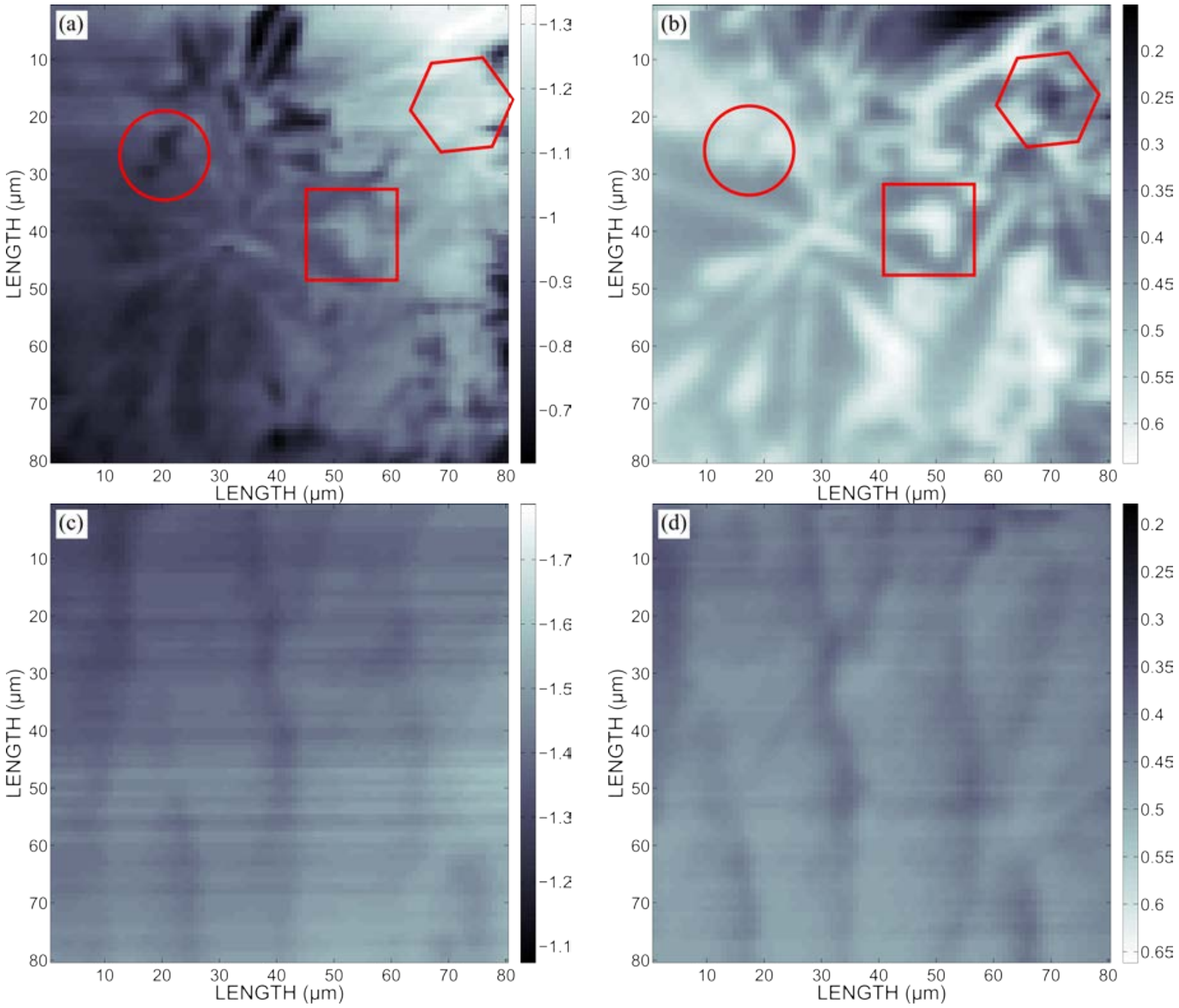

Figure 4-21: SECM of (a, b) smooth polycrystalline and (c, d) heteroepitaxial BDD "A" in (a, c) 1 mM $Ru(NH_3)_6^{3+}$ in 0.1 M KCl and (b, d) 1 mM $Fe(CN)_6^{4-}$ in 0.1 M KCl. The current range for the heteroepitaxial BDD in (c) and (d) is scaled to match, respectively (a) and (b), with units in nA.

The SECM images of the polished heteroepitaxial BDD “A” are shown in **Figure 4-21** (c, d). They immediately indicate a very different behaviour to that of the polycrystalline diamond: instead, the electrochemical mapping with both mediators produced very similar results, with identical regions of higher and lower activity. The horizontal stripes are due to subtle bench vibrations during the measurements, while a vertical pattern similar to the unpolished state (**Figure 4-20**) was observed. This is attributed to a likely doping inhomogeneity arising from the off-axis growth process discussed before. The B-doped layer was grown on top of a diamond interlayer possessing a “serrated” surface comprised of step terraces and risers, with the latter farther away from the [001] growth direction than the former [64]. Despite a progressive smoothing of these features during growth of the B-doped layer, the exposed growth sectors are believed to incorporate B in different proportions, causing local differences in electrical conductivity which remained visible after polishing. With the surface consisting of a smooth and well-defined crystallographic plane[5] with no grain boundaries, the surface termination is expected to be very homogeneous across the whole area, causing both mediators to display variations in the local conductivity, which explains the very similar SECM results in **Figure 4-21** (c, d).

To overcome this intrinsic problem of off-axis growth, a new sample was employed for further SECM experiments, the heteroepitaxial BDD “B”, first mentioned in chapter 4.5.1 and not analysed up to this point. It was polished after each diamond growth step, meaning that the B-doped layer did not inherit from the interlayer the step-like surface with its distinct growth sectors, and also that any final morphology that could interfere with the SECM maps was removed. The polished heteroepitaxial BDD “B” electrode resulted therefore very smooth, with a surface RMS roughness of ~0.1 nm within $1 \times 1\,\mu m^2$ and no long-range features, except for very faint polishing lines. The SECM scans of this sample are shown in **Figure 4-22**.

The SECM images in **Figure 4-22** (a, b) are presented, respectively, in the same scale as in **Figure 4-21** (c, d), showing very clearly a much improved electrochemical homogeneity of the heteroepitaxial BDD “B” relative to the as-grown heteroepitaxial BDD “A”. Barely any feature can be discerned in the images, contrary to the SECM of the other samples. The minimum and maximum current values measured for all three types of electrode are listed in **Table 4-4** for comparison. The values confirm what is visible in the SECM maps: the heteroepitaxial sample “B” produced the smallest current variation of all samples, which we attribute to improved doping homogeneity and improved surface smoothness.

In **Figure 4-22** (c, d) the same SECM images as in (a, b) are shown, but scaled to within the measured current range. In this way some features can be distinguished, *i.e.* regions of darker and brighter contrast, stripes and lines. We attribute them to a combination of: 1) imperfections caused by the polishing step, such as kinks; 2) a slight angle of the sample relative to the scan direction of the probe; 3) subtle vibrations of the bench during measurement, all contributing to variations of the current.

---

[5] Approximately (001), *i.e.* disregarding the off-axis angle and any further slight tilt due to mechanical polishing.

Table 4-4: Current values measured from the SECM scans of all three types of sample (polished polycrystalline BDD, as-grown heteroepitaxial sample “A” and polished heteroepitaxial sample “B”).

Sample	**$Ru(NH_3)_6^{3+}$**			**$Fe(CN)_6^{4-}$**		
	Min. (nA)	**Max. (nA)**	**Δ (nA)**	**Min. (nA)**	**Max. (nA)**	**Δ (nA)**
Smooth polycrystalline BDD	−0.627	−1.33	−0.703	0.151	0.634	0.483
Heteroepitaxial BDD “A”	−0.127	−1.59	−0.320	0.347	0.494	0.147
Heteroepitaxial BDD “B”	−0.604	−0.785	−0.181	0.246	0.312	0.066

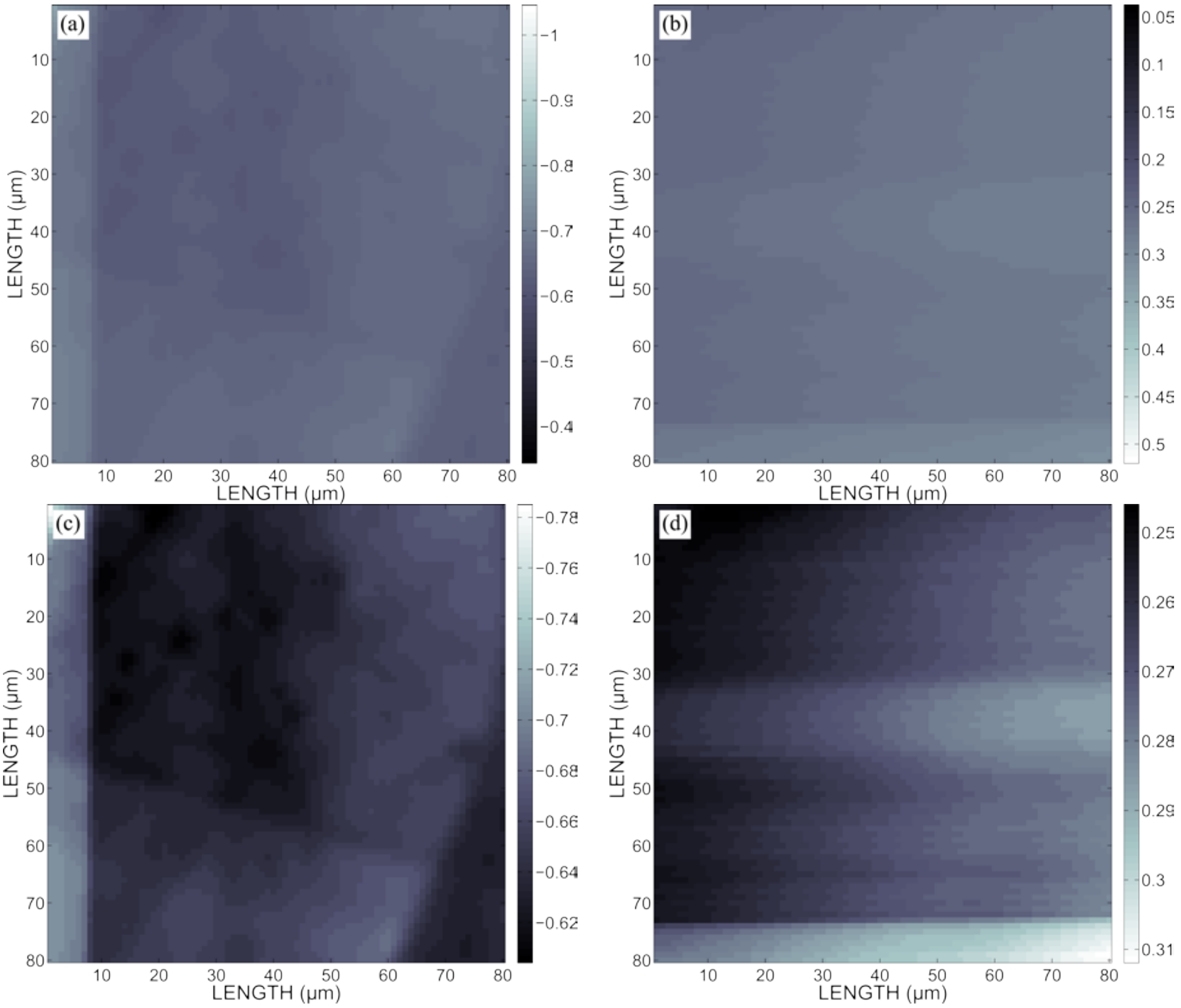

Figure 4-22: SECM (units in nA) of the twice-polished heteroepitaxial BDD “B” (a, c) in 1 mM $Ru(NH_3)_6^{3+}$ in 0.1 M KCl and (b, d) in 1 mM $Fe(CN)_6^{4-}$ in 0.1 M KCl. The maps (a) and (b) are scaled, respectively, to the maps from **Figure 4-21** (c) and (d), while the maps (c) and (d) are constrained to the measured current scale.

As a complement to the SECM measurements, the spatial variation in electrochemical activity was investigated by the electrodeposition of platinum nanoparticles, which is expected to form areas of higher and lower particle densities depending on the local electrochemical activity on the surface. The deposition process was carried out in 2 mM K_2PtCl_6 in 0.5 M H_2SO_4 by holding the potential at a constant −0.2 V for approximately 2 minutes, until a total of 10 mC had passed through the electrode. The results are shown in **Figure 4-23**.

With similar total Pt loading on the surface, the three electrodes exhibited entirely different distributions of nanoparticles and morphology under SEM. Strong aggregation of platinum particles was found on certain regions of the polished polycrystalline BDD electrode, in accordance with the spatial distribution of electrochemical activity observed in SECM images, which was attributed to different boron uptake at different crystal facets. In contrast, a more homogeneous distribution of platinum particles was found on the as-grown heteroepitaxial single crystal diamond "A", although still following the surface roughness and local variations of electrochemical activity which caused the SECM pattern shown in **Figure 4-20**. Finally, the twice polished heteroepitaxial diamond "B" produced a very homogeneous distribution of Pt particles across the whole surface, confirming the results from the SECM images shown in **Figure 4-22**. With a closer look at **Figure 4-23** (f) it is possible to recognise a diagonal line pattern of Pt nanoparticles, which is attributed to faint grooves on the surface from the last mechanical polishing step.

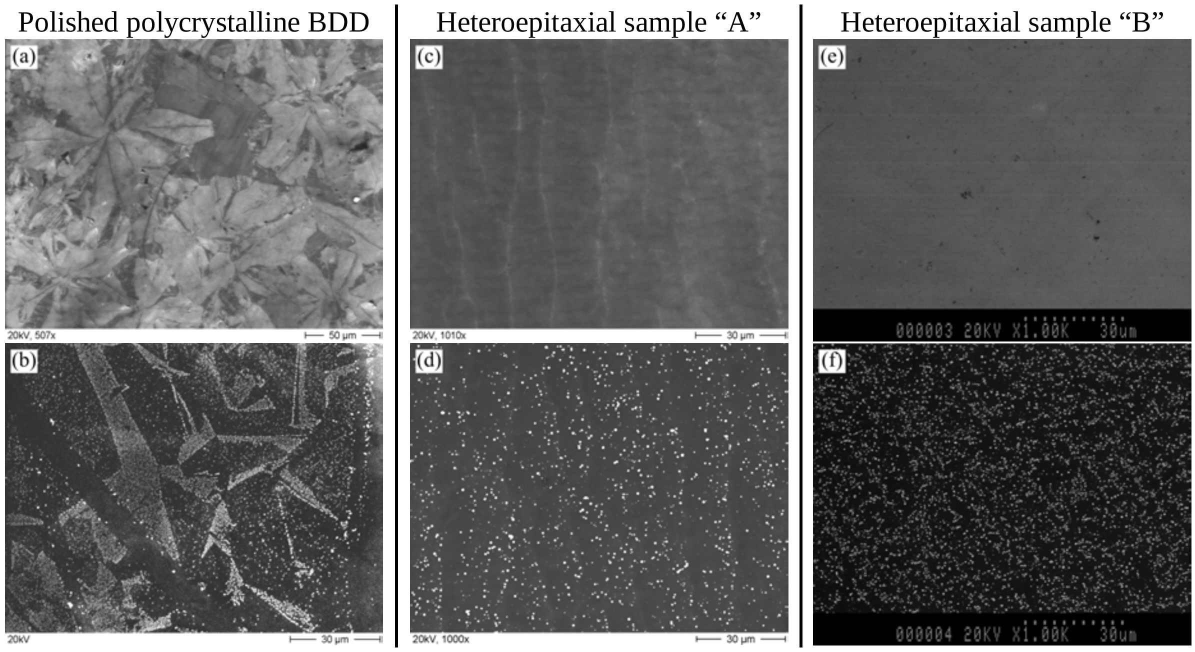
Polished polycrystalline BDD

Heteroepitaxial sample "A"

Heteroepitaxial sample "B"

Figure 4-23: SEM pictures before and after Pt deposition of (a, b) polished polycrystalline BDD, (c, d) as-grown heteroepitaxial sample "A" and (e, f) doubly polished heteroepitaxial sample "B". A higher density of Pt particles correlates with zones of higher current (or electrochemical activity) from previous SECM measurements. The sample "B" shows the highest homogeneity.

4.7 Conclusion and final remarks

In this chapter, samples of B-doped diamond heteroepitaxially grown on Ir/YSZ/Si(001) were used for the first time as electrodes in electrochemistry experiments and for the characterisation of their electrochemical properties. The experiments were done in parallel with polycrystalline (polished and as-grown) B-doped diamond electrodes for comparison, and the results were analysed and discussed in light of previous works reported in the literature for polycrystalline diamond and diamond single crystals. Standard outer-sphere and inner-sphere redox couples, respectively $\mathrm{Ru(NH_3)_6^{3+/2+}}$ and $\mathrm{Fe(CN)_6^{3-/4-}}$, were used with CV (cyclic voltammetry) to evaluate electron transfer rate constants, k_0, and to assess qualitatively the state of the diamond surface in terms of O/H-termination and presence of defects such as grain boundaries and non-diamond phases. Different methods were employed to calculate the rate constants, such as the Nicholson method, *DigiSim*® simulation and EIS (impedance spectroscopy) measurements. The results were complemented by a Mott-Schottky analysis and by experiments using more complex redox couples, such as methyl viologen (MV) and anthraquinone (AQDS), the latter providing important results concerning the electrodes' susceptibility to fouling due to adsorption. Finally, SECM (scanning electrochemical microscopy) maps in $\mathrm{Ru(NH_3)_6^{3+/2+}}$ and $\mathrm{Fe(CN)_6^{3-/4-}}$ provided clear pictures of the electrochemical (in)homogeneity across the surface of the electrodes, establishing a clear distinction between the different types of diamond and supporting the results from the previous experiments.

Overall, the heteroepitaxial diamond exhibited superior merits of electrochemical properties when compared to the standard types of diamond electrode (as-grown, rough polycrystalline and polished polycrystalline diamond), behaving very similarly to high-quality (homoepitaxially grown) B-doped diamond single crystals. In most cases when the heteroepitaxial diamond did not perform as well, it was due to its slightly higher resistivity due to the lower B-doping level achieved with the examined samples, or because its more pure surface does not possess specific chemical sites – which are usually present in polycrystalline diamond and are in fact defects in the diamond structure – to catalyse certain reactions.

The heteroepitaxial diamond showed a wider potential window and a lower background current, which are attributed partially to the lower doping, but also to its purer surface and lack of grain boundaries. From EIS and SECM measurements, the heteroepitaxial diamond showed much superior homogeneity of electrochemical activity, without the prominent highs and lows of electric current distributed across the surface, as seen for the polycrystalline sample. Consistent electron transfer rate constants were measured from Nicholson's method, *DigiSim*® simulation and EIS. The rate constant measured in $\mathrm{Ru(NH_3)_6^{3+}}$ is mostly influenced by the density of electronic states at the electrode near the formal potential of this redox mediator. The lower rate constant for the heteroepitaxial diamond suggests a lower density of electronic states near the Fermi level, in agreement with the lower carrier density measured by Mott-Schottky analysis. The cyclic voltammograms of the heteroepitaxial diamond presented a large peak-peak separation and yielded very low k_0 for $\mathrm{Fe(CN)_6^{4-}}$, a mediator that requires sp^2 carbon impurities and oxygen surface termination to catalyse the electron transfer. The sluggish kinetics in $\mathrm{Fe(CN)_6^{4-}}$, plus homogeneous SECM maps, indicate that the heteroepitaxial diamond has a superior crystalline quality, more homogeneous conductivity, higher purity and homogeneous O-termination. Since the heteroepitaxial diamond presented a larger flatband potential from Mott-Schottky analysis when compared to the polycrystalline sample, poor O-termination is unlikely to be the cause for the sluggish kinetics in $\mathrm{Fe(CN)_6^{4-}}$. Instead, the heteroepitaxial diamond must possess a purer and cleaner surface without sp^2 carbon. This sample also showed a large overpotential for the $MV^{2+/+/0}$ redox system and the absence of a MV^0 stripping peak, which is attributed to the larger flatband potential and wider space charge region arising from the lower doping level compared to the polycrystalline sample. Both the heteroepitaxial single crystal and the as-grown polycrystalline diamond demonstrate a resistance to the adsorption of ADQS, although weak adsorption is still visible on the polycrystalline sample, likely due to polishing-induced and grain boundary-related surface defects.

In summary, the obtained results are promising and place the B-doped diamond single crystal grown on Ir/YSZ/Si(001) as a potential alternative to polycrystalline diamond electrodes for certain applications [1], namely those involving sensing of species in solution (electroanalysis), since the heteroepitaxial diamond electrode offers lower background current and is more selective than the less pure polycrystalline material. The heteroepitaxial diamond is well-placed to be the electrode of choice when sensitivity is paramount, while having size advantage over homoepitaxial diamond single crystals. Furthermore, the aspect of surface purity, which is a key issue for surface functionalisation with target-specific molecules (*e.g.* for bio-sensing, energy harvesting and electroanalysis), is also achieved with heteroepitaxial diamond.

As it was demonstrated, better performances than those observed in this work are still possible once the doping level is maximised without compromising the crystalline quality of the diamond, and when special care is taken to keep the surface as flat as possible to avoid doping inhomogeneity, which affects the conductivity. The electrochemistry studies presented in this thesis could be in a future work extended to (111)-oriented films, which should provide higher doping levels and, thus, higher conductivity.

References

1. Yasuaki Einaga, John S. Foord, and Greg M. Swain; Diamond electrodes: Diversity and maturity. *MRS Bulletin*, 2014. **39**(06): p. 525-532. DOI: 10.1557/mrs.2014.94.
2. John S. Foord; *Diamond Electrochemical Sensors*, in *CVD Diamond for Electronic Devices and Sensors*, 2009, John Wiley & Sons, Ltd.
3. Richard G Compton, John S Foord, and Frank Marken; Electroanalysis at Diamond-Like and Doped-Diamond Electrodes. *Electroanalysis*, 2003. **15**(17): p. 1349-1363. DOI: 10.1002/elan.200302830.
4. Michael C. Granger, Malgorzata Witek, Jishou Xu, Jian Wang, Mateusz Hupert, Amy Hanks, Miles D. Koppang, James E. Butler, Guy Lucazeau, Michel Mermoux, Jerzy W. Strojek, and Greg M. Swain; Standard Electrochemical Behavior of High-Quality, Boron-Doped Polycrystalline Diamond Thin-Film Electrodes. *Analytical Chemistry*, 2000. **72**(16): p. 3793-3804. DOI: 10.1021/ac0000675.
5. György Fóti, Didier Gandini, Christos Comninellis, André Perret, and Werner Haenni; Oxidation of Organics by Intermediates of Water Discharge on IrO_2 and Synthetic Diamond Anodes. *Electrochemical and Solid-State Letters*, 1999. **2**(5): p. 228-230. DOI: 10.1149/1.1390792.
6. Enric Brillas, Ignasi Sirés, Conchita Arias, Pere Lluís Cabot, Francesc Centellas, Rosa María Rodríguez, and José Antonio Garrido; Mineralization of paracetamol in aqueous medium by anodic oxidation with a boron-doped diamond electrode. *Chemosphere*, 2005. **58**(4): p. 399-406. DOI: 10.1016/j.chemosphere.2004.09.028.

7. J. Weng, J. Xue, J. Wang, J. Ye, H. Cui, F. Sheu, and Q. Zhang; Gold-Cluster Sensors Formed Electrochemically at Boron-Doped-Diamond Electrodes: Detection of Dopamine in the Presence of Ascorbic Acid and Thiols. *Advanced Functional Materials*, 2005. **15**(4): p. 639-647. DOI: 10.1002/adfm.200400049.
8. Chiaki Terashima, Tata N. Rao, Bulusu V. Sarada, Nicolae Spataru, and Akira Fujishima; Electrodeposition of hydrous iridium oxide on conductive diamond electrodes for catalytic sensor applications. *Journal of Electroanalytical Chemistry*, 2003. **544**(0): p. 65-74. DOI: 10.1016/S0022-0728(03)00066-4.
9. M. A. Rodrigo, P. A. Michaud, I. Duo, M. Panizza, G. Cerisola, and Ch. Comninellis; Oxidation of 4-Chlorophenol at Boron-Doped Diamond Electrode for Wastewater Treatment. *Journal of The Electrochemical Society*, 2001. **148**(5): p. D60-D64. DOI: 10.1149/1.1362545.
10. D. Gandini, E. Mahé, P. A. Michaud, W. Haenni, A. Perret, and Ch Comninellis; Oxidation of carboxylic acids at boron-doped diamond electrodes for wastewater treatment. *Journal of Applied Electrochemistry*, 2000. **30**(12): p. 1345-1350. DOI: 10.1023/a:1026526729357.
11. M. Panizza, P. A. Michaud, G. Cerisola, and Ch Comninellis; Electrochemical treatment of wastewaters containing organic pollutants on boron-doped diamond electrodes: Prediction of specific energy consumption and required electrode area. *Electrochemistry Communications*, 2001. **3**(7): p. 336-339. DOI: 10.1016/S1388-2481(01)00166-7.
12. Yuki Honda, Tribidasari A. Ivandini, Takeshi Watanabe, Kazutaka Murata, and Yasuaki Einaga; An electrolyte-free system for ozone generation using heavily boron-doped diamond electrodes. *Diamond and Related Materials*, 2013. **40**(0): p. 7-11. DOI: 10.1016/j.diamond.2013.09.001.
13. Michael C. Granger and Greg M. Swain; The Influence of Surface Interactions on the Reversibility of Ferri/Ferrocyanide at Boron-Doped Diamond Thin-Film Electrodes. *Journal of The Electrochemical Society*, 1999. **146**(12): p. 4551-4558. DOI: 10.1149/1.1392673.
14. Jason A. Bennett, Jian Wang, Yoshiyuki Show, and Greg M. Swain; Effect of sp^2-Bonded Nondiamond Carbon Impurity on the Response of Boron-Doped Polycrystalline Diamond Thin-Film Electrodes. *Journal of The Electrochemical Society*, 2004. **151**(9): p. E306-E313. DOI: 10.1149/1.1780111.
15. I. Duo, A. Fujishima, and Ch Comninellis; Electron transfer kinetics on composite diamond (sp^3)–graphite (sp^2) electrodes. *Electrochemistry Communications*, 2003. **5**(8): p. 695-700. DOI: 10.1016/S1388-2481(03)00169-3.
16. L. Diederich, O. M. Küttel, P. Aebi, and L. Schlapbach; Electron affinity and work function of differently oriented and doped diamond surfaces determined by photoelectron spectroscopy. *Surface Science*, 1998. **418**(1): p. 219-239. DOI: 10.1016/S0039-6028(98)00718-3.
17. Takeshi Kondo, Yasuaki Einaga, Bulusu V. Sarada, Tata N. Rao, Donald A. Tryk, and Akira Fujishima; Homoepitaxial Single-Crystal Boron-Doped Diamond Electrodes for Electroanalysis. *Journal of The Electrochemical Society*, 2002. **149**(6): p. E179-E184. DOI: 10.1149/1.1471548.
18. R. Ramesham; Cyclic voltammetric response of boron-doped homoepitaxially grown single crystal and polycrystalline CVD diamond. *Sensors and Actuators B: Chemical*, 1998. **50**(2): p. 131-139. DOI: 10.1016/S0925-4005(98)00214-7.
19. J. van de Lagemaat, D. Vanmaekelbergh, and J. J. Kelly; Electrochemistry of homoepitaxial CVD diamond: energetics and electrode kinetics in aqueous electrolytes. *Journal of Electroanalytical Chemistry*, 1999. **475**(2): p. 139-151. DOI: 10.1016/S0022-0728(99)00344-7.
20. Yu V. Pleskov, Yu E. Evstefeeva, M. D. Krotova, V. V. Elkin, V. M. Mazin, V. Ya Mishuk, V. P. Varnin, and I. G. Teremetskaya; Synthetic semiconductor diamond electrodes: The comparative study of the electrochemical behaviour of polycrystalline and single crystal boron-doped films. *Journal of Electroanalytical Chemistry*, 1998. **455**(1–2): p. 139-146. DOI: 10.1016/S0022-0728(98)00175-2.
21. Yu V. Pleskov, Yu E. Evstefeeva, M. D. Krotova, V. Ya Mishuk, V. A. Laptev, Yu N. Pal'yanov, and Yu M. Borzdov; Synthetic Semiconductor Diamond Electrodes: Electrochemical Characteristics of Individual Faces of High-Temperature-High-Pressure Single Crystals. *Russian Journal of Electrochemistry*, 2002. **38**(6): p. 620-625. DOI: 10.1023/a:1016050501268.
22. Carl H. Hamann, Andrew Hamnett, and Wolf Vielstich; *Electrochemistry*, 2nd ed., 2007, Wiley-VCH Verlag GmbH.

23. Krishnan Rajeshwar; *Fundamentals of Semiconductor Electrochemistry and Photoelectrochemistry*, 1st ed., Semiconductor Electrodes and Photoelectrochemistry, ed. A. J. Bard, M. Stratmann, and S. Licht. Vol. 6, 2002, Wiley-VCH Verlag GmbH.
24. Cynthia G. Zoski; *Handbook of Electrochemistry*, 1st ed., 2007, Elsevier.
25. Allen J. Bard and Larry R. Faulkner; *Electrochemical Methods: Fundamentals and Applications*, 2nd ed., 2001, John Wiley & Sons, Inc.
26. S. U. M. Khan, R. C. Kainthla, and J. O. M. Bockris; The redox potential and the Fermi level in solution. *The Journal of Physical Chemistry*, 1987. **91**(23): p. 5974-5977. DOI: 10.1021/j100307a032.
27. Mark E. Orazem and Bernard Tribollet; *The Electrochemical Society Series*, in *Electrochemical Impedance Spectroscopy*, 2008, John Wiley & Sons, Inc.
28. Peter T. Kissinger and William R. Heineman; Cyclic voltammetry. *Journal of Chemical Education*, 1983. **60**(9): p. 702. DOI: 10.1021/ed060p702.
29. R. S. Nicholson; Theory and Application of Cyclic Voltammetry for Measurement of Electrode Reaction Kinetics. *Analytical Chemistry*, 1965. **37**(11): p. 1351-1355. DOI: 10.1021/ac60230a016.
30. *BASi DigiSim® Simulation Software for Cyclic Voltammetry*. [cited 2015]; URL: http://www.basinc.com/products/ec/digisim/.
31. Digby D. Macdonald; Reflections on the history of electrochemical impedance spectroscopy. *Electrochimica Acta*, 2006. **51**(8–9): p. 1376-1388. DOI: 10.1016/j.electacta.2005.02.107.
32. *Scribner Associates Inc.* [cited 2015]; URL: http://www.scribner.com/software/scribner-associates-software-downloads/160-zplot-and-zview-for-windows-software-downloads.
33. *Princeton Applied Research*. [cited 2015]; URL: http://www.princetonappliedresearch.com/Our-Products/Electrochemical-Software/ZSimpWin.aspx.
34. C. H. Hsu and F. Mansfeld; Technical Note: Concerning the Conversion of the Constant Phase Element Parameter Y_0 into a Capacitance. *Corrosion*, 2001. **57**(9): p. 747-748. DOI: 10.5006/1.3280607.
35. Chenming C. Hu; *Modern Semiconductor Devices for Integrated Circuits*, 1st ed., 2009, Prentice Hall.
36. M. Fischer, S. Gsell, M. Schreck, R. Brescia, and B. Stritzker; Preparation of 4-inch Ir/YSZ/Si(001) substrates for the large-area deposition of single-crystal diamond. *Diamond and Related Materials*, 2008. **17**(7–10): p. 1035-1038. DOI: 10.1016/j.diamond.2008.02.028.
37. S. Gsell, M. Fischer, Th. Bauer, M. Schreck, and B. Stritzker; Yttria-stabilized zirconia films of different composition as buffer layers for the deposition of epitaxial diamond/Ir layers on Si(001). *Diamond and Related Materials*, 2006. **15**(4–8): p. 479-485. DOI: 10.1016/j.diamond.2005.10.041.
38. S. Gsell, M. Fischer, M. Schreck, and B. Stritzker; Epitaxial films of metals from the platinum group (Ir, Rh, Pt and Ru) on YSZ-buffered Si(111). *Journal of Crystal Growth*, 2009. **311**(14): p. 3731-3736. DOI: 10.1016/j.jcrysgro.2009.04.034.
39. Michael V. Mirkin, Fu-Ren F. Fan, and Allen J. Bard; Scanning electrochemical microscopy part 13. Evaluation of the tip shapes of nanometer size microelectrodes. *Journal of Electroanalytical Chemistry*, 1992. **328**(1–2): p. 47-62. DOI: 10.1016/0022-0728(92)80169-5.
40. Greg M. Swain; *Chapter 4 Electroanalytical applications of diamond electrodes*, in *Semiconductors and Semimetals*, E.N. Christoph and R. Jürgen, Editors, 2004, Elsevier.
41. I. Duo, C. Levy-Clement, A. Fujishima, and C. Comninellis; Electron Transfer Kinetics on Boron-Doped Diamond Part I: Influence of Anodic Treatment. *Journal of Applied Electrochemistry*, 2004. **34**(9): p. 935-943. DOI: 10.1023/b:jach.0000040525.76264.16.
42. R. Ramesham; Determination of flatband potential for boron doped diamond electrode in 0.5 M NaCl by AC impedance spectroscopy. *Thin Solid Films*, 1998. **322**(1–2): p. 158-166. DOI: 10.1016/S0040-6090(97)00920-6.
43. S.R. Morrison; *Electrochemistry at Semiconductor and Oxidized Metal Electrodes*, 1st ed., 1980, Plenum Press, New York.
44. Ian D. Raistrick, Donald R. Franceschetti, and J. Ross Macdonald; *Theory*, in *Impedance Spectroscopy*, 2005, John Wiley & Sons, Inc.
45. N. Bonanos, B. C. H. Steele, and E. P. Butler; *Applications of Impedance Spectroscopy*, in *Impedance Spectroscopy*, 2005, John Wiley & Sons, Inc.
46. N. R. Wilson, S. L. Clewes, M. E. Newton, P. R. Unwin, and J. V. Macpherson; Impact of grain-dependent boron uptake on the electrochemical and electrical properties of

polycrystalline boron doped diamond electrodes. *Journal of Physical Chemistry B*, 2006. **110**(11): p. 5639-5646. DOI: 10.1021/jp0547616.
47. Sabine Szunerits, Michel Mermoux, Alexandre Crisci, Bernadette Marcus, Pierre Bouvier, Didier Delabouglise, Jean-Pierre Petit, Sebastian Janel, Rabah Boukherroub, and Lilin Tay; Raman Imaging and Kelvin Probe Microscopy for the Examination of the Heterogeneity of Doping in Polycrystalline Boron-Doped Diamond Electrodes. *The Journal of Physical Chemistry B*, 2006. **110**(47): p. 23888-23897. DOI: 10.1021/jp064429+.
48. Katherine B. Holt, Allen J. Bard, Yoshiyuki Show, and Greg M. Swain; Scanning Electrochemical Microscopy and Conductive Probe Atomic Force Microscopy Studies of Hydrogen-Terminated Boron-Doped Diamond Electrodes with Different Doping Levels. *The Journal of Physical Chemistry B*, 2004. **108**(39): p. 15117-15127. DOI: 10.1021/jp048222x.
49. Zbigniew Galus and Robert Alexander Chalmers; *Fundamentals of electrochemical analysis*, 1st ed., 1994, Ellis Horwood.
50. Richard L. McCreery, Kristin Kneten Cline, Christie Allred McDermott, and Mark T. McDermott; Control of reactivity at carbon electrode surfaces. *Colloids and Surfaces A: Physicochemical and Engineering Aspects*, 1994. **93**(0): p. 211-219. DOI: 10.1016/0927-7757(94)02899-0.
51. K. K. Cline, Mark T. McDermott, and Richard L. McCreery; Anomalously Slow Electron Transfer at Ordered Graphite Electrodes: Influence of Electronic Factors and Reactive Sites. *The Journal of Physical Chemistry*, 1994. **98**(20): p. 5314-5319. DOI: 10.1021/j100071a023.
52. A. E. Bohe, J. R. Vilche, K. Jüttner, W. J. Lorenz, and W. Paatsch; Investigations of the semiconductor properties of anodically formed passive layers on Zn and of ZnO single crystals in different aqueous electrolytes by EIS. *Electrochimica Acta*, 1989. **34**(10): p. 1443-1448. DOI: 10.1016/0013-4686(89)87186-5.
53. Yu V. Pleskov, V. V. Elkin, M. A. Abaturov, M. D. Krotova, V. Ya Mishuk, V. P. Varnun, and I. G. Teremetskaya; Synthetic semiconductor diamond electrodes: elucidation of the equivalent circuit for the case of frequency-dependent impedance. *Journal of Electroanalytical Chemistry*, 1996. **413**(1–2): p. 105-110. DOI: 10.1016/0022-0728(96)04620-7.
54. R. De Gryse, W. P. Gomes, F. Cardon, and J. Vennik; On the Interpretation of Mott-Schottky Plots Determined at Semiconductor/Electrolyte Systems. *Journal of The Electrochemical Society*, 1975. **122**(5): p. 711-712.
55. Masahide Ito and Theodore Kuwana; Spectroelectrochemical study of indirect reduction of triphosphopyridine nucleotide: I. Methyl viologen, ferredoxin-TPN-reductase and TPN. *Journal of Electroanalytical Chemistry and Interfacial Electrochemistry*, 1971. **32**(3): p. 415-425. DOI: 10.1016/S0022-0728(71)80144-4.
56. C. L. Bird and A. T. Kuhn; Electrochemistry of the viologens. *Chemical Society Reviews*, 1981. **10**(1): p. 49-82. DOI: 10.1039/cs9811000049.
57. Fulian Qiu, Richard G. Compton, Frank Marken, Shelley J. Wilkins, Christiaan H. Goeting, and John S. Foord; Laser Activation Voltammetry: Selective Removal of Reduced Forms of Methyl Viologen Deposited on Glassy Carbon and Boron-Doped Diamond Electrodes. *Analytical Chemistry*, 2000. **72**(11): p. 2362-2370. DOI: 10.1021/ac991392z.
58. Jishou Xu, Qingyun Chen, and Greg M. Swain; Anthraquinonedisulfonate Electrochemistry: A Comparison of Glassy Carbon, Hydrogenated Glassy Carbon, Highly Oriented Pyrolytic Graphite, and Diamond Electrodes. *Analytical Chemistry*, 1998. **70**(15): p. 3146-3154. DOI: 10.1021/ac9800661.
59. Manuel P. Soriaga and Arthur T. Hubbard; Determination of the orientation of adsorbed molecules at solid-liquid interfaces by thin-layer electrochemistry: aromatic compounds at platinum electrodes. *Journal of the American Chemical Society*, 1982. **104**(10): p. 2735-2742. DOI: 10.1021/ja00374a008.
60. Pierre-Nicolas Volpe, Pierre Muret, Franck Omnes, Jocelyn Achard, François Silva, Ovidiu Brinza, and Alix Gicquel; Defect analysis and excitons diffusion in undoped homoepitaxial diamond films after polishing and oxygen plasma etching. *Diamond and Related Materials*, 2009. **18**(10): p. 1205-1210. DOI: 10.1016/j.diamond.2009.04.008.
61. Kristin R. Kneten and Richard L. McCreery; Effects of redox system structure on electron-transfer kinetics at ordered graphite and glassy carbon electrodes. *Analytical Chemistry*, 1992. **64**(21): p. 2518-2524. DOI: 10.1021/ac00045a011.

62. Piehong Chen, Mark A. Fryling, and Richard L. McCreery; Electron Transfer Kinetics at Modified Carbon Electrode Surfaces: The Role of Specific Surface Sites. *Analytical Chemistry*, 1995. **67**(18): p. 3115-3122. DOI: 10.1021/ac00114a004.

63. Shihua Wang and Greg M. Swain; Spatially Heterogeneous Electrical and Electrochemical Properties of Hydrogen-Terminated Boron-Doped Nanocrystalline Diamond Thin Film Deposited from an Argon-Rich $CH_4/H_2/Ar/B_2H_6$ Source Gas Mixture. *The Journal of Physical Chemistry C*, 2007. **111**(10): p. 3986-3995. DOI: 10.1021/jp0669557.

64. Michael Mayr, Christian Stehl, Martin Fischer, Stefan Gsell, and Matthias Schreck; Correlation between surface morphology and defect structure of heteroepitaxial diamond grown on off-axis substrates. *physica status solidi (a)*, 2014: p. 2257-2263. DOI: 10.1002/pssa.201431210.

5 Diamond-based Schottky diodes for high power applications

5.1 Introduction

In recent times, diamond-based high power devices [1, 2] have been more intensely investigated than ever, thanks to diamond's extreme electrical and thermal properties. Diamond has superior merits relative to gallium nitride (GaN), silicon carbide (SiC) and especially silicon (Si, the most dominant semiconductor material), for diamond has a wide bandgap of 5.5 eV, high breakdown field of up to 20 MV cm^{-1} [3], high hole and electron mobility ($\mu_p = 1800\,\mathrm{cm}^2\,\mathrm{V}^{-1}\,\mathrm{s}^{-1}$ and $\mu_n = 2200\,\mathrm{cm}^2\,\mathrm{V}^{-1}\,\mathrm{s}^{-1}$) [4], high thermal conductivity ($2200\,\mathrm{W\,m}^{-1}\,\mathrm{K}^{-1}$), it can operate at high temperatures (>200 °C), etc. Schottky diode, compared to other diamond power devices (bipolar transistors [5], junction field-effect transistors [6, 7], Schottky p-n diodes [8], etc.), is the most promising structure, due to the high breakdown voltages reported (2.5 kV [9], 6.7 kV [10], 10 kV [11] and 8-12 kV [12]) and the architectural progress being made towards minimising Ohmic losses and improving device stability under high temperature [13-20].

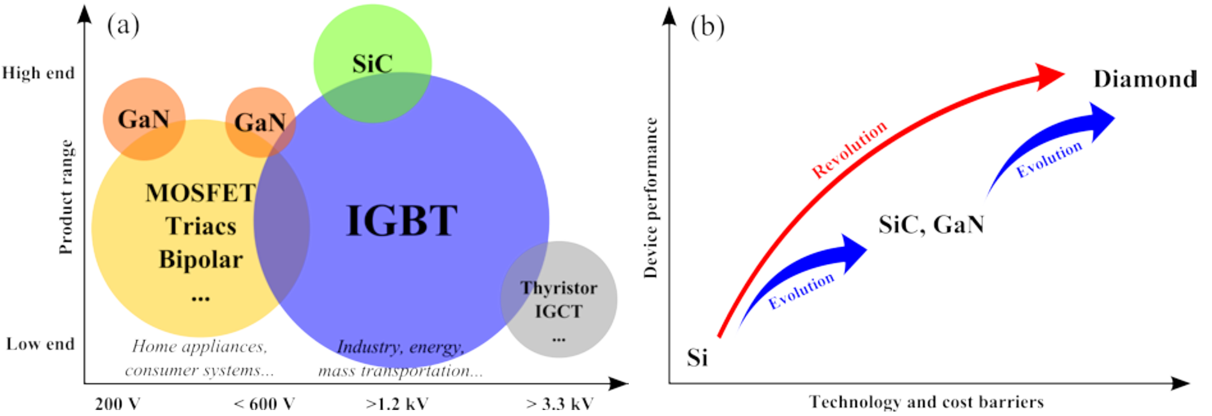

Figure 5-1: (a) Power device technology positioning (2015) [21]. (b) Two approaches within the semiconductor technology roadmap for power electronic devices (2013) [22].

The main motivation behind the development of wide-bandgap semiconductor devices for power electronics is to increase the efficiency of the many energy conversion steps between generation and end-user, which is estimated to be around 20% [4]. Recent figures show that the global market for power semiconductor devices is estimated to be about $11.5 billion and growing by roughly 10% each year [21]. Common power devices include two-terminal devices such as rectifiers and fast recovery diodes, as well as three-terminal devices, *e.g.* thyristors, GTOs (gate turn-off thyristor), IGCTs (integrated gate-commutated thyristors), MOSFETs (metal-oxide-semiconductor field-effect transistors) and IGBTs (insulated gate bipolar transistors). Major application areas include electric power transmission and distribution systems, traction drives and motor control, as well as switch-mode power supplies. Perhaps the most demanding application is within power distribution, where HVDC (high voltage direct current) converters operate at hundreds of kilovolts and hundreds of megawatt levels, but with low switching frequency, typically 50 or 60 Hz. Thyristors, and to some extent IGBTs, are used in these applications (see **Figure 5-1** (a) for a graphical representation). At the other end of the spectrum are switch-mode power supplies. These operate at much higher frequencies (kilohertz) but with lower power loads (kilowatts). For such applications MOSFETs and IGBTs are commonly used.

Despite silicon being by far the dominant semiconductor material for high-voltage and high-power applications, it suffers from a moderate thermal conductivity (~150 W m^{-1} K^{-1}), a bandgap of 1.1 eV that limits operation to below 200 °C, and relatively low breakdown fields (~0.3 MV cm^{-1}). The maximum breakdown voltage of silicon-based Schottky rectifiers has been limited by the increase in the resistance of the drift region. Commercially available devices are generally rated at breakdown voltages of less than 100 V. The much lower resistance of the drift region for silicon carbide, for example, enables the development of Schottky rectifiers with very high breakdown voltages. These devices not only offer fast switching but also eliminate the large reverse recovery current observed in high-voltage silicon p-i-n rectifiers. This reduces switching losses not only in the rectifier but also in the IGBTs used within the power circuits. Here, the advantages of using diamond to produce such rectifiers become evident. Diamond offers the largest benefits as a semiconductor material for power electronics applications (see **Figure 5-1** (b)), but its widespread application is hindered by the difficulties in synthesising and processing high-quality material in scalable quantities. Nevertheless, the rapid progress in synthesis technology has made it possible to produce $10 \times 10\,\mathrm{mm}^2$, highly pure homoepitaxial diamond layers by CVD, while even larger areas are being achieved by other technological approaches such as tiling and heteroepitaxial growth on Ir [23]. In comparison, other semiconducting materials, such as SiC, are already available in wafer sizes up to 150 mm. From an economic perspective, the establishment of future diamond-based active devices will depend heavily on an increase of wafer size above 2″, as well as on a decrease of defect density. While ref. [22] quotes the necessity of very low dislocation densities down to ~10^2 cm^{-2}, such estimations are in fact doubtful due to the lack of systematic data on the correlation between dislocation density and device performance. The effect of dislocations seems to vary depending on the type of material and on the specific device structure, as will be discussed below.

Nevertheless, it is clear that the development of economically viable diamond material for high power electronics requires tackling two main fronts: size and defect density. Large sizes is one of the inherent advantages of heteroepitaxial growth of diamond on Ir/YSZ/Si(001), whereas defect density remains relatively high (~10^7 cm^{-2} in the best cases [24]) compared to homoepitaxial single crystals (10^4-10^6 cm^{-2} [25]) grown on HPHT by CVD. The high dislocation density in heteroepitaxial diamond arises from the nucleation and growth/coalescence mechanism inherent to the technique (see section 1.3). Several strategies to reduce the density of dislocations in diamond are being studied and developed, which may involve 1) fine-tuning the growth conditions, 2) pre-treating the diamond substrate with fine polishing procedures, 3) engineering the surface morphology to control the propagation of the dislocations by shaping [26], by off-axis growth [27], or by ELO (epitaxial lateral overgrowth) [28].

Despite the relatively high density of dislocations, heteroepitaxial diamond on Ir has reached a level where first solid-state prototypes can already be produced and evaluated [29]. More recently, heteroepitaxial diamond-based p-n junction diodes for UV emission (235 nm) have been demonstrated [30]. Their relatively poor performance is attributed to the orders of magnitude higher density of dislocations compared to homoepitaxial diamond-based diodes, manifesting in a prominent defect-related electroluminescence (400-450 nm) in forward bias. In contrast, GaN-based light-emitting diodes were reported to be very insensitive to high dislocation densities in excess of 2×10^{10} cm^{-2}, which was attributed to the ionic nature of bonding in III-V nitrides [31].

In the case of power devices from wide-bandgap materials, the effect of dislocations on their performance seems to depend on the particular device architecture. On the one hand, dislocations are reported to act as traps for the charge carriers, effectively reducing the charge mobility/density and therefore increasing the resistivity of the material, leading to higher breakdown voltages [32, 33]. On the other hand, dislocations are deemed to increase the leakage current of the device, resulting in premature breakdown [34, 35]. Such contradicting effects appear to depend upon the direction of charge flow relative to the orientation of the dislocations. For example, in vertical structures the current will flow parallel to the threading dislocations and across different layers/materials, whereas in horizontal or pseudo-vertical structures the current will flow mostly perpendicular to the threading dislocations, along the drift layer, which is most critical to the performance. The charged nature of the dislocations [36] or the segregation of dopants along the dislocation lines [37, 38] can shunt a vertical structure, while in a horizontal one they are simply trapping/scattering centres. This suggests that optimised device architecture could reduce the negative effects of high dislocation densities, despite the pursued goal to achieve the purest, most defect-free materials [39]. In the case of diamond-based high power devices, these aspects haven’t been studied in sufficient detail to provide a clear picture of how detrimental the dislocations are to the device performance. Consequently, it is still to be seen if high switching and rectifying performances can be achieved with diamond-based diode structures possessing a high density of dislocations. The diamond/Ir/YSZ/Si(001) is, therefore, an ideal platform for this investigation, while backed by a great potential for large scale production that other platforms don’t quite match.

Hence, the main aim of this work was firstly to pioneer the demonstration of functional Schottky barrier diodes (SBD) produced with heteroepitaxial diamond on Ir and, secondly, to pursue higher performances through optimisation of the device structure. For this purpose, different structures (pseudo-vertical and vertical) and different metals (Ni and Ir) for the metal-semiconductor junction were tested. The devices were produced and characterised by different techniques in order to extract the current-voltage behaviour in forward and reverse bias, and to understand the performance-limiting factors.

5.2 Metal-semiconductor junction

There are two kinds of metal-semiconductor junctions: a) the junction between a metal and a lightly doped semiconductor (drift region), which exhibits rectifying *I*-*V* characteristics (**Figure 5-2**) due to the formation of a Schottky barrier, and b) the junction between a metal and a heavily doped semiconductor, which behaves as low-resistance Ohmic contact (basically electrical shorts). Ohmic contacts are an important part of semiconductor devices and have a significant influence on the performance of high-speed transistors, whereas Schottky rectifiers (or diodes) play an important role in fast switching and high power electronic applications, due to reduced power loss and faster response compared to p-n junction devices [40].

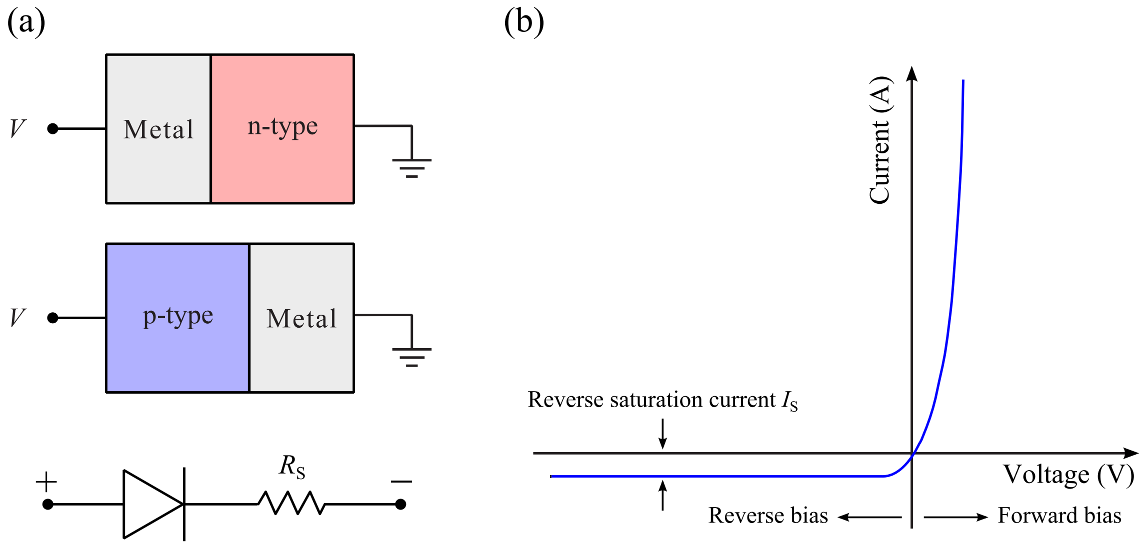

Figure 5-2: (a) Representation of a Schottky diode consisting of either an n-type (above) or a p-type (middle) semiconductor, along with the electronic representation of a forward-biased diode with a series resistance R_S (below). (b) The current-voltage behaviour of a diode.

5.2.1 Schottky barrier

The energy diagram of a metal-semiconductor junction in equilibrium is shown in **Figure 5-3**. The Fermi level E_F is flat because no voltage is applied across the junction, *i.e.* no bias. To the left of the junction, the energy band diagram is that of an n-type/p-type semiconductor. To the right of the junction is the energy band diagram of a metal, with the energy states below E_F almost totally filled and the states above E_F almost empty. The most important feature of this energy diagram is the energy barrier at the metal-semiconductor interface. It is characterised by the Schottky barrier height, ϕ_B, which is a function of both the metal and the semiconductor. In both figures there is a depletion layer adjacent to the semiconductor-metal interface, where E_F is close to neither E_{CB} nor E_{VB} (such that the density of electrons n and the density of holes p are approximately zero).

The Schottky barrier height is the most important parameter of a metal-semiconductor contact, with $\phi_{\mathrm{B,n}}$ and $\phi_{\mathrm{B,p}}$ depending on the work function ϕ_{M} of the metal and the electron affinity of the semiconductor, χ_{S}, according to equation (5.2.1).

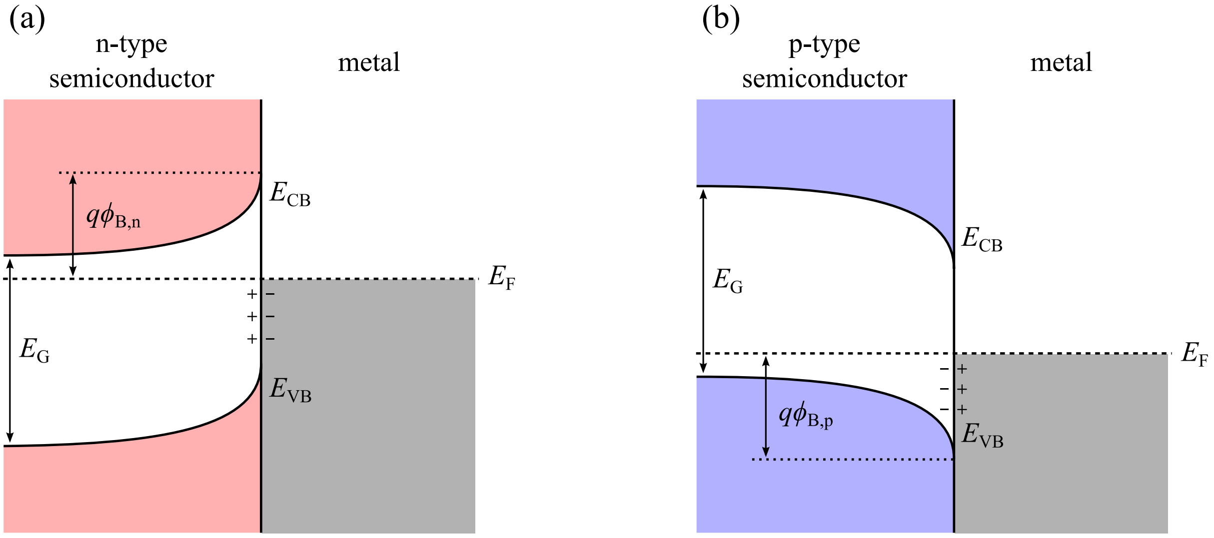

Figure 5-3: Energy band diagrams of metal-semiconductor contacts. The Schottky barrier heights depend on the metal and semiconductor materials. (a) $\phi_{\mathrm{B,n}}$ is the barrier against electron flow between the metal and the n-type semiconductor. (b) $\phi_{\mathrm{B,p}}$ is the barrier against hole flow between the metal and the p-type semiconductor.

$$\phi_{\mathrm{B}} = \phi_{\mathrm{M}} - \chi_{\mathrm{S}} \tag{5.2.1}$$

This expression is quantitatively true only when the Fermi level at the interface lies close to the neutrality level (see **Figure 5-4**) of the surface/interface states in the bandgap and the net charge is close to zero. Otherwise, surface states which arise from the termination of the crystal will play a role in the energy band diagram. On metallic surfaces, they are known to lead to a surface dipole which contributes to the work function of the metal surface. On semiconductors, the presence of charged (acceptor/donor-like) surface states in the bandgap is known to cause what is termed “Fermi level pinning”. This effect leads the Fermi level being “fixed” around a certain position, regardless of the metal work function, and equation (5.2.1) remains only qualitatively true. Pinning does not happen on every semiconductor surface, however, because surface states are not positioned in the bandgap of some semiconductors, such as the non-polar (110) surfaces of III-V semiconductors. A more accurate relationship than equation (5.2.1) has to take into account the polarisability of the semiconductor and the density of energy states at the interface [40]. In the case of diamond-metal junctions, the effect of interfacial states has been modelled by several authors, who took into account surface states for the calculation of the Schottky barrier height [41].

The Schottky barrier on diamond-metal junctions is strongly influenced by the surface termination of the diamond, in a similar way to the liquid-semiconductor interface discussed in

Chapter 4. H-termination is known to reduce the electron affinity down to −1.3 eV, causing upward band bending, while O-termination promotes the opposite effect, with $\chi_S \leq 1.7$ eV [42]. For diamond-based high power Schottky rectifiers, O-termination is desired in order to increase the barrier and reduce the leakage current that would cause premature breakdown, despite the higher barrier leading to a higher on-state voltage drop. Also, the oxygenated diamond surface is more stable at high temperatures, contributing to the device stability.

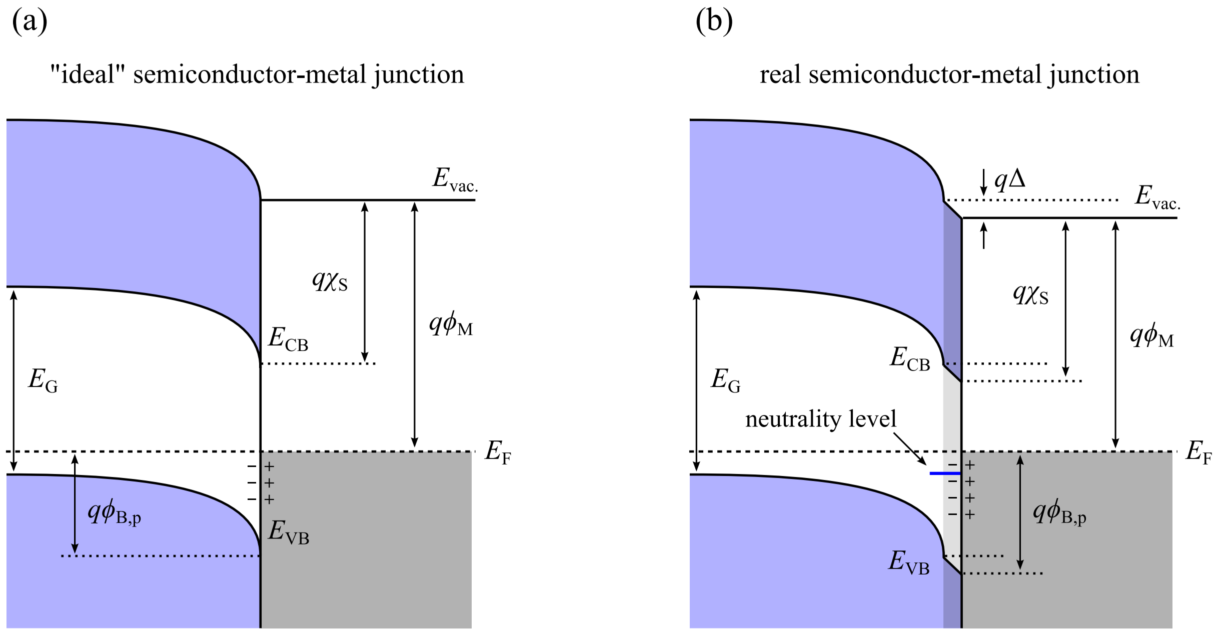

Figure 5-4: (a) An “ideal” p-type semiconductor-metal contact and (b) a real p-type semiconductor-metal contact with a characteristic dipole layer at the interface.

5.2.2 Forward conduction

Current flow across the metal-semiconductor junction can be produced by the application of a negative (or positive) bias to the n-type (or p-type) side. This produces a shift in the energy band structure as illustrated in **Figure 5-5** (a). Current flow across the interface then occurs mainly due to majority carriers – electrons (or holes) for an n-type (or p-type) semiconductor. The current transport across the contact can take place via four basic processes [2]:

1. *Thermionic emission*: the transport of majority carriers from the semiconductor into the metal over the potential barrier;
2. *Tunnelling:* the transport of majority carriers by quantum mechanical tunnelling through the potential barrier;
3. *Recombination*: the transport of electrons and holes into the depletion region, followed by their recombination;
4. *Minority carrier*: the transport of minority carriers from the metal into the neutral region of the semiconductor, followed by recombination.

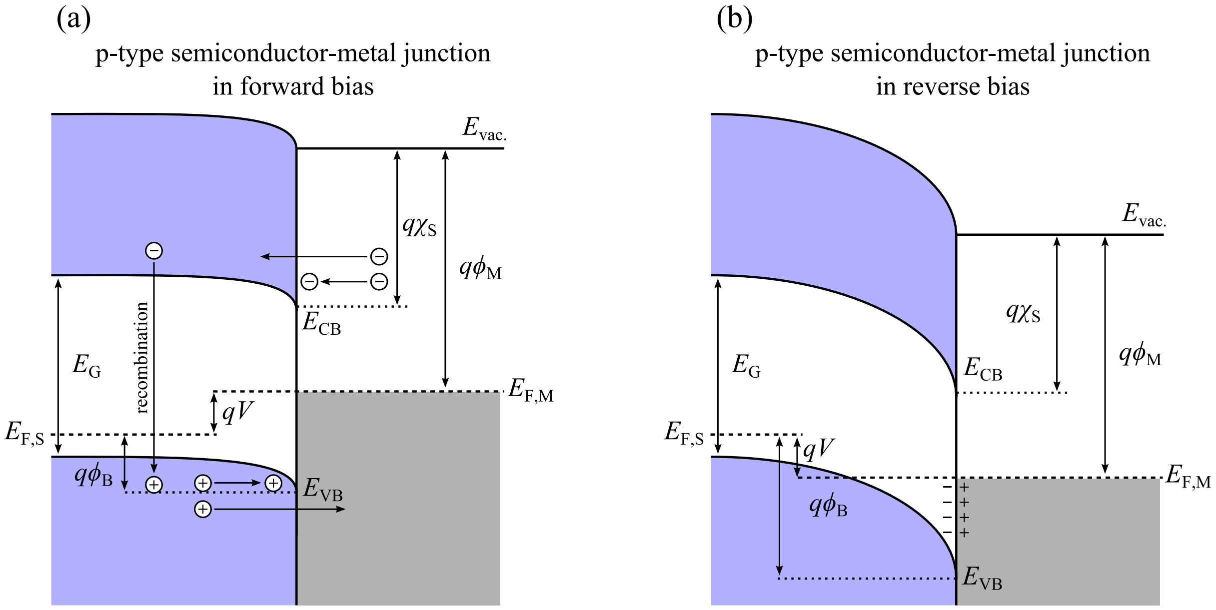

(a) p-type semiconductor-metal junction in forward bias

(b) p-type semiconductor-metal junction in reverse bias

Figure 5-5: Band diagram of an "ideal" p-type semiconductor-metal junction in (a) forward bias and (b) reverse bias.

The doping concentration in the semiconductor must be relatively low in power rectifiers to support the reverse bias. In this way, the potential barrier is not sharp enough to allow substantial tunnelling current, because the depletion layer is then relatively wide. The recombination current in the space charge region is observable only at very low on-state current levels. The current transport due to the injection of minority carriers is usually negligible unless the Schottky barrier height is large, which is usually undesirable in power Schottky rectifiers because of the on-state voltage drop increasing with the barrier height [2]. Consequently, current flow by thermionic emission is the dominant current transport mechanism in high mobility semiconductor Schottky rectifiers, and so, the diode law (*Shockley equation*) can be written as [43]:

$$I = \underbrace{AA^{*}T^{2}\exp\left(-\frac{q\phi_{\mathrm{B}}}{k_{\mathrm{B}}T}\right)}_{I_{\mathrm{S}}}\left[\exp\left(\frac{qV_{\mathrm{D}}}{nk_{\mathrm{B}}T}\right)-1\right] \tag{5.2.2}$$

where A (m^2) is the junction area, T (K) is the absolute temperature, q (C) is the elementary charge, ϕ_{B} (eV) is the Schottky barrier height, k_{B} (m^2 kg s^{-2} K^{-1}) is the Boltzmann constant, V_{D} (V) is the potential across the diode, n is the ideality factor, I_{S} (A) is the saturation current shown in **Figure 5-2** (b) and A^{*} (A m^{-2} K^{-2}) is the effective Richardson constant, given by:

$$A^{*} \equiv \frac{4\pi q m^{*} k_{\mathrm{B}}^{2}}{h^{3}} \tag{5.2.3}$$

where m^{*} (kg) is the effective mass and h (m^2 kg s^{-1}) is Planck's constant. For free electrons the Richardson constant is 1.2×10^{6} A m^{-2} K^{-2}. Silicon and silicon carbide have effective values of, respectively, 1.1×10^6 and 1.46×10^6 A m^{-2} K^{-2}. The value for diamond is often taken to be 0.9×10^6 A m^{-2} K^{-2} [15, 44], although deviations due to different material qualities may exist [45].

Equation (5.2.2) is based upon the superimposition of the current fluxes from the metal and the semiconductor, which balance out at zero bias, and it holds true for both positive and negative voltages. At forward bias, the exponential term in square brackets becomes dominant. In the case of power Schottky rectifiers, the necessary thick, lightly doped drift region below the Schottky contact introduces a series resistance, R_S (see **Figure 5-2** (a)), which causes a voltage drop V_R across the drift region and increases the on-state voltage drop of the power Schottky rectifier. In reality, R_S will be a sum of bulk and contact resistances of the whole device, all of which can be detrimental to the performance. With the voltage drop V_R across R_S, the current through the diode will be given by:

$$I = \frac{V - V_\mathrm{D}}{R_\mathrm{S}} \tag{5.2.4}$$

where V_D (V) is the voltage drop across the junction and V (V) the applied bias. Rewriting equation (5.2.4) applying equation (5.2.2) gives:

$$I = I_\mathrm{S}\left[\exp\left(\frac{q\left(V - IR_\mathrm{S}\right)}{nk_\mathrm{B}T}\right) - 1\right] \tag{5.2.5}$$

One possibility to solve equation (5.2.5) is to do it numerically. Usually the *I*-*V* curves are obtained experimentally and the above equation is fitted to the data points using specialised software. From this fitting several parameters of interest are obtained, such as R_S, ϕ_B and *n*. Once knowing the current, the voltage drop V_D across the junction can be obtained from equation (5.2.4).

5.2.3 Reverse blocking

When a reverse bias is applied to the Schottky rectifier, the voltage is supported across the drift region with the maximum electric field, E_M, located at the metal-semiconductor contact. The energy band diagram corresponding to this condition is illustrated in **Figure 5-5** (b). The maximum electric field is related to the applied reverse voltage in a unidimensional structure as [2]:

$$E_\mathrm{M} = \sqrt{\frac{2qN}{\varepsilon_\mathrm{S}}\left(V + V_\mathrm{bi}\right)} \tag{5.2.6}$$

where N (m^{-3}) is the density of donors or acceptors in the semiconductor, ε_S (F m^{-1}) is the dielectric constant and V_bi (V) is the built-in potential.

The leakage current for Schottky rectifiers is comprised of three components [2]:

1. Space charge generation current arising from the depletion region;
2. Diffusion current arising from carrier generation in the neutral region;
3. Thermionic emission current across the metal-semiconductor contact.

When the barrier height is relatively small, such as in silicon Schottky rectifiers (0.6-0.7 V), the thermionic emission component is dominant and the leakage current I_L can be obtained from equation (5.2.2). Since the typical reverse bias voltages are much greater than the thermal energy, $k_\mathrm{B}T/q$, the exponential term in the square brackets becomes very small and equation (5.2.2) becomes simply:

$$I \cong \underbrace{AA^{*}T^{2}\exp\left(-\frac{q\phi_\mathrm{B}}{k_\mathrm{B}T}\right)}_{I_\mathrm{S}} \cong I_\mathrm{L} \tag{5.2.7}$$

Equation (5.2.7) shows that the leakage current due to the thermionic emission process is a strong function of the Schottky barrier height and the temperature. To reduce the leakage current and the power dissipation in reverse bias, a large Schottky barrier height is therefore required. The expression above also shows that an increase in temperature leads to a rapid increase in leakage current. If the power dissipation due to the leakage current becomes dominant, the resulting increase in the device temperature produces a positive feedback mechanism, which can lead to unstable operation of the Schottky rectifier due to thermal runaway. Diamond, with its high thermal conductivity, is less prone to this problem than other semiconductors, especially when the Schottky barrier height is kept at higher values to further reduce the leakage current, despite increasing the on-state voltage drop. This makes diamond the ideal material for high power rectifiers.

The reverse bias behaviour of a Schottky diode is in fact more complicated than the above considerations. With increasing reverse bias the leakage current will increase and eventually lead to the premature breakdown of the device, due to a combination of the following effects [2]:

1. *Image force lowering*: the electrostatic attraction between opposite charges at both sides of the junction leads to a decrease of the potential near the interface on the semiconductor side. The combination of this force potential with the potential caused by the Schottky barrier lowers the overall barrier against charge flow across the junction and can lead to a substantial increase of the leakage current. The change in the Schottky barrier height can be given as a function of the maximum electric field, E_M, as:

$$\Delta\phi_\mathrm{B} = \sqrt{\frac{qE_\mathrm{M}}{4\pi\varepsilon_\mathrm{S}}} \tag{5.2.8}$$

2. *Avalanche multiplication*: with increasing negative bias and increasing leakage current, electrons with high energy crossing the junction trigger an impact ionisation process, which releases bound electrons and multiplies the number of charge carriers reaching the edge of the depletion layer by a factor M, which is a function of E_M and the depletion layer width w_D;
3. *Tunnelling*: it arises from quantum-mechanics that with increasing reverse bias, and hence increasing electric field across the semiconductor, the probability of charge carriers crossing the Schottky barrier will also increase, contributing to the leakage current. The thermionic field emission model for the tunnelling current leads to a barrier lowering effect proportional to the square of the electric field at the metal-semiconductor interface.

High bandgap materials such as SiC and diamond require larger reverse bias than low bandgap materials such as silicon to initiate an avalanche breakdown. It turns out, for example in SiC devices, that barrier lowering and tunnelling are the dominant effects causing the increase in leakage current, which can be written as:

$$I_\mathrm{S} \cong AA^{*}T^{2}\exp\left(-\frac{q\phi_\mathrm{B}}{k_\mathrm{B}T}\right)\exp\left(\frac{q\Delta\phi_\mathrm{B}}{k_\mathrm{B}T}\right)\exp\left(C_\mathrm{T}E_\mathrm{M}^{2}\right) \tag{5.2.9}$$

where C_T is a tunnelling coefficient. **Figure 5-6** illustrates the reverse bias current-voltage behaviour when barrier lowering and tunnelling are considered, *i.e.* applying equation (5.2.9).

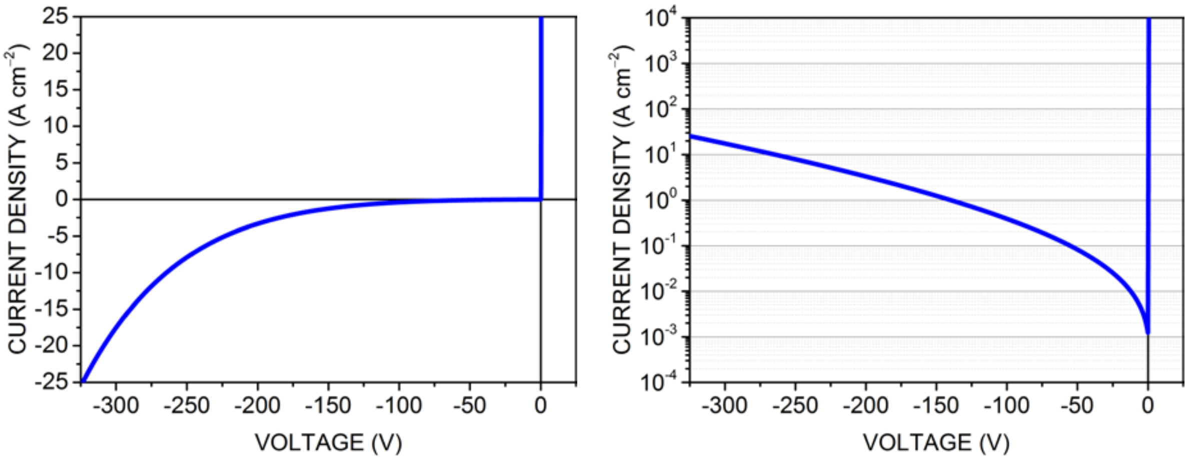

Figure 5-6: Current-voltage curve of a non-ideal diamond-based Schottky diode in (a) linear scale and (b) semi-logarithmic scale. The reverse bias leakage current is modelled by equation (5.2.9) and the forward bias current is modelled by equation (5.2.5). A series resistance $R_\mathrm{S} = 52\ \Omega$ and a carrier density in the drift layer $N_\mathrm{A} = 3.5\times10^{16}\ \mathrm{cm}^{-2}$ were chosen, along with an arbitrary tunnelling coefficient $C_\mathrm{T} = 0.3\times10^{-16}\ \mathrm{m}^2\ \mathrm{V}^{-2}$. The smaller C_T is, the higher the breakdown voltage.

5.2.4 Device capacitance

The reverse-blocking voltage is supported across a depletion region in the power Schottky rectifier as shown in **Figure 5-5** (b). The thickness of the depletion region w_{D} is related to the applied reverse bias voltage by [2]:

$$w_{\mathrm{D}} = \sqrt{\frac{2\varepsilon_{\mathrm{S}}}{qN}\left(V + V_{\mathrm{bi}}\right)} \tag{5.2.10}$$

In a simplified model, the metal-semiconductor junction can be treated as a parallel-plate capacitor, and the capacitance is given as:

$$C = \frac{\varepsilon_{\mathrm{S}} A}{w_{\mathrm{D}}} \tag{5.2.11}$$

Equations (5.2.10) and (5.2.11) put together result in the Mott-Schottky (MS) relationship, which was also applied in the characterisation of the semiconductor-electrolyte interface in chapter 4. It can be used to determine the built-in potential V_{bi} and the charge carrier density N from C-V measurements:

$$\frac{1}{C^2} = \frac{2}{qN\varepsilon_{\mathrm{S}} A^2}\left[\left(V + V_{\mathrm{bi}}\right) - \frac{k_{\mathrm{B}}T}{q}\right] \tag{5.2.12}$$

5.3 Device structure

The performance of power rectifiers, namely diamond Schottky diodes, is also dependent on their construction. The electric field in the material, the presence and arrangement of defects in the crystal, the metal contact interface and geometry, thicknesses, doping concentration, etc., all play a role, as well as technological aspects (*e.g.* forward conduction *vs.* reverse blocking requirements). The trade-off between increasing the breakdown voltage and reducing the on-state resistance to achieve a better rectification with lower power dissipation is represented by the $V_{\mathrm{br}}/R_{\mathrm{on}}$ relationship in equation (5.3.1) [1]:

$$\frac{V_{\mathrm{br}}}{R_{\mathrm{on}}} = \frac{1}{2} q E_{\mathrm{M}} \mu_{\mathrm{p}} p \tag{5.3.1}$$

where q (C) is the elementary charge, E_{M} (V m^{-1}) the breakdown field, μ_{p} (m^2 V^{-1} s^{-1}) the hole mobility and p (m^{-3}) the hole density.

Specifically for unipolar devices, *Baliga's figure of merit* (BFM) is commonly taken for the performance rating and comparison among different semiconductor materials [2, 39]:

$$\mathrm{BFM} = \frac{V_{\mathrm{br}}^2}{R_{\mathrm{on}} A} = \varepsilon_{\mathrm{S}} \mu_{\mathrm{p}} E_{\mathrm{M}}^3 \tag{5.3.2}$$

where A (cm^2) is area of the Schottky junction. Note: $R_{\mathrm{on}} A = R_{\mathrm{S}}$ (Ω cm^2).

The reduction of R_{on} can be achieved with smaller drift layer thickness, higher doping, defect-free material, as well as by improving Ohmic contacts. On the other hand, V_{br} can be increased by using a larger drift layer thickness, lower doping, and by reducing the leakage current with a higher Schottky barrier height (*i.e.* by choosing a metal with appropriate work function) and by minimising structural defects in the semiconductor. While in general a higher conductivity will compromise the breakdown voltage, V_{br} can be improved by optimising the device design.

5.3.1 Edge termination

The role of edge termination is to distribute the electric field in the vicinity of the edge of the metallic contact, thereby increasing the attainable blocking voltage of the device. It is critical to its operation and reliability. Without effective edge termination, strong field enhancement at the contact edge cannot be avoided, which causes premature avalanche breakdown [1]. Several types of edge termination have been demonstrated in wide bandgap semiconductors: guard rings, metal field plates extending over an insulating surface layer, resistive Schottky barrier field plates and junction-termination extension. Because there is no shallow n-dopant for diamond and because diffusion after ion implantation is not possible, field plates are preferred and have been demonstrated in diamond Schottky rectifiers [16, 18]. An illustration is shown in **Figure 5-7** (b).

5.3.2 Vertical structure

The theoretical breakdown field for diamond is very high, $E_{\mathrm{M}} > 10\ \mathrm{MV\ cm^{-1}}$, but it likely requires defect-free material and an effective edge termination before it can be achieved. Fields up to 4 MV cm^{-1} have been measured in intrinsic CVD diamond single crystals [9]. One of the difficulties with diamond is the incomplete activation of the shallowest known dopant, boron, at room temperature. This leads to $p \ll N_{\mathrm{A}}$ and lower $V_{\mathrm{br}}/R_{\mathrm{S}}$. Increasing N_{A} will also have the side-effect of reducing charge mobility, so this is not a viable solution.

One way to take advantage of the high mobility in diamond and have at the same time a high density of charge carriers is to adopt a vertical metal-intrinsic-p$^+$ (m-i-p$^+$) structure (see **Figure 5-7**). The doping concentration of the p$^+$ layer is chosen to be very high ($N_{\mathrm{A}} > 10^{19}$ cm^{-3}), preferably above the metallic transition ($N_{\mathrm{A}} > 3 \times 10^{20}$ cm^{-3}), resulting in a high hole density from the complete activation of boron acceptors. Then the charge carriers can be injected into the intrinsic layer from the p^+ layer in forward bias, while high breakdown voltages can still be sustained in reverse bias. Another advantage of this structure is that the electric field is evenly distributed across the intrinsic region at reverse bias.

At high forward bias the current across the diode becomes limited by the free carrier space charge in the intrinsic layer, and the voltage drop across the drift layer obeys the Mott-Gourney relationship [1]:

$$V_{\mathrm{D}} = \sqrt{\frac{8d^3 I}{9\varepsilon_{\mathrm{S}}\mu_{\mathrm{p}} A}} \qquad (5.3.3)$$

where d (m) is the thickness of the drift layer and μ_{p} ($\mathrm{m}^2\ \mathrm{V}^{-1}\ \mathrm{s}^{-1}$) the hole mobility. It is clear from this expression that in order to minimise V_{D} one needs a thin intrinsic layer and high hole mobility. The minimum thickness is, however, limited by the minimum desired breakdown voltage of the device and by its breakdown field strength, according to equation (5.3.1).

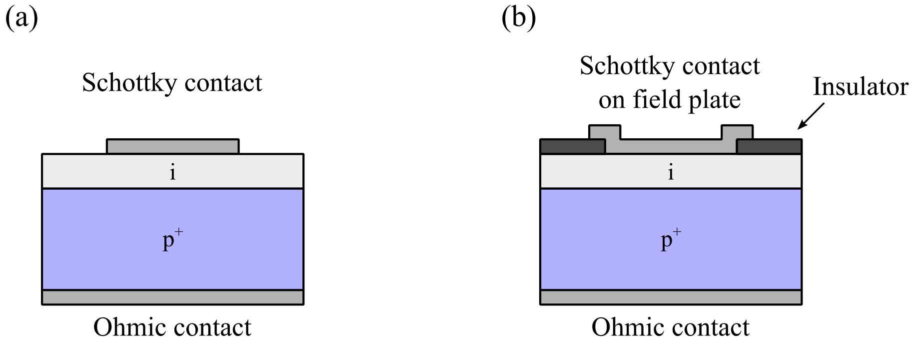

Figure 5-7: Vertical m-i-p^+ diode structure (a) without field plate and (b) with field plate.

One of the difficulties with this vertical structure is the necessity to have a p^+ layer thick enough to provide mechanical stability for the whole device, which should be a few hundred µm thick at least. Achieving such thickness is not practical with certain types of MWPCVD reactors (including the ASTeX used throughout this work), which require growth times of several days. Furthermore, heavy B-doping can be rather unstable and lead to the formation of defects on the sample. Therefore, to avoid such complications and to take advantage of the best quality diamond substrates, a pseudo-vertical structure can be adopted instead.

5.3.3 Pseudo-vertical structure

A diamond Schottky diode built as a pseudo-vertical structure consists of a thin heavily B-doped layer grown on a thick diamond substrate, followed by growth of an intrinsic drift layer on top (see **Figure 5-8**). It has the advantage of requiring a more practical thin B-doped layer, and of inheriting mechanical stability from the diamond substrate.

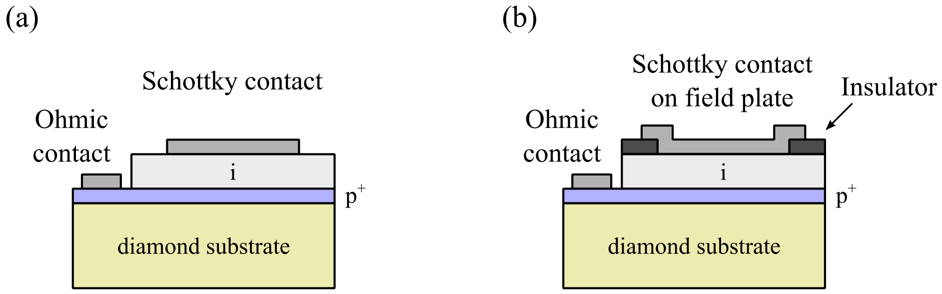

Figure 5-8: Pseudo-vertical m-i-p diode structure (a) without field plate and (b) with field plate.

5.3.4 Vertical back-etched structure

A noticeable disadvantage of the two previous structures is the need to grow an intrinsic layer on top of a metallic B-doped layer, a process that can induce the formation of interfacial defects which propagate into the layer that is supposed to be defect-free. This can happen mostly due to the lattice mismatch between undoped and heavily B-doped diamond, as discussed earlier in chapter 3. This problem is aggravated when the surface to be overgrown is first subjected to mechanical polishing.

In order to avoid these problems, we devised a different strategy: a back-etched vertical structure. It consists of 1) preparing a diamond substrate of the highest quality; 2) growing a thick (couple 100 µm) B-doped layer on top; 3) back-etching the diamond substrate down to the desired thickness of *ca.* 20 µm [46] and using it as the drift layer. In this way the stress due to the lattice mismatch at the interface accommodates in the B-doped layer, which isn’t as detrimental to the performance of the diamond SBD. Potential downsides of this approach are the long deposition time, which can lead to unstable growth and formation of defects, and the increase of the series resistance of the device with the higher thickness.

5.4 Experimental

In this work, several heteroepitaxial diamond-based SBDs were fabricated:

1. The first type of sample consisted of nickel-diamond junctions in a pseudo-vertical SBD structure with a thin drift layer of ~2 µm;
2. The second type of sample consisted of iridium-diamond junctions in a vertical back-etched SBD structure with a thick drift layer of ~20±5 µm;
3. The third type of sample consisted of iridium-diamond junctions in a regular vertical SBD structure with a thin drift layer of ~2.5 µm;

4. The last type of sample consisted of nickel diamond junctions in a regular vertical SBD structure with a thin drift layer of ~1 µm.

5.4.1 Nickel-diamond pseudo-vertical structure

The first Schottky devices prepared were nickel-diamond junctions in a pseudo-vertical configuration. This is a more easily achievable structure that doesn't involve growth of thick B-doped layer or thinning of the substrate. Nickel, with a work function of roughly 5 eV, was firstly chosen as a metal contact based on good performance demonstrated in the literature [19], and for being readily available and easy to handle.

The sample preparation steps are illustrated in **Figure 5-9**: 1) A diamond substrate[1] of ~1 mm thickness was grown on Ir/YSZ/Si(001), 6° off-axis, and 2) subsequently made freestanding with chemical (acid) and mechanical (scaife polishing) removal of the support substrate. 3) The surface was then polished mechanically, followed by RIE (reactive ion etching) in Ar/Cl_2 atmosphere for 1 h, in order to remove *ca.* 3 µm of diamond and take away the damaged layer caused by the mechanical polishing step. 4) Subsequently a metallic (p^{++}) B-doped layer was grown by MWPCVD to a thickness of ~7 µm, followed by growth of what was intended to be an intrinsic or a lightly B-doped (p^{-}) drift layer. This layer turned out to be a ~2 µm p^{+} layer with an estimated density of acceptors $N_\mathrm{A} = 2 \times 10^{18}\ \mathrm{cm}^{-3}$ due to the high B background in the reactor from previous processes[2]. 5) Next, a strip of the p^{++} layer was exposed by RIE using a shadow mask, in order to enable a back contact for the diodes. 6) The diamond sample was then subjected to an acid treatment in a boiling mixture of concentrated $\mathrm{H_2SO_4} + \mathrm{HCl} + \mathrm{HNO_3}$ (roughly 1:1:1) for 30 min to remove non-diamond phases and metal contaminants [47] and to promote an oxygen termination[3] of the diamond surface. Then a strip of Ti(20 nm)/Pt(250 nm) was deposited by e-beam evaporation (process pressure of ~10^{-6} mbar) on the exposed p^{++} area of the diamond by means of a shadow mask. 7) An annealing step at 600 °C in atmosphere (under Ar flow of *ca.* 50 sccm) was performed to promote an Ohmic contact between the diamond and the Ti/Pt layer. 8) Finally, the sample was placed again in the e-beam evaporator for the deposition of 25 circular Ni pads on top of the p^{+} (drift) layer using another shadow mask.

---

[1] Sample identification: MFAIX336.

[2] The reactor was subjected beforehand to a H_2+CO_2 plasma cleaning step for 6 hours. The subsequent growth step for the drift layer included CO_2 added to the gas phase to reduce B incorporation, a strategy discussed before in chapter 2.

[3] See section 7.2 for further information on chemical O-termination of our diamond samples.

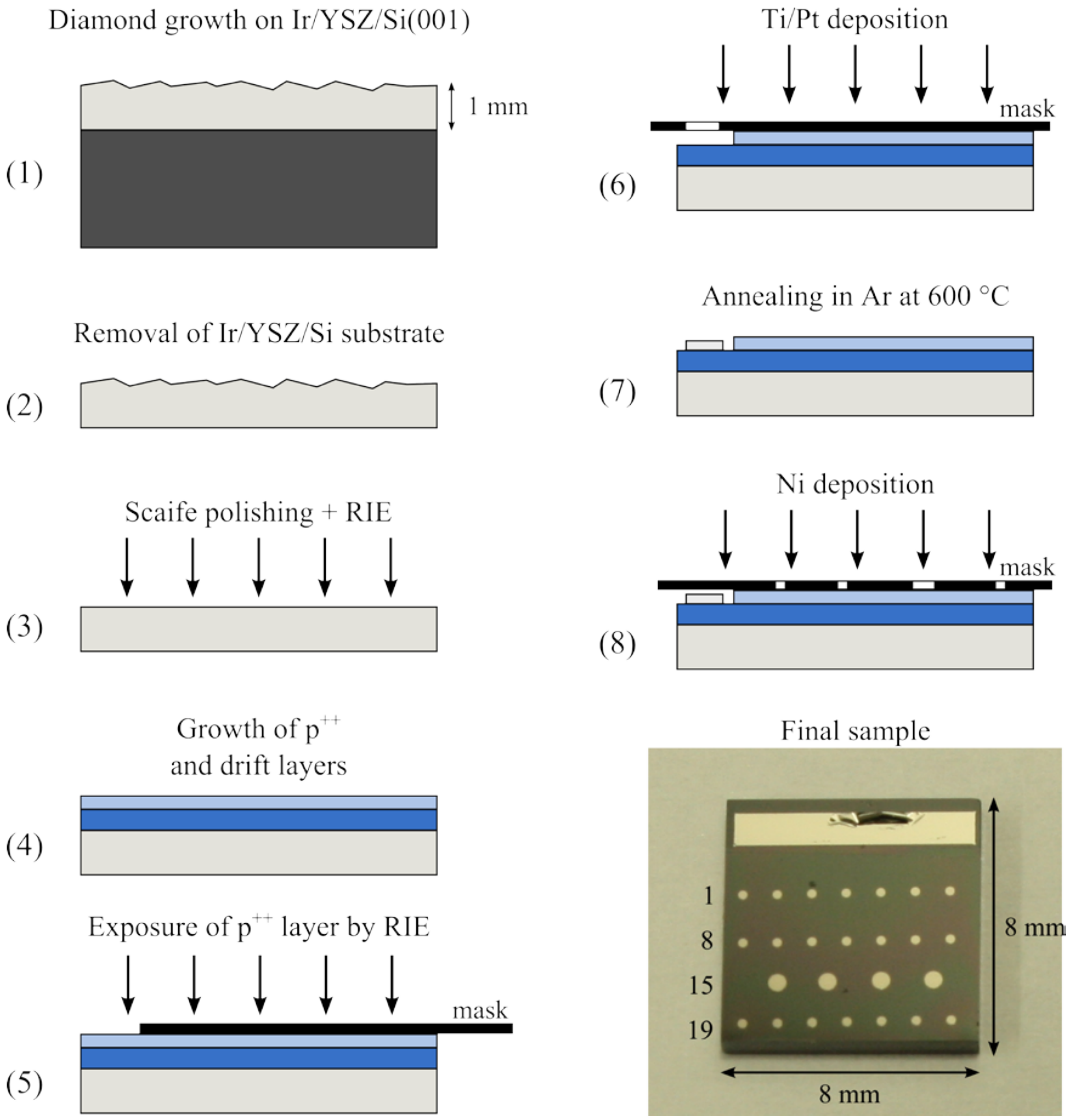

Figure 5-9: Fabrication steps of 25 nickel-diamond junctions in a pseudo-vertical configuration. Electrode areas: $A_{\mathrm{small}} = 4.91\times10^{-4}$ cm^2 and $A_{\mathrm{large}} = 1.96\times10^{-3}$ cm^2. Consult the text for a detailed description of the process.

5.4.2 Iridium-diamond vertical structure

5.4.2.1 *Thick drift layer (type a)*

The next Schottky devices prepared were iridium-diamond junctions in a vertical configuration. A back-etch approach was taken in order to use the higher quality of the ~1 mm thick undoped diamond substrate. The sample preparation was rather challenging, as the laser-cutting and mechanical polishing steps easily lead to wedge formation, causing significant thickness inhomogeneity over the sample area. With this structure we also wanted to exploit our know-how with epitaxial iridium deposition to pioneer the creation of a Schottky junction capable of sustaining high operation temperatures due to the high melting point of this metal (~2500 °C) and strong bonding with carbon, which would in principle result in a very stable performance. Furthermore, iridium has a work function similar to nickel. Ir-diamond Schottky diodes were, to the best of our knowledge, never reported.

The sample preparation steps are illustrated in **Figure 5-10**: 1) A diamond substrate[4] of ~1 mm thickness was grown on Ir/YSZ/Si(001), 6° off-axis along [110], and 2) subsequently made freestanding with chemical (acid) and mechanical (scaife polishing) removal of the support substrate. 3) The surface was then polished mechanically, followed by RIE (reactive ion etching) in Ar/SF_6 atmosphere until ~4 µm of diamond was removed along with the damage caused by mechanical polishing. 4) Subsequently a metallic (p^{++}) B-doped layer was grown by MWPCVD to a thickness of ~300 µm. This layer had to be made thick in order to ensure mechanical stability/integrity of the device. 5) The backside of the diamond substrate was then laser-cut, mechanically polished and subjected to RIE until a thickness of roughly 20±5 µm was achieved. 6) Next, the sample was subjected twice to air plasma treatment (one run for each side, 5 min each at 0.6 mbar) to O-terminate the diamond surface[5]. 7) Using e-beam evaporation, metallic contacts were prepared in two steps: first the iridium contacts were evaporated on the surface of the drift layer using a shadow mask, up to a thickness of ~140 nm (process pressure of 10^{-6}–10^{-5} mbar, sample holder heated to ~450 °C, deposition rate of ~0.002 nm s^{-1} for the first ~10 nm, ~0.004 nm s^{-1} for the next ~11 nm and finally ~0.02 nm s^{-1} until the final thickness). Such parameters are used for epitaxial deposition of Ir [48]. Second, a large circular Ti(20 nm)/Pt(130 nm) contact was evaporated on the exposed p^{++} (heavily B-doped) side of the diamond by means of a shadow mask (process pressure of 10^{-6}–10^{-5} mbar, sample holder heated to ~450 °C). 8) The evaporation steps were followed by a 2 h annealing step at 500 °C while in vacuum inside the evaporation chamber. The final device can be seen in **Figure 5-10** (9).

---

[4] Sample identification: MFAIX235.

[5] Consult section 7.2 for further information on the surface O-termination by air plasma treatment.

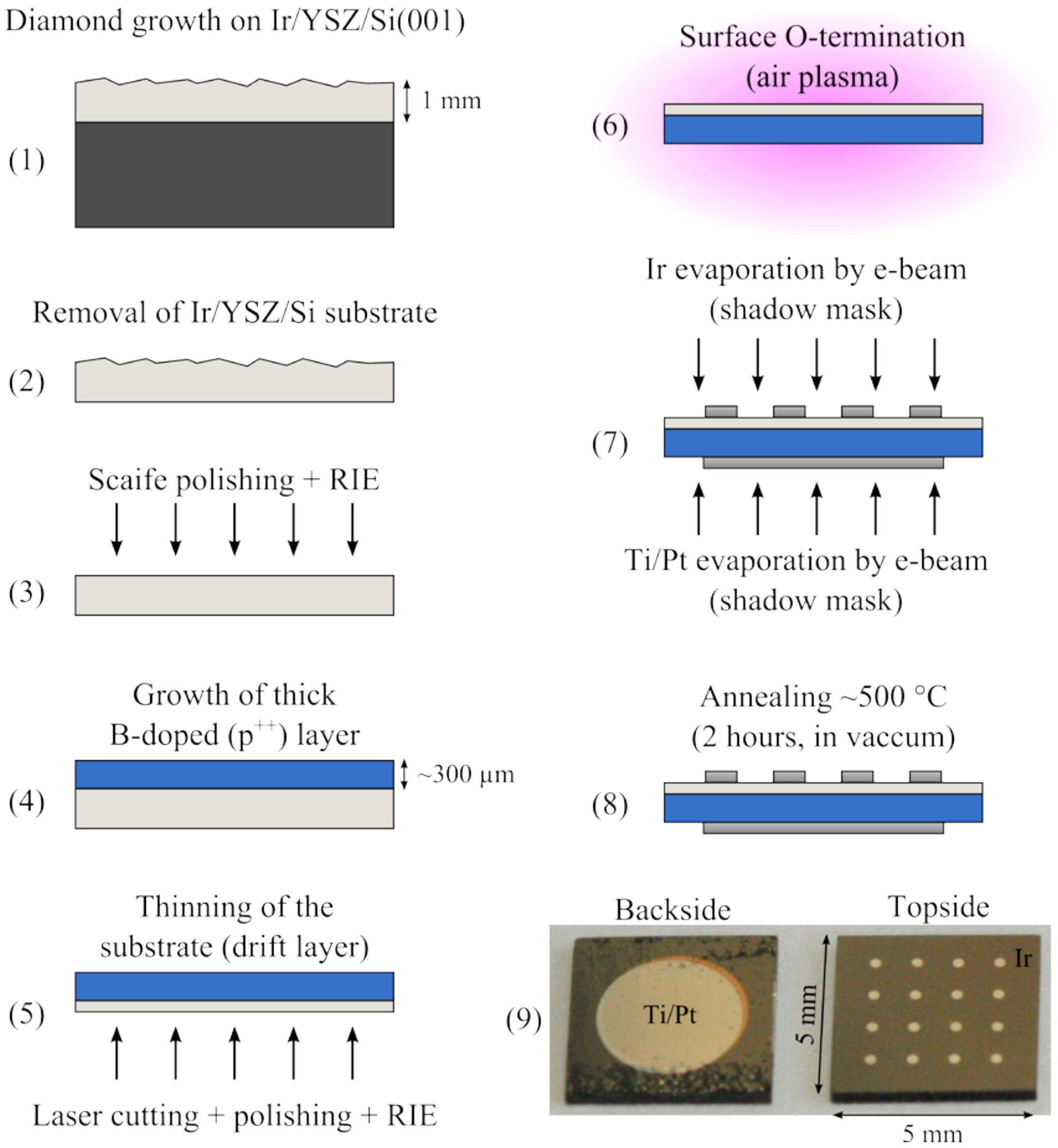

Figure 5-10: Fabrication steps of 16 iridium-diamond junctions in a vertical configuration. Electrode area: $A = 4.91\times10^{-4}\ \mathrm{cm}^2$. Consult the text for a detailed description of the process.

5.4.2.2 *Thin drift layer (type b)*

A second version of the Ir-diamond Schottky diodes was produced in a similar way to the previous, but following a regular vertical structure. Here, the original undoped diamond substrate was back-etched until completely removed, leaving only the thick B-doped layer. After a RIE step to remove polishing-induced defects, a ~2.5 µm thick intrinsic layer was grown on the B-doped layer by MWPCVD in a boron-free reactor (see **Figure 5-11** for an illustration). Mott-Schottky analysis yielded and estimated density of acceptors between $N_\mathrm{A} = 6\times10^{16}\ \mathrm{cm}^{-3}$ and $N_\mathrm{A} = 1\times10^{17}\ \mathrm{cm}^{-3}$ in the drift layer, depending on the device/diode measured. The sample preparation differed from the previous one in the steps highlighted below in **Figure 5-11**.

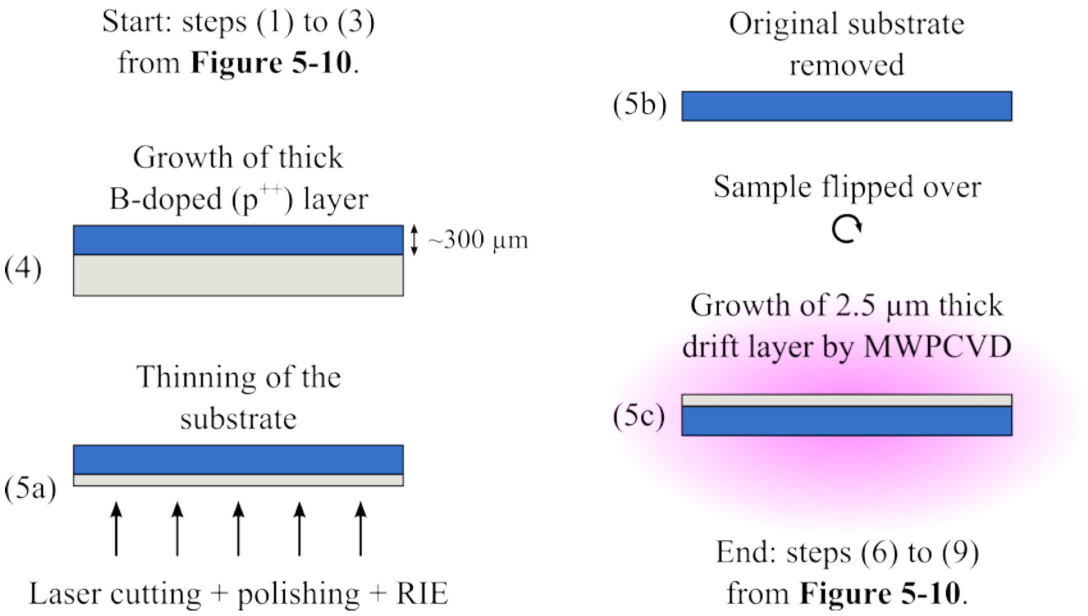

Figure 5-11: Modified fabrication steps of 16 iridium-diamond junctions in a vertical SBD configuration. Steps 5a to 5c substitute step 5 in **Figure 5-10** for this sample. Electrode area: $A = 4.91\times10^{-4}\ \mathrm{cm}^2$. Consult the text for a detailed description of the process.

5.4.3 Nickel-diamond vertical structure

At a later stage the same substrate and diode structure used for the Ir-diamond vertical structure “type b” was reset and nickel Schottky contacts were used. To remove the Ir contacts the sample was lightly polished and subjected to RIE for 4 minutes, leading to a drift layer thickness of 1.2±0.2 µm. Then the sample was cleaned in hydrogen plasma for 5 minutes and O-terminated in air plasma for 5 minutes. Subsequently, Ni contacts were evaporated (without heating or annealing) in the same manner as before (see **Figure 5-10** (9)) to form 16 contacts. The Ohmic Ti/Pt contact on the backside survived the processes and was not changed. At this stage, the substrate is not anymore a pristine diamond, because a few of the former iridium-diamond diodes were biased to breakdown, causing damage. Nevertheless a few functioning nickel diamond diodes could be obtained.

5.4.4 Electrical characterisation

The DC behaviour (current density *vs.* voltage, or *J-V* curves) of the devices was characterised in forward and reverse bias at room temperature, in air and/or in Fluorinert[6] using a home-made apparatus, consisting essentially of two adjustable metallic tips to contact the sample, installed in a Faraday cage and connected to a Keithley 6517B electrometer with coaxial cables. The electrometer was operated with a high current resolution down to 10^{-6} pA, however, the background noise was in the range of ~0.2 pA.

---

[6] Fluorinert™ (3M) is a high dielectric strength fluid used to prevent surface discharge during reverse bias.

Impedance spectroscopy (IS) and capacitance-voltage (*C*-*V*) measurements were performed at room temperature with the same apparatus, but connected to a Gamry Interface 1000 potentiostat/galvanostat.

The measured electrical data was acquired through supporting hardware and software, and treated/fitted using various tools, such as purpose-built *MATLAB* programs and proprietary analytical software supplied with the equipment.

5.5 Results and discussion

5.5.1 Pseudo-vertical, nickel-diamond diode

5.5.1.1 Current-voltage behaviour and forward bias performance

An initial survey of the Ni-diamond SBDs was performed by measuring the current-voltage behaviour of a few selected devices, from −2 to 2 V, in air and at room temperature. The results are shown in **Figure 5-12**:

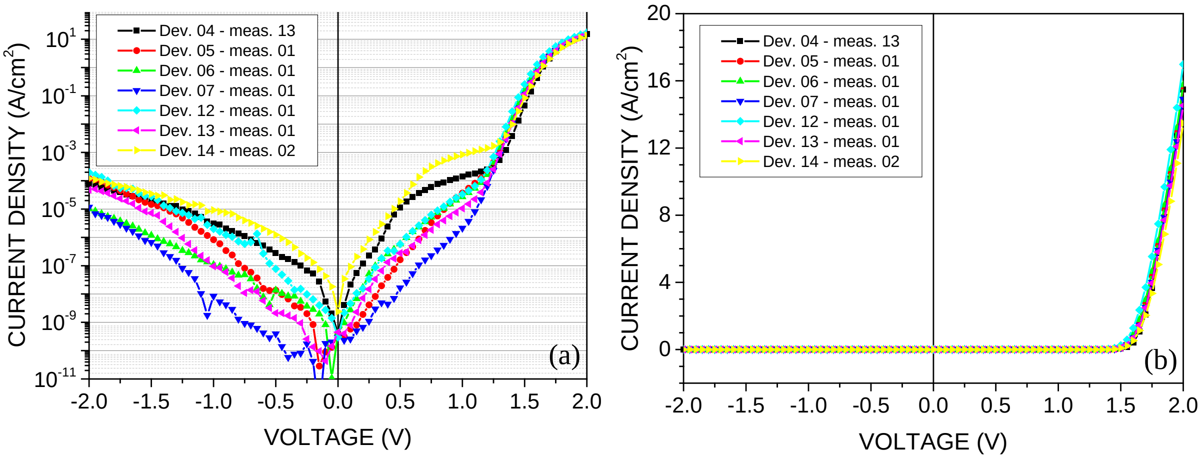

Figure 5-12: *J*-*V* curves of several Ni-diamond Schottky diodes (sample type #1) for an overall performance overview, displayed in (a) semi-log and (b) linear scale. The curves are identified by their respective device and measurement number.

The *J*-*V* curves in **Figure 5-12** all show a diode-like behaviour, with low current at reverse bias (less than 1 mA cm^{-2}) and at least ~5 orders of magnitude higher current at forward bias (up to 10 A cm^{-2}), when operating in Ohmic regime. The curves are very similar, although, when plotted in semi-logarithmic scale, some display a prominent bulge at low forward bias. A common feature to all the curves is a steep increase of saturation/leakage current for increasing reverse bias, *i.e.* from 0 to −2 V the current increases by ~5 orders of magnitude. From extrapolation of the right-hand portion of the curves (quasi-linear, Ohmic regime), a turn-on voltage of ~1.6 V was estimated.

Out of all measured devices, the best and the worst were selected for a more detailed analysis. Their respective current-voltage curves were acquired and fitted to equation (5.2.5) for the extraction of the Schottky barrier height, ideality factor and series resistance. The results are shown in **Figure 5-13** (a) and (b), respectively for the best (04) and for the worst (14) device.

The device 04 displayed a very competitive performance, with rectification ratio of ~10^{10}, $\phi_B \cong 1.4$ eV and $R_S \cong 14$ mΩ cm^2, which are very close to the state of the art values obtained with high-quality diamond single crystals (*i.e.* rectification ratio of ~10^{10}, $\phi_B \cong 1.4$-1.6 eV for either pseudo-vertical WC-diamond SBD or for vertical Ni-diamond SBD, $R_S \cong 9.8$ mΩ cm^2) [15, 18, 19, 34]. The ideality factor has a respectable value of ~1.7, although still relatively high compared to the best reported values close to unity [15], pointing to increased recombination in the space charge region [49].

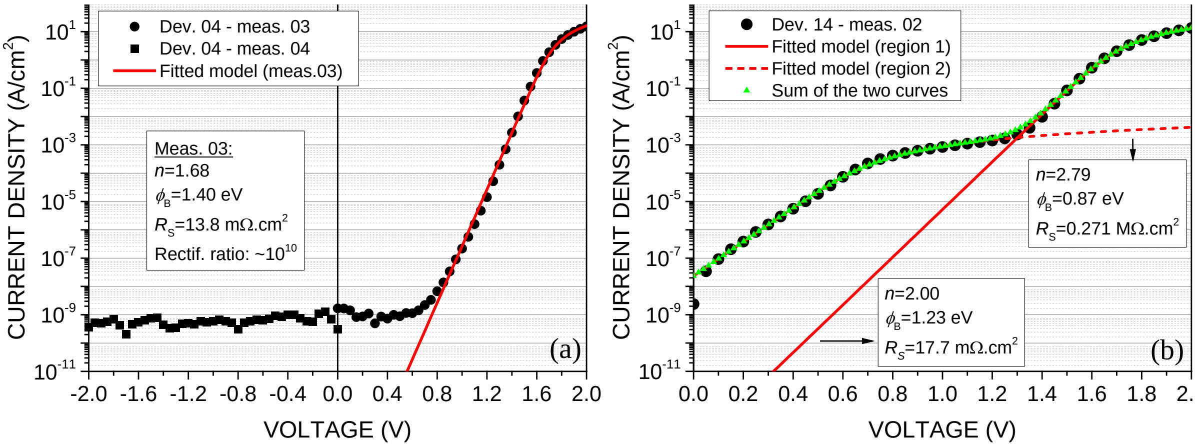

Figure 5-13: Fitting of *J-V* curves from (a) device 04 (sample type #1), showing very competitive rectification ratio and series resistance, and from (b) device 14, showing worse performance and high non-linear parasitic shunt component (region 2).

Device 14, the worst performing case shown in **Figure 5-13** (b), has two components: region 1, attributed to the Ni-diamond Schottky barrier, and region 2, attributed to an existing parasitic shunt component, which is visible at low forward bias. The total *J-V* curve of device 14 was well-modelled by the sum of both components, each fitted to equation (5.2.5), *i.e.* they are both diode-like. In fact almost all devices showed parasitic current, to a lesser or greater degree, but in device 14 it is the highest, while in device 04 (and also device 08) it is the lowest, or effectively non-existent. The standard fitting of equation (5.2.5) for parameter extraction from each device always disregarded the parasitic region, which would otherwise lead to inaccuracies. In the case of device 14, region 1 indicates worse rectifying properties than the average, with lower barrier height and higher ideality factor. The parameters from all devices are summarised in **Table 5-1** for comparison.

5.5.1.2 Reverse bias and breakdown voltage

Among the most important properties of a high power rectifier is its ability to withstand high a negative bias without suffering breakdown, while displaying low leakage current. In order to test the breakdown characteristics of our Ni-diamond SBDs, a few devices were selected for *J-V* measurements at negative bias. The results are shown in **Figure 5-14**.

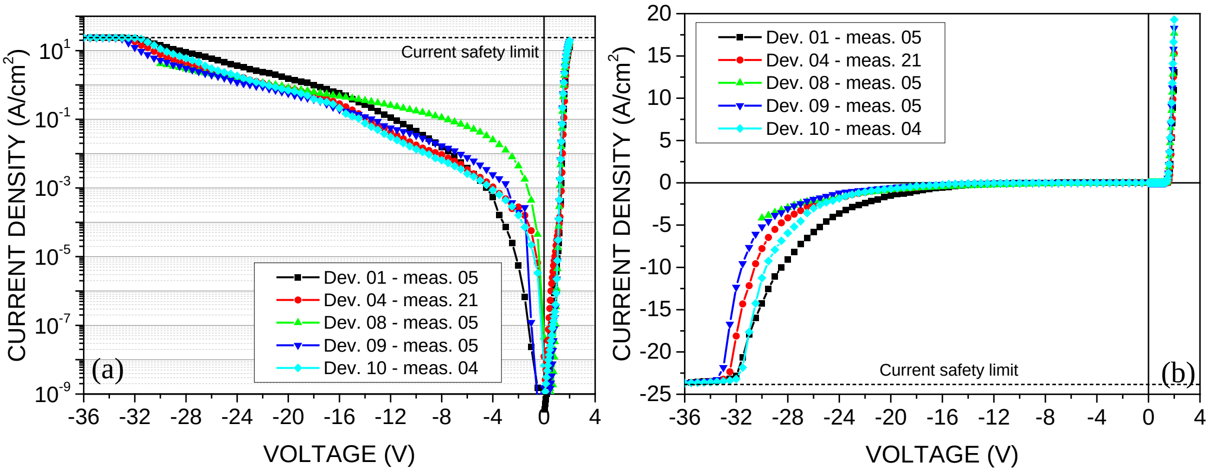

Figure 5-14: *J-V* curves of a few devices (sample type #1) in reverse bias in (a) semi-logarithmic and (b) linear scale, displaying an early breakdown.

In the *J-V* curves above, the reverse blocking regime at negative bias is contrasted with the forward conduction regime at positive bias. While the maximum[7] forward current is achieved at ~2 V, a maximum leakage current is achieved at *ca.* −32 V, after increasing exponentially from about −4 V. This represents a rather premature breakdown and a reverse current profile that bears similarities with the simulated breakdown in **Figure 5-6**, indicating that the breakdown mechanism is a combination of tunnelling and image force lowering of the Schottky barrier.

The maximum electric field E_M can be estimated from equation (5.2.6) written as:

$$E_\mathrm{M} = \sqrt{\frac{2qN_\mathrm{A}V_\mathrm{br}}{\varepsilon_\mathrm{S}}}, \tag{5.5.1}$$

but without an abrupt breakdown, *i.e.* a sudden jump in the current at a defined V_br, it is difficult to visually pinpoint an exact breakdown voltage, unlike often observed in the literature for single crystal diamond-based Schottky diodes, with few exceptions [46]. In this particular report, Brezeanu *et al.* took as breakdown voltage the value given by the tangent line to the steep part of the curve in linear scale, which in our case in **Figure 5-14** (b) would correspond to roughly −30 V. From equation (5.5.1) it becomes evident that the high density of acceptors of $N_\mathrm{A} = 2\times10^{18}$ cm^{-3} in the drift layer is one of the main reasons for the breakdown voltage being so low, because a higher charge carrier density will

---

[7] The maximum current here refers to the maximum value allowed by the Keithley 6517B electrometer.

enhance the impact ionisation process as the electric field increases [2], leading to a premature breakdown. Taking $V_{\mathrm{br}} = -30$ V and applying equation (5.5.1), the maximum electric field is estimated as $E_{\mathrm{M}} = 6.3$ MV cm^{-1}, which is still well below the record high 20 MV cm^{-1} [3] and higher than the maximum electric field value of $E_{\mathrm{M}} = 4$ MV cm^{-1} [9, 50] reported for Schottky structures without edge termination, such as the one studied here. The corresponding Baliga's figure of merit would be 65.22 kW cm^{-2}. However, defining the breakdown voltage by a current threshold gives distinct results (**Table 5-1**).

In order to further analyse the breakdown behaviour, impedance spectroscopy (IS) measurements of a selected device was done before and after biasing until breakdown. The complex impedance was measured over a wide frequency range and plotted as Nyquist plots in **Figure 5-15**. The data was fitted to a model representing the metal-semiconductor interface, consisting of a capacitor C_{P} (depletion layer capacitance), a parallel resistor R_{P} (shunt resistance) and a series resistor R_{S} (the sum of all series resistances in the device), as shown in the inset of figure (a).

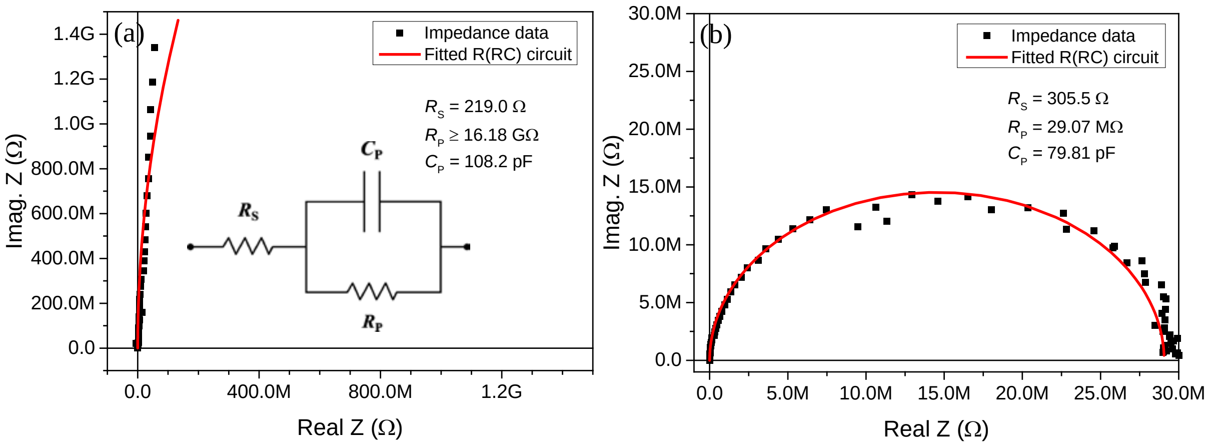

Figure 5-15: IS measurements of device 01 (sample type #1) (a) before and (b) after breakdown. Notice how the parallel resistance R_{P} decreased by ~3 order of magnitude from (a) to (b), indicating a much larger shunt component and effective destruction of the junction.

The impedance results above show a modification of the electrical characteristics of device 01 after breakdown, with the most prominent change being in the parallel (or shunt) resistance, which decreased by ~3 orders of magnitude. This evidences that the Ni-diamond junction was permanently damaged after breakdown. A lower shunt resistance will lead to higher leakage current, as in fact observed later with another Ni-diamond device (**Figure 5-17**).

At this point, it is already possible to infer that our Ni-diamond SBDs are comparable in performance to reported single crystal SBDs of similar structure, particularly in forward conduction. When considering that the breakdown voltage was strongly defined by the high charge carrier density of $N_{\mathrm{A}} = 2\times10^{18}$ cm^{-3}, and that a maximum breakdown field of $E_{\mathrm{M}} \cong 4$ MV cm^{-1} could also be achieved without field plate, there is no evidence that the high dislocation density of the heteroepitaxial diamond substrate is being detrimental to the performance. The lack of edge termination is still likely a predominant factor in the observed premature breakdown. In a recent publication, Kawarada *et al.* [51] showed that a breakdown voltage of *ca.* −600 V can be expected from a fully optimised diode structure with a similar charge carrier density $N \cong 10^{18}$ cm^{-3} in the drift layer. Based on these considerations, we conclude that our devices are not limited at this stage by the material, but rather by structure/design.

5.5.1.3 *Annealing*

In order to investigate the quality and stability of our Ni-diamond junction, the substrate/sample was annealed for 1 hour at 400 °C in a tubular oven under Ar flow (50 sccm). After this annealing step, the remaining devices (19 to 24) were electrically characterised and analysed in a similar way as before. **Figure 5-16** shows averaged *J-V* curves of those devices, before and after annealing.

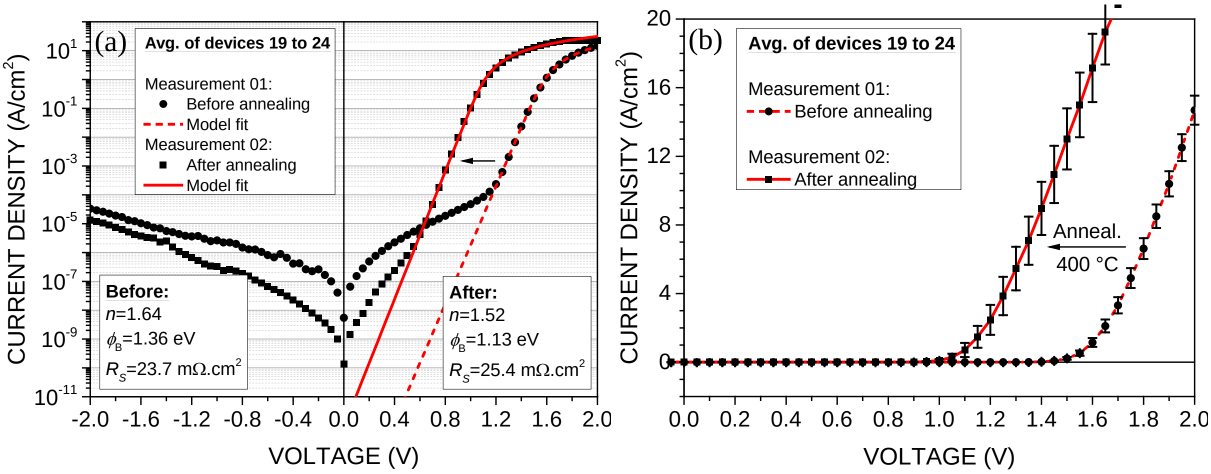

Figure 5-16: Averaged pre- and post-annealing *J-V* curves in (a) semi-logarithmic and (b) linear scale. Sample type #1.

The annealing step produced visible changes in performance and parameters of the diodes, with the most noticeable one being the reduction of the turn-on voltage from ~1.6 to ~1.1 V. The ideality factor improved by ~8% and the Schottky barrier height decreased by ~17%, while the series resistance increased by ~7%. As n and R_S are competing factors in the fitting routine[8], their relatively small variations after annealing may not be real. This leaves ϕ_B as the only significant parameter change. A direct consequence of a reduced Schottky barrier height is a lower turn-on voltage.

Another visible change in the *J-V* curve after annealing was a reduction of the parasitic current, *i.e.* the "bulge" or "belly" at low bias voltages, by roughly 2 orders of magnitude, which accounted for a slight improvement of the rectification ratio.

In order to analyse whether the SBDs can be restored to their previous state or not, an annealing step was applied to a selected device which was previously biased until breakdown. Its

---

[8] *I.e.* if the series resistance is fixed at lower values, the ideality factor increases for the best fit.

current-voltage profiles were measured before and after each step and the results are shown in **Figure 5-17**.

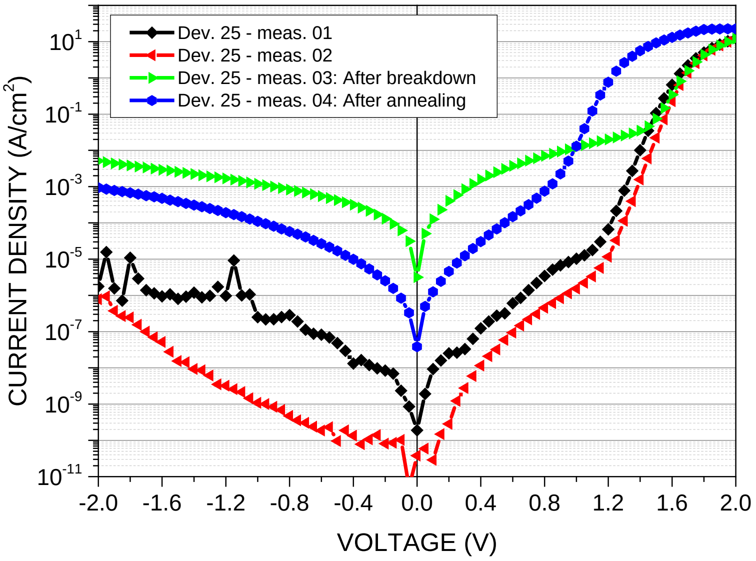

Figure 5-17: *J-V* curves of device 25 (sample type #1) before and after breakdown, and annealed after breakdown. Despite the suffered deterioration, the device undergoes a small improvement after annealing.

The *J-V* curves above show a clear deterioration of the Ni-diamond SBD after breakdown, with several orders of magnitude higher leakage current (green curve) than the pre-breakdown curves (black and red). However, after annealing (blue curve) an improvement of the leakage current of about 1 order of magnitude is observed, as well as a reduction of the turn-on voltage similar to the observed case in **Figure 5-16**.

We explain the improvement of the SBDs after annealing in terms of passivation of shunt paths with the rearrangement of chemical bonds and defects in the Ni-diamond junction. This rearrangement might have been, for example, at the expense of O-termination, leading to a modification of the electron affinity, of interfacial states and of the charge neutrality level, thus changing the effective Schottky barrier height.

In order to further substantiate this interpretation, Mott-Schottky analysis of a selected device was performed before and after annealing. This technique allows from equation (5.2.12) not only the estimation of the charge carrier density, but also the built-in potential of the semiconductor-metal junction, which is determined by the work function of the metal, by the electronic affinity of the semiconductor and by the presence of interfacial states [41]. The results of the MS analysis are shown in **Figure 5-18**.

The figure shows a change of the *C-V* profile: the initial slope (black curve) became more negative after annealing (red curve) and the intersection at $1\big/C_{\mathrm{S}}^{2}=0$ shifted from ~2.1 to ~1.4 V, which corresponds to V_{bi}. This result is a clear indication of a chemical change in the Ni-diamond interface, because the reduction of the built-in potential is correlated with a smaller band bending at the interface, which, in its turn, is strongly dependent on the factors described above. The decrease in built-in potential would, at first glance, point to a reduction of oxygen coverage of the diamond surface, but obtaining precise information about the real chemical environment at the interface requires the use of other techniques. From our results, we can conclude that the Ni-diamond interface changed and that the band bending was reduced by roughly 0.6 V, a comparable change to the turn-on voltage in **Figure 5-16** for a similar device.

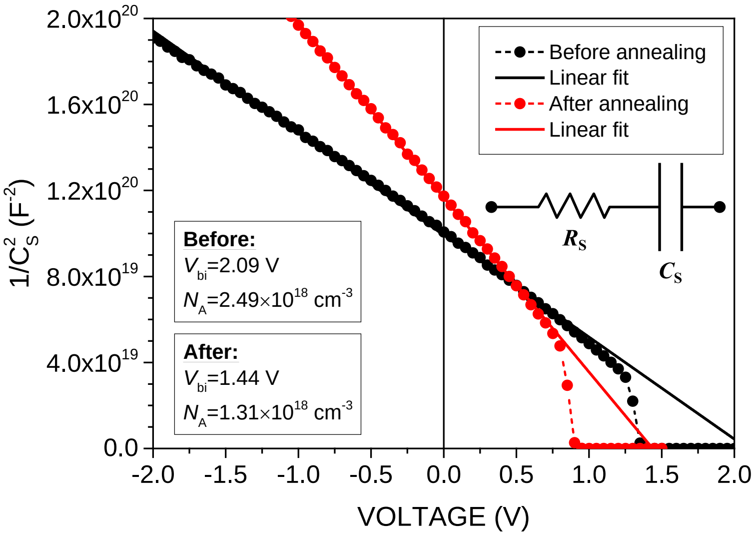

Figure 5-18: Mott-Schottky curves of device 06 (sample type #1) before and after annealing, measured at 10 kHz.

The results from the Mott-Schottky analysis above can be compared with the parameters extracted from the *J*-*V* curves of device 06 (**Table 5-1**). The built-in potential, V_{bi}, and the Schottky barrier height, ϕ_{B}, are related by the following equation [41]:

$$\phi_{\mathrm{B}} = V_{\mathrm{bi}} + V_{\mathrm{p}} + \mathrm{k_B} T/q \tag{5.5.2}$$

where V_{p} is the energy difference between the top of the valence band and the Fermi level in the semiconductor, which can be estimated[9] as approximately 0.26 eV for $N_{\mathrm{A}} \cong 10^{18}\ \mathrm{cm}^{-3}$. Using this relationship and taking $\phi_{\mathrm{B}} = 1.35\ \mathrm{eV}$ (**Table 5-1**), a built-in potential of 1.06 V can be estimated, which is roughly 1 V lower than the estimated value from MS analysis.

The reason for this discrepancy is believed to be due to an uncompensated series resistance, *i.e.* during the Mott-Schottky measurement the applied voltage is divided between the semiconductor-metal junction and other resistive elements in the circuit (*e.g.* drift layer, contacts, cables, etc.). Following the case of device 06, by using equation (5.2.4) and applying $V = 2.09\ \mathrm{V}$ (the applied bias when the band is flat), $V_{\mathrm{D}} = 1.06\ \mathrm{V}$ (which becomes the real potential drop across the SBD) and the

---

[9] The density of free holes at room temperature (usually being treated as the doping concentration), which is obtained by *C*-*V* measurements, is not the same as the actual doping concentration, due to the high ionisation energy of B acceptors. The doping concentration is also necessary for the estimation of V_{p}. Based on data from the literature (see **Figure 1-17**) [52, 53], for $p \approx N_{\mathrm{A}} \cong 10^{18}\ \mathrm{cm}^{-3}$, the real doping density was estimated to be approximately $[\mathrm{B}] \cong 10^{19}\ \mathrm{cm}^{-3}$.

previously measured series resistance $R_S = 20.9$ mΩ cm^2 (equivalent to 42.6 Ω) the current results in $I = 2.15\times10^1$ A cm^{-2}, which matches the maximum current measured for all devices (see **Figure 5-12**) at 2 V forward bias. In this way we could cross-check the data and confirm that the built-in potential measured by MS analysis is overestimated by an uncompensated series resistance, and that the Schottky barrier height measured from *J*-*V* curves is a reliable value.

Table 5-1: Summary of the parameters obtained for 14 Ni-diamond Schottky diodes (sample type #1), before annealing, from fitting of *J*-*V* profiles. A nominal breakdown voltage was defined for when the current density is ≥ 0.1 A cm^{-2}. The best and worst parameters are highlighted. Baliga's figure of merit (BFM) is also presented.

Device:	***n***	ϕ_B **(eV)**	R_S **(mΩ cm^2)**	V_{br} **(V)**	E_{max} **(MV cm^{-1})**	**BFM (kW cm^{-2})**
01	1.54	1.46	23.2	−11.9	3.96	6.10
02	1.84	1.27	19.1	-	-	-
03	1.60	1.38	24.4	−12.3	4.02	6.20
04	1.68	1.40	13.8	−19	4.97	26.16
05	1.75	1.32	19.1	−8.7	3.36	3.96
06	1.68	1.35	20.9	-	-	-
07	1.60	1.41	22.5	-	-	-
08	1.47	1.44	24.8	−7.64	3.15	2.35
09	1.52	1.40	23.7	−13.6	4.2	7.80
10	1.54	1.39	22.3	−14.6	4.35	9.56
11	1.69	1.31	19.2	−11.4	3.84	6.77
12	1.77	1.30	18.4	-	-	-
13	1.62	1.39	22.7	-	-	-
14	2.00	1.23	17.7	-	-	-
Avg. ± Std.	1.66 ± 0.14	1.36 ± 0.06	20.8 ± 3	−12.4 ± 3.3	3.98 ± 0.53	8.61±6.94

5.5.2 Vertical iridium-diamond diode

5.5.2.1 Current-voltage behaviour and forward bias performance

An initial survey of the Ir-diamond "type b" SBDs was performed by measuring the current-voltage behaviour of all the 16 devices, from −4 to 4 V, in air and at room temperature. The results are shown in **Figure 5-19**:

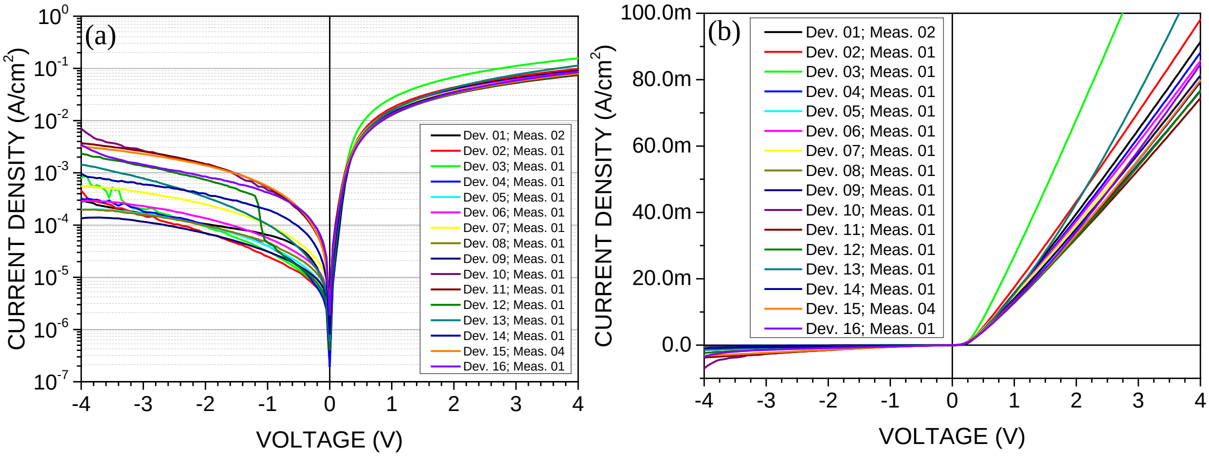

Figure 5-19: *J*-*V* curves of all "type b" Ir-diamond Schottky diodes (sample type #3) for an overall performance overview, displayed in (a) semi-logarithmic and (b) linear scale.

Upon inspection of the *J*-*V* curves above, clear differences from the Ni-diamond SBDs can be identified. To start with, forward current values are smaller by ~2 orders of magnitude, and the leakage current at reverse bias is higher by roughly a similar factor, translating into a rectification ratio of no more than ~10^3. In contrast, the Ni-diamond SBDs displayed a ratio of ~10^5 and a best value of 10^{10}. The curves above also show a lower turn-on voltage, which was estimated as ~0.32 V, and higher on-state/series resistance. While low turn-on voltage is advantageous in forward bias, overall the Ir-diamond SBDs "type b" display worse rectification than the Ni-diamond counterparts.

For a more detailed analysis, the two best performing Ir-diamond diodes were measured and the current-voltage curves fitted to equation (5.2.5). The results are shown in **Figure 5-20**.

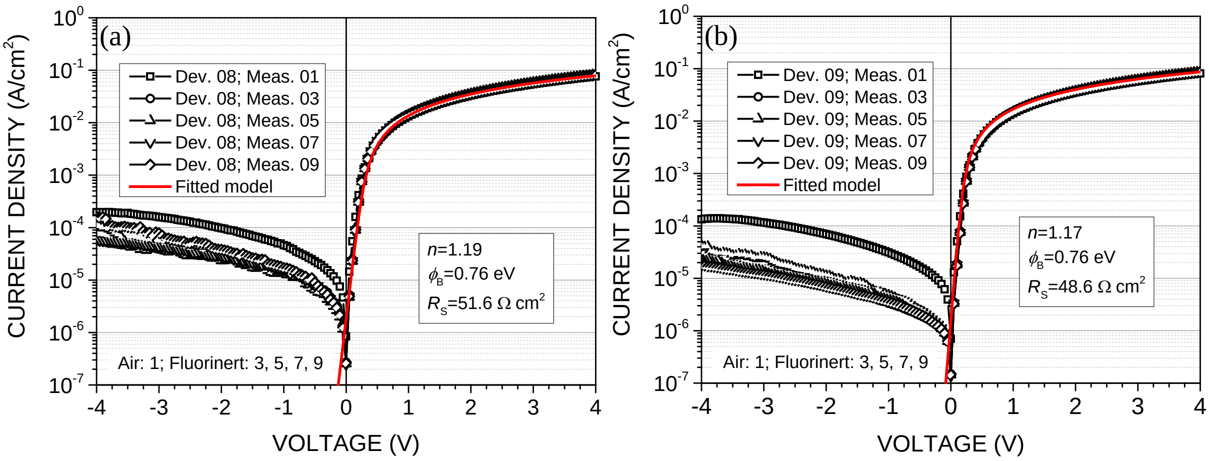

Figure 5-20: *J*-*V* curves of the two best performing "type b" Ir-diamond Schottky diodes (sample type #3), respectively (a) device 08 and (b) device 09. The series resistance of ~50.1 Ω cm² is equivalent to ~102 kΩ, which is ~3 orders of magnitude higher than for the Ni-diamond diode. The leakage current was lower in excess of 1 order of magnitude when the devices were measured in Fluorinert rather than in air.

The characterisation of devices 08 and 09 above yielded a Schottky barrier height of $\phi_B \cong 0.76$ eV, which is about half the value obtained for the nickel-diamond diodes before annealing

(~1.36 eV), and still lower by ~0.37 eV than the value after annealing. As discussed earlier, a lower Schottky barrier is advantageous for forward conduction by keeping the turn-on voltage low, but on the other hand, the saturation/leakage current is drastically increased, resulting in worse rectification and poorer blocking. The lower Schottky barrier height for the Ir-diamond SBDs is consistent with the lower turn-on voltage of ~0.32 V.

The series resistance $R_S \cong 100\,\mathrm{k\Omega}$ (~50.1 Ω cm^2) also resulted very high when compared with the ~42.5 Ω (~20.8 mΩ cm^2) obtained for the Ni-diamond SBDs, which explains the lower forward current of ~10^{-1} A cm^{-2}. An increase is rather expected due to the drift layer having a much lower doping level[10] than before and also because the whole device is much thicker, with a ~300 µm thick B-doped layer. Considering the drift layer thickness $d = 2.5\,\mu\mathrm{m}$, the device area $A = 4.91\times10^{-4}$ cm^{-2} and the above series resistance, the resistivity (specific resistance) $\rho = 1.7\times10^{5}\,\Omega\,\mathrm{cm}$ can be estimated, which is in line with the expected value for a B doping level in the range of $10^{17}\,\mathrm{cm}^{-3}$ (see **Figure 1-14**). So we conclude that main reason for the high series resistance is the more resistive drift layer and that the thick B-doped layer and the metallic contacts add a less significant contribution to it.

Despite the lower Schottky barrier height and higher series resistance, the ideality factor resulted even closer to 1 than for the Ni-diamond SBDs, which is an indication of reduced recombination in the space charge region [49]. The reason for this is not clear, but we speculate that it could be related to the lower impurity concentration in the drift layer causing a sufficient increase in charge carrier mobility to overcome the increased depletion layer width, thus reducing the probability of recombination as the charge carriers cross the depletion layer. However, a more careful investigation of the electrical properties of the drift layer in both types of SBD, as well as greater knowledge of their specific types of defects would have to be pursued in order to confirm this hypothesis. The fact that the ideality factor and the series resistance of the Ni-diamond SBDs effectively did not change after annealing is a strong indication that n is more dependent on the electrical properties of the diamond.

5.5.2.2 Reverse bias and breakdown voltage

The reverse bias behaviour of the same two best performing Ir-diamond “type b” SBDs was also investigated in the same manner as for the Ni-diamond SBDs. The measured reverse current-voltage profiles can be seen in **Figure 5-21**.

---

[10] From Mott-Schottky analysis, the estimated density of acceptors was $N_A \le 10^{17}\,\mathrm{cm}^{-3}$.

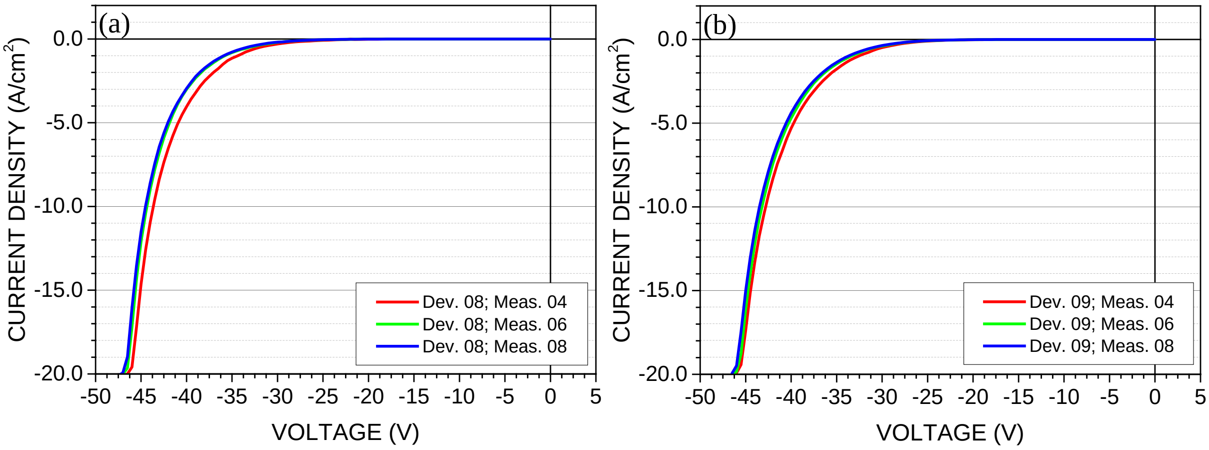

Figure 5-21: *J-V* curves in reverse bias of the two best performing "type b" Ir-diamond Schottky diodes (sample type #3), respectively (a) device 08 and (b) device 09, measured in Fluorinert.

Looking at the *J-V* curves above and comparing them with those from the Ni-diamond SBDs in **Figure 5-14** (b), their similarities are noticeable. The Ir-diamond diodes behave in a very similar way to the Ni-diamond ones in reverse bias, displaying both an exponential increase of the saturation/leakage current, which was attributed to the image force lowering effect discussed earlier.

Despite the lower doping level in the drift layer, the breakdown voltage did not result substantially higher, but instead presented values in the range of −45 V. From equation (5.5.1), taking $N_A = 1\times10^{17}\ \text{cm}^{-3}$, a breakdown field of $E_M \cong 1.7\ \text{MV cm}^{-1}$ can be estimated, which is almost 4 times lower than the maximum electric field obtained with the Ni-diamond SBDs. If the Ir-diamond SBDs had experienced the same E_M as the former, the resulting V_{br} would have been around −600 V, but instead the measured value was more than an order of magnitude smaller. According to Kawarada *et al.* [51], a fully optimised structure with similar density of acceptors in the drift layer should withstand breakdown voltages above 1 kV. The reason for the poor blocking in our Ir-diamond device is believed to be related to the smaller Schottky barrier height, which in turn leads to higher leaking current densities and premature breakdown, and also attributed to the lack of edge termination.

Combining the results from forward and reverse bias, Baliga's figure of merit for the Ir-diamond "type b" SBDs results in $\text{BFM} = 0.04\,\text{kW cm}^{-2}$, which is ~3 orders of magnitude lower than the value obtained for the Ni-diamond SBDs.

Turning our attention to the Ir-diamond "type a" SBDs, their reverse bias current-voltage profiles were measured and shown in **Figure 5-22** for comparison.

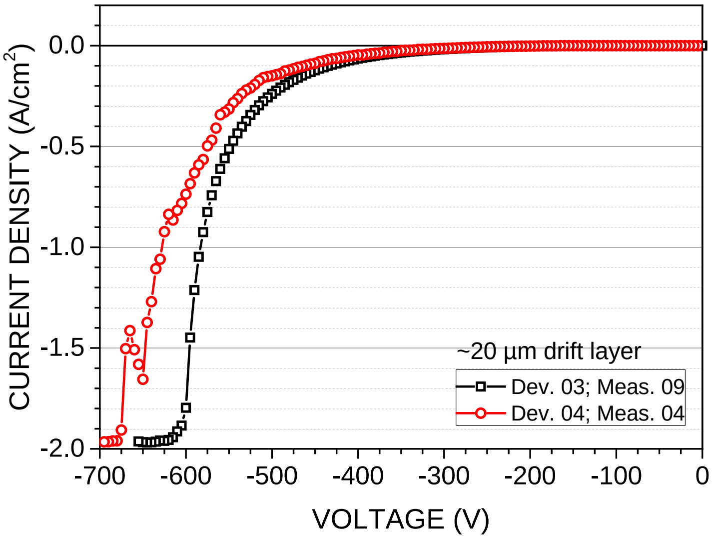

Figure 5-22: *J-V* curves in reverse bias of the highest blocking "type a" Ir-diamond Schottky diodes (sample type #2) with a drift layer of ~20 µm. These are the devices produced by the "back etch" procedure.

The *J-V* curves above display the same exponential behaviour as measured for the previous devices, however the breakdown voltage results much higher, in the range of −600 to −700 V. These values show the significance of having a properly insulating drift layer for the improvement of the breakdown voltage, despite the performance coming at the cost of forward conduction. With a ~10 times thicker drift layer than the "type b" SBDs, from equation (5.3.1) V_{br} should increase by the same factor because of the higher series resistance. In this way, the highest part of the applied potential is expected to be supported by the bulk diamond instead of the metal-semiconductor junction. Nevertheless, it is positive to register for the first time high breakdown voltages for heteroepitaxial diamond grown on Ir/YSZ/Si(001) and verify that this material can support hundreds of volts despite its high density of dislocations. These breakdown voltage values set a new target for future heteroepitaxial diamond-based SBDs.

5.5.3 Vertical nickel-diamond diode

In order to investigate the causes of the poor performance of the iridium-diamond diodes we opted to use the same substrate and structure and produce a comparable nickel-diamond version, expecting then a similar Schottky barrier height as for the SBDs in the pseudo-vertical structure, as well as stronger rectification and reverse bias performance.

5.5.3.1 Current-voltage behaviour and forward bias performance

Following the same procedure as before, the *J-V* characteristic of the vertical Ni-diamond Schottky diodes (~1.2 µm thick drift layer) were measured and summarised in **Figure 5-23**.

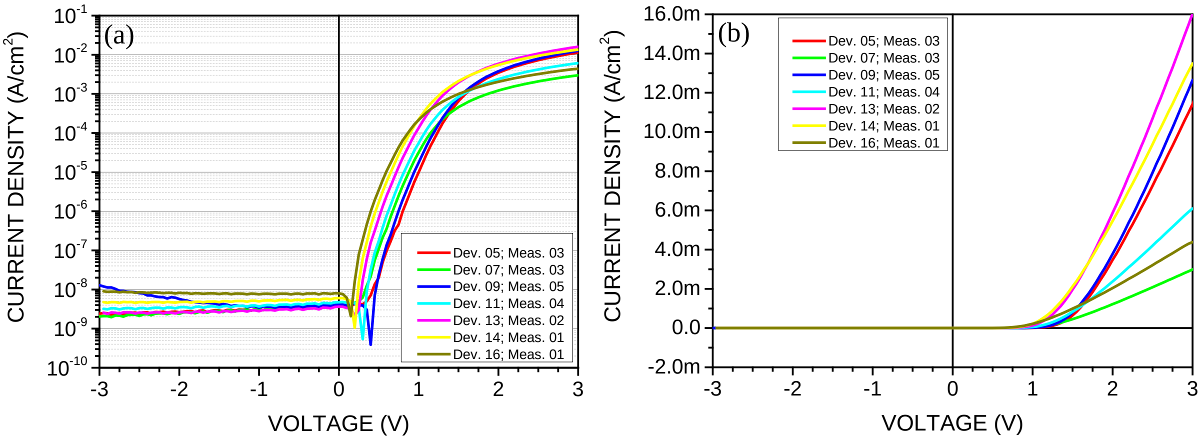

Figure 5-23: *J-V* curves of the best performing Ni-diamond Schottky diodes (sample type #4) in (a) semi-logarithmic and (b) linear scale, all measured with the sample immersed in Fluorinert.

Upon analysis of the curves above, and comparing them to the Ir-diamond diodes (**Figure 5-20**), one observes that the rectification ratio increased from ~10^3 to ~10^7 and that the turn-on voltage increased from ~0.32 V to roughly 1.4 V.

The *J-V* curve of device number 13, identified as the best, yielded the following parameters after fitting to equation (5.2.5): $n = 3.8$, $\phi_B = 0.90$ eV, $R_S = 0.19$ MΩ (~106 Ω cm^2). With exception of the Schottky barrier height, all parameters resulted worse for the Ni-diamond SBDs than for the Ir-diamond SBDs. The Schottky barrier height being almost 0.5 eV lower for this device than for the pseudo-vertical Ni-diamond SBDs, and only ~0.14 eV higher than the Ir-diamond SBDs, points towards significant differences in the junction, most likely related to surface termination. That is, the pseudo-vertical Ni-diamond SBD would have higher oxygen coverage and therefore more positive electron affinity, resulting in higher energy barrier for charge carriers.

The most unexpected result of all is the increase of the series resistance, which should have in fact decreased due to the thinning of the drift layer from ~2.5 to ~1.2 µm. This suggests again a more fundamental problem related to either the Ni-diamond interface and/or perhaps to the Ti/Pt-B:diamond interface.

At this point we can only speculate whether the Ti/Pt-B:diamond interface was damaged after the plasma treatments (RIE, hydrogen plasma and air plasma) and/or whether the air plasma treatment for O-termination of the diamond was not as beneficial as suggested by our XPS survey (see section 7.2). This could explain why in every case where the samples were treated by air plasma to O-terminate the surface the SBDs suffered with small ϕ_B, whereas the Schottky barrier height of the pseudo-vertical Ni-diamond diodes (O-terminated chemically) resulted in a competitive ~1.4 eV. A more in-depth investigation of these issues will be left for a future work.

5.5.3.2 Reverse bias and breakdown voltage

A few vertical Ni-diamond SBDs were selected for breakdown voltage measurements like for the previous devices. The results are shown in **Figure 5-24**.

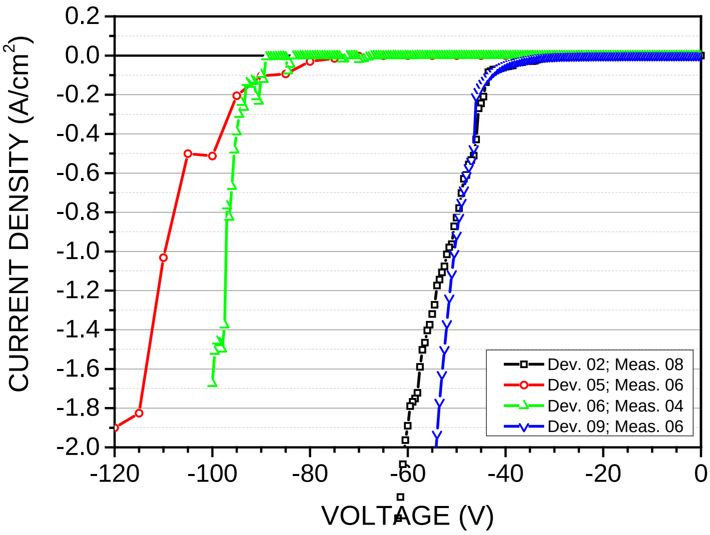

Figure 5-24: *J-V* curves in reverse bias of a few Ni-diamond Schottky diodes (sample type #4) in a vertical structure with a ~1.2 µm thick drift layer. All curves were measured in Fluorinert.

Comparing the curves above with those from the vertical Ir-diamond diodes (**Figure 5-21**), an improvement of at least ~20 V is observed. Some devices broke down at even higher values of roughly −100 V, which is a substantial improvement over the previous −45 V, considering that it’s a recycled substrate with a thinner drift layer. This result can be attributed to the higher Schottky barrier height and to the higher series resistance.

Combining the results at forward and reverse bias, the (recycled) vertical Ni-diamond SBDs yielded a $\mathrm{BFM} = 0.12\,\mathrm{kW\,cm^{-2}}$ at best, which is more than 2 orders of magnitude smaller than the best devices in this work: the pseudo-vertical Ni-diamond SBDs.

5.6 Conclusion and final remarks

The work presented in this chapter concerned the evaluation of Schottky barrier diodes (SBDs) fabricated out of heteroepitaxial diamond grown on Ir/YSZ/Si(001) for high power switching applications.

In a first step, proof of concept was demonstrated with SBDs fabricated following a pseudo-vertical (or lateral) structure, employing Ni as the metal for the semiconductor-metal junction. Due to initial experimental constraints, the drift layer was grown in a MWPCVD reactor with a high B background, leading to high doping level and SBDs with suboptimal rectification properties. Nevertheless, the pseudo-vertical Ni-diamond SBDs displayed rather good forward bias behaviour, with excellent series resistance $R_S \cong 13.8\ \mathrm{m\Omega\,cm^2}$, respectable Schottky barrier height $\phi_B \cong 1.36$ eV, and an excellent rectification ratio of ~10^{10}. Reported state-of-the-art SBDs fabricated with high-quality diamond single crystals (several of them with smaller device areas and use of edge termination) present comparable or only slightly better values (*i.e.* rectification ratio of ~10^{10}, $\phi_B \cong 1.4$-1.6 eV for either pseudo-vertical WC-diamond SBD or for vertical Ni-diamond SBD, and $R_S \cong 9.8\ \mathrm{m\Omega\ cm^2}$) [15, 18, 19, 34]. The high doping level in the drift layer of our device and the lack of edge termination led, however, to poor reverse bias behaviour and premature breakdown voltages of only several 10 V. The final result was a device with a low BFM of 26.16 kΩ $\mathrm{cm^{-2}}$ or 65.22 kΩ $\mathrm{cm^{-2}}$ in the best case, depending on the criterion for the breakdown voltage.

During preparation of this thesis chapter, Schottky diode structures on heteroepitaxial diamond grown on Ir (deposited on Si(001) with an undisclosed buffer layer in between) were also demonstrated by another group [54]. With a drift layer of ~1 µm, dislocation density of $10^8\ \mathrm{cm^{-2}}$, $N_A = 4\times10^{16}\ \mathrm{cm^{-3}}$, $R_S \cong 76.3\ \mathrm{m\Omega\ cm^2}$ and $\phi_B \cong 1.49$ eV, this device has reached a breakdown voltage of *ca.* −52 V (breakdown field of ~1 MV $\mathrm{cm^{-1}}$) without edge termination. From those parameters a BFM of 35.42 kΩ $\mathrm{cm^{-2}}$ could be determined. Despite their final figure being apparently better, after a more detailed comparison of our devices, the merits of our pseudo-vertical Ni-diamond SBDs become clear, particularly because of the difference in doping level. By reducing N_A from 2×10^{18} to $4\times10^{16}\ \mathrm{cm^{-3}}$ a drastic increase of the breakdown voltage (factor of ~50) can be, in theory, expected for our device. With further optimisation of the doping concentration and the thickness of the drift layer, as well as the adoption of edge termination still to be done, our pseudo-vertical Ni-diamond SBDs turned out to be more than a proof of concept. They stand as an excellent platform with much more performance to be extracted from.

In a second step, we have shown for the first time diamond-based SBDs with Ir as the Schottky contact, in an attempt to profit, on a later stage, from the high melting point of this metal for stable high-temperature device operation, and from the fact that Ir can grow epitaxially on diamond, forming an abrupt interface with strong bonds. At the same time we explored the use of vertical device structures. Overall, all Ir-based devices have shown worse merits, mainly represented by smaller Schottky barrier height and higher series resistance. These results translated into lower rectification ratio of ~10^3, worse conductivity at forward bias, relatively low breakdown voltages and BFM values of 2-3 orders of magnitude lower than that for the pseudo-vertical Ni-diamond SBDs. Nevertheless, the Ir-diamond SBDs still need to be investigated more carefully and in a similar platform as that used for the pseudo-vertical Ni-diamond SBDs, in order to isolate and eliminate the encountered problems of high resistivity and possibly damaged diamond surface due to plasma etching processes. A strong indication of Ir not being the cause of poor performance was observed when the vertical SBDs were recycled to be used with Ni Schottky contacts, as the gain in performance with Ni was virtually none.

Despite the issues with the vertical structures, high breakdown voltages of −700 V to −600 V could be measured for SBDs with ~20 µm thick drift layers fabricated out of heteroepitaxial diamond. To the best of our knowledge, these are the highest reported values for this type of material. Added to the very good performance of our pseudo-vertical Ni-diamond SBDs, these values are a good indication that heteroepitaxial diamond grown on Ir/YSZ/Si(001) with dislocation densities of

10^7-10^8 cm^{-2} can indeed be applied as functional devices for high-power electronics and join the competition against other wide bandgap materials. See figure below.

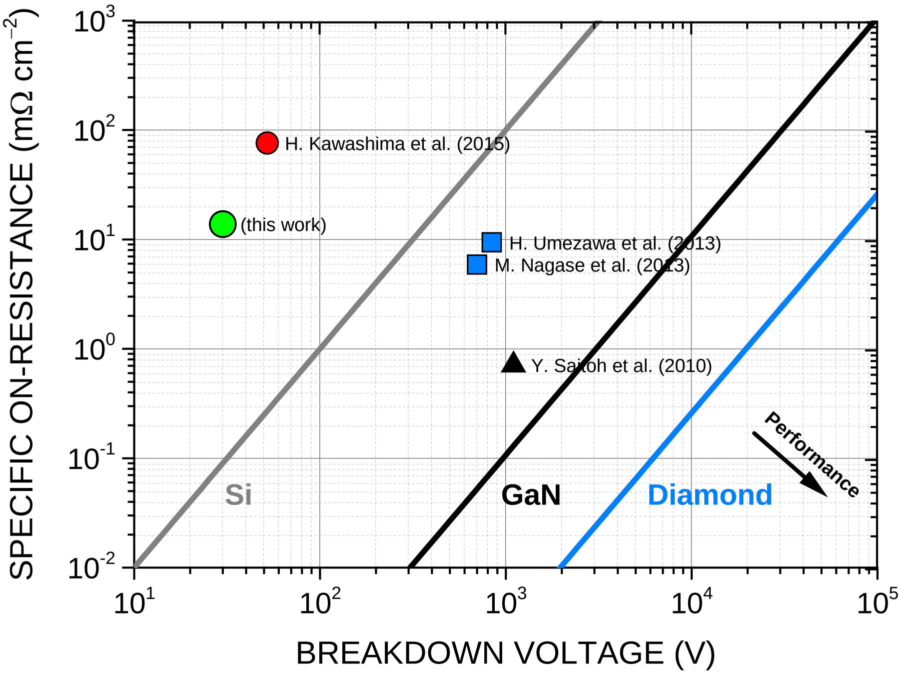

Figure 5-25: Figure of merit of different wide-bandgap semiconductor-based SBDs: (green circle) best heteroepitaxial diamond-based SBD from this work (sample type #1); (red circle) heteroepitaxial diamond-based SBD from Japan [54], (blue squares) best single crystal diamond-based SBDs [17, 18]; (black triangle) best GaN-based SBD [39]. The diagonal lines are approximate theoretical limits for the three materials, Si, GaN and diamond, calculated from equation (5.3.2).

References

1. Jan Isberg; *High-Power Switching Devices*, in *CVD Diamond for Electronic Devices and Sensors*, 2009, John Wiley & Sons, Ltd.
2. Baliga B. Jayant; *Fundamentals of Power Semiconductor Devices*, 1st ed., 2008, Springer US.
3. M. I. Landstrass, M. A. Plano, M. A. Moreno, S. McWilliams, L. S. Pan, D. R. Kania, and S. Han; Device properties of homoepitaxially grown diamond. *Diamond and Related Materials*, 1993. **2**(5–7): p. 1033-1037. DOI: 10.1016/0925-9635(93)90269-8.
4. J. Millan, P. Godignon, and A. Perez-Tomas; Wide Band Gap Semiconductor Devices for Power Electronics. *Automatika*, 2012. **53**(2): p. 107-116. DOI: 10.7305/automatika.53-2.177.
5. Hiromitsu Kato, Kazuhiro Oyama, Toshiharu Makino, Masahiko Ogura, Daisuke Takeuchi, and Satoshi Yamasaki; Diamond bipolar junction transistor device with phosphorus-doped diamond base layer. *Diamond and Related Materials*, 2012. **27–28**(0): p. 19-22. DOI: 10.1016/j.diamond.2012.05.004.
6. Takayuki Iwasaki, Yuto Hoshino, Kohei Tsuzuki, Hiromitsu Kato, Toshiharu Makino, Masahiko Ogura, Daisuke Takeuchi, Tsubasa Matsumoto, Hideyo Okushi, Satoshi Yamasaki, and Mutsuko Hatano; Diamond Junction Field-Effect Transistors with Selectively Grown n$^+$-Side Gates. *Applied Physics Express*, 2012. **5**(9): p. 091301. DOI: 10.1143/APEX.5.091301.
7. M. Kasu, K. Ueda, Y. Yamauchi, A. Tallaire, and T. Makimoto; Diamond-based RF power transistors: Fundamentals and applications. *Diamond and Related Materials*, 2007. **16**(4–7): p. 1010-1015. DOI: 10.1016/j.diamond.2006.12.046.

8. Toshiharu Makino, Satoshi Tanimoto, Yusuke Hayashi, Hiromitsu Kato, Norio Tokuda, Masahiko Ogura, Daisuke Takeuchi, Kazuhiro Oyama, Hiromichi Ohashi, Hideyo Okushi, and Satoshi Yamasaki; Diamond Schottky-pn diode with high forward current density and fast switching operation. *Applied Physics Letters*, 2009. **94**(26): p. 262101-3. DOI: 10.1063/1.3159837.
9. D. J. Twitchen, A. J. Whitehead, S. E. Coe, J. Isberg, J. Hammersberg, T. Wikstrom, and E. Johansson; High-voltage single-crystal diamond diodes. *Electron Devices, IEEE Transactions on*, 2004. **51**(5): p. 826-828. DOI: 10.1109/TED.2004.826867.
10. J. E. Butler, M. W. Geis, K. E. Krohn, Jr. J. Lawless, S. Deneault, T. M. Lyszczarz, D. Flechtner, and R. Wright; Exceptionally high voltage Schottky diamond diodes and low boron doping. *Semiconductor Science and Technology*, 2003. **18**(3): p. S67. DOI: 10.1088/0268-1242/18/3/309.
11. Pierre-Nicolas Volpe, Pierre Muret, Julien Pernot, Franck Omnès, Tokuyuki Teraji, Yasuo Koide, François Jomard, Dominique Planson, Pierre Brosselard, Nicolas Dheilly, Bertrand Vergne, and Sigo Scharnholz; Extreme dielectric strength in boron doped homoepitaxial diamond. *Applied Physics Letters*, 2010. **97**(22): p. 223501. DOI: 10.1063/1.3520140.
12. W. Huang, T. P. Chow, J. Yang, and J. E. Butler; High-voltage diamond Schottky rectifiers. *International Journal of High Speed Electronics and Systems*, 2004. **14**(03): p. 872-878. DOI: 10.1142/S0129156404002971.
13. A. Traoré, P. Muret, A. Fiori, D. Eon, E. Gheeraert, and J. Pernot; Zr/oxidized diamond interface for high power Schottky diodes. *Applied Physics Letters*, 2014. **104**(5): p. 052105. DOI: 10.1063/1.4864060.
14. Alexandre Fiori, Tokuyuki Teraji, and Yasuo Koide; Thermal stabilization and deterioration of the WC/p-type diamond (100) Schottky-barrier interface. *physica status solidi (a)*, 2014. **211**(10): p. 2363-2366. DOI: 10.1002/pssa.201431216.
15. A. Fiori, T. Teraji, and Y. Koide; Diamond Schottky diodes with ideality factors close to 1. *Applied Physics Letters*, 2014. **105**(13): p. 133515. DOI: 10.1063/1.4897315.
16. A. Nawawi, K. J. Tseng, Rusli, G. A. J. Amaratunga, H. Umezawa, and S. Shikata; Design and optimization of planar mesa termination for diamond Schottky barrier diodes. *Diamond and Related Materials*, 2013. **36**(0): p. 51-57. DOI: 10.1016/j.diamond.2013.04.009.
17. M. Nagase, H. Umezawa, and S. Shikata; Vertical Diamond Schottky Barrier Diode Fabricated on Insulating Diamond Substrate Using Deep Etching Technique. *Electron Devices, IEEE Transactions on*, 2013. **60**(4): p. 1416-1420. DOI: 10.1109/ted.2013.2247609.
18. Hitoshi Umezawa, Yukako Kato, and Shin-ichi Shikata; 1 Ω On-Resistance Diamond Vertical-Schottky Barrier Diode Operated at 250 °C. *Applied Physics Express*, 2013. **6**(1): p. 011302. DOI: 10.7567/APEX.6.011302.
19. S. Koné, H. Schneider, K. Isoird, F. Thion, J. Achard, R. Issaoui, S. Msolli, and J. Alexis; An assessment of contact metallization for high power and high temperature diamond Schottky devices. *Diamond and Related Materials*, 2012. **27–28**(0): p. 23-28. DOI: 10.1016/j.diamond.2012.05.007.
20. Hitoshi Umezawa and Shin-ichi Shikata; Leakage current analysis of diamond Schottky barrier diodes operated at high temperature. *Japanese Journal of Applied Physics*, 2014. **53**(4S): p. 04EP04. DOI: 10.7567/JJAP.53.04EP04.
21. Yole Développement; *Status of Power Electronics Industry 2015*. [cited 2015]; URL: http://www.i-micronews.com/power-electronics-report/product/status-of-power-electronics-industry-2015.html.
22. Yole Développement; *Diamond Materials for Semiconductor Applications*. [cited 2015]; URL: http://www.i-micronews.com/power-electronics-report/product/diamond-materials-for-semiconductor-applications.html.
23. Matthias Schreck, Jes Asmussen, Shinichi Shikata, Jean-Charles Arnault, and Naoji Fujimori; Large-area high-quality single crystal diamond. *MRS Bulletin*, 2014. **39**(06): p. 504-510. DOI: 10.1557/mrs.2014.96.
24. C. Stehl, M. Fischer, S. Gsell, E. Berdermann, M. S. Rahman, M. Traeger, O. Klein, and M. Schreck; Efficiency of dislocation density reduction during heteroepitaxial growth of diamond for detector applications. *Applied Physics Letters*, 2013. **103**(15): p. 151905. DOI: 10.1063/1.4824330.
25. J. Achard, A. Tallaire, V. Mille, M. Naamoun, O. Brinza, A. Boussadi, L. William, and A. Gicquel; Improvement of dislocation density in thick CVD single crystal diamond films by

coupling H_2/O_2 plasma etching and chemo-mechanical or ICP treatment of HPHT substrates. *physica status solidi (a)*, 2014: p. n/a-n/a. DOI: 10.1002/pssa.201431181.

26. Alexandre Tallaire, Jocelyn Achard, Ovidiu Brinza, Vianney Mille, Mehdi Naamoun, François Silva, and Alix Gicquel; Growth strategy for controlling dislocation densities and crystal morphologies of single crystal diamond by using pyramidal-shape substrates. *Diamond and Related Materials*, 2013. **33**(0): p. 71-77. DOI: 10.1016/j.diamond.2013.01.006.
27. Michael Mayr, Martin Fischer, Oliver Klein, Stefan Gsell, and Matthias Schreck; Interaction between surface structures and threading dislocations during epitaxial diamond growth. *physica status solidi (a)*, 2015. **212**(11): p. 2480-2486. DOI: 10.1002/pssa.201532243.
28. Yutaka Ando, Takashi Kamano, Kazuhiro Suzuki, and Atsuhito Sawabe; Epitaxial Lateral Overgrowth of Diamonds on Iridium by Patterned Nucleation and Growth Method. *Japanese Journal of Applied Physics*, 2012. **51**(Copyright (c) 2012 The Japan Society of Applied Physics): p. 090101. DOI: 10.1143/JJAP.51.090101.
29. M. Kubovic, A. Aleksov, M. Schreck, Th Bauer, B. Stritzker, and E. Kohn; Field effect transistor fabricated on hydrogen-terminated diamond grown on $SrTiO_3$ substrate and iridium buffer layer. *Diamond and Related Materials*, 2003. **12**(3–7): p. 403-407. DOI: 10.1016/S0925-9635(03)00068-2.
30. D. Takeuchi, T. Makino, H. Kato, M. Ogura, N. Tokuda, T. Matsumoto, D. Kuwabara, H. Okushi, and S. Yamasaki; Free exciton luminescence from a diamond p–i–n diode grown on a substrate produced by heteroepitaxy. *physica status solidi (a)*, 2014: p. n/a-n/a. DOI: 10.1002/pssa.201431167.
31. S. D. Lester, F. A. Ponce, M. G. Craford, and D. A. Steigerwald; High dislocation densities in high efficiency GaN-based light-emitting diodes. *Applied Physics Letters*, 1995. **66**(10): p. 1249-1251. DOI: 10.1063/1.113252.
32. Akihiro Hinoki, Junjiroh Kikawa, Tomoyuki Yamada, Tadayoshi Tsuchiya, Shinichi Kamiya, Masahito Kurouchi, Kenichi Kosaka, Tsutomu Araki, Akira Suzuki, and Yasushi Nanishi; Effects of Traps Formed by Threading Dislocations on Off-State Breakdown Characteristics in GaN Buffer Layer in AlGaN/GaN Heterostructure Field-Effect Transistors. *Applied Physics Express*, 2008. **1**(1): p. 011103. DOI: 10.1143/APEX.1.011103.
33. Akhilesh Pandey, S. P. Chowdhury, Sandeep Dalal, Anand Kumar, Shankar Dutta, R. Raman, and A. K. Kapoor; *Study of Oxygen Implantation in GaN/Sapphire*, in *Physics of Semiconductor Devices*, V.K. Jain and A. Verma, Editors, 2014, Springer International Publishing.
34. Hitoshi Umezawa, Natsuo Tatsumi, Yukako Kato, and Shin-ichi Shikata; Leakage current analysis of diamond Schottky barrier diodes by defect imaging. *Diamond and Related Materials*, 2013. **40**(0): p. 56-59. DOI: 10.1016/j.diamond.2013.09.011.
35. L. McCarthy, I. Smorchkova, H. Xing, P. Fini, S. Keller, J. Speck, S. P. DenBaars, M. J. W. Rodwell, and U. K. Mishra; Effect of threading dislocations on AlGaN/GaN heterojunction bipolar transistors. *Applied Physics Letters*, 2001. **78**(15): p. 2235-2237. DOI: 10.1063/1.1358358.
36. D. Cherns and C. G. Jiao; Electron Holography Studies of the Charge on Dislocations in GaN. *Physical Review Letters*, 2001. **87**(20): p. 205504. DOI: 10.1103/PhysRevLett.87.205504.
37. S. Hashimoto, Y. Yoshizumi, T. Tanabe, and M. Kiyama; High-purity GaN epitaxial layers for power devices on low-dislocation-density GaN substrates. *Journal of Crystal Growth*, 2007. **298**(0): p. 871-874. DOI: 10.1016/j.jcrysgro.2006.10.117.
38. Patrick J. McNally, P. A. F. Herbert, T. Tuomi, M. Karilahti, and J. A. Higgins; Analysis of the impact of dislocation distribution on the breakdown voltage of GaAs-based power varactor diodes. *Journal of Applied Physics*, 1996. **79**(11): p. 8294-8297. DOI: 10.1063/1.362470.
39. Yu Saitoh, Kazuhide Sumiyoshi, Masaya Okada, Taku Horii, Tomihito Miyazaki, Hiromu Shiomi, Masaki Ueno, Koji Katayama, Makoto Kiyama, and Takao Nakamura; Extremely Low On-Resistance and High Breakdown Voltage Observed in Vertical GaN Schottky Barrier Diodes with High-Mobility Drift Layers on Low-Dislocation-Density GaN Substrates. *Applied Physics Express*, 2010. **3**(8): p. 081001. DOI: 10.1143/APEX.3.081001.
40. Chenming C. Hu; *Modern Semiconductor Devices for Integrated Circuits*, 1st ed., 2009, Prentice Hall.
41. A. Nawawi, K. J. Tseng, Rusli, G. A. J. Amaratunga, H. Umezawa, and S. Shikata; Characterization of vertical Mo/diamond Schottky barrier diode from non-ideal I–V and C–V measurements based on MIS model. *Diamond and Related Materials*, 2013. **35**(0): p. 1-6. DOI: 10.1016/j.diamond.2013.03.002.

42. F. Maier, J. Ristein, and L. Ley; Electron affinity of plasma-hydrogenated and chemically oxidized diamond (100) surfaces. *Physical Review B*, 2001. **64**(16): p. 165411. DOI: 10.1103/PhysRevB.64.165411.
43. Simon M. Sze and Kwok K. Ng; *Physics of Semiconductor Devices*, 3rd ed., 2006, Wiley.
44. K. Ueda, K. Kawamoto, T. Soumiya, and H. Asano; High-temperature characteristics of Ag and Ni/diamond Schottky diodes. *Diamond and Related Materials*, 2013. **38**(0): p. 41-44. DOI: 10.1016/j.diamond.2013.06.007.
45. William F. Paxton, Travis Wade, Mick Howell, Norman Tolk, Wang P. Kang, and Jim L. Davidson; Thermionic emission characterization of boron-doped microcrystalline diamond films at elevated temperatures. *physica status solidi (a)*, 2012. **209**(10): p. 1993-1995. DOI: 10.1002/pssa.201228114.
46. M. Brezeanu, T. Butler, N. Rupesinghe, S.J. Rashid, M. Avram, G.A.J. Amaratunga, F. Udrea, M. Dixon, D. Twitchen, A. Garraway, D. Chamund, and P. Taylor; Single crystal diamond M–i–P diodes for power electronics. *IET Circuits, Devices & Systems*, 2007. **1**(5): p. 380-386. DOI: 10.1049/iet-cds:20060379.
47. Tokuyuki Teraji; *Chemical Vapor Deposition of Homoepitaxial Diamond Films*, in *Physics and Applications of CVD Diamond*, 2008, Wiley-VCH Verlag GmbH & Co. KGaA.
48. S. Gsell, M. Fischer, M. Schreck, and B. Stritzker; Epitaxial films of metals from the platinum group (Ir, Rh, Pt and Ru) on YSZ-buffered Si(111). *Journal of Crystal Growth*, 2009. **311**(14): p. 3731-3736. DOI: 10.1016/j.jcrysgro.2009.04.034.
49. Christo Papadopoulos; *Junctions and Diodes*, in *Solid-State Electronic Devices: An Introduction*, 2014, Springer New York.
50. A. Vescan, I. Daumiller, P. Gluche, W. Ebert, and E. Kohn; High temperature, high voltage operation of diamond Schottky diode. *Diamond and Related Materials*, 1998. **7**(2–5): p. 581-584. DOI: 10.1016/S0925-9635(97)00200-8.
51. Atsushi Hiraiwa and Hiroshi Kawarada; Figure of merit of diamond power devices based on accurately estimated impact ionization processes. *Journal of Applied Physics*, 2013. **114**(3): p. 034506. DOI: 10.1063/1.4816312.
52. E. Kohn and A. Denisenko; *Doped Diamond Electron Devices*, in *CVD Diamond for Electronic Devices and Sensors*, 2009, John Wiley & Sons, Ltd.
53. A. Deneuville; *Chapter 4 Boron doping of diamond films from the gas phase*, in *Semiconductors and Semimetals*, E.N. Christoph and R. Juergen, Editors, 2003, Elsevier.
54. Kawashima Hiroyuki, Noguchi Hitoshi, Matsumoto Tsubasa, Kato Hiromitsu, Ogura Masahiko, Makino Toshiharu, Shirai Shozo, Takeuchi Daisuke, and Yamasaki Satoshi; Electronic properties of diamond Schottky barrier diodes fabricated on silicon-based heteroepitaxially grown diamond substrates. *Applied Physics Express*, 2015. **8**(10): p. 104103. DOI: 10.7567/APEX.8.104103.

6 Summary and outlook

This thesis is devoted to investigations of heteroepitaxial boron-doped diamond grown on Ir/YSZ/Si(001) by MWPCVD (microwave plasma-enhanced chemical vapour deposition). The present work encompasses 4 main areas of investigation, from synthesis (*i.e.* growth environment and interaction of gas precursors), to structural properties (*i.e.* doping, stress and defects) and finally to application in the fields of electrochemistry and high-power switching.

Heteroepitaxial diamond on Ir has inherent advantages compared to other types of diamond (*i.e.* homoepitaxial single crystals and polycrystalline diamond) for combining the attributes of large area, well-defined crystalline orientation, and a level of density of defects (*i.e.* dislocations) which has been improving substantially over the last years. This development is enabling heteroepitaxial diamond on Ir to be used in advanced applications where before only homoepitaxial single crystals could provide the necessary electrical and optical properties. As many high-end applications rely on semiconducting or metallic diamond, boron-doping is a topic of fundamental importance.

In the first part of this thesis a thorough investigation of *in situ* B-doping of diamond during heteroepitaxial growth on Ir/YSZ/Si(001) was performed. Optical emission spectroscopy (OES) enabled the monitoring of species in the gas phase involved in the growth by MWPCVD. It was demonstrated how important it is to have knowledge and control over the background B contamination of the CVD reactor in order to produce accurate doping concentrations and doping profiles. Without this knowledge the optimisation of the semiconducting properties of diamond for device fabrication cannot be achieved. In order to improve the control over the available doping range in reactors contaminated with B, it was shown that controlled addition of oxygen by adding CO_2 to the feedstock gas reduces the boron-related BH emission signal in the OE spectra in a proportional way, which leads to a controlled reduction of incorporated B in the diamond lattice. However, it was shown that this strategy is limited by a concomitant reduction of the growth rate with increasing O/C ratio in the feed gas, and that, as a consequence, the absolute amount of carbon needs to be increased in a proportional way to maintain the growth rate. OES has subsequently shown that under this condition, the BH emission signal is not as strongly reduced as before, and that the decrease of B incorporation is, therefore, not as strong. The knowledge of the interplay between these growth parameters enables a very careful control of the growth and semiconducting properties of B-doped heteroepitaxial diamond. Furthermore, this study suggests that OES may be applied as a powerful standard tool for the precise control of doping processes, by using the measured BH emission signal to automatically adjust the composition in the feed gas during the CVD growth process.

Boron in the gas phase (*e.g.* intentional from a gas precursor or from background contamination) was found to have a dramatic effect on the nitrogen-induced growth rate enhancement of diamond. Despite addition of nitrogen in the gas phase being known to accelerate diamond growth by up to a factor of 10, it was observed that a few ppm of B in the gas phase is enough to completely inhibit this effect up to concentrations of $\geq 2000\,\text{ppm}\ N_2$. A strategy to restore the catalytic effect of nitrogen was employed by using oxygen to reduce the boron background. Systematic experiments have demonstrated that this is indeed possible, and that a well-defined threshold exists for the $\left[\mathrm{N}/\mathrm{B}\right]_{\mathrm{gas}}$ ratio in the gas phase separating standard (non-accelerated) growth from catalysed (accelerated) growth. OES studies of concomitant addition of B and N in the gas phase revealed that neither the BH emission signal is affected by addition of nitrogen, nor is the nitrogen-related CN emission signal affected by addition of boron. This behaviour strongly supports that the influence of boron on the nitrogen-induced growth rate enhancement must take place on the immediate surface of the diamond during growth, and not by mutual interaction in the gas phase. From this knowledge, considerations of the incorporation efficiencies of N and B in the diamond lattice then applied to the measured $\left[\mathrm{N}/\mathrm{B}\right]_{\mathrm{gas}}$ threshold for the growth rate enhancement, led to the estimation that the threshold coincides with an incorporation ratio of $\left[\mathrm{N}/\mathrm{B}\right]_{\mathrm{incorp.}}=1$. Growth rate enhancement requires an excess of nitrogen, resulting in $\left[\mathrm{N}/\mathrm{B}\right]_{\mathrm{incorp.}}>1$. In order to corroborate this hypothesis, elastic recoil detection analysis (ERDA) of diamond films grown with $\left[\mathrm{N}/\mathrm{B}\right]_{\mathrm{gas}}$ around the threshold was performed, yielding the remarkable result that, indeed, the incorporated N/B at the threshold is in the order of unity, with an averaged experimental value of 1.88±0.35.

The present result suggests a simple mechanism where the inhibition of the growth rate enhancement by nitrogen takes place via a local coadsorption of B and N. The formed BN pair is then overgrown and incorporated as a BN unit. The final proof of the incorporation of BN units may be obtained in future HRTEM and/or FTIR experiments. It can be expected that these results will improve our understanding of the growth mechanism and dopant incorporation in diamond and stimulate further theoretical work.

In the second part of this thesis, focus was given to the study of structural properties of boron-doped heteroepitaxial diamond on Ir, with special attention to the effects of B-doping of films with high dislocation densities. It was found that high dislocation densities in B-doped films also lead to the formation of high compressive or tensile stress depending on the deposition temperature, in a similar way to undoped films, which is explained in terms of the “effective climb” of dislocations. It was demonstrated that the stress state in the B-doped films is, therefore, dependent not only on the well-known lattice expansion due to B incorporation, but also on the additional stress caused by the deposition temperature. Consequently, the knowledge of the components of the stress tensor, *i.e.* a biaxial component and a hydrostatic component, is necessary in order to deduce the correct values for B concentration in the films from standard techniques, *e.g.* X-ray diffraction (XRD) and cathodoluminescence (CL). This result is not only relevant for heteroepitaxial diamond, but also for homoepitaxial diamond, since high dislocation densities are often observed during (111)-oriented homoepitaxial growth and they can also be introduced by sample preparation (*e.g.* mechanical polishing).

The knowledge of the stress state in the B-doped heteroepitaxial diamond films enabled a correct assessment and comparison of various techniques for the determination of the B incorporation in the films, including CL, XRD and SIMS (secondary ion mass spectroscopy), which allowed the measurement of an incorporation efficiency of ~20% for high-to-heavy doping (*i.e.* $\left[\mathrm{B}\right]>10^{20}\,\mathrm{cm}^{-3}$).

Imaging of dislocations for the reliable estimation of dislocation densities on plasma-etched undoped and B-doped heteroepitaxial diamond films was also investigated. A broad survey of etch parameters (*i.e.* gas composition, process pressure and temperature) was carried out, showing distinct etching behaviour depending on the etchant and also depending on whether the sample is undoped or B-doped. Two main types of etch-pit were identified: 1) inverted square pyramids with edges aligned along $\langle 110\rangle$ and 2) inverted square pyramids with edges aligned along $\langle 100\rangle$. Their asymmetric shape along the $[110]$ direction was found to be a pure geometric effect due to the off-axis direction of the diamond along the same direction. In these studies it was also shown that not only addition of oxygen via CO_2 to the hydrogen plasma enhances etch-pit formation (*i.e.* defect selectivity), but also B present in the gas phase (either intentionally or from background contamination) produces a similar enhancement. Furthermore, it was found that both pressure and temperature during etching play a major role in the final shape of the etch-pits, while the measured etch-pit densities remain effectively unaltered. The depth of the etch-pits (*i.e.* the angle of the 4 inner facets of the pyramid relative to the base plane) was found to depend strongly on the process temperature, and that a sharp switch from near-$\{112\}$ to near-$\{115\}$ facets takes place at 150 mbar, while a switch from near-$\{115\}$ to near-$\{117\}$ facets takes place at 50 mbar, with increasing temperature. These results have shown that the previously reported formation of near-$\{113\}$ facets is not a universal property of etch-pits, but rather process dependent.

Understanding the properties of dislocations in B-doped diamond is fundamental not only for the development of efficient strategies to reduce their density in the material, but also to understand their influence on the electrical properties of electronic devices such as p-n junctions and Schottky barrier diodes. The role of dislocations in the performance of diamond-based devices is currently very much unclear, *i.e.* it is still open whether single dislocations represent killer defects which have to be avoided completely or whether appreciable levels of dislocations are acceptable for a reasonable device performance (see situation for GaN devices). Therefore, dislocations in heavily B-doped heteroepitaxial diamond films were closely investigated in this thesis by HRTEM and auxiliary techniques, yielding several important results. Contrary to reported observations on undoped diamond grown with and without nitrogen, the dislocations in the B-doped film were found to propagate exclusively along $[001]$. Dislocations with an inclination of 15° relative to $[001]$ from the substrate switched to 0° once threading through the B-doped layer. Dislocations reaching the surface were found to terminate at etch-pits formed after an etch step, supporting the previous etch studies. By selecting different extinction conditions, both edge- and 45° mixed-type dislocations with Burgers vector $\vec{b} = a/2\langle 101\rangle$ were identified in the B-doped layer, in accordance with previous reports on undoped diamond. Combined EELS (electron energy loss spectroscopy) and HR ADF-STEM (high-resolution annular dark-field scanning transmission electron microscopy) analyses have shown for the first time that dislocations in the B-doped layer are enriched with B and that the intermittent contrast pattern typically observed along the dislocation line is correlated with an intermittent B-enrichment. From analysis of the strain field around a dislocation core combined with EELS spectra, it was shown that B-enrichment occurs in the region of tensile strain of the dislocation. Finally, EELS spectra from the dislocation core have shown that part of the incorporated B is in a perfect tetrahedral environment, while part is embedded in a lower coordination, as indicated by the presence of a π^* signal in the EELS spectra. The incorporation of B in lower coordination, which has been reported before to be present at twin and grain boundaries, was observed here for the first time also at individual dislocations.

In the third part of this thesis, highly-heavily B-doped heteroepitaxial diamond films grown on Ir/YSZ/Si(001) were applied for the first time as electrodes for electrochemical sensing. A thorough characterisation of heteroepitaxial diamond electrodes was performed by a variety of standard electrochemical techniques and the results were compared with polycrystalline diamond electrodes and with results from single crystal diamond-based electrodes in the literature. Inner-sphere and outer-sphere redox mediators were used to evaluate rate constants and to assess the surface quality of the material from cyclic voltammetry and impedance spectroscopy measurements. The resistance to fouling was evaluated with a more complex mediator and SECM (scanning electrochemical microscopy) maps of the surface of the electrodes were performed in order to investigate their electrochemical homogeneity. The results have clearly demonstrated that B-doped heteroepitaxial diamond electrodes possess remarkable performance, surpassing the ubiquitous polycrystalline diamond electrodes and equalling single crystal diamond electrodes in terms of background current (*i.e.* higher sensitivity), potential window (*i.e.* large available potential range of ~3.3 V for redox reactions), selectivity and homogeneity (*i.e.* the surface is remarkably pure in terms of phase, with absence of sp^2 carbon, and in terms of O-termination), and resistance to fouling (*i.e.* less prone to surface contamination by polar adsorbates). Boron-doped heteroepitaxial diamond has, therefore, established itself as a superior material to polycrystalline diamond for electrochemical sensing applications, and superior as well to single crystal diamond due to its inherent availability in larger areas.

In the last part of this thesis, heteroepitaxial diamond on Ir/YSZ/Si(001) was pioneered as Schottky barrier diodes (SBDs) for high-power switching applications. Several device structures were investigated using either Ni or Ir for the Schottky contact. It was successfully demonstrated that heteroepitaxial diamond-based SBDs can reach performances in forward bias on the same level as single crystal diamond-based SBDs with low dislocation densities and optimised structure which includes field-plate, despite the suboptimal device structure adopted in this work. The best heteroepitaxial diamond-based SBD (Ni-diamond junction) has shown excellent merits, such as low series resistance $R_S \cong 13.8\ \text{m}\Omega\ \text{cm}^2$, Schottky barrier height $\phi_B \cong 1.36$ eV and high rectification ratio of $\sim 10^{10}$. In reverse bias an effective blocking was compromised by the relatively high doping level in the drift layer, which resulted in a low breakdown voltage of −30 V and a Baliga’s figure of merit of $65.22\ \text{k}\Omega\ \text{cm}^{-2}$. The use of Ir for the Schottky contact was also pioneered in this work. This metal was expected to form a stable and temperature-resistant junction with an atomically sharp interface, surpass the performance of Pt-diamond and compete with WC-diamond junctions. However, SBDs fabricated with Ir resulted in poorer performance than the Ni-diamond counterparts for reasons that still need to be investigated in more detail. It is suspected that oxygen-termination of the surface by air-plasma etching before the junction was made may have damaged the diamond and, consequently, deteriorated the Ir-diamond interface. An investigation of this possibility will be left for a future work. Nonetheless, it was clearly demonstrated that heteroepitaxial diamond can indeed perform as Schottky rectifiers, and that much higher performances can still be achieved simply by optimising the device structure (*e.g.* with a more careful control over the drift layer thickness, of its B-doping level, and by employing edge-termination to homogenise the electric field near the metal-semiconductor junction). No clear evidence was found of detrimental effects of high dislocation densities. Finally, the best Schottky diode presented in this thesis, despite sub-optimised, was able to match and even surpass the later demonstrated heteroepitaxial diamond-based SBD from a Japanese group, a result which is highly motivating and which makes a bold statement about the huge potential for heteroepitaxial diamond on Ir/YSZ/Si(001) to be applied in high-end electronic applications.

Overall, the present thesis brings significant contributions not only to the understanding and to the improvement of B-doped heteroepitaxial diamond, but also to the understanding of B-doping and diamond growth in general, as the processes occurring in the gas phase during synthesis and the processes influencing the structural properties of diamond are of interest to the whole diamond community. Furthermore, with the B-doped diamond electrodes and the diamond-based Schottky diodes, heteroepitaxial diamond can, along with other materials, be part of the solution for what is arguably one of the most critical challenges that mankind faces in this century: the need to produce clean and renewable energy and to use this energy in an efficient manner. The work presented in this thesis contributes, therefore, with a humble step in this direction.

7 Supplementary information

7.1 Characterisation of the Burgers vectors of [001] dislocations by TEM

The following weak-beam dark-field (WBDF) TEM images were obtained in [110]-oriented FIB foil. In this orientation, all the dislocations, except the edge dislocations with Burgers vector $\vec{b} = a/2\left[110\right]$, can be identified. Indeed, all the diffraction vectors offered by the [110] zone axis are perpendicular to this Burgers vector, leading to the invisibility of this family of dislocations. The WBDF image of **Figure 7-1** was obtained with $g = 2\bar{2}0$ in the same region shown in **Figure 3-26** in section 3.4.3. It exhibits dislocations parallel to the [001] direction. In the WBDF image of **Figure 7-2** obtained with $g = 004$, some dislocations indicated by "E" in **Figure 7-1** vanished. This confirms that these dislocations are edge dislocations of type $\vec{b} = a/2\left[1\bar{1}0\right]$. The WBDF image of **Figure 7-3** has been obtained using the diffraction vector $g = 1\bar{1}1$. In this image, the dislocations labelled "M1" in **Figure 7-1** are invisible even though they present a small residual contrast due to the presence of Boron at the dislocation core, which can affect the diffraction contrast and the extinction conditions. This indicates that these dislocations are 45° mixed dislocations with Burgers vector of type $\vec{b} = a/2\left[10\bar{1}\right]$ or $\vec{b} = a/2\left[011\right]$. Indeed, these two vectors make an angle of 45° with the line of the dislocations, *i.e.* [001]. **Figure 7-4** shows WBDF image obtained with $g = \bar{1}11$. In this image the dislocations labelled "M2" in **Figure 7-1** vanished. They are 45° dislocations with Burgers vector $\vec{b} = a/2\left[101\right]$ or $\vec{b} = a/2\left[01\bar{1}\right]$. Again, a small residual contrast due to Boron segregation can be observed.

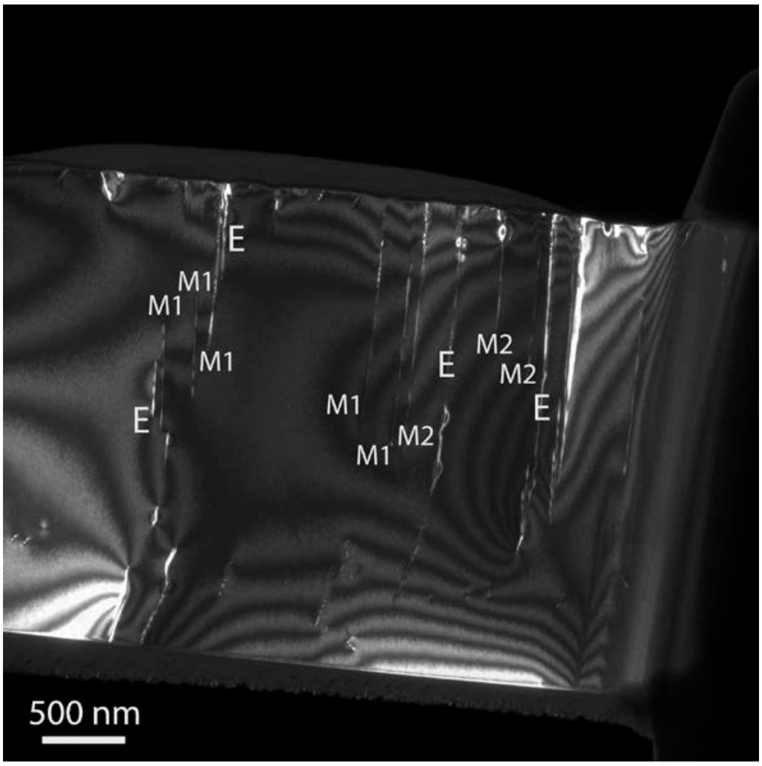

Figure 7-1: WBDF image obtained with $g = \bar{2}20$. Edge dislocations are indicated by “E”, while 45° mixed-type dislocations are labelled “M1” and “M2”.

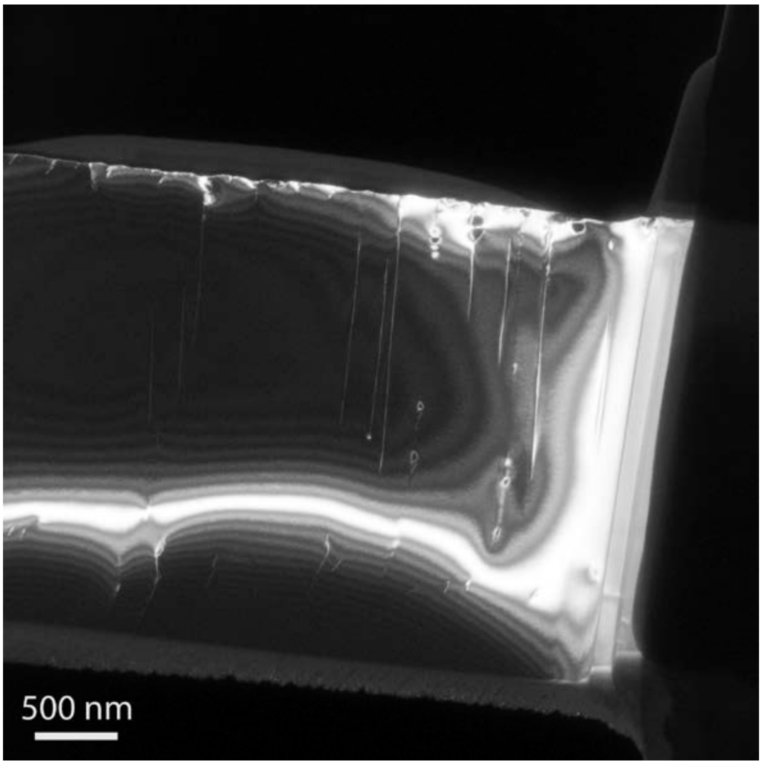

Figure 7-2: WBDF image obtained with $g = 004$.

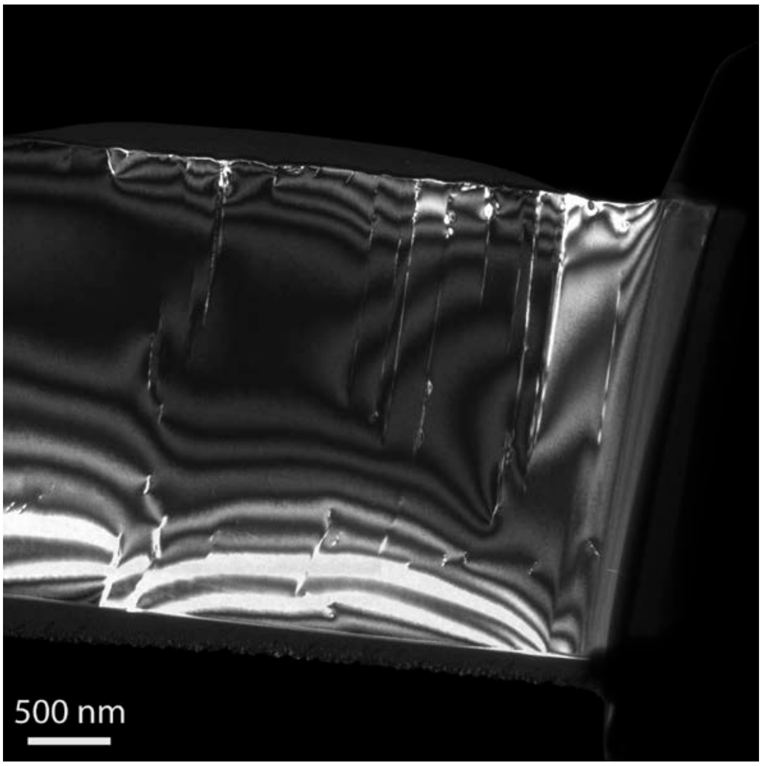

Figure 7-3: WBDF image obtained with $g = 1\bar{1}1$.

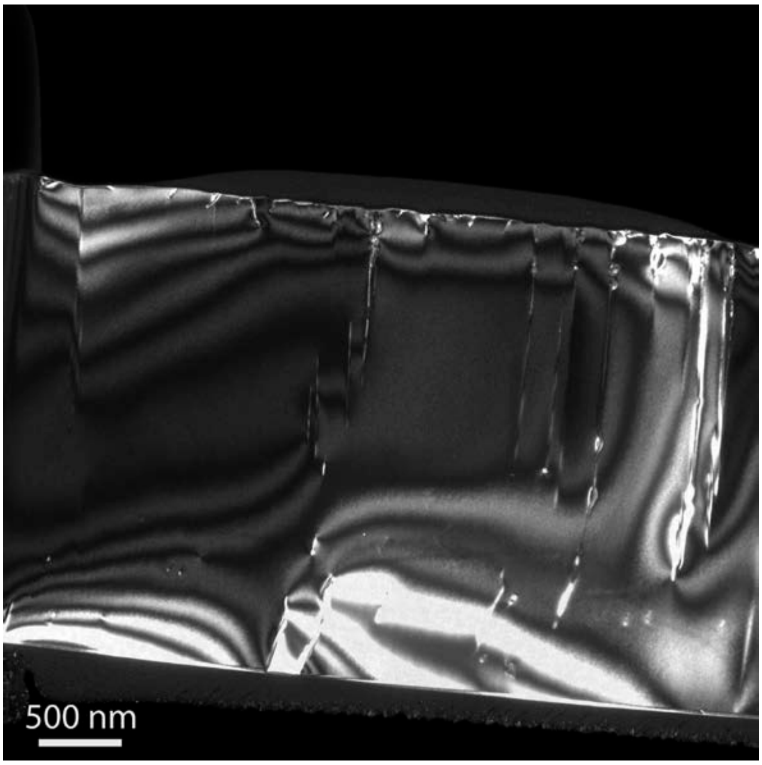

Figure 7-4: WBDF image obtained with $g = \bar{1}11$.

7.2 Evaluation of O-terminated B-doped diamond by XPS

Oxygen termination is a necessary step in the fabrication of diamond-based Schottky diodes, because it defines very strongly the Schottky barrier height by increasing the electron affinity up to 1.7 eV, which is crucial to the device's performance. In our laboratories we have three possible methods readily available to O-terminate diamond: 1) annealing in air at ~500 °C for 1 hour; 2) low pressure (0.6 mbar) air plasma treatment for 5 min; 3) hot chemical bath in boiling concentrated $H_2SO_4 + HCl + HNO_3$ (roughly 1:1:1) for 30 min. Chemical and plasma processes are the most common in the literature, therefore we focussed on those two. In order to find out which O-termination is most effective, we sent our standard heteroepitaxial B-doped diamond samples for XPS (X-ray photoelectron spectroscopy) analysis, courtesy of Johanna Larsson from the group of Prof. John Foord, University of Oxford. **Figure 7-5** shows the results of plasma treatment and **Figure 7-6** shows the results of the chemical treatment. Peak fitting was done with *CasaXPS* and normalisation by the Scofield RSFs.

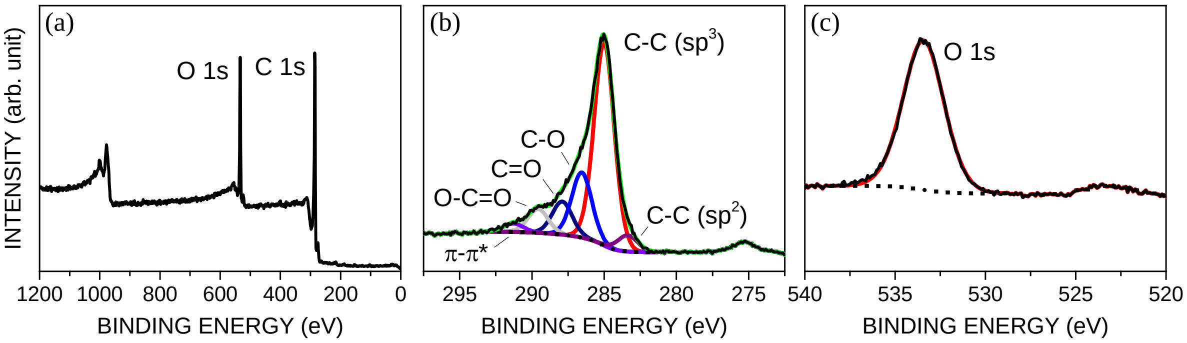

Figure 7-5: XPS of the B-doped sample treated in air plasma. (a) Survey scan; (b) C 1s region; (c) O 1s region. (b) and (c) are plotted in the same vertical scale.

The O/C ratio in the plasma-treated sample is surprisingly high; 10-15% is common for oxygen adsorbed on a polycrystalline B-doped diamond; 20% oxygen in the sample may suggest that O has been absorbed into the carbon layers. The number of oxygen functionalities (**Figure 7-5** (b)) is consistent with a large amount of oxygen.

Table 7-1: Normalised areas of O 1s and C 1s and the relative amount of O to C in the plasma-treated sample.

	O 1s	**C 1s**	**O/C**
Normalised area **%**	2491.07	10485.47	0.2375 **23.8**

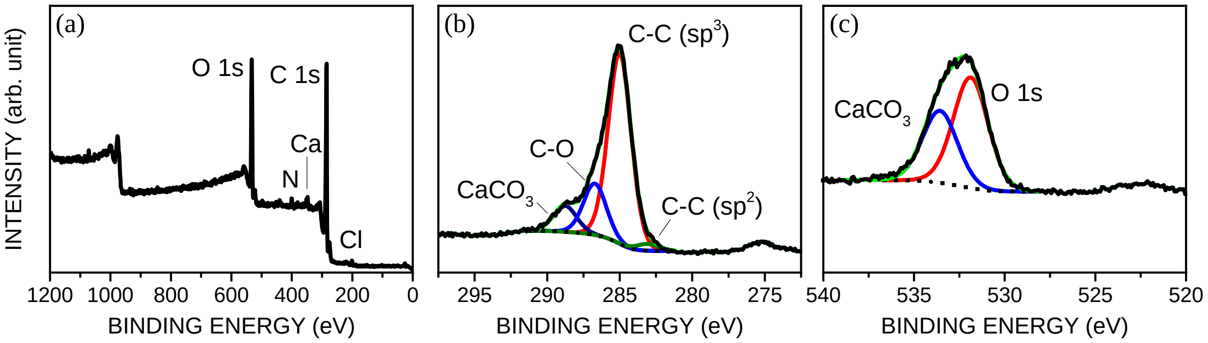

Figure 7-6: XPS of the B-doped sample treated chemically. (a) Survey scan; (b) C 1s region; (c) O 1s region. (b) and (c) are plotted in the same vertical scale, as is the $CaCO_3$ region (**Figure 7-7**). Note in (a) the presence of other functionalities in the C 1s region: N, Ca and Cl.

At first glance, the sample treated chemically shows a higher O/C than the plasma-treated one, but this is likely due to the presence of $CaCO_3$. If this contribution is ignored, the O/C ratio results therefore smaller. Note in **Figure 7-6** (a) the presence of more functionalities in the C 1s region, including Ca, N and Cl, which are likely impurities from the acids and tools used in the chemical process.

Table 7-2: Normalised areas of O 1s and C 1s and the relative amount of O to C in the sample treated chemically.

	O 1s	**C 1s**	**O/C**
Normalised area (total peak)	2005.69	7243.09	0.277
Normalised. Area (without $CaCO_3$)	1214.53	6556.21	0.185
%			**27.7 or 18.5**

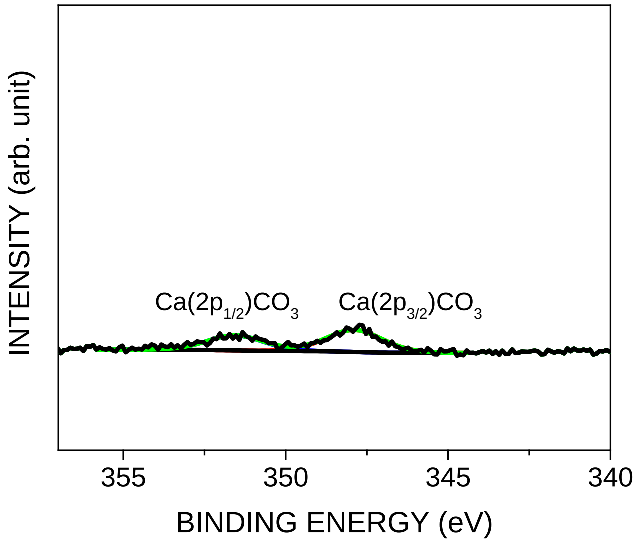

Figure 7-7: $CaCO_3$ region of the chemically treated sample.

The ratio of Ca to oxygen in **Table 7-4** matches the stoichiometric proportions of $CaCO_3$, supporting that the actual O coverage in the chemically treated sample is smaller than in the plasma-treated sample. The nature of the chemical process is, therefore, less efficient to O-terminate diamond than the air plasma treatment, and with the side-effect of leaving traces of undesired contaminants on the surface.

Table 7-3: Normalised areas of Ca 2p and C 1s and the Ca to C ratio in the sample treated chemically.

	Ca 2p	**C 1s**	**Ca/C**
Normalised area	265.36	7243.09	0.0366
%			**3.7**

Table 7-4: Normalised areas of Ca 2p and O 1s in the $CaCO_3$ environment (see **Figure 7-7**), and the Ca to O ratio in the sample treated chemically.

	Ca 2p	**O 1s ($CaCO_3$)**	**Ca/O**
Normalised area	265.36	791.16	0.335
%			**33.5**

Acknowledgements

I would like to acknowledge and thank everyone who was involved directly or indirectly in my PhD work during the last 5+ years, and who helped me achieve this milestone. My sincerest thank you:

- To the members of the committee, Prof. Dr Bernd Stritzker, Prof. Dr Hubert Krenner, Prof. Dr Achim Wixforth and Prof. Dr Gert-Ludwig Ingold for the interest in my work, for their diligence and kindness in accepting the roles of first, second and third examiners, and chairman, respectively.
- To my supervisor Dr Matthias Schreck, who gave me the opportunity to work in such a high-quality scientific environment and to be part of an exciting research community. Having him as a supervisor has been truly a privilege, and I am sure that his influence in my work will go beyond this thesis. Thank you for all the support during my stay in Augsburg.
- To my colleagues, Dr Stefan Gsell and Dr Martin Fischer, for all the help and support inside and outside the lab, and especially for the hundreds of substrates which were pivotal to my work. As you say, *“One sample is no sample!”*
- To my colleagues, Michael Weinl and Alexander Hartwig, for making our office a *cool* place to be and for helping one another with scientific, technical and humorous matters.
- To my colleague Christian Stehl for all the help inside and outside the lab and for his contribution with **Figure 1-12**.
- To my colleagues Michael Mayr and Björn-Christoph Gallheber for helping one another with our PhD work, for proofreading this thesis, and above all for the *cool* atmosphere, great sense of humour and tea sessions. Thanks to Michael Mayr for his contribution with **Figure 3-1**.
- To all the professors, scientists and former PhD students from the MATCON project, who all contributed to a very enjoyable period of my PhD. Special thanks goes to Dr Wiebke Janssen and Dr Roberta Caterino for our projects, secondments and hanging out together around Europe during various workshops and conferences.
- To Dr Jingping Hu, Dr Liang Chen and Prof. Dr John S. Foord for the fruitful cooperation which culminated in chapter 4 of this thesis, and to Johanna Larsson from the same group for contributing with supplementary XPS measurements in subchapter 7.2.
- To Dr Stuart Turner and his colleagues for the fruitful cooperation which materialised in subchapter 3.4 of this thesis.
- To Dr Andreas Bergmaier for his valuable contribution with ERD measurements in chapter 2.
- To apl. Prof. Dr Helmut Karl for his kind assistance with SIMS measurements.
- To Wolfgang Reiber and Wolfgang Brückner for their kind assistance with technical issues.
- To my former colleague Dr Cláudio Nico for his contribution with **Figure 1-20**.
- To all my friends who offered their support in various ways, especially to: Dr Marta Ferreira, Dr Naomi Dunning-Foreman and Dr Vasco Fernandes.

Résumé of the author

Personal data:

Name:	André F. Sartori
Date of birth:	13.12.1984
Place of birth:	Ribeirão Preto, SP – Brazil
Citizenship:	Brazilian, Italian
E-mail:	afsartori@outlook.com

Academic background:

01 Dec 2010 – 30 Apr 2016	**Research Associate (Wissenschaftlicher Mitarbeiter) at *Experimentalphysik IV, Universität Augsburg* (Germany)** From 01.01.2015 to 30.04.2016: Development of diamond-based Schottky rectifiers for high-power switching applications. Conclusion of PhD. From 01.12.2013 to 31.12.2014: BMBF funding (Contract No. 05K13WAA): synthesis (CVD) and characterisation of diamond-based substrates, electrodes and devices for high-end applications in the fields of semiconducting, electrochemistry and renewable energies. From 01.12.2010 to 30.11.2013: Early Stage Researcher in the EU-funded MATCON project (Materials and Interfaces for Energy Conversion and Storage, FP7/2009–2013) for the synthesis, characterisation and development of diamond-based substrates, electrodes and semiconducting devices for high-end applications. Website: www.matcon.nu.
21 Apr 2008 – 21 Jun 2010	**Research assistant (Protocol *Enérgica Sol*) at the Physics Department of *Universidade de Aveiro* (Portugal)** From 22.06.2009 to 21.06.2010: Development of rigid and flexible prototype modules/panels comprised of thin-film dye-sensitized solar cells for large-scale production. Patent application (PT104869). From 21.04.2008 to 21.06.2009: Research and development of low-cost dye-sensitized solar cells (photovoltaics), aiming for large-scale production.
26 Sep 2007 – 16 Dec 2009	**Master in Engineering Physics at *Universidade de Aveiro* (Portugal)** Title of Master thesis: "*Variação Temporal do Desempenho de Dye-Sensitized Solar Cells*" ("Variation of the performance of dye-sensitized solar cells over time")
28 Oct 2003 – 13 Nov 2008	**Bachelor in Engineering Physics at *Universidade de Aveiro* (Portugal)** Title of Bachelor thesis: "*Sistema Electrónico Autónomo de Aquisição De Dados Em Escala Temporal*" ("Autonomous electronic system for data acquisition over time")

List of publications:

First authorship

- **André F. Sartori** and Matthias Schreck; *Mutual interaction of N, B, and O during heteroepitaxial diamond growth: Triggering the nitrogen induced growth acceleration*. physica status solidi (a), 2014. 211(10): p. 2290-2295. DOI: 10.1002/pssa.201431239.
- **A. F. Sartori**, M. Fischer, S. Gsell, W. Janssen, K. Haenen, M. Schreck; *Heteroepitaxial diamond p-n diodes on Ir/YSZ/Si(001): growth and characterization*. Oral presentation at the International Conference on Diamond and Carbon Materials, 2-5 September, 2013, Riva del Garda, Italy.
- **A. F. Sartori**, C. Stehl, M. Fischer, S. Gsell, M. Schreck; *Dislocations in doped and undoped heteroepitaxial diamond crystals grown on Ir/YSZ/Si(001) visualized by etch pit formation*. Poster presentation at the Hasselt Diamond Workshop 2013 - SBDD XVIII, 27.02-01.03, 2013, Hasselt, Belgium.
- **André F. Sartori**, Martin Fischer, Stefan Gsell, and Matthias Schreck; *In situ boron doping during heteroepitaxial growth of diamond on Ir/YSZ/Si*. physica status solidi (a), 2012. 209(9): p. 1643-1650. DOI: 10.1002/pssa.201200221. ***Editor's choice.***
- **A. F. Sartori**, M. Fischer, S. Gsell, M. Schreck; *In-situ boron doping during heteroepitaxial growth of diamond on Ir/YSZ/Si(001)*. Oral presentation at the Hasselt Diamond Workshop 2012 - SBDD XVII, 14-16 March, 2012, Hasselt, Belgium.
- **A. F. Sartori**, M. Fischer, S. Gsell, M. Schreck, B. Stritzker; *Growth and Characterization of Boron-Doped Heteroepitaxial Diamond Films*. Poster presentation at the 22nd European conference on Diamond, Diamond-Like Materials, Carbon Nanotubes and Nitrides, 4-8 September, 2011, Garmisch-Partenkirchen, Germany.
- **A. F. Sartori**, A. F. da Cunha and L. C. Costa; *A Study of Dye-Sensitised Solar Cells' Electrical Performance Over Time and Its Limiting Factors*. Poster presentation at the ICOOPMA10 – 4th International Conference on Optical, Optoelectronic and Photonic Materials and Applications, 15-20 August, 2010, Budapest, Hungary.

Co-authorship

- Matthias Schreck, Michael Mayr, Oliver Klein, Martin Fischer, Stefan Gsell, **André F. Sartori**, Björn-Christoph Gallheber; *Multiple role of dislocations in the heteroepitaxial growth of diamond: a brief review.* physica status solidi (a), 2016. DOI: 10.1002/pssa.201600119.
- Stuart Turner, Hosni Idrissi, **André F. Sartori**, Svetlana Korneychuck, Yinggang Lu, Jo Verbeeck, Matthias Schreck, and Gustaaf Van Tendeloo; *Direct imaging of boron segregation at dislocations in B:diamond heteroepitaxial films*. Nanoscale, 2016. DOI: 10.1039/c5nr07535a.
- Jingping Hu, Liang Chen, **André F Sartori**, Matthias Schreck, John S Foord; *Electrochemical characterization of highly boron-doped heteroepitaxial (001) single crystalline diamond*. In preparation.
- P. A. Fernandes, P. M. P. Salomé, **A. F. Sartori**, J. Malaquias, A. F. da Cunha, Björn-Arvid Schubert, J. C. González, and G. M. Ribeiro; *Effects of sulphurization time on Cu_2ZnSnS_4 absorbers and thin films solar cells obtained from metallic precursors*. Solar Energy Materials and Solar Cells, 2013. 115: p. 157-165. DOI: 10.1016/j.solmat.2013.03.032.
- P. A. Fernandes, **A. F. Sartori**, P. M. P. Salome, J. Malaquias, A. F. da Cunha, M. P. F. Graca, and J. C. Gonzalez; *Admittance spectroscopy of Cu_2ZnSnS_4 based thin film solar cells*. Applied Physics Letters, 2012. 100(23): p. 233504-4. DOI: 10.1063/1.4726042.